2015

Reconstitution and Topological Analysis of Caveolin-1 in Model Membrane Systems

Kyle Todd Root
Lehigh University

Reconstitution and Topological Analysis of Caveolin-1 in Model Membrane Systems

by

Kyle T. Root

A Thesis

Presented to the Graduate and Research Committee

of Lehigh University

in Candidacy for the Degree of

Doctor of Philosophy

in

Chemistry

Lehigh University

January 2016

Approved and recommended for acceptance as a dissertation in partial fulfillment of the requirements for the degree of Doctor of Philosophy.

Kyle T. Root
Reconstitution and Topological Analysis of Caveolin-1 in Model Membrane Systems

_____
Date

_____
Dissertation Director
Kerney Jebrell Glover

_____
Accepted Date

Committee Members:

_____
Robert A. Flowers, II

_____
Linda Lowe-Krentz

_____
Damien Thévenin

ACKNOWLEDGMENTS

This dissertation was truly a “labor of love” and during this experience, many others helped carry the weight along the way. First, I must thank my adviser, Professor Kerney Jebrell Glover, for providing me with a challenging and exciting research project that I have taken much away from. I cannot stress enough how Dr. Glover, through guidance, and friendship has helped me grow as a problem solver, scientist, and an individual. He has truly instilled in me the type of work ethic and level of commitment that is required to make progress in research. I also would like to thank the members of my thesis committee: Professor Robert Flowers, Professor Linda Lowe-Krentz, and Professor Damien Thévenin who have all imparted upon me their scientific wisdom, help, and support over the years. I would like to thank Dr. Larry Courtney for his advice and gifts in synthesis pertaining to my project. I also need to give a word of thanks and appreciation to Dr. Wonpil Im who has contributed to my project immensely through our fruitful collaboration. I would like to give special thanks to my current and former lab mates: Sarah Plucinsky, Dr. Maxim Chudaev, Dr. Monica Rieth, and Dr. Jinwoo Lee as they have also been a source of scientific discussion, insight, and support over the years. They have helped make my time in the Glover lab a true joy. I also need to thank my friend Dr. Dong Li for his scientific insights. I would like to thank undergraduates who I have interacted with as a mentor and who have contributed to my research - they are too numerous to list. This work is dedicated to my family who have fostered and encouraged my love of science and who without, this dream may have never been a reality.

TABLE OF CONTENTS

List of Figures ix

List of Tables xii

List of Reaction Schemes xiii

List of Appendices xiv

List of Abbreviations xv

Abstract 1

Chapter 1. Caveolae, Caveolin, and Lipid Environments for the Biophysical Characterization of Membrane Proteins 3

- Caveolae 3
- Caveolin 5
- Caveolin Structure 9
- Membrane Proteins and Model Membranes Used in Biophysical Studies 17
- Biophysical Methods Used to Characterize Membrane Proteins 26

Chapter 2. Development of Perfluorooctanoic Acid as a Tool for Vesicle Formation and Caveolin-1 Topology Analysis 35

- Abstract 35
- Introduction 37
- Materials and Methods 40
  - Vesicle Formation 40
  - Protein Expression, Purification, and Mutagenesis 40
  - Reconstitution of $^{HSVFLAG}Cav1_{62-178}$ into Phospholipid Vesicles 43
  - Gel Filtration Experiments 44
  - Sodium Carbonate Extraction 44
  - Entrapment Assays 44
  - Dynamic/Static Light Scattering Experiments 46
  - Western Blot Analysis 47
  - Protease Protection Assay 48
- Results and Discussion 49

Characterization of Vesicle Formation using Gel Filtration Chromatography, Dynamic/Static Light Scattering, and Entrapment of Solutes 49
Reconstitution and Topological Evaluation of $^{HSVFLAG}Cav1_{62-178}$ 62
Conclusions 70
Chapter 3. Does Caveolin-1 Contain a Membrane Embedded Turn? 78
Abstract 78
Introduction 80
Materials and Methods 82
NMR spectroscopy 82
Single Tryptophan Mutant Cloning, Expression, and Reconstitution into Bicelles 82
Determination of λ_{max} for Single Tryptophan Mutants 84
Building a Structural Model for *In Silico* Analysis of Caveolin-1 84
Multiple 100 ns and 1 μs caveolin-1 simulations in DMPC bilayers 86
Results and Discussion 89
Probing the secondary structure of $Cav1_{82–136}$ 89
Defining the $Cav1_{82–136}$ Intramolecular Fold in a Lipid Bilayer 90
Evaluation of the Orientation and Membrane Depth of $Cav1_{82-136}$ in a DMPC Bilayer 95
Conclusions 105
Chapter 4. Cysteine Scanning Mutagenesis of Full Length Caveolin-1 Helps to Explain Its Multi-Faceted Interactome 111
Abstract 111
Introduction 112
Materials and Methods 116
Determination of gel (liquid ordered) to fluid (liquid disordered) transition temperatures for bicellar solutions 116
Cloning and Construction of Caveolin-1 Mutants 117
Protein Expression 118
Non-denaturing Purification of $^{mychis}Cav1_{1-178}$ into Phospholipid Bicelles using Mini-Nickel Spin Column for Circular Dichroism Spectroscopy Measurements 118
Circular Dichroism Spectroscopy Measurements 119
Large Scale Preparation of $^{mychis}Cav1_{1-178}$ into Phospholipid Bicelles for Analytical Ultracentrifugation Experiments 120
Sedimentation Equilibrium Experiments of $^{mychis}Cav1_{1-178}$ 121
Native Membrane Preparation from E. coli and Reconstitution into q_{eff} = 1.0 Bicelles 122
Chemical Accessibility Assays 123
SDS-PAGE and Immunoblotting 124

Image and Data Analysis 124
Results and Discussion 126
Construction of Helix-1 Cysteine Mutants and Chemical Accessibility Assay Principle 126
Validation of Bicelles using Fluorescence Anisotropy Measurements 127
Evaluation of the $^{mychis}Cav1_{1-178}$ Oligomeric State in Bicelles 130
Evaluation of Single Cysteine Mutants Effect on $^{mychis}Cav1_{1-178}$ Secondary Structure 133
Analysis of the CSD Topology Using Cysteine Scanning Accessibility Studies 136
Conclusions 153
Chapter 5. The Lipid Environment and Proline at Position 110 Modulate the Aqueous Exposure of Caveolin-1 157
Abstract 157
Introduction 159
Materials and Methods 165
Protein Expression and Purification 165
Labeling of $Cav1_{62-178}$(C133) with Dansyl Aziridine 166
Protein Reconstitution 167
Far and Near UV Circular Dichroism Spectroscopy 168
Tryptophan λ_{max} Determination and Fluorescence Quenching 169
Fluorescence Resonance Energy Transfer Experiments 170
Results and Discussion 172
Construct Design and Protein Reconstitution 172
Far and near UV Circular Dichroism Spectroscopy 173
Tryptophan λ_{max} Determination and Fluorescence Quenching: Comparison of $Cav1_{62-178}$ and $Cav1_{62-178}$ P110A Constructs 181
Tryptophan λ_{max} Determination, and Fluorescence Quenching of $Cav1_{62-178}$ Constructs: a Comparison of Micellar Environments 189
Fluorescence Resonance Energy Transfer Experiments: Comparison of Differing Micelle Environments 194
Conclusions 200
Chapter 6. Applications of Indole-PE: A Novel Lipid with a Tryptophan Headgroup for Use in Quenching Studies 205
Abstract 205
Introduction 206
Materials and Methods 208
$^{HSVFLAG}Cav1_{62-178}$ Single Tryptophan Mutant Cloning, Expression, and Reconstitution into Bicelles 208

Determination of λ_{max} for Single Tryptophan Mutants 209
Synthesis and Purification of Indole-PE 209
Reconstitution of Indole-PE into Vesicles and Bicelles 211
Measurement of Indole-PE Excitation and Emission Spectra 212
Measurement of Bilayer Permeability of Iodide and Acrylamide using Large Unilamellar Vesicles with Reconstituted Indole-PE 212
Fluorescence Quenching of Indole-PE and Single Tryptophan Mutants Reconstituted Into DMPC/DHPC Bicelles 213
Results and Discussion 215
Synthesis and Purification of Indole-PE 215
Bilayer Permeability of Commonly Used Quenchers 219
Tryptophan Scanning of Caveolin-1 in Bicelles Using Indole-PE as a Molecular Ruler 219
Conclusions 229
References 233
Vita 253

LIST OF FIGURES

Figure 1-1. Transmission electron micrographs and cartoon of caveolae 3
Figure 1-2. Caveolae functions in the cell 4
Figure 1-3. Sequence alignment of caveolin-1 across species 6
Figure 1-4. Sequence alignment of caveolin across human isoforms 7
Figure 1-5. Domain map of caveolin-1 10
Figure 1-6. Hydropathy plot of caveolin-1 12
Figure 1-7. Probing of Caveolin-1 termini using glycosylation mapping 14
Figure 1-8. Ambiguities in the caveolin-1 topology model 15
Figure 1-9. Mechanisms of caveolin induced membrane curvature 17
Figure 1-10. Model membranes 19
Figure 1-11. Detergents used in membrane protein research 21
Figure 1-12. Bicelle forming lipids and detergents 24
Figure 1-13. Simplified Jablonski diagram 28
Figure 2-1. Structure of PFOA 38
Figure 2-2. Gel filtration traces for vesicles formed using PFOA followed by refractive index 51
Figure 2-3. Elution volume of vesicles as a function of NaCl Concentration 52
Figure 2-4. Dynamic light scattering data for vesicles formed by detergent dialysis 54
Figure 2-5. Size of vesicles as a function of NaCl concentration 55
Figure 2-6. Variation of vesicle R_h as a function of the scattering angle and Zimm plot for vesicles formed by detergent dialysis 56
Figure 2-7. Theoretical entrapment volume plot for EYPC vesicles 59
Figure 2-8. Glucose-6-Phosphate entrapment experiment 61
Figure 2-9. Western blot analysis of reconstituted $^{HSVFLAG}Cav1_{62-178}$ 64
Figure 2-10. Limited proteolysis assay principle 65
Figure 2-11. Limited proteolysis assay evaluated by Western blot analysis 66
Figure 3-1. *In silico* model of caveolin-1in a planar DMPC bilayer 85
Figure 3-2. Chemical shift index plot of $Cav1_{82-136}$ 90
Figure 3-3. Population distribution for angle between H1 and H2 92
Figure 3-4. Rotation angle distribution of for H1 and H2 93
Figure 3-5. Amino acid side chain interactions of residues in H1 and H2 94

Figure 3-6. Population distribution of the $Cav1_{82-136}$ tilt angle 96
Figure 3-7. Population distribution for H1 and H2 independent tilt angles 97
Figure 3-8. Distance from the bilayer center for W85, W98, G108, I109, P110, W115 and W128 99
Figure 3-9. Procedure for the vesicle to bicelle transition technique 101
Figure 3-10. Fluorescence emission spectra for $Cav1_{82-136}$ single tryptophan mutants 102
Figure 3-11. Overlay of TROSY-HSQC spectra of $Cav1_{82-136}$ and $Cav1_{82-136}$(4F) .. 103
Figure 3-12. Topological disposition of $Cav1_{82-136}$ in a DMPC bilayer 105
Figure 4-1. Domain map of caveolin-1 highlight the CSD 112
Figure 4-2. Assay principle for cysteine scanning mutagenesis 127
Figure 4-3. Anisotropy as a function of $\boldsymbol{q}$ 130
Figure 4-4. Purification traces for large scale expression of $^{mychis}Cav1_{1-178}$ 131
Figure 4-5. Sedimentation equilibrium profiles for $^{mychis}Cav1_{1-178}$ 132
Figure 4-6. Reconstitution strategy to obtain highly pure $^{mychis}Cav1_{1-178}$ in bicelles 134
Figure 4-7. Far UV CD spectra for 30 $^{mychis}Cav1_{1-178}$ single cysteine mutants 135
Figure 4-8. Western blot analysis of membrane translocation of $^{mychis}Cav1_{1-178}$ single cysteine mutants 137
Figure 4-9. Comparison of cholesterol and cholesteryl hemisuccinate 138
Figure 4-10. Time course of the biotin-maleimide reaction for $^{mychis}Cav1_{1-178}$ single cysteine mutants 139
Figure 4-11. Biotinylation of single cysteine mutants of $^{mychis}Cav1_{1-178}$ in phospholipid bicelles composed of DMPC/DHPC and DMPC/DHPC/CHS 141
Figure 4-12. Relative biotinylation and average relative biotinylation plots for $^{mychis}Cav1_{1-178}$ single cysteine mutants DMPC/DHPC bicelles 142
Figure 4-13. Relative biotinylation and average relative biotinylation plots for $^{mychis}Cav1_{1-178}$ single cysteine mutants DMPC/DHPC/CHS bicelles 144
Figure 4-14. Speculative cartoon of $^{mychis}Cav1_{1-178}$ topology in DMPC/DHPC bicelles 149
Figure 4-15. Speculative cartoon of $^{mychis}Cav1_{1-178}$ topology in DMPC/DHPC/CHS bicelles 151
Figure 5-1. Comparison of cholesterol and cholesterol-PEG600 173
Figure 5-2. Far UV CD spectra for $Cav1_{62-178}$ constructs reconstituted in DPC micelles or DPC:cholesterol-PEG600 micelles 175

Figure 5-3. Near UV CD spectra for $Cav1_{62-178}$ constructs reconstituted in DPC micelles or DPC:cholesterol-PEG600 micelles 180

Figure 5-4. Steady state tryptophan emission profiles for $Cav1_{62-178}$ constructs in DPC micelles or DPC:cholesterol-PEG600 micelles 182

Figure 5-5. Modified Stern-Volmer quenching curves for $Cav1_{62-178}$ constructs in DPC micelles or DPC:cholesterol-PEG600 micelles 184

Figure 5-6. . Comparison of λ_{max} values obtained from tryptophan emission profile fits 188

Figure 5-7. Comparison of f_a values obtained from modified Stern-Volmer plots ... 194

Figure 5-8. Dansyl aziridine labeling of $Cav1_{62-178}$(C133) and

FRET assay principle 196

Figure 5-9. UV-Vis absorbance profile for dansyl aziridine labeled

$Cav1_{62-178}$(C133) 197

Figure 5-10. Comparison of dansyl-tryptophan FRET for $Cav1_{62-178}$ reconstituted into DPC micelles and DPC:cholesterol-PEG600 micelles 199

Figure 6-1. HPLC Purification trace, MALDI-TOF mass spectrum, ^{1}H NMR spectrum, and ^{31}P NMR spectrum for indole-PE 216

Figure 6-2. Vesicle permeability of acrylamide and iodide assessed using indole-PE 219

Figure 6-3. Excitation and emission spectra for indole-PE in bicelles 220

Figure 6-4. Quenching analysis of indole-PE in bicelles 221

Figure 6-5. Fluorescence emission spectra for $^{HSVFLAG}Cav1_{62-178}$ single tryptophan mutants reconstituted into bicelles 223

Figure 6-6. Stern-Volmer plots for $^{HSVFLAG}Cav1_{62-178}$ single tryptophan mutants reconstituted into bicelles 224

Figure 6-7. Modified Stern-Volmer plots for $^{HSVFLAG}Cav1_{62-178}$ single tryptophan mutants reconstituted into bicelles 225

Figure 6-8. Parameters from fluorescence analysis (λ_{max}, K_{SV}, f_a) as a function of sequence position for single tryptophan mutants and comparison to indole-PE 227

LIST OF TABLES

Table 1-1. Sequence identity as a percentage for caveolin-1 across species 6
Table 1-2. Sequence identity as a percentage for human caveolin isoforms 7
Table 2-1. Table of vesicle sizes obtained using DLS 57
Table 4-1. Table of relative biotinylation averages 146
Table 5-1. Table of secondary structure components for $Cav1_{62-178}$ constructs 177
Table 5-2. λ_{max} and $\Delta\lambda_{max}$ values obtained for single tryptophan mutants of $Cav1_{62-178}$ and $Cav1_{62-178}$ P110A 188
Table 5-3. f_a and Δf_a values obtained for single tryptophan mutants of $Cav1_{62-178}$ and $Cav1_{62-178}$ P110A 194
Table 6-1. Averaged values of tryptophan λ_{max}, K_{SV}, and f_a determined for indole-PE and $^{HSVFLAG}Cav1_{62-178}$ 228

LIST OF REACTION SCHEMES

Reaction Scheme 6-1. Synthesis of indole-PE 215

LIST OF APPENDICES

Appendix 2-1. Sequences of Protein Constructs Utilized in Chapter 2 72
Appendix 2-2. Mutagenesis Primers Utilized in Chapter 2 73
Appendix 2-3. PCR Cycling Conditions 74
Appendix 2-4. Transformation Protocols 75
Appendix 2-5. Starter and Media Recipes 76
Appendix 2-6. Auto-Induction Growth Protocol 77
Appendix 3-1. Average Values of Parameters for $Cav1_{82-136}$ from MD Simulations 108
Appendix 3-2. Sequences of Protein Constructs Utilized in Chapter 3 109
Appendix 3-3. Mutagenesis Primers Utilized in Chapter 3 110
Appendix 4-1. Sequences of Protein Constructs Utilized in Chapter 4 155
Appendix 4-2 Mutagenesis Primers Utilized in Chapter 4 156
Appendix 5-1 Sequences of Protein Constructs Utilized in Chapter 5 203
Appendix 5-2. Mutagenesis Primers Utilized in Chapter 5 204
Appendix 6-1. Sequences of Protein Constructs Utilized in Chapter 6 230
Appendix 6-2. Mutagenesis Primers Utilized in Chapter 6 232

LIST OF ABBREVIATIONS

AUC: Analytical Ultracentrifugation

BAR Domain: Bin-Amphiphysin-Rvs Domain

Biotin-Maleimide: N^{α}-(3-Maleimidylpropionyl)Biocytin

Cav1: Caveolin-1

CBC: Critical bicelles forming concentration

CD: Circular Dichroism Spectroscopy

CHAPSO: 3-[(3-Cholamidopropyl)dimethylammonio]-2-hydroxy-1-propanesulfonate

CHS: Cholesteryl hemisuccinate

CMC: Critical Micelle Concentration

CRAC: Cholesterol Recognition/Interaction Amino Acid Consensus Motif

CSD: Caveolin Scaffolding Domain

CSI: Chemical Shift Index

DMPC: 1,2-dimyristoyl-*sn*-glycero-3-phosphocholine

DHPC: 1,2-dihexanoyl-*sn*-glycero-3-phosphocholine

DHePC: 1,2-diheptanoyl-*sn*-glycero-3-phosphocholine

DLS: Dynamic Light Scattering

DPC: n-dodecylphosphocholine

DPH: 1,6-Diphenyl-1,3,5-hexatriene

DPPC: 1,2-dipalmitoyl-*sn*-glycero-3-phosphocholine

DTT: Dithiothreitol

EDTA: ethylenediaminetetraacetic acid

eNOS: Endothelial Nitric Oxide Synthase

EYPC: Egg Yolk Phosphatidylcholine

FRET: Fluorescence Resonance Energy Transfer

HFIP: 1,1,1,3,3,3-Hexafluoroisopropanol

HPLC: High Performance Liquid Chromatography

HSQC: Heteronuclear Single Quantum Coherence Spectroscopy

IMD: Intramembrane Domain

LMPG: 1-myristoyl-2-hydroxy-sn-Glycero-3-[Phospho-rac-(1-glycerol)]

MALDI-TOF: Matrix Assisted Laser Desorption-Ionization Time of Flight Mass Spectrometry

MD: Molecular Dynamics

MDAG: Minimal Non-Inducing Media with Glucose

MW: Molecular Weight

MWCO: Molecular Weight Cut Off

NMR: Nuclear Magnetic Resonance Spectroscopy

NOESY: Nuclear Overhauser enhancement spectroscopy

PBS: Phosphate Buffered Saline

PE: Phosphatidylethanolamine

PEG: Polyethylene glycol

PFOA: Perfluorooctanoic Acid

POPC - 1-palmitoyl-2-oleoyl-*sn*-glycero-3-phosphocholine

SDS-PAGE: Sodium Dodecylsulfate Polyacrylamide Gel Electrophoresis

SLS: Static Light Scattering

TBS: Tris Buffered Saline

TBST: Tris Buffered Saline with Tween

TCEP: *tris*(2-carboxyethyl)phosphine

TROSY: Transverse Relaxation-Optimized Spectroscopy

UV: Ultraviolet

UV/VIS: Ultraviolet/Visible

ABSTRACT

Caveolae are 50-100 nm invaginations in the plasma membrane of eukaryotes that are involved in a number of important cellular processes. The integral membrane protein, caveolin-1, is a key architectural component within caveolae. Despite the preeminent role that caveolin holds in maintaining functional caveolae, there is no three-dimensional structure available. Part of understanding the three-dimensional structure of caveolin requires defining its depth within the biological membrane. Only a hazy picture of caveolins topology exists, it is known that the global topology of the protein is such that the N- and C- termini reside on the cytoplasmic face of the membrane. In this body of work, the topological disposition of the integral membrane protein caveolin-1 reconstituted into model membrane systems is elucidated using biochemical and biophysical techniques. Chapter 1 is provided to give adequate background needed to familiarize the reader with the body of knowledge pertaining to the caveolin protein, vehicles for studying membrane proteins, as well as biophysical techniques that are employed in the remaining chapters. In Chapter 2, the characterization of a major methodological advancement using perfluorooctanoic acid-lipid mixtures to reconstitute protein into liposomes by detergent dialysis is presented. This chapter tackled the challenge of natively refolding caveolin-1 from a highly-purified denatured state and may be useful for reconstitution studies in general. In Chapter 3, a combined biophysical approach using fluorescence spectroscopy, nuclear magnetic resonance, and molecular dynamics simulations is taken to generate a model of caveolin-1 (residues 82-136) within a lipid bilayer. These studies strongly suggested that caveolin contains a membrane embedded turn, an unusual motif in membrane proteins. Chapter 4 deepens and supports

the model presented in Chapter 3 by employing cysteine scanning mutagenesis to examine the accessibility of the caveolin-1 scaffolding domain (residues 82-101), a region which is critical to the proteins function. These studies pinpoint the caveolin scaffolding domain as being the region of the protein that first enters the bilayer and provide a clear rationale for how this region can interact with a diverse group of soluble and membrane bound ligands. Chapter 5 examines the topological significance of two major factors thought to impact the caveolin-1 conformation and aqueous exposure, a highly conserved proline residue (P110) located within the putative intramembrane turn region and the inclusion of cholesterol. Near and far ultraviolet circular dichroism measurements paired with single tryptophan mutant λ_{max} and fluorescence quenching experiments provide insight into structural and accessibility changes that the P110A mutation and translocation of the protein into a cholesterol rich environment bring about. Chapter 6 details the synthesis of a novel lipid that contains an indole headgroup (indole-PE) as well as its potential as a molecular ruler in fluorescence studies. Importantly this probe draws light on the behavior of commonly employed tryptophan fluorescence quenching reagents and aids in the interpretation of tryptophan fluorescence quenching experiments performed on caveolin-1 single tryptophan mutants reconstituted into phospholipid bicelles.

Chapter 1. Caveolae, Caveolin, and Lipid Environments for the Biophysical Characterization of Membrane Proteins

Caveolae

The biological membrane has a number of roles within the cell; it provides protection of the cells interior from the harsh outer environment, gives the cell its identity, allows nutrient influx, waste secretion, compartmentalizes cellular organelles, and localizes specific homeostatic processes. Caveolae (plural caveola) are 50-100 nm invaginations that are dispersed throught the plasma membrane of eukaryotic organisms, bulging inwards towards the cytoplasm. These structures were first observed using electron microscopy in the 1950's (Figure 1-1 A-C) [1,2].

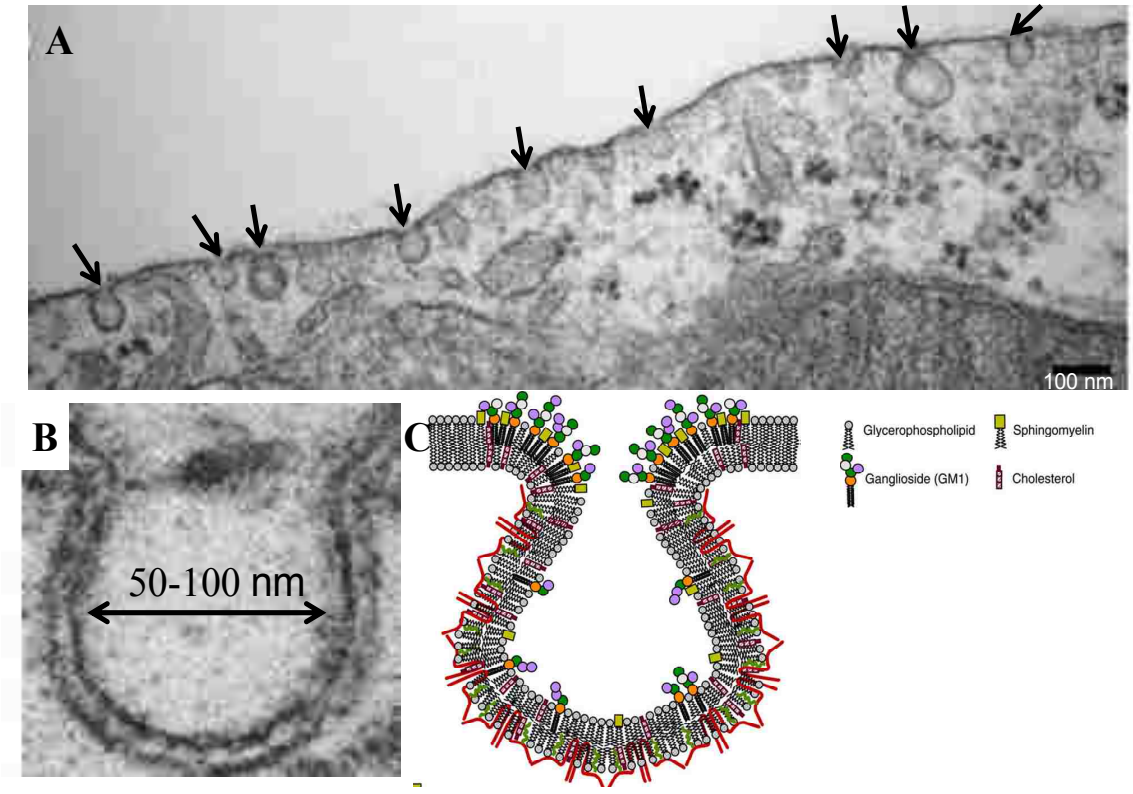

Figure 1-1. A) Transmission electron micrograph of caveola scattered across the surface of the plasma membrane (arrows). **B)** Close up image of a single caveolae which are 50-100 nm in diameter. **C)** Cartoon showing the molecular constituents enriched in caveolae: Cholesterol, gangliosides, glycerophospholipids, sphingomyelin, and the membrane protein caveolin [24].

Since their initial discovery, caveolae have been observed in many cell types including adipocytes, endothelial cells, fibroblasts, and smooth muscle cells [1,3-5]. Furthermore, caveolae appear to be associated with the entire metazoan (vertebrate and invertebrate animal branch) branch of opisthokonta [6], highlighting the biological importance of these highly curved microdomains. Such high levels of conservation is owed to the multitude of functions ascribed to caveolae, which include mechanoprotection, non-clatherin mediated endocytosis, and most notably, signal transduction (Figure 1-2) [7-10].

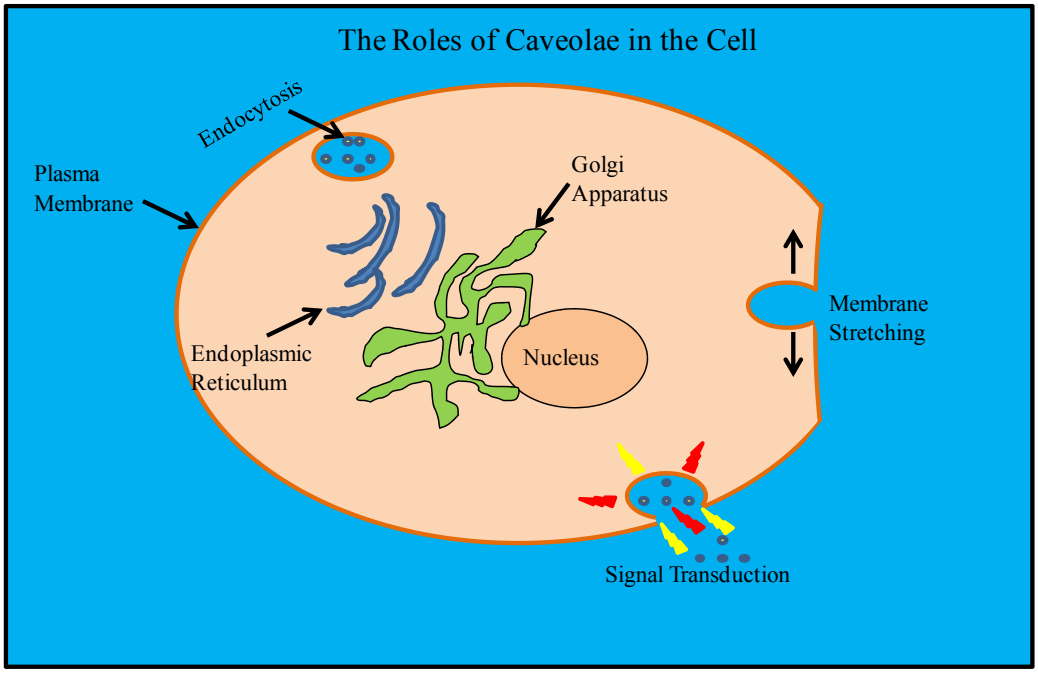

Figure 1-2. Diagram of a cell detailing the proposed functions attributed to caveolae.

When a force is exerted upon a cellular membrane causing it to stretch, caveolae dissipate; therefore caveolae can act as a lipid reservoir, and this helps avoid mechanical rupture of the cell [11]. Once the force is removed, caveolae reform. The flask-like shape of caveolae facilitates the endocytotic budding off from the membrane, and they can carry various biomolecules to other regions of the cell [12]. Furthermore, they have also been implicated in viral entry into cells through endocytosis [13-15]. Caveolae aid the cell

by acting as signaling hubs; specific examples of proteins which are thought to be regulated within caveolae include endothelial nitric oxide synthase, Src tyrosine kinases, H-ras, and G protein α-subunits [16-21]. A transmission electron micrograph of caveola along the cell surface is shown in figure 1-1A. Figure 1-1B displays a close up image of a single caveolae [22-24]. Caveolae also have a unique lipid composition that differs from that of the plasma membrane (Figure 1-1C). They are enriched in cholesterol (twice the amount in the bulk membrane) and sphingolipids - although recent studies have cast doubt on the latter from being significantly greater than what is found in the bulk plasma membrane [25,26]. Importantly, cholesterol is thought to be a stabilizing factor to caveolae by providing structural support. Evidence of cholesterol providing structural support comes from studies where cells were treated with cholesterol depleting drugs resulted in caveolae that had a dramatically flattened morphology [27,28]. The most important and abundant protein in caveolae is the integral membrane protein caveolin. Gene silencing studies have shown that when caveolin is not expressed, there is a *complete disappearance* of caveolae from the cell surface [16]. Additionally, expression of caveolin in cell lines and organisms that do not normally express the protein has been shown to induce the formation of caveolae [29,30]. These studies have implicated caveolin as an architect of caveolae morphology. Despite the plethora of functions that are ascribed to caveolae, the exact molecular details of caveolin structure, oligomeric behavior, and topology have remained mysterious from a biophysical perspective.

Caveolin

The gene encoding for caveolin is found in eukaryotic organisms ranging from *C. elegans* (roundworm) up to *H. sapiens* (humans) (Figure 1-3A, Table 1-1) [31,32].

Interestingly caveolae formation has not been observed in *C. elegans,* but has been confirmed for *D. rerio* (zebra fish) [33]. In humans, there are three isoforms of the protein that have been identified; caveolin-1, -2, and -3, each having a molecular weight of roughly 22 kDa (Figure 1-4, Table 1-2).

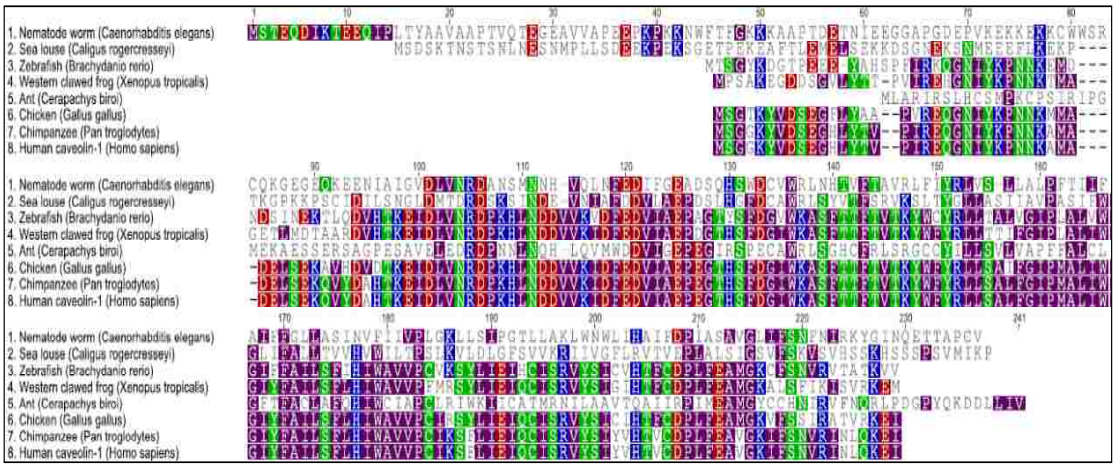

Figure 1-3. Sequence alignment for caveolin-1 across species. Conserved hydrophobic, polar uncharged, negatively charged, and positively charged residues are shown in *purple*, *green*, *red*, and *blue* respectively.

Species	Nematode	Sea louse	Ant	Zebra fish	Frog	Chicken	Chimp	Human
Nematode	100	21.6	22.9	25.4	22.3	22.8	26.1	26.1
Sea louse	21.6	100	18.8	27.5	26.5	27.1	27.1	27.1
Ant	22.9	18.8	100	27.4	23.8	25.6	25.6	25.6
Zebra fish	25.4	27.5	27.4	100	68.5	72.9	72.9	72.9
Frog	22.3	26.5	23.8	68.5	100	78.9	75	75
Chicken	22.8	27.1	25.6	72.9	78.9	100	86.5	86.5
Chimp	26.1	27.1	25.6	72.9	75	86.5	100	100
Human	26.1	27.1	25.6	72.9	75	86.5	100	100

Table 1-1. Sequence identity as a percentage for caveolin-1 across species.

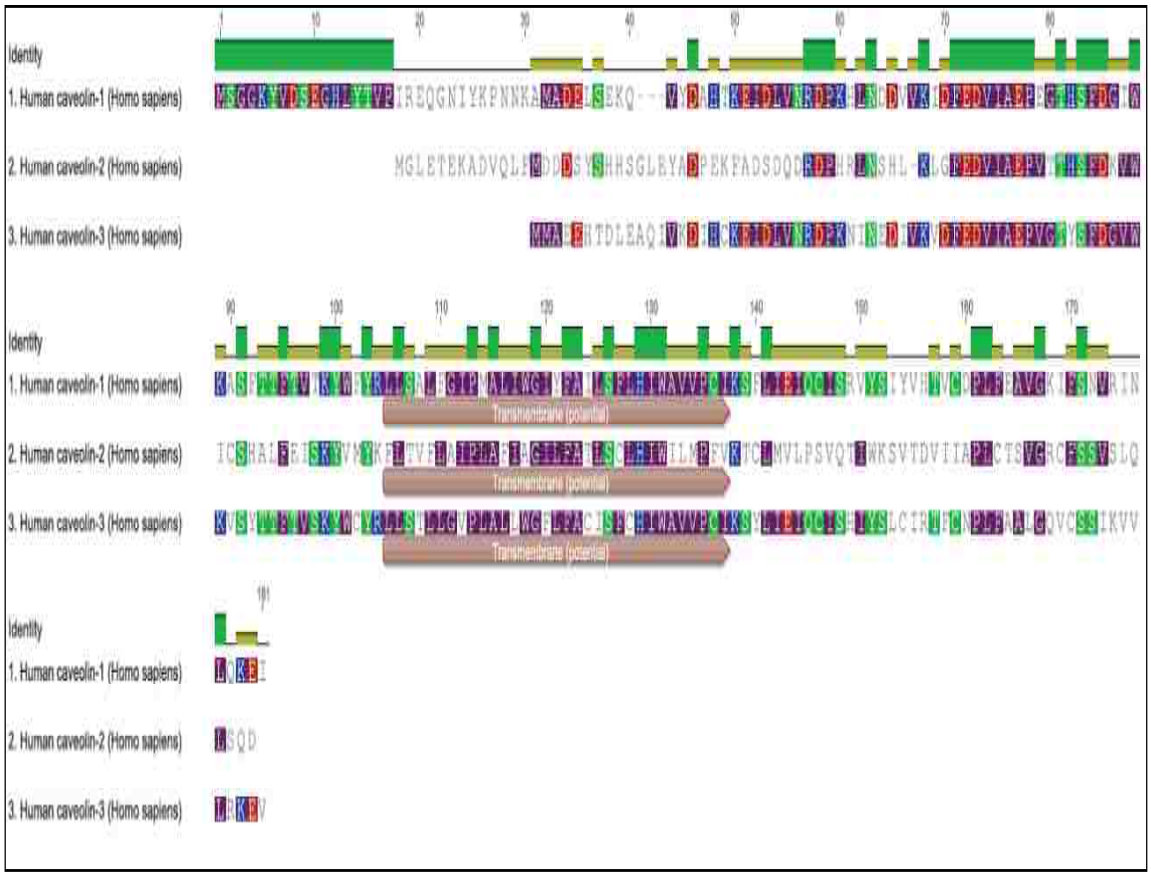

Figure 1-4. Sequence alignment of caveolin isoforms from humans. Conserved hydrophobic, polar uncharged, negatively charged, and positively charged residues are shown in *purple*, *green*, *red*, and *blue* respectively. The "Identity" bar indicates the level of amino acid conservation where *green* and *yellow* regions indicate identical and similar respectively. Transmembrane regions are indicated below the sequence of each isoform.

Caveolin Isoform	Caveolin-1	Caveolin-2	Caveolin-3
Caveolin-1	100	33.1	62.9
Caveolin-2	33.1	100	34
Caveolin-3	62.9	34	100

Table 1-2. Sequence identity as a percentage across human isoforms.

Caveolin-1 is the most ubiquitously expressed of the isoforms and is found in many cell types. It is present either as caveolin-1α (178 amino acid) or an N- terminally truncated caveolin-1β form (missing the first 33 amino acids) [34]. It is thrice palmitoylated at positions 133, 143, and 156, which has been shown to be unimportant for trafficking of

the protein to the plasma membrane, downplaying any structural role for this post-translational modification [35]. Caveolin-2 is often co-expressed with caveolin-1 and interestingly, (akin to *C. elegans* caveolin) cannot form caveolae on its own [36]. Caveolin-3 has the ability to form caveolae on its own and is specifically found within skeletal muscles cells, smooth muscle cells, and cardiac myocytes [37-39].

Caveolins homo- and hetero-oligomerize into Triton-X-114 resistant 200, 400, and 600 kDa complexes *in vivo*, and this oligomeric activity is postulated to provide structural stability to caveolae [40-42]. However, it is not clear how these complexes arise *in vivo*, and recent *in vitro* studies have suggested that caveolin-1 cannot homo-oligomerize in the absence of cellular components [43]. More recent examinations of the molecular components of the caveolar coat have revealed that caveolin homo- and hetero-oligomers are associated with another family of membrane proteins known as cavins, and that cavins are necessary for the formation of caveolae [44]. It has been shown using fluorescence correlation spectroscopy studies of fluorescent protein tagged caveolin and cavins that the four members of the cavin protein family (cavin1-4) associate with caveolin in a 1:4 stoichiometry. It has been observed that different cell types express different complements of the cavin isoforms. It is thought that the different complements of cavin-caveolin complexes may be in part responsible for the functional diversity of caveolae across cell types [45]. Studies on caveolin-1 have suggested that the protein binds cholesterol on a 1:1 molar ratio, however, the exact site of binding and the structural implications on caveolin are poorly characterized [19,46].

It cannot go without mention that caveolin misregulation and disfunction has been implicated in a number of human disease states. This fact has largely been responsible in

generating vast interest in the caveolin proteins. This list of diseases that caveolin has been implicated in is large, a non-exhaustive list includes: cancer, diabetes, cardiovascular disease, atherosclerosis, pulmonary fibrosis, and muscular degenerative diseases [47-56]. In terms of how misregulation of the caveolin protein is involved with disease, there appears to be tissue specificity. For example, caveolin-1 up-regulation is associated with increased metastasis of prostate cancers [57]. On the other hand, caveolin knock-out mice showed increased tumor proliferation, pointing to a role of caveolin as a tumor suppressor [58,59]. Clearly, there is a delicate balance of caveolin expression levels required for proper cell function. Very few specific mutations are associated with disease states; however, a prominent example is in breast cancer where there is a mutation of proline 132 to leucine in caveolin-1. The molecular mechanism of how this mutation disrupts normal caveolin function has been uncovered, where improper oligomeric behavior (dimerization) results in the retention of the protein in the Golgi apparatus [43,60,61]. An analogous mutation in caveolin-3, P104L, has also been shown to be associated with cardiomyapathies and results in poor myoblast function [62,63]. Therefore, proper structuring of caveolin is critical to many aspects of cellular homeostasis.

Caveolin Structure

Caveolin-1 is typically divided up into four structural domains: The N-terminal domain, the scaffolding domain, the intramembrane domain, and the C-terminal domain (Figure 1-5). Each of these domains is suggested to contribute to caveolin function in a variety of ways. The domains will be discussed in the context of caveolin-1 as it is the subject of this dissertation.

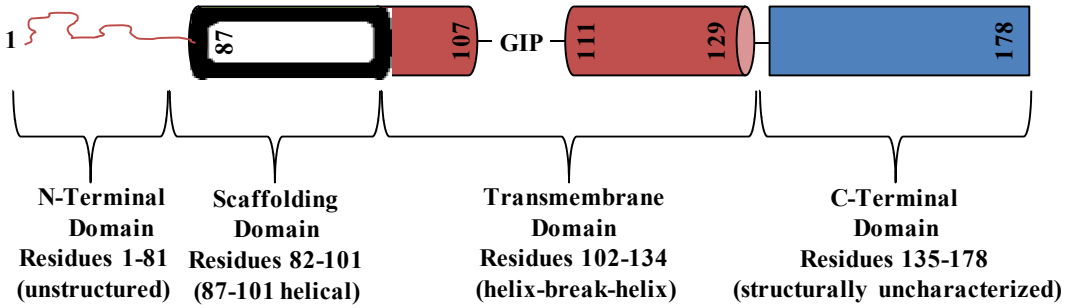

Figure 1-5. Domain map of caveolin-1. Each domain is color coded and the degree to which the secondary structure is known is indicated.

The soluble N-terminal domain (residues 1-81) is the most highly variant region of the protein across human isoforms and across species, differing in both its length and amino acid composition. It has been implicated in various aspects of caveolin behavior such as enhancing cholesterol binding and being important to caveolin filament assembly [64,65]. It has been shown to be unstructured by circular dichroism (CD) spectroscopy [65]. Primary sequence analysis algorithms have also suggested the presence of a single amphipathic helix, which may interact with the membrane surface [66].

The next domain in caveolin has been dubbed the caveolin scaffolding domain (CSD, residues 82-101). This domain has been implicated in a number of caveolins proposed functions. In particular, the CSD is thought to govern caveolins association with binding partners as it interacts with a number of cell signaling proteins (Src-like kinases, Ha-Ras, endothelial nitric-oxide synthase (eNOS), and G protein α-subunits), associates with cholesterol, and has been shown to be important for caveolin-1 oligomeric behavior *in vivo* [16-21]. Early models of caveolin structure based on sequence analysis predicted this region to have an amphipathic α-helix stretching from residues 80-92 in caveolin-1 [66]. Helical character in this region has been supported by a number of

studies employing NMR and CD spectroscopy [67,68]. However, recent solid-state NMR studies suggest that the CSD may adopt β-strand character in the presence of cholesterol. Due to the exotic conditions of these experiments (very high concentrations of truncated caveolin-based peptides), it is not clear if the β-strand character is an artifact of irrelevant protein aggregation, or if it is indeed an effect of cholesterol on the protein [69].

The C-terminus (residues 135-178) has a variety of purported functions that include membrane binding, signaling interactions, and mediating oligomeric behavior [40]. It is also the region of the protein that contains two of the three sites of palmitoylation on caveolin-1; these post translational modifications may help anchor this portion of the protein to the membrane. Little is known about the C-terminal domain in terms of the secondary structure; however, helix prediction software and NMR studies currently being undertaken in the Glover lab indicate that it may be composed of a long amphipathic α-helix that rests on the surface of the membrane.

The most highly conserved domain across isoforms and across species is the intramembrane domain (IMD residue 102-134 in caveolin-1). This region was predicted to be composed of two transmembrane α-helices separated by a 3-4 residue break using primary sequence analysis algorithms [66]. Recent NMR spectroscopy experiments performed on the 96-136 region of caveolin-1 have supported this postulation and identified two α-helices, one stretching from residues 96-107 and the other stretching from residues 111-128. These residues were separated by a three residue unstructured region consisting of a glycine (108), isoleucine (109), and proline (110). Importantly, these studies have pinpointed the IMD as being the structural core of the protein [70]. The three residues that break the helices have unique character that seems to be critical for

maintaining a well structured protein and they may represent a turn [70]. Glycine and proline are commonly found in turns, due to their conformational freedom and rigidity respectively, therefore this hypothesis is very reasonable. The IMD has been shown to be membrane embedded using a carbonate extraction method, which distinguishes surface associated membrane proteins from integral membrane proteins [71,72]. Analysis of the primary sequence using transmembrane prediction software indicates that caveolin-1 has an unusually long 33 amino acid stretch that is predicted to be membrane embedded because it is predominantly populated with aromatic and aliphatic amino acids (Figure 1-6).

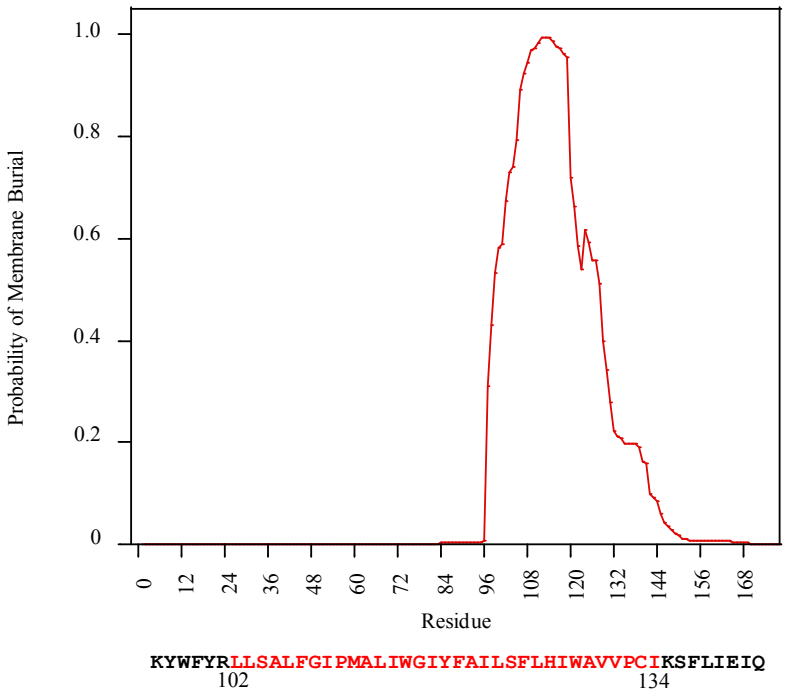

Figure 1-6. Hydropathy plot generated using the primary sequence of caveolin-1. The predicted 33 amino acid transmembrane sequence is indicated (*red*) and spans residues 102-134.

This differs from the length of most single spanning transmembrane helices which are 20-25 amino acids in length.

Therefore, caveolin is too long to span the bilayer once but too short to span the bilayer multiple times. Essentially, this sequence analysis inferred two models, one in which the long 33 amino acid stretch was highly tilted and traversed the bilayer as a single spanning α-helix, or one where the N- and C- termini rested on the same side of the membrane and would require a *dramatic* turn within the transmembrane sequence. The first study that examined the directionality of the termini used cell surface biotinylation probes and pointed to a single spanning α-helix with the N-terminus being cytoplasmic and the C-terminus resting outside of the cell [73]. Around the same time, a competing group performed studies that probed the location of the N- and C- termini using *in vivo* immuno-fluorescence. The immuno-fluorescence study failed to see labeling of the caveolin protein using antibodies directed to either terminus unless the cells were permeabilized, suggesting that both termini are luminal [71]. This issue was finally resolved when the biotinylation experiment was revisited and it was determined that an impurity in the earlier study was giving a false positive [42]. In support of the immuno-fluorescence studies, and finally leading the field to a topological consensus, a study where a caveolin-1 construct with glycosylation epitopes at each of its termini was translated *in vitro* in the presence of dog pancreas microsomes was not glycosylated (Figure 1-7) [74].

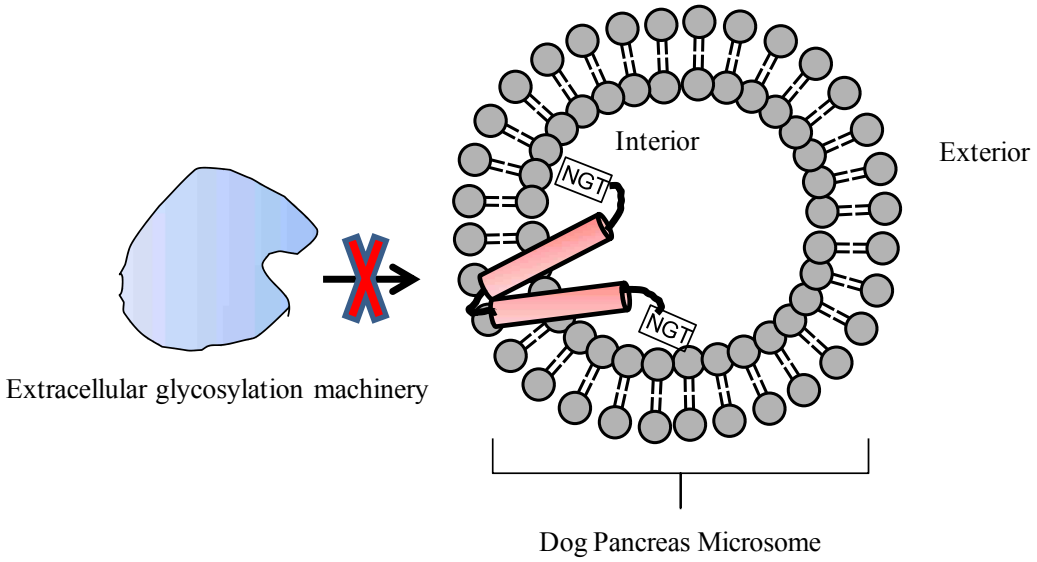

Figure 1-7. Early glycosylation epitope (asparagine/glycine/threonine) mapping study of caveolin-1 indicated that the N- and C- termini were inaccessible using an *in vitro* transcription/translation system.

This meant that neither of the epitopes were accessible to extracellular glycosylation machinery, adding support for the termini having an intracellular location. Combining sequence analysis and the aforementioned studies, along with the fact that the protein contains no soluble interruptions within its predicted transmembrane sequence, lead to the postulation that caveolin may contain an unusual intramembrane turn. As mentioned above, the protein contains a triplet of amino acids at positions 108, 109, and 110 which have been shown to be critical to structuring the protein and are implicated as the turn region. Other lines of evidence have suggested that the proline located at position 110 is critical to the orientation of caveolin-1 in the bilayer as well [75-77]. When considering that proline 110 is conserved across species and isoforms, it is clear that the position must play a biologically critical role. This topic will be explored in later chapters of this work. Although the topology of caveolin in the cell has been characterized with respect to the location of its termini, many aspects of the topology remain uncharacterized. For

instance, does caveolin automatically adopt the U-shaped topology in membranes, or is this conformation controlled by cellular insertion machinery? Additionally, it is unclear where the transmembrane region enters and exits the membrane. Also, the question as to the exposure of the turn region remains unanswered (membrane buried or aqueous exposed). Besides these questions, the importance of specific amino acids within caveolins sequence in maintaining the unique topology remains to be an open question and one that should be addressed. Answering these topological questions may help explain how this protein influences the curvature of lipid bilayers. The core objective of this work is to draw light on these very pertinent topological ambiguities that surround caveolin (Figure 1-8).

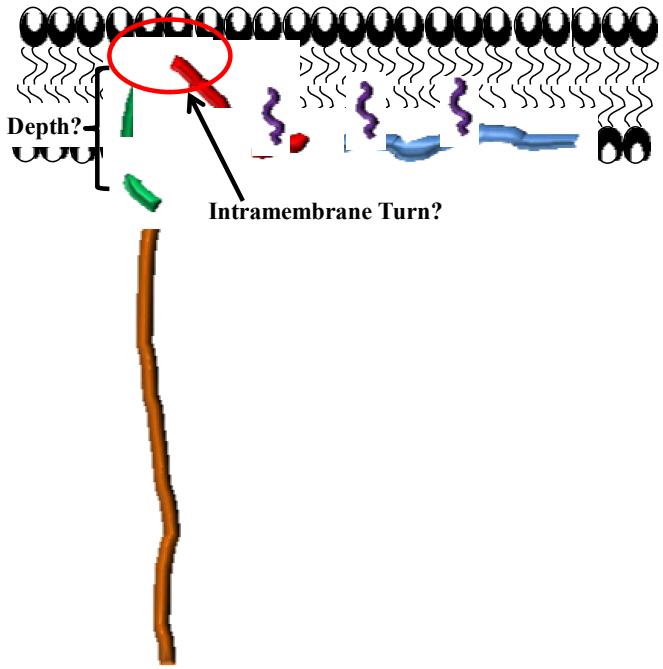

Figure 1-8. Cartoon representation of the putative caveolin-1 topology detailing the controversy surrounding the protein's disposition in the lipid bilayer. Each domain is color coded: N-terminal (*orange*), scaffolding (*green*), intramembrane (*red*), and C-terminal (*blue*). Palmitoylation sites are shown in purple.

With the N- and C- termini residing on the same side, and no evidence of a soluble interruption, this rare motif may have functional consequences in terms of how the protein creates membrane curvature, and this idea is strongly supported by the high degree of sequence identity of the IMD between species. Two possible mechanisms of how caveolins intramembrane region being inserted with the N- and C- termini on the same side could generate membrane curvature include: asymmetric insertion of the protein within the bilayer or asymmetric sequestration of cholesterol to one side of the membrane [78-80] (Figure 1-9). Both are plausible models of how caveolin could cause negative membrane curvature, and integral membrane proteins containing hairpin turns (such as the reticulons) are found to help generate highly curved organelles such as the endoplasmic reticulum [81,82]. In the first model, caveolin inserts into the membrane and places more of its surface area within the inner leaflet of the membrane than the outer leaflet, acting like a wedge (Figure 1-9A). This would displace more lipids in the inner leaflet than the outer and cause an asymmetric stretching effect. Furthermore, oligomerization of caveolin into arrays would exacerbate this action, and could help explain the dramatic level of curvature observed in caveolae. The second possibility plays upon the idea that caveolin-1 recruits and holds cholesterol. Cholesterol has a small polar headgroup compared to its hydrophobic region, and this would displace more phospholipid tails in the inner leaflet if it were asymmetrically sequestered to it. Similar to the effect of placing a majority of the proteins surface area within one leaflet, this would cause an asymmetric bending of the bilayer (Figure 1-9B). Again, more caveolin molecules interacting through oligomerization behavior would result in more cholesterol within a confined space and this could enhance the membrane bending. It is reasonable

to consider that the two mechanisms could work together in generating and stabilizing the high degree of curvature within a caveola.

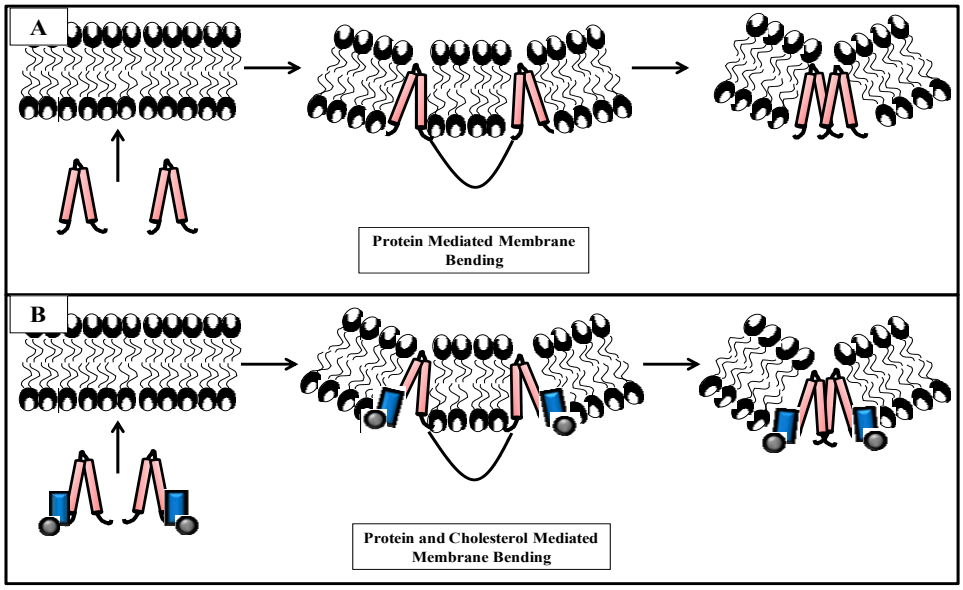

Figure 1-9. Two plausible mechanisms for membrane curvature generation by caveolin-1. **A)** Caveolin asymmetrically perturbs the inner leaflet more than the outer, acting as a wedge. **B)** Caveolin sequesters cholesterol predominantly to the inner leaflet and disrupts the balance of lipids that have large hydrophobic cross sections. Both mechanisms could be enhanced by oligomeric behavior. Caveolin is represented as two cylinders in a wedge-like conformation. Cholesterol is indicated with its hydroxyl headgroup (*grey*) and hydrophobic portion (*blue*).

Membrane Proteins and Model Membranes Used in Biophysical Studies

The biological membrane is comprised of bilayer forming phospholipids, sterols, and importantly, about 50% (*w/w*) of the cell membrane is made up of membrane proteins that are critical for survival. Membrane proteins account for roughly 33% of the genome and about 50% or more of drug targets [83-85]. There are a number of different types of membrane proteins, and these include: membrane anchored proteins, peripheral membrane proteins, and integral membrane proteins. Membrane anchored proteins are those that have been acylated or prenylated at one or more amino acids in their sequence, and this post-translational modification is responsible for holding the protein near the

membranes surface. The nature of these modifications is thought to target soluble and membrane proteins to specific domains (i.e. caveolae) [86]. Peripheral membrane proteins are often associated with the surface of the membrane through electrostatic interactions of their charged groups with the polar head groups of the lipid bilayer. Integral membrane proteins, such as caveolin, contain a high percentage of consecutive aliphatic or aromatic amino acids which make them extremely insoluble in the aqueous milieu and much more at home within the lipid bilayer. By burying their hydrophobic portions in the bilayer, they can avoid the entropic penalty of ordered water surrounding their large non-polar surface area. All of these types of membrane proteins require a lipid bilayer to properly study their structure and function because they are very hydrophobic and therefore, will often aggregate, precipitate, or adopt irrelevant conformations within purely aqueous environments [87-89]. Furthermore, the identity of the lipids is also critical to the proteins activity and fold in some cases [90]. The need for a hydrophobic environment for membrane proteins has made them very challenging to study and likely contributes to the lack of membrane protein structures compared to their soluble counterparts [85].

There is a large variety of different systems that can be used to mimic the natural plasma membrane environment that membrane proteins require for solubilization, proper structuring, and activity. In this thesis work, three types of membrane mimetic systems are used and include: micelles, vesicles, and bicelles, all of which are commonly employed for biophysical studies in the field of membrane protein research (Figure 1-10) [91-96]. Each of these mimics carries with it its own advantages and caveats.

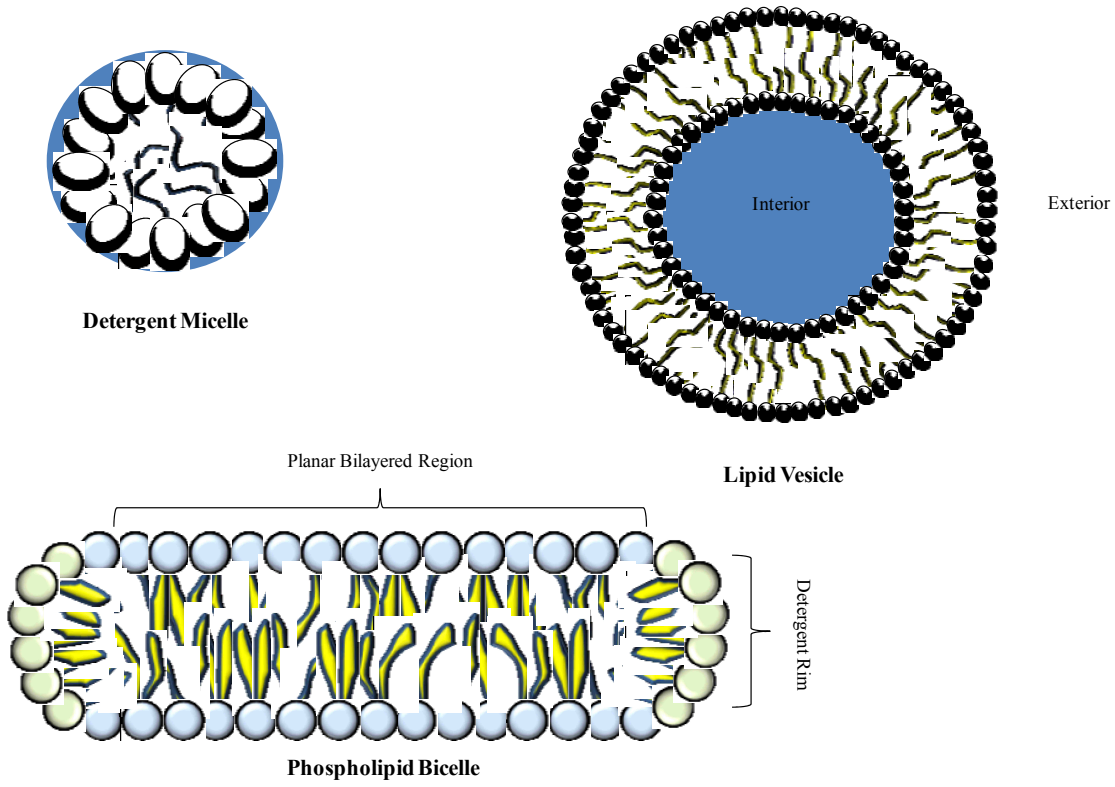

Figure 1-10. Cross sectional views of the three types of native bilayer mimics that are typically utilized in membrane protein structure and functional studies including micelles, vesicles, and bicelles.

Micelles are aggregates of amphipathic surfactants, which in water place their hydrophobic moieties together to avoid the entropic penalty of structured water coverage creating an oil droplet that is surrounded by an ionic (sodium dodecylsulfate, lyso-myristoylphosphatidylglycerol), zwitterionic (dodecylphosphocholine, Empigen BB®), or polar headgroup (octyl-β-D-glucoside, Triton-X-100) coating (Figure 1-11). Micelle forming amphiphiles have a large headgroup size compared to their hydrophobic tail region and therefore have a cone-like molecular shape, which upon aggregation, allows them to support a high degree of curvature, giving the micelles a spherical, prolate, or oblate shape [97]. Micelles are typically a few nanometers in diameter. They are dynamic

in nature, where a specific concentration of monomeric detergent is required to saturate the solution before they start forming aggregates; this parameter is called the critical micelle concentration (CMC). Detergent micelles have been used almost exclusively in membrane protein structural determinations by both NMR and X-Ray crystallography, are typically used in membrane protein purification procedures, are easy to work with, and can support membrane protein function [98-101]. Additionally, the secondary structure of membrane proteins is usually preserved in micelles [102]. However, they have disadvantages in that they lack a bilayer, limiting them for topological studies examining protein depth and orientation. Micelles also have a much more curved surface than the native bilayer; this aspect can have a negative effect on membrane protein conformation [103]. They allow extensive water penetration, which could disrupt potentially important intra- or intermolecular interactions required for specific folding and activity [104]. They also cannot support biologically relevant quantities of cholesterol, a molecule which can be critical for the structure and function of some membrane proteins [105]. Small amounts of phospholipid can often be doped into micelles, and these structures are termed "mixed micelles" [106]. Often times, one must optimize the specific properties of chain length, headgroup size, and charge to find the most suitable detergent to uphold a specific membrane protein's structure and function [107].

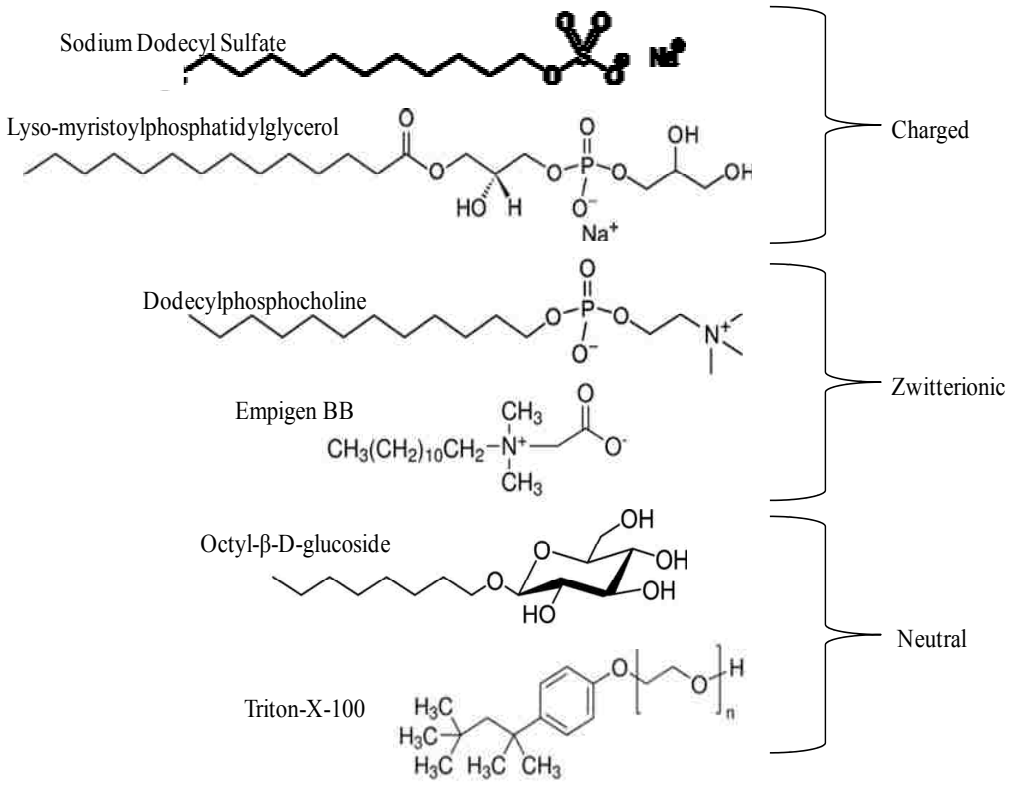

Figure 1-11: Various detergents commonly employed in the purification and study of membrane proteins.

Vesicles are spherical, static aggregates that are composed of bilayer forming amphipathic molecules with the ability to entrap solutes within their hollow interior. A liposome is a type of vesicle composed of diacylglycerophospholipids, which have a glycerol backbone, a phosphate headgroup, and two acyl chains. The phosphate headgroup is linked to the glycerol backbone via a phosphoester bond. Headgroups on phospholipids vary in their charge and size. In terms of the headgroups on phospholipids, eukaryotic organisms are composed of zwitterionic phosphatidylcholine, and phosphatidylethanolamine, and to a lesser extent negatively charged phosphatidylserine, phosphatidylglycerol, phosphatidylinositol, and phosphatidic acid. The lipid chains are linked to the glycerol backbone via an ester bond. The chains vary in their length and degree of unsaturation. Typically the lipids in the biological membrane are 16-20

carbons in length and have 1 or more sites of unsaturation within their chain. The identity of the headgroup, chain length, and degree of unsaturation contribute to a specific melting temperature (T_m) for lipid bilayers. The T_m is used to describe the degree of order in the acyl chain region. At low temperatures, the acyl chains are fully extended and this is called the gel or liquid ordered phase. At high temperatures, the acyl chains are highly mobile and disordered, and this is called the fluid or liquid disordered phase. Physically the T_m represents the halfway point between these two states where half of the lipid population is ordered and half is disordered. The T_m of bilayers is a very important parameter biologically as it allows embedded proteins to interact. The fluidity of the bilayer can also be modulated by the addition of cholesterol which causes a broadening of the T_m (increase).

The roughly equivalent surface area of the headgroup and chain regions allow phospholipids to pack together in a cylindrical fashion, limiting the amount of curvature that they can uphold. Due to the hydrophobic effect, they form roughly planar bilayered structures that close to avoid exposure of the planar regions edges to water, and hence the spherical shape of the liposome. Liposomes can have a single bilayer (unilamellar vesicles) or like an onion, multiple bilayers (multilamellar vesicles). Single shelled liposomes are typically divided up into three classes depending on their size: small unilamellar vesicles (15-50 nm in diameter), large unilamellar vesicles (100-400 nm in diameter), and giant unilamellar vesicles (>500 nm). Advantages to using vesicles include their near cell-like dimensions, which reduces curvature induced defects on reconstituted proteins, and an actual lipid bilayer. They also have a distinct interior and exterior which can be useful in transport studies on channel forming proteins as well as

lysis/fusion assays of membrane proteins that require the release of entrapped solutes to observe their activity [108-110]. This property is also important for topological studies, to examine a reconstituted protein's depth and orientation in membranes [111,112]. They can incorporate a wide variety of biologically relevant lipids, including cholesterol. The downside to vesicles is that they are often quasi-stable when they are small, tending towards fusion. They scatter significant amounts of light which can be burdensome in some spectroscopic techniques. Additionally, liposomes have not been successfully employed for structural determinations of membrane proteins because their large size makes them hard to adapt to crystallization and NMR studies.

Bicelles are discoidal lipid aggregates that spontaneously form when long chain phospholipids (1,2-dimyristoyl-*sn*-glycero-3-phosphocholine (DMPC) or 1,2-dipalmitoyl-*sn*-glycero-3-phosphocholine (DPPC)) and short chain phospholipids/specific detergent molecules ((1,2-dihexanoyl-*sn*-glycero-3-phosphocholine (DHPC), 1,2-diheptanoyl-*sn*-glycero-3-phosphocholine (DHePC), or 3-[(3-Cholamidopropyl)dimethylammonio]-2-hydroxy-1-propanesulfonate (CHAPSO)) are mixed in aqueous solution (Figure 1-12) [113,114].

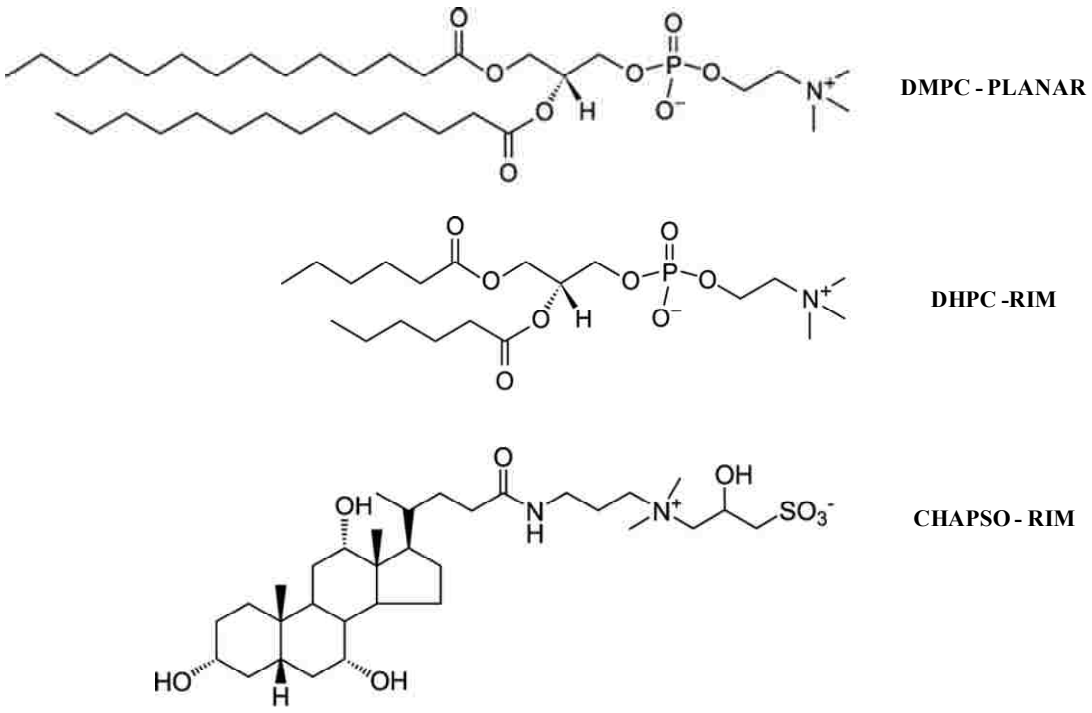

Figure 1-12. Chemical structure of bicelle forming species utilized throughout the course of this work.

These structures are characterized by lipid segregation where long-chain phospholipids (DMPC and DPPC) form a planar bilayered region and the detergent molecules (DHPC, DHePC, and CHAPSO) create a curved rim region packed around the bilayer, shielding it from exposure to the aqueous environment. Similar to micelles, the detergent is in exchange with the aqueous environment and there is a critical bicelle forming concentration, or CBC. These structures typically range in size from 2.5 – 20 nm in length, and their size is tuned by a property know as ***q***, which is the molar ratio of the long-chain lipid to the detergent [94,115,116]. With larger, ***q*** values, the length of the bilayered region increases, and the disks take on a larger diameter. This is one way in which the tunable nature of bicelles makes them advantageous to use in structural studies. For example, a ***q*** = 1.0 has a planar bilayered region that is about 147 Å in diameter and can support membrane protein behaviors such as oligomerization [113]. Due to the dynamic

nature of the detergent, one must consider the overall lipid percentage in the sample. For example, at low lipid percentage in solution, a much greater amount of detergent relative to the long chain phospholipid is in exchange, giving rise to a larger q than would be expected. For this reason it is important to prepare bicelles with knowledge of their CBC and generate them according to their q_{eff}, ([long chain phospholipid]/([long chain phospholipid]$_{total}$-[long chain phospholipid]$_{free}$)). Bicelles can hold a variety of different phospholipids, have melting temperatures which are close to that of liposomes composed of pure phospholipids, and can contain biologically relevant amounts of cholesterol (albeit only at high temperatures) and therefore can mimic the native cellular environment nicely [117-121]. Their ability to hold longer chain lipids allows the modulation of bicelle thickness. They can also be loaded with lipids that have negatively or positively charged headgroups allowing for modification of their surface charge. Additionally, they scatter very little light making them ideal for spectroscopic studies. Bicelles have a true bilayer and this allows for topological, functional, and structural determinations to be performed on proteins reconstituted into them [93,94,116,122-124]. They have disadvantages which include the fact that they cannot be used to determine membrane protein orientation, and proteins incorporated into them can be prone to "rim" effects (a micelle like environment), especially at low q values. In most studies q values ranging from q= 0.3-3.0 are used, however, low q values are considered to be less biologically relevant due to the limited size of the bilayered region and increased detergent intermixing, making them more similar to a mixed micelle.

Biophysical Methods Used to Characterize Membrane Proteins

The characterization of membrane proteins requires not only the study of their secondary structure and three-dimensional folds, but also knowledge of their aggregation state and their degree of penetration into the bilayer. The combinations of these parameters give an image of a membrane protein which can help explain how it functions, and in some cases, a better understanding of the protein can lead to new therapeutics or an understanding of disease mechanisms. For instance, it is now known that many membrane receptors bind a variety of ligands through secondary, allosteric binding sites. These secondary binding sites can be utilized to modulate receptor selectivity and activity which can bring about dramatic changes in how individuals respond to drugs which, without the use of allostery could result in drugs having many unintended side-effects [125]. The biophysical study of membrane proteins is critical to bring about new developments in the treatment of disease.

Although the secondary structure of proteins can be characterized by a number of techniques, in this body of work, the most common method used is circular dichroism. Circular dichroism examines how molecules absorb right and left handed circularly polarized light differentially, and is due to presence of chirality. The peptide bond has slight double bond character and therefore contains a weak but broad $n \rightarrow \pi^*$ transition around 220 nm and a somewhat stronger $\pi \rightarrow \pi^*$ transition at 190 nm. Because the α-helix motif in proteins is a chiral structure, it absorbs right and left handed polarized light very differently than the other major structural motifs in proteins (maxima at 190 nm and minima at 208 nm and 222 nm). The β-sheet also has its own characteristic absorption profile (minimum at 217 nm) [126]. Furthermore, the α-helix and β-sheet give rise to

different spectral signatures than the random coil secondary structure (minimum at 204 nm). Many proteins contain a mixture of these different secondary structure motifs. With information of the proteins concentration and circular dichroism spectra, the contributions of different secondary structure motifs can be estimated using prediction algorithms and can yield specific information about how much α-helical, β-sheet, and random coil character a polypeptide contains.

Circular dichroism can also yield qualitative information about the tertiary structure of proteins by examining the 260-320 nm region, and is referred to as the near ultraviolet (UV) CD [126]. The absorption of light in this region is due to the presence of tryptophan, tyrosine, and phenylalanine residues. Each one of these residues gives rise to region specific peaks in a CD spectrum at 290-305 nm (primarily tryptophan), 275-282 nm (primarily tyrosine), and 255-270 nm (phenylalanine). These features can be considered as a "fingerprint" of the tertiary structure (due to the functional groups being held asymmetrically) and can be used to compare protein mutants, truncations, or lipid environments in terms of their structural impact. However, this method is not advanced enough to give specific structural information one would obtain from solution NMR or X-ray crystallography. Nonetheless, examination of the near UV spectra remains useful for comparisons sake.

Another important method that can be employed to gain insight into the topology, dynamic behavior, membrane organization, and oligomeric behavior of a protein is fluorescence spectroscopy [127]. These studies require either the use of the naturally fluorescent amino acids (tryptophan, tyrosine, and phenylalanine), expression of fluorescent protein fusion constructs to the protein of interest (i.e. green fluorescent

protein), or the conjugation of a fluorescent molecule such as dansyl or fluorescein by covalent bond formation to the species of interest [128,129]. Fluorescence occurs when an electron within a chromaphore is excited by a particular wavelength of light. This electron then relaxes back to its ground state after some time being excited, the average time a fluorophore spends in its excited state is known as the fluorescent lifetime (Figure 1-13). Rather than going through non-radiative decay, when a molecule fluoresces a photon is released, usually at a lower frequency than the photon that was absorbed (The frequency change is known as the "Stoke's shift"). With an environmentally sensitive fluorophore, the process can yield information about the micro-environment surrounding the molecule as fluorescence lifetimes are typically linked to dynamic processes that are occurring locally. This is only true if the dynamic process occurs within the lifetime of the excited state (fluorescence lifetimes typically range from μsec-nsec, tryptophan fluorescence usually ranges from 0.1-8 ns) [127,130].

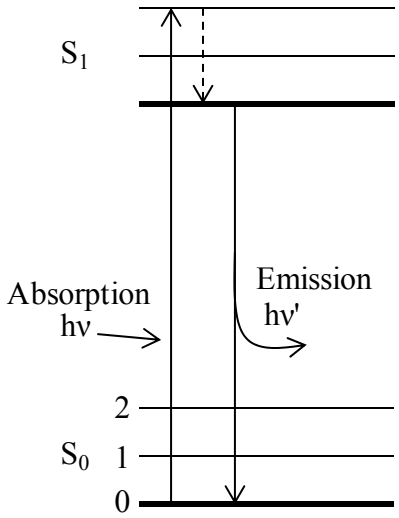

Figure 1-13. Simplified Jablonski diagram. Absorption of a photon by a fluorophore excites an electron from its ground state (S_0) to the excited state (S_1). The excited electron then relaxes to the lowest vibrational state of S_1 on a fast timescale. The electron then falls back to its ground state giving off a photon of lower frequency.

Using the native fluorophore tryptophan for fluorescent studies of proteins has many advantages. One particular advantage is that tryptophan can be selectively excited over the other fluorescent amino acids by irradiation using the 295 nm wavelength (the red edge of the tryptophan's excitation spectrum). In doing so, the emission spectrum will yield information specific to the environment surrounding the sequence location of tryptophan groups. Another is that tryptophan is an environmentally sensitive fluorophore. This is owed to the fact that there is large electron density redistribution in the asymmetric indole ring after the absorption of a photon that leads to a significant dipole moment compared to tryptophan in its ground state [131]. Once in the excited state, solvent-solute, or solute-solute interactions can occur that change the emission peak shape or emission maximum. These spectral properties are easily recorded using a fluorometer and can be determined by fitting the spectrum of the protein to a log-normal equation (equation 1-1):

$$I(\lambda) = I_0 exp\left[\frac{ln2}{ln^2\rho} ln^2\left(1 + \frac{(\lambda - \lambda_{max})(\rho^2 - 1)}{\rho\Gamma}\right)\right]$$

where I_0 is the intensity observed at the wavelength of maximum intensity (λ_{max}), Γ is the peak width at $I_0/2$ (peak shape), and ρ is the asymmetry of the peak [132,133].

The λ_{max} of tryptophan ranges from 308-360 nm depending on the environment. For instance, upon the dipole reorientation of tryptophan, the organization of solvent molecules around tryptophan in its excited state may be perturbed and causes a shift in the λ_{max} of the protein. Generally, factors that contribute shifts are described by the modified Lippert equation (equation 1-2):

$$\Delta v \approx |\Delta\mu|^2 \left[\frac{2(\varepsilon - 1)}{2\varepsilon + 1} - \frac{2(n^2 - 1)}{2n^2 + 1}\right] \frac{^{\tau}F}{^{\tau}F + ^{\tau}R}$$

This equation relates the spectral shift in wave numbers ($\Delta\nu$) between the excited and ground state to changes in the dipole moment ($\Delta\mu$), the dielectric constant of the medium (ε), the time of dipole relaxation of the tryptophan (T_R) in comparison to the lifetime of fluorescence (T_F). In the most simplistic sense when it comes to interpreting the location of tryptophan groups within membranes, the dielectric constant is a major factor. For a tryptophan buried in the membrane (small ε), the stokes shift would be less than that for a tryptophan buried in the aqueous environment (large ε). However, due to the complexity of interactions that can occur within protein microenvironments, and the typical scenario where a protein contains more than one tryptophan, the degree of spectral shift alone must be interpreted carefully alongside orthogonal techniques.

When considering proteins containing only one tryptophan residue, the emission spectra typically fall into three categories [134-136]. The most red shifted spectra, having λ_{max} values ranging from 346-350 nm (Class III) are considered to be aqueous exposed. The most blue-shifted spectra, having λ_{max} values ranging from 330 -333 nm (Class I) are considered to be buried deeply within the tertiary structure of a protein or a lipid bilayer. In between these two classes, a tryptophan group with an emission that ranges from 340-344 nm (Class II) would be considered to be located at interfaces such as the one between the aqueous environment and the hydrophobic core of the membrane. These classes are a result of many investigations into the location of tryptophan's within both soluble and membrane proteins, where the majority of cases contain species within these discrete states of fluorescent emission. By no means do these narrow definitions capture the full range of emission spectra possible, as hybrids of classes, which reflect conformational flexibility, phase, and oligomeric distributions, can be observed. The shape of the peak is

also important, where Γ can give information about the heterogeneity of the distribution of fluorophores [133]. For instance, if two different proteins each have a single tryptophan with the same λ_{max} but different Γ values, the protein with a larger Γ could be in multiple conformations, or showing other dynamic behaviors.

Another method employing fluorescence spectroscopy utilizes the ability of particular substances to quench fluorescence. A number of species can quench tryptophan including acrylamide, cobalt, and iodide. The mechanism of fluorescence quenching is not entirely understood, but for halogens such as iodide, it is thought that intersystem crossing to an excited triplet state is promoted by spin-orbit coupling of the excited fluorophore and the halogen. In the triplet state, the emission from the fluorophore becomes slow and may be quenched by other processes [127]. Quenching can be dynamic or static in nature. Dynamic quenching results from diffusion mediated collision between the fluorophore, whereas static quenching is a result in the formation of a complex with the fluorophore. Methods of telling the two apart from one another include performing quenching experiments at various temperatures and looking at the trend. With static quenching, complex formation is typically less favored at higher temperatures and the amount of quenching decreases whereas collisional quenching is enhanced due to the increased rate of collisions. Collisional quenching is described by either the Stern-Volmer equation for quenching or the modified Stern-Volmer equation. Upon successive additions of quencher, tryptophan fluorescence is quenched at different efficiencies depending on its chemical environment. This technique is used for tryptophan groups which are buried within the core of a folded protein, as well as those

which are buried within a biological membrane [137]. The Stern-Volmer equation (equation 3) takes the form:

$$\frac{I_0}{I} = 1 + K_{SV}[Q]$$

where I_0 and I are the initial fluorescence and fluorescence after addition of quencher respectively, K_{SV} is the Stern-Volmer quenching constant of the entire population of the fluorophores (K_{SV} is the concentration in which 50% of the total fluorescence intensity is quenched, and is the product of the bimolecular quenching k_q constant and the lifetime of the fluorophore in the absence of the quencher, τ_0), and [Q] is the concentration of quencher. However, if the plot is not perfectly linear and deviates towards the *x*-axis, then this is indicative of there being an accessible and buried fraction of fluorophores. Stern-Volmer quenching curves generated from the quenching data can also be fit to a double reciprocal plot (Modified Stern-Volmer plot, equation 1-4) that assumes a buried and accessible population to give:

$$\frac{I_0}{I_0 - I} = \frac{1}{f_a K_a[Q]} + \frac{1}{f_a}$$

where I_0 and I are the initial fluorescence and fluorescence after addition of quencher respectively, K_a is the Stern-Volmer quenching constant of the accessible fraction (K_a is the concentration in which 50% of the fluorescence intensity of the accessible fraction is quenched), f_a is the fraction of the initial fluorescence that is accessible to the quencher, and [Q] is the concentration of quencher. The f_a value is useful and can be used much like λ_{max} to interpret the location of tryptophan residues, where more highly exposed tryptophan residues will have f_a values approaching 1 and tryptophans deeply embedded within a hydrophobic matrix such as the lipid bilayer will have f_a values that approach 0.

However, f_a values can have a large degree of error associated with them as the measurement extrapolates to an infinite quencher concentration (the *y*-intercept represents quenching at an infinite quencher concentration, as [Q]→∞, the first term in equation 1-4 becomes ~0), far away from the practical concentrations used within experiments. Nonetheless, the f_a value can be more useful than K_{SV} when comparing different constructs, as it does not require knowledge of the fluorescence lifetime for interpretation.

Another useful fluorescence technique which is used to give information about the conformational freedom of a fluorophore is fluorescence anisotropy. When a fluorophore is excited with polarized light, the emission can also be polarized [127]. The amount of the emission that maintains polarization is described by its anisotropy (*r*). Anisotropies greater than zero are observed if some of the population of the fluorophores have their absorption transition moments oriented along the electric vector of the incident light. If the molecules are randomly oriented, then there is no preferential excitation due to the polarized light and anisotropies close to zero are observed. Anisotropy can be determined by a comparison of the measured intensity of emitted light from a sample which has been excited by vertically and horizontally polarized light (with respect to the *z*-axis). Anisotropy is given by the equation (equation 1-5):

$$r = \frac{I_{VV} - GI_{VH}}{I_{VV} - 2GI_{VH}}$$

where I_{VV} and I_{VH} are the emitted intensities of the fluorophore with the excitation polarizer oriented vertically and the emission polarizer oriented vertically or horizontally respectively, and G is the G-factor which is the ratio of sensitivities for vertically and horizontally polarized light (defined as I_{HV}/I_{VV}).

Finally, fluorescence resonance energy transfer (FRET) can also be used to give information about fluorophores in solution. In this technique, an initially excited donor molecule (D) is excited using incident light and gives off an emission. If this emission spectrum overlaps with another fluorophore's excitation spectrum, the second fluorophore can then be an acceptor (A) and will undergo an emission. The transfer of energy that causes the acceptors emission is a photonless event and is highly dependent on the distance between the two species (there is an R^6 dependence on the efficiency of this transition event). Most FRET events are 50% efficient in the 20-60 Å range making this technique a useful molecular ruler for macromolecular distance measurements [127]. The efficiency of an energy transfer event is measured using the fluorescence intensity of the donor in absence and presence of the acceptor and is described by the following equation (equation 1-6):

$$E = 1 - \frac{F_{DA}}{F_D}$$

Where F_{DA} and F_D are the fluorescence intensity of the donor in the presence and absence of the acceptor, respectively. If one has knowledge of the R_0 value for a given donor acceptor pair, an estimate of distance can be made from the following equation (equation 1-7):

$$E = \frac{R_0^6}{R_0^6 + r^6}$$

Where E is the FRET efficiency, R_0 is the radius of 50% transfer efficiency and r is the distance (reliable only within $2R_0$).

Chapter 2. Development of Perfluorooctanoic Acid as a Tool for Vesicle Formation and Caveolin-1 Topology Analysis

ABSTRACT

The study of membrane proteins has become a major research interest because they have a central role in maintaining proper cellular function and also have potential as targets in the treatment of disease states. A major challenge in working with recombinant membrane proteins is their reconstitution into a biologically relevant lipid bilayer environment where they achieve a refolded state and are functionally active. The detergent dialysis technique, which utilizes mixtures of egg phosphatidylcholine with protein dissolved in cholate or octylglucoside, is often used to incorporate membrane proteins into lipid vesicles. Although useful, these lipid-detergent systems are not able to reconstitute highly pure, insoluble membrane proteins such as caveolin-1. The failure of these commonly used detergents in reconstituting caveolin-1 warranted the use of novel lipid-detergent mixtures. The removal of perfluorooctanoic acid (PFOA) from mixtures of phosphatidylcholine and PFOA results in the formation of small unilamellar vesicles with a hydrodynamic radius of approximately 11 nm. The presence of vesicles was confirmed by gel filtration, dynamic light scattering, and glucose entrapment. Increasing the amount of sodium chloride in the dialysate leads to the formation of larger vesicles with a hydrodynamic radii ranging from 12-70 nm. Moreover, cholesterol can be incorporated into the vesicles (up to 40% by mol). Using this method, various caveolin-1 constructs can be effectively reconstituted into vesicles. Evidence of incorporation of the caveolin-1 protein into vesicles with or without cholesterol was shown by gel filtration followed by Western blot analysis. Sodium carbonate extraction methodologies showed

that the reconstituted protein was embedded within the bilayer. Consistent with caveolin being a non-pore forming peptide, a real time entrapment study showed that the permeability of entrapped solutes was not markedly enhanced by the incorporation of the protein into vesicles. A limited proteolysis assay to examine the topology of reconstituted caveolin-1 was developed and showed a mixed topology where 60 % of reconstituted caveolin-1 was present as a single spanning membrane helix and 30% of the protein was present with a native topology with the N- and C- termini on the same side of the membrane.

INTRODUCTION

The cell membrane is composed of a phospholipid bilayer that is enriched with membrane proteins. Biological membranes typically contain approximately 50% protein content by weight. Membrane proteins have a myriad of cellular functions including selective transport, catalysis, and signal transduction. They also play a role in the structure and architecture of cellular membranes [138]. The utility of membrane proteins has not gone unnoticed by organisms, where approximately 33% of most genomes encode for these proteins [31]. Membrane proteins are difficult to characterize in terms of their structure and function due to obstacles in expression and solubility. For this reason, unique approaches must be taken to study these highly insoluble proteins.

Detailed characterization of membrane protein structure and function *in vitro* requires reconstitution of the protein into phospholipid environments that mimic the native bilayer. Unilamellar vesicles are often used to meet these ends because they have a single bilayer shell and can be constructed using mixtures of natural lipids such as egg yolk phosphatidylcholine (EYPC) [139]. Vesicles are static and hollow giving them a distinct interior and exterior that is similar to the cell, making them ideal for the topological characterization of reconstituted membrane proteins. Additionally, vesicles are amenable to the incorporation of biologically relevant amounts of cholesterol which may be important for maintaining the structure of some membrane proteins [140].

Detergents can be used to solubilize membrane proteins and lipids, and their subsequent dialysis results in the formation of unilamellar vesicles. In many cases, β-D-octylglucoside, or sodium cholate are the detergents of choice in vesicle formation for membrane protein reconstitution, as they are mild and non-denaturing [96,141]. Although β-

D-octylglucoside and sodium cholate are useful for the solubilization of membrane proteins that already exist in lipid-protein complexes, or membrane proteins which have amphipathic characteristics, these mild detergent are not powerful enough to solubilize extremely hydrophobic membrane proteins such as caveolin-1, the principle protein component of cholesterol rich membrane invaginations known as caveolae. Perfluorooctanoic acid (PFOA) is an octanoic acid analogue where the aliphatic hydrocarbons have been replaced by fluorine atoms (Figure 2.1). PFOA has been shown to be effective for the solubilization of various membrane proteins [142]. In addition, fluorous surfactants have also been shown to be an effective aid in refolding experiments using soluble proteins [143,144]. For these reasons, PFOA was investigated in its use as a detergent that could both solubilize caveolin-1 and facilitate its reconstitution into vesicles. Advantageously, the adoption of the native fold of caveolin-1 can be evaluated by probing the location of its termini; the natively folded protein would maintain the hallmark feature of the protein where the N- and C- termini are coincident to the same side of the membrane. Therefore, caveolin serves as an excellent test case for the development of the PFOA dialysis method as a way of refolding membrane proteins.

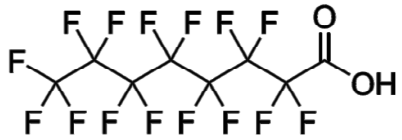

Figure 2-1. Chemical structure of PFOA.

In this chapter, PFOA is shown to be a detergent that can produce vesicles by the dialysis of EYPC-PFOA mixtures. The vesicles were formed in the presence of sodium chloride and cholesterol, and the effect of these solutes on vesicle size was examined by gel filtration and dynamic light scattering (DLS). It was found that the addition of

sodium chloride allows for size tuning of the vesicles (11-77 nm) and that cholesterol can be incorporated into vesicles at physiologically relevant concentrations. Static light scattering (SLS) was used to show that the vesicles were hollow spheres. Additionally the vesicles have the ability to entrap solutes in the absence and presence of caveolin. It was demonstrated that a caveolin-1 construct containing the complete membrane interacting domain (residues 62-178), a portion which has been shown to dictate many of the protein's critical functions *in vivo*, can be reconstituted into lipid vesicles using PFOA [145]. Upon PFOA mediated reconstitution, caveolin-1 behaved as an integral membrane protein when evaluated using the method of carbonate extraction. The addition of the protein was shown to cause a slight increase in the leakage rate of entrapped contents, consistent with a modest degree of bilayer disruption. A limited proteolysis method revealed a mixture of topologies upon reconstitution, with the majority of the protein (~60%) being in a misfolded, transmembrane orientation with the N- terminus located on the interior of the vesicle and the C-terminus located on the exterior and the remainder of the population was fully exposed to cleavage by the protease. Although this attempt to refold the protein was met with limited success, the results indicate that that a complex set of biological conditions are likely critical to forming caveolins hallmark topology. Nonetheless, the detergent dialysis approach using PFOA-lipid-protein mixtures will serve as a general method for the reconstitution of membrane proteins into lipid vesicles.

MATERIALS AND METHODS

Vesicle Formation

Typically, 50 mg of EYPC (Avanti Polar Lipids, Alabaster, AL) dissolved in chloroform was dried down to a film under a stream of nitrogen with gentle heating at 37°C in a 10 mL glass vial. Next, a buffer containing 300 mM PFOA (Oakwood Products, West Columbia, SC), 10 mM Tris-HCl pH 8.0 was added to the EYPC to achieve a final lipid concentration of 20 mM. The mixture was then sonicated until it became transparent. For samples containing cholesterol, cholesterol (Avanti Polar Lipids, Alabaster, AL) was added at 5, 20, and 40 mol % while maintaining the final concentration of EYPC and cholesterol at 20 mM. The resulting solution was then added to a 10 kD MWCO slide-a-lyzer G2 dialysis cassette (Thermo scientific, Rockford, IL.), and was dialyzed against 2 L of 10 mM Tris-HCl pH 8.0 with various concentrations of NaCl added which did not exceed 150 mM. The mixture was dialyzed for three days with buffer exchanges every 24 hours to ensure complete removal of PFOA.

Protein Expression, Purification, and Mutagenesis

For these studies, the gene encoding for a biologically relevant caveolin-1 construct containing residues 62-178 flanked by double antibody epitopes (HSV and FLAG) on both the N- and C- termini was purchased from Genscript Corporation (Piscataway, NJ) ($^{HSVFLAG}Cav1_{62-178}$) [145]. The primary sequence is indicated in Appendix 2-1. The underlined portion denotes residues 62-178 of caveolin-1. A few conservative mutations were made to the native protein sequence and are indicated by bolding. Three sites of palmitoylation, at positions 133, 143, and 156, which are not essential to caveolin-1 trafficking to the membrane were mutated to serine to avoid disruptive and

biologically irrelevant disulfide bonding [35]. Additionally, a non-conserved methionine at position 111 was mutated to leucine based on sequence homology to caveolin-3 in order to facilitate separation of the protein from the TrpLE protein used to direct protein expression into inclusion bodies. The protein was cloned into according to the methodologies described in Diefenderfer et al [146,147]. Specifically, the protein was cloned into a pET24a between BamHI and EcoRI restriction sites, downstream from a gene encoding for the Trp leader protein (cloned between NdeI and BamHI).

Truncated versions of $^{HSVFLAG}Cav1_{62\text{-}178}$ were generated to create a ladder for use in sodium dodecylsulfate polyacrylamide gel electrophoresis (SDS-PAGE) experiments that reflected the molecular weight shifts of our construct after treatment with enterokinase. All mutant constructs were prepared using the Quik change site-directed mutagenesis kit (Agilent Technologies, Santa Clara, CA). To mimic the N-terminal cleavage of the protein by enterokinase, a methionine residue was placed immediately after the N-terminal FLAG site, therefore, the HSV-FLAG portion would be removed during the protein preparation by CNBr cleavage (see Diefenderfer et al). To mimic the C-terminal cleavage of the protein by enterokinase, a stop codon was inserted immediately after the second FLAG cleavage site. Doubly truncated $Cav1_{62\text{-}178}$ was generated using a combination of the two mutations above. Primers were designed using the free web-based primerX program (Bioinformatics.org). Primer sequences are indicated in Appendix 2-2. The PCR conditions utilized to generate mutant constructs are described in Appendix 2-3. Following PCR, 1 μL of DpnI (New England Biolabs, Ipswich, MA) was added to the reaction test tube and the reaction was incubated at room temperature overnight. This allowed digestion of methylated DNA, ridding the reaction

mixture of the template. Transformation of the mutant plasmid was accomplished as described in Appendix 2-4 by adding 1 μL of reaction mixture to 50 μL ultra-competent XL-1 Blue *E. coli* cells. All constructs were confirmed to be correct by DNA sequencing.

The plasmid was transformed into BL21DE3 cells for expression of the protein as described in Appendix 2-4. The protein was expressed using the auto-induction protocol described by Studier et al [147]. Briefly, cells were grown from a glycerol (15%) freezer stock in MDG media (Appendix 2-5) for 16-24 hours. After this time period, a 1:1000 dilution of the culture was made into 1L ZYM-5052 media (Appendix 2-5). The growths were harvested by centrifugation at 5000 *x g* for 30 minutes at 4°C after the exponential growth phase (typically 10-16 hours, denoted by the leveling out of the optical density at 600 nm for the culture).

Purification of $^{HSVFLAG}Cav1_{62-178}$ to homogeneity was carried out akin to Diefenderfer et al with slight modification. The cell pellet was first washed using 0.9% (*w/v*) saline solution at a volume that was 20% of the original culture volume. Next, the pellet was taken up into 400 mL of a buffer composed of 20% (*w/v*) sucrose dissolved in 10 mM Tris-HCl, pH 8.0. The pellet was homogenized using sonication for 15 minutes at 4℃. The lysate was then centrifuged at 27,500 *x g* for 2 hours at 25℃. The pellet was then taken up into 400 mL of 1% (*v/v)* Triton-X-100 and the sonication/centrifugation steps were repeated. The next step was a modification to the method by Diefenderfer et al*,* in place of three 400 mL Tris-HCl washes after spinning down triton-X-100 insoluble Trp-Leader $^{HSVFLAG}Cav1_{62-178}$ inclusion body pellets, a single 400 mL wash using a buffer containing 40% isopropyl alcohol, 50 mM Tris-HCl wash was

utilized. The pellet was sonicated into this buffer at a duty cycle of 40 % and an output of 5 for 15 minutes at 4°C with rapid stirring. The inclusion bodies were then re-pelleted by centrifugation at 27,500 *x g* for 2 hours at 4°C. The pellet was then subjected to cyanogen bromide cleavage (0.2 g CNBr) to remove the Trp leader fusion partner and was subsequently isolated using reverse phase high performance liquid chromatography (HPLC). The chromatographic conditions were 80% water/20% acetic acid going to 80% n-butyl alcohol/20% acetic acid at a 1%/minute gradient using a Phenomenex (Torrance, CA) C4 Jupiter column with a 15 μm particle size. The resultant peak was dried down using a SpeedVac® concentrator. The resulting film was dissolved in 1,1,1,3,3,3-hexafluoroisopropanol (HFIP) at a concentration of 0.5 mg/mL and was lyophilized overnight. Aliquots were stored at -20°C until use. All protein concentrations were determined using a micro BCA assay kit (Thermo scientific, Rockford, IL). The identity of the protein was confirmed using matrix assisted laser desorption-ionization time of flight mass spectrometry (MALDI-TOF).

Reconstitution of $^{HSVFLAG}Cav1_{62-178}$ into Phospholipid Vesicles

Lyophilized $^{HSVFLAG}Cav1_{62-178}$, was dissolved in 300 mM PFOA, 10 mM Tris-HCl pH 8.0 to a concentration of 1 mg/mL. The appropriate volume of the 1 mg/mL $^{HSVFLAG}Cav1_{62-178}$ stock was added to the lipid-detergent solution (discussed in the section above) so that the $^{HSVFLAG}Cav1_{62-178}$ to lipid ratio was 1:6000. All other steps were carried out as described above. For experiments containing $^{HSVFLAG}Cav1_{62-178}$, 0-150 mM NaCl was included in the dialysis buffer.

Gel Filtration Experiments

For gel filtration experiments, a 3 mL preparation of vesicles was concentrated down to 600 μL using an Amicon ultrafiltration unit (10 kD MWCO) (Thermo scientific, Rockford, IL.). Next, the sample was passed through a Versapore 5 μM syringe filter to remove any large particulates. The sample was injected onto a Sepharose 4B column equilibrated with 10 mM Tris-HCl pH 8.0, 150 mM NaCl. The elution of vesicles was monitored using a refractive index detector.

Sodium Carbonate Extraction

After forming the $^{HSVFLAG}Cav1_{62-178}$ containing vesicles, a 600 μL sample was diluted to 1.75 mL using ice cold 100 mM Na_2CO_3 pH 11.5. The vesicles were then incubated on ice for 30 minutes. After this time period, the sample was spun 193,911 *x g* at 4 °C for 2 hours with a Beckman L8-55M ultracentrifuge using a Beckman SW 55 Ti rotor. The pelleted lipid was then washed with 1.75 mL ice cold water and was centrifuged at 193,911 *x g* at 4 °C for an additional 10 minutes. The sample was then re-suspended into 10 mM Tris-HCl pH 8.0. A small amount of this stock was then diluted to an expected $Cav1_{62-178}$ concentration of 10 μg/mL using SDS loading buffer, assuming that all the protein would be associated with the pellet. The sample was analyzed by SDS-PAGE followed by Western blotting, as described in proceeding sections to detect the presence of $^{HSVFLAG}Cav1_{62-178}$.

Entrapment Assays

Vesicles were prepared as described previously except 90 mg/mL glucose with either 100 mM NaCl for non-protein containing vesicles, or 50 mM NaCl for

$^{HSVFLAG}Cav1_{62-178}$ containing vesicles, was included in the dialysis buffer. The last dialysis exchange was performed at 4°C. After dialysis, the external buffer was exchanged quickly using a 2 mL Zeba® spin (Thermo Fisher, Rockford, IL) desalting column equilibrated with 10 mM Tris-HCl pH 8.0, 150 mM NaCl. Next, a 180 μL aliquot of vesicles was lysed using Triton-X-100 added to a final concentration of 1.0%. After 30 minutes, the glucose content was measured using a standard enzymatic glucose assay. A vesicle free solution containing 10 mM Tris-HCl pH 8.0, 150 mM NaCl, 90 mg/mL glucose was used as a control. The amount of phospholipid in the sample was determined by the method of Stewart [148].

Leakage over time was examined qualitatively by the entrapment of glucose-6-phosphate which cannot permeate the bilayer passively (glucose can). Vesicles were formed as described above except 1.3 mg/mL glucose-6-phosphate (Alfa Aesar, Ward Hill, MA) with either 100 mM NaCl for non-protein containing vesicles, or 50 mM NaCl for $^{HSVFLAG}Cav1_{62-178}$ containing vesicles, was included in the dialysis buffer. After dialysis the external buffer was exchanged quickly using a 500 μL Zeba® spin desalting column equilibrated with 10 mM Tris-HCl pH 8.0, 150 mM NaCl. This step was repeated to ensure complete removal of the sugar. Next, 70 μL of a standard glucose-6-phosphate assay mixture was added to the 30 μL of the vesicle preparation giving a final concentration of the following reagents, 1 mM MgCl2, 25 μM NADP+ (Sigma Aldrich, St. Louis, MO), 500 μM 2-(4-Iodophenyl)-3-(4-nitrophenyl)-5-(2,4-disulfophenyl)-2H-terazolium (Dojindo Molecular Technologies, Rockville, MD), 7 μM 1-Methoxy-5-methylphenazinium methyl sulfate (Sigma Aldrich, St. Louis, MO), 200 mU/mL glucose-6-phosphate dehydrogenase (Sigma Aldrich, St. Louis, MO), 40 mM Tris-HCl pH 8.5 [149].

The absorbance at 440 nm was monitored versus time for 400 minutes. The contents were then released by lysis of the vesicles using Triton-x-100 added to a final concentration of 1%. The absorbance was then monitored for an additional time period, to obtain the signal for the completely processed vesicular contents.

Dynamic/Static Light Scattering Experiments

DLS and SLS experiments were employed to estimate vesicle size and shape. For these experiments, 100 μL of vesicles were diluted into 2.5 mL of distilled water in a glass scintillation vial. Three or more measurements were obtained for each sample, and the results were averaged. All experiments were carried out at 25°C. For these experiments the viscosity and refractive index were assumed to be that of water, having values of 0.8900 cP and 1.332 respectively.

For these experiments a Brookhaven Instruments LLS spectrometer equipped with a solid state laser operating at 532 nm was used. The scattered light from the sample was detected at 90°. Size information was obtained using a 9000AT multi-channel correlator. The field correlation function was analyzed to determine the translational diffusion constant by the constrained regularized CONTIN method to yield the hydrodynamic radius (R_h) from the Stokes-Einstein equation (Equation 2-1):

$$R_h = \frac{k\mathrm{T}}{6\pi\eta\mathrm{D}}$$

Where k is the Boltzmann's constant, T is the temperature, η is viscosity of the solvent, and D is the diffusion constant.

For static light scattering experiments, a commercial ALV/CGS3 goniometer dynamic light scattering system equipped with solid state HeNe Laser operating at 632.8 nm was used. The R_h was determined at angles ranging from 50-135° at 5° increments using 3 × 10s measurements. Three lipid concentrations were analyzed from a preparation of vesicles that had 100 mM NaCl in the dialysis buffer (400, 200, and 100 μg/mL total lipid). Measurements were repeated three times at each concentration of lipid utilized. The refractive index and viscosity were taken to be that of water and the dη/dc (change in RI as a function of concentration) was assumed to be 0.16. ALVSTAT software was utilized to generate a Zimm plot [150] in order to obtain the radius of gyration (R_g) from extrapolation of the Kc/R versus q^2 line to a concentration of zero using the following equation (Equation 2-2):

$$\frac{Kc}{R} = \frac{1}{M_w(1 - \frac{1}{3}R_g^2 q^2)} + 2A_2 c$$

where K is an optical constant, *c* is the mass concentration of particles scattering in solution, M_w is an estimate of the particles molecular weight, and R is the normalized scattering ratio.

Western Blot Analysis

$^{HSVFLAG}Cav1_{62\text{-}178}$-containing vesicles were diluted to a protein concentration of 10 μg/mL using Lamelli loading buffer. The sample was centrifuged at 20,000 *x g* for 3 minutes, followed by heating at 100 °C for 3 minutes. The protein was resolved on a 15% acrylamide gel for 20 minutes at 100 V and then 150 V for an additional 80 minutes. Protein bands were transferred to a 0.2 μm nitrocellulose blot paper and washes were

performed according to well established protocols. Alkaline phosphatase conjugated anti-FLAG (Sigma, St. Louis, MO) was used as the primary antibody for detection of the protein bands. The protein bands were visualized by development with the NBT-BCIP colorimetric reagent. Images were collected using the Biorad Gel Doc XR+ and band densities were analyzed using Biorad's Image Labs software (Biorad, Hercules, CA).

Protease Protection Assay

$^{HSVFLAG}Cav1_{62-178}$-containing vesicle solutions were diluted to a protein concentration of 10 μg/mL using 10 mM Tris-HCl pH 8.0, 50 mM NaCl. 50 μL of the diluted sample was treated with 2 ng of enterokinase light chain. The reaction was left to proceed for 5 hours at room temperature. The enterokinase cleavage reaction was terminated by the addition of 100 mM phenylmethylsulfonyl fluoride to 1 mM for a five minute incubation period. The samples were then subjected to Western blot analysis described in the previous section.

RESULTS AND DISCUSSION

Characterization of Vesicle Formation using Gel Filtration Chromatography, Dynamic/Static Light Scattering, and Entrapment of Solutes

The detergent dialysis technique has been successfully employed to reconstitute membrane proteins into vesicles. Membrane proteins are typically solubilized using detergents such as octylglucoside, deoxycholate, and Triton X-100 which are amenable to the detergent dialysis method [151]. Unfortunately, the detergents commonly used to solubilize membrane proteins for reconstitution aren't powerful enough to completely solubilize and de-aggregate the caveolin-1 transmembrane domain. Highly pure, de-lipidated $Cav1_{62-178}$ is soluble into 300 mM PFOA at concentrations up to 3 mg/mL. Moreover, PFOA can readily solubilize lipids. Advantageously, PFOA has a high CMC (~10-30, buffer dependent) so it is easily dialyzable and has been shown to have a reasonable dialysis half-life of 10 hours [142]. For these reasons PFOA was chosen as a detergent that could be employed as an alternative to those typically used in membrane protein reconstitution studies.

When forming vesicles, the preparations were not visibly turbid unless sodium chloride was included in the outer buffer or cholesterol/protein was added to the mixture. Upon centrifugation at 20,000 *x g* of the vesicles formed in only 10 mM Tris-HCl, no lipid precipitated out of solution after three days of dialysis. This indicated that the lipid was in solution, but the particles formed were too small to scatter significant amounts of light. On the other hand, when as little as 25 mM sodium chloride was included in the buffer, the vesicles showed turbidity after two days of dialysis. At concentrations 200 mM or above, significant precipitation of the lipid was observed resulting in low vesicle

yields, and therefore examinations of species formed at high ionic strength was not carried out.

To examine differences in the size and homogeneity of vesicles upon the addition of NaCl, cholesterol, and protein, gel filtration and dynamic light scattering experiments were carried out. The chromatograms generated for vesicles formed with NaCl, cholesterol, and $^{HSVFLAG}Cav1_{62\text{-}178}$ are shown in Figure 2-2. All traces showed Gaussian distributions in the particle sizes indicating that the vesicle formation process is well controlled and results in homogeneous species. However, as vesicle preparations increased in size, more aggregated material was observed to elute at the void indicating that additives can cause some inhomogeneity in the formation dynamics.

Elution volumes decreased as the NaCl concentration included in the vesicle formation buffer increased, indicating an increase in the size of the vesicles formed (Figure 2-2 A). Interestingly, the elution volume showed a sigmoidal relationship with respect to the concentration of NaCl that the vesicles were formed in (Figure 2-3). This indicates that the size of vesicles formed largely depends on the ionic strength of the medium. Above 100 mM NaCl the vesicles all eluted at the void volume and separation of the well defined vesicles from any large aggregates formed was not possible using Sepharose 4B.

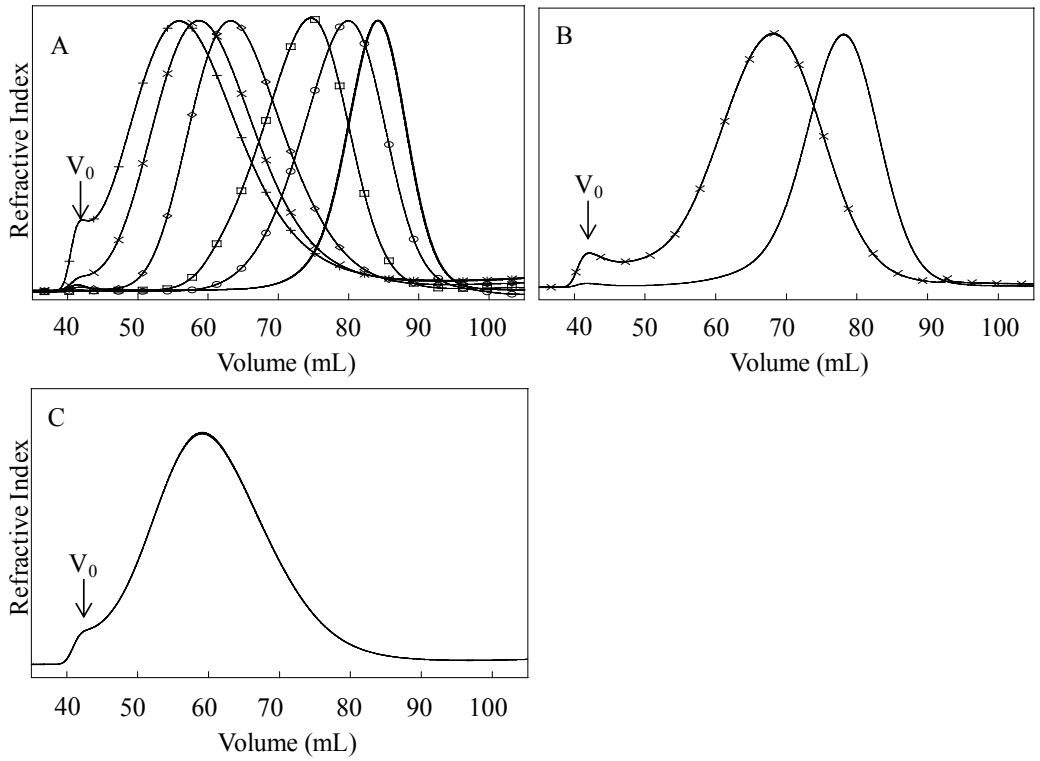

Figure 2-2. **A)** Refractive index traces of vesicles formed in the presence of 0 mM (–), 25 mM (○), 37.5 mM (□), 50 mM (◊), 75 mM (×), and 100 mM (+) of NaCl. **B)** Refractive index traces of vesicles formed with a PC:Cholesterol ratio of 80:20 (–) and a PC:Cholesterol ratio of 60:40 (×). **C)** Refractive index trace of vesicles formed in the presence of $^{HSVFLAG}Cav1_{62\text{-}178}$. This preparation included 50 mM NaCl and had a protein to lipid ratio of 1:6000. Void volumes denoted by an arrow.

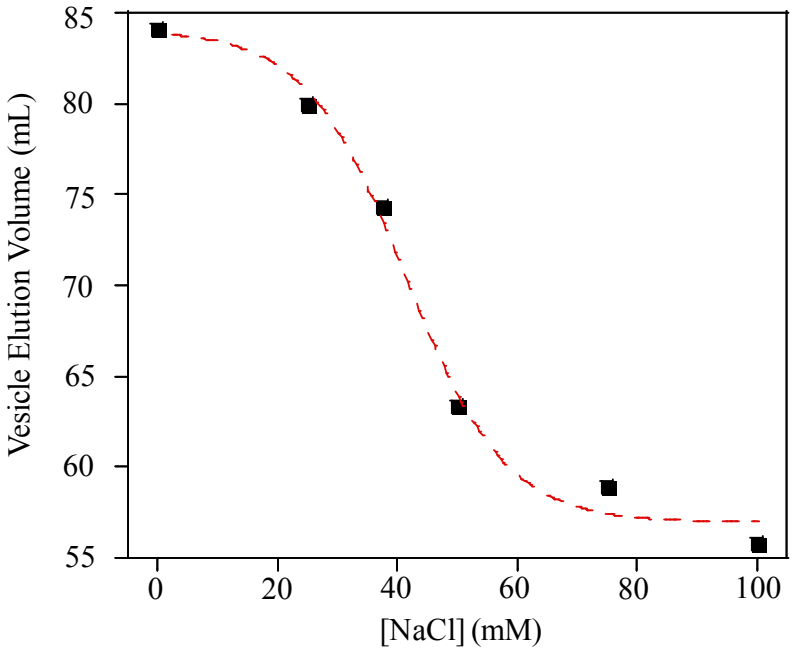

Figure 2-3. Elution volume as a function of NaCl concentration that was maintained during vesicle formation.

The addition of cholesterol at 20 and 40 mol % resulted in more precipitate that had to be removed by centrifugation before injection of the sample onto the sepharose 4B column. The addition of cholesterol also decreased the elution volume of vesicles prepared, suggesting that the sterol increases the size of the vesicles (Figure 2-2 B). The addition of cholesterol also broadened the peaks indicating a wider distribution of vesicle sizes. The amount of material eluting at the void volume was insignificant for the addition of 20% by mol cholesterol but increased somewhat for 40% by mol cholesterol. However, the voided material and the well-defined vesicular population were still resolved.

There appeared to be a limit to the amount of protein that could be included in the lipid-detergent mixture during the dialysis without resulting in significant precipitation of lipid and protein, and it was found that a 1:6000 ratio of protein to lipid was required to

yield homogenous preparations of vesicles. The addition of $^{HSVFLAG}Cav1_{62-178}$ at a 1:6000 protein to lipid ratio decreased the elution volume of the vesicle peak when compared to vesicles that were formed in the absence of $^{HSVFLAG}Cav1_{62-178}$ formed in the presence of 50 mM sodium chloride (Figure 2-2 C). Inclusion of the protein also resulted in a somewhat broader elution profile, indicating that the protein alters the heterogeneity of the vesicle preparation. This result is consistent with a size increase of the vesicles which is likely a consequence of $Cav1_{62-178}$ changing the vesicle formation dynamics. Species eluting at the void were insignificant when compared to the major peak, indicating that the vesicle formation process is well controlled at the specified ratio.

Size determinations of the approximate hydrodynamic radius of vesicles came from DLS measurements (Figure 2-4 and Table 2-1). The vesicle size trends using DLS were consistent with elution volumes from gel filtration experiments where larger sizes were always correlated with lessened elution volumes. It was observed that the smallest species (0 mM NaCl added), which formed vesicles of about 11 nm in radius, were unstable and after several days the appearance of a large 230 nm aggregate was detected by DLS. The fusion of these species may be a consequence of limited space to pack the large EYPC headgroups within a highly curved sphere and would result in a large amount of curvature strain, which would be relieved by aggregation of the small particles into larger vesicles. This type of behavior is commonly observed for small unilamellar vesicles (less than 30 nm in diameter) which fuse to form larger more stable vesicles[133]. Anomalous binding of membrane proteins to the bilayer surface as opposed to integration into the hydrophobic core has been reported during reconstitution procedures using

vesicles of this size [152]. Due to the instability of these particles, they were not characterized further in terms of their ability to entrap solutes.

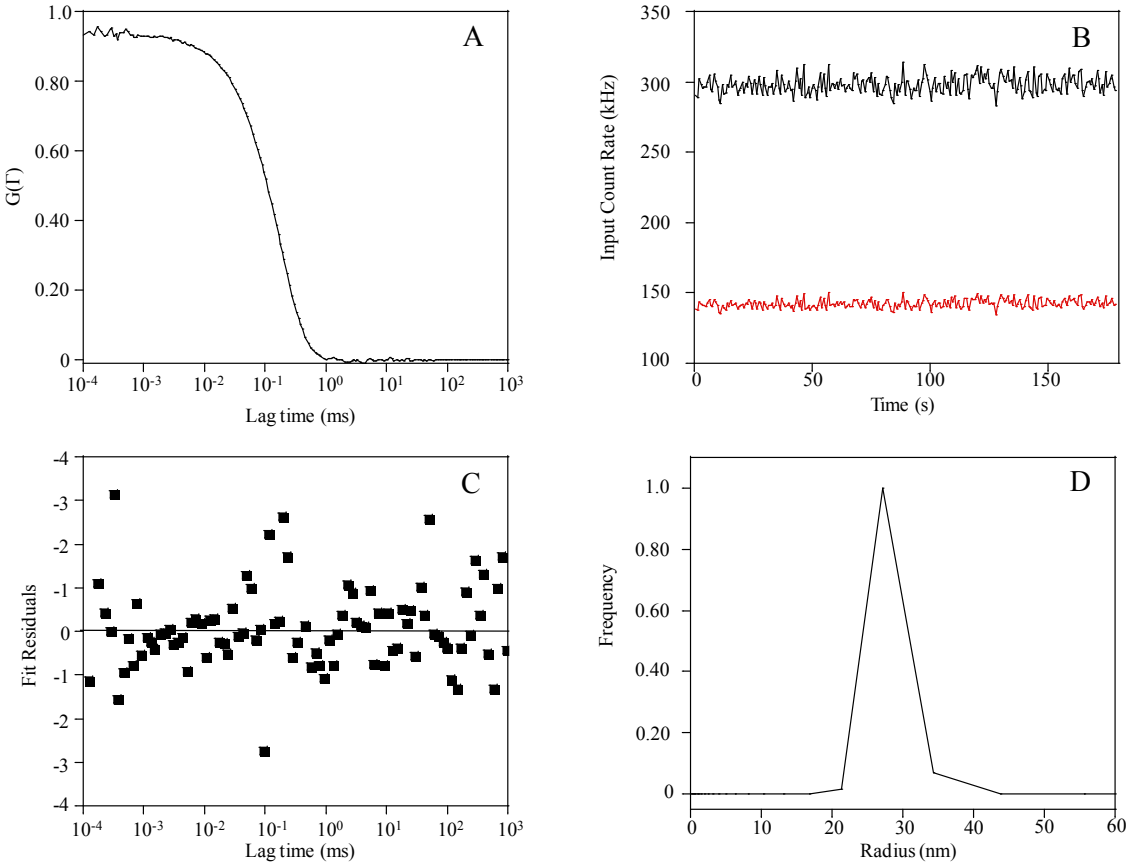

Figure 2-4. Data obtained using dynamic light scattering for vesicles formed in the presence of 100 mM NaCl. **A)** Regularized correlation function derived from fluctuations in scattered light as a function of the measurement time. **B)** Count rate obtained by two correlators show tiny undulations in the scattered intensity hitting the detectors indicative of a single population of small species. **C)** Residuals of the regularized correlation function fit that was used to derive the diffusion constant for utilization in the Stoke's-Einstein equation. **D)** Histogram of particle sizes from fitting of the correlation function and obtainment of the diffusion constant showing a very narrow distribution.

All other vesicle preparations showed that a single population of vesicles was formed. In contrast to vesicles formed without sodium chloride, the addition of 50-100 mM sodium chloride generated vesicles that were stable for one week at 4°C with very little change in size (Figure 2-5). The effect of NaCl on vesicle size is very interesting and may be

related to changes in the rate of detergent removal. It has been shown that vesicle sizes that result from the detergent dialysis method are related to the rate of detergent removal, where fast rates of removal result in small, monodisperse species [153]. Therefore, NaCl may result in slower PFOA removal, possibly by lowering the CMC of the detergent due to screening ionic repulsion of the negatively charged headgroup [154]. In agreement with gel filtration data, the size of the vesicles increased in a sigmoidal fashion (Figure 2-5).

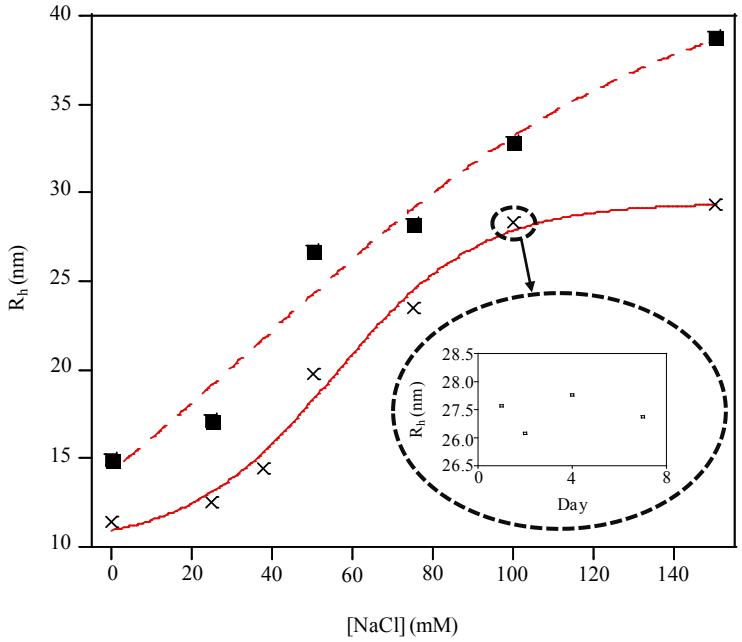

Figure 2-5. The size of vesicles obtained by DLS experiments show a sigmoidal trend for both protein lacking (solid line) and protein containing (dashed line) vesicles. The inset shows that the size of the vesicles formed in the presence of 100 mM NaCl are stable over a period of 1 week.

Advantageously, the addition of salt allowed for fine tuning of vesicle size, which could be used to examine curvature dependence on membrane protein activity/reconstitution behavior and in the case of fluorescence experiments, or to produce smaller vesicles which scatter less light.

A static light scattering experiment was employed on vesicles formed in the presence of 100 mM NaCl. This technique can give information about the radius of

gyration (R_g) and the molecular weight of a molecule diffusing in solution. These parameters are derived from variations in the scattered intensity of particles in solution as a function of the measurement angle and concentration. The combination of the R_g and R_h can be used to give shape information (sphere, rods, disks, worm-like structures) (Figure 2-6). The vesicles formed using the PFOA method did not vary in size upon changing the angle of detection significantly, supporting a spherical structure. This technique can also tell the difference between a hard sphere (non-vesicular) and a hollow sphere (vesicle) by using a Zimm plot to determine the radius of gyration and comparing it to the radius of hydration. Extrapolation to lipid concentration of zero yields a line with a slope that can be used to derive the R_g. For a hard sphere R_g/R_h=0.77 whereas for a hollow sphere $R_g \sim R_h$. For the vesicle preparation tested, the R_h was determined to be 27.01 ± 0.30 nm and the R_g was determined to be 25.42 ± 1.53 nm yielding a ratio of the two values close to 1 (~0.94) supporting the existence of hollow spheres.

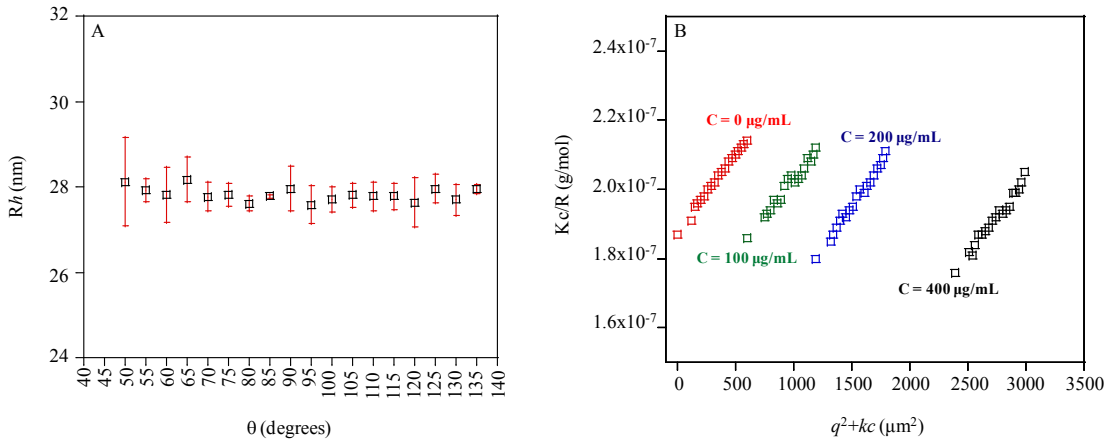

Figure 2-6. A) The R_h was invariant as a function of the scattering angle, providing evidence for the existence of a spherical particle. **B)** A Zimm plot generated using a static light scattering experiment for different vesicle concentrations allows for extrapolation of the R_g, proving the vesicles are hollow spheres.

In agreement with gel filtration data, cholesterol is shown to increase the hydrodynamic radius of the vesicles (Table 2-1). Doubling of the cholesterol content from 20% by mol to 40% by mol accounted for a roughly 10 nm growth in the size of the vesicles. These vesicles are close in size to those that have been observed for PC-cholesterol mixtures when prepared by sonication at the same mol % [155]. Importantly this method can incorporate cholesterol into vesicles at concentrations relevant to caveolae [26].

When vesicles with reconstituted $^{HSVFLAG}Cav1_{62-178}$ were prepared at different NaCl concentrations they were on average larger than those formed in the absence of protein. Generally, $^{HSVFLAG}Cav1_{62-178}$ vesicles were 5-10 nm larger (about 6 nm on average) than their purely lipid counterparts (Figure 2-5 and Table 2-1).

[NaCl] mM	Caveolin (-) Rh (nm)	Caveolin (+) Rh (nm)	Cholesterol (mol %)	Rh (nm)
0	11.39 ± 0.14	14.91 ± 0.10	20	12.41 ± 1.60
25	12.52 ± 0.28	17.11 ± 0.36	40	22.93 ± 2.20
37.5	14.48 ± 1.70	-		
50	19.81 ± 0.84	26.75 ± 0.68		
75	23.54 ± 0.68	28.22 ± 1.0		
100	28.28 ± 1.70	32.89 ± 0.66		
150	29.30 ± 2.0	38.79 ± 0.89		

Table 2-1. Table of vesicle sizes obtained using DLS.

Considering that a 7 nm size increase occurs when comparing vesicles formed using 50 mM NaCl in the presence or absence of caveolin, it is clear that the integration of the protein must profoundly change the vesicle formation dynamics. This is especially remarkable when considering that there are only about 4 $^{HSVFLAG}Cav1_{62-178}$ molecules per vesicle using a 1:6000 protein to lipid ratio. For instance when glucose, which is highly polar and would not likely interact with the lipids and detergents, was included in the formation buffer at a 500 mM concentration, there was no change in vesicle elution time compared to when it was absent. This supports the idea that $^{HSVFLAG}Cav1_{62-178}$ was

integrated into the volume of the bilayer and was not simply entrapped. Interestingly, the addition of protein alters the sigmoidal behavior observed for non-protein containing vesicles where there is a less steep transition going from small unilamellar vesicles to large unilamellar vesicles and the curve doesn't seem to level off clearly by the final point tested. It is possible that the protein's presence results in alterations in the formation dynamics of the vesicles. The final size of vesicle formed by detergent dialysis is related to the size of the mixed micelle that is present just prior to the onset of solubilization (in this case, onset of vesicle formation) [153]. Therefore, the protein could alter the size of the mixed micelle just prior to vesicle formation. For subsequent studies, vesicles containing protein were formed in the presence of 50 mM NaCl because these vesicles were consistent with the size of a caveola (50-100 nm diameter), making the vesicles an ideal mimic in terms of the curvature that caveolin-1 would experience in the native membrane. In addition, these vesicles were stable over long periods of time if kept at 4°C.

One important property that defines vesicles versus other bilayer mimics is that they have a distinct interior and exterior, and this makes them ideal for topology assays that assess the orientation of proteins reconstituted into them. To assess if the vesicles were static and hollow, a classic glucose entrapment experiment was performed to show that polar solutes present during the formation process can be encapsulated inside the vesicles. First, the internal volume of the vesicles was calculated by the method of Huang and Mason using the R_h obtained from DLS experiments [156]. This analysis assumes a 4.5 nm thickness of the bilayer and surface area of 0.70 nm^2 for each lipid. A

calibration plot was generated based on this theoretical treatment and was used to link glucose entrapment to the size of the vesicles (Figure 2-7).

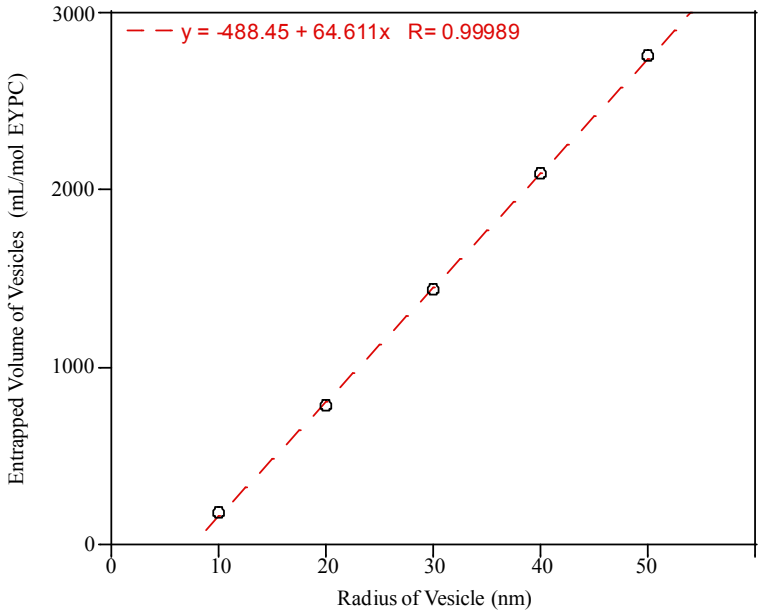

Figure 2-7. Entrapped volume of vesicles as a function of their size. This plot was used to obtain theoretical amounts of glucose that would be entrapped by EYPC vesicles in the size range generated for the studies performed.

Using the internal volume entrapment parameter it is possible to assess if the vesicles are static by measuring the mass of glucose entrapped per mass of lipid and comparing it to an expected value based on a given vesicle size and loaded glucose concentration. For this experiment, vesicles formed in the presence of 100 mM NaCl for pure lipid vesicles or 50 mM NaCl for $^{HSVFLAG}Cav1_{62-178}$ vesicles (1:6000 protein to lipid ratio) were used since vesicles of approximately the same size are formed using both methods. Based on theoretical calculations, the entrapped volume for non-protein loaded vesicles was 0.155 µg glucose/µg lipid. The actual entrapped volume was determined to be 0.133 µg glucose/µg lipid. The two values are with 14% of each other, indicating that the vesicles are static and hollow, in agreement with the SLS studies. This is also evidence of

unilamellar vesicle preparations as multilamellar vesicles entrap much less than the theoretical value based on a sphere with only a single bilayer. For the protein loaded vesicles, the entrapped volume was found to be 0.116 μg glucose/μg lipid. This agreed well with the theoretical value of 0.140 μg glucose/μg lipid. The two values are within 17% of each other, indicating that the $^{HSVFLAG}Cav1_{62-178}$ does not significantly alter the encapsulation properties of the vesicles formed. As mentioned the inclusion of glucose in the formation buffer had no effect on the size of the vesicles formed. Furthermore, the closeness of the experimental value to the theoretical value supports the accuracy of DLS measurements. Although glucose entrapment proves that the vesicles are hollow and likely unilamellar, it does not give data on the integrity of the vesicles over time.

To evaluate the permeability of the vesicles as a measure of stability over time, glucose-6-phospate, which cannot pass through bilayers due to its -2 charge, was entrapped in vesicles with and without $^{HSVFLAG}Cav1_{62-178}$. Un-entrapped material was removed using desalting resin and then glucose-6-phosphate dehydrogenase was added to the exterior of the vesicles. This enzyme is large and will not be able to access entrapped glucose and will thereby only process glucose-6-phophate that leaks through the vesicles. Once the glucose-6-phosphate dehydrogenase processes the glucose-6-phosphate by oxidizing the anomeric carbon, $NADP^+$ is reduced to NADPH which then reduces 2-(4-Iodophenyl)-3-(4-nitrophenyl)-5-(2,4-disulfophenyl)-2H-terazolium and produces a yellow colored formazan [157]. After roughly 400 minutes at room temperature the vesicles were lysed with Triton-X-100 detergent to assess the total levels of glucose-6-phosphate entrapped. Figure 2-8 shows the entrapment study result. It was observed that over time there is very slow leakage rate in both protein containing and non-protein containing

vesicles. There was a slight difference with the protein containing vesicles being somewhat more permeable (roughly 4 fold) than those prepared in the absence of the protein (Figure 2-8 inset). After the addition of detergent, there was a large increase in the signal as the substrate became available to glucose-6-phosphate dehydrogenase confirming that glucose-6-phosphate was entrapped. It is surprising that the permeability would be altered by the addition of $^{HSVFLAG}Cav1_{62\text{-}178}$ to the vesicles given that it is not a pore forming peptide. Reports of leakage of entrapped vesicle contents from the reconstitution of transmembrane proteins such as mellitin do exist, although the mechanism is still unclear. Nonetheless, it is likely that the vesicles are intact and contents on the interior would not be accessible to larger species, such as enzymes.

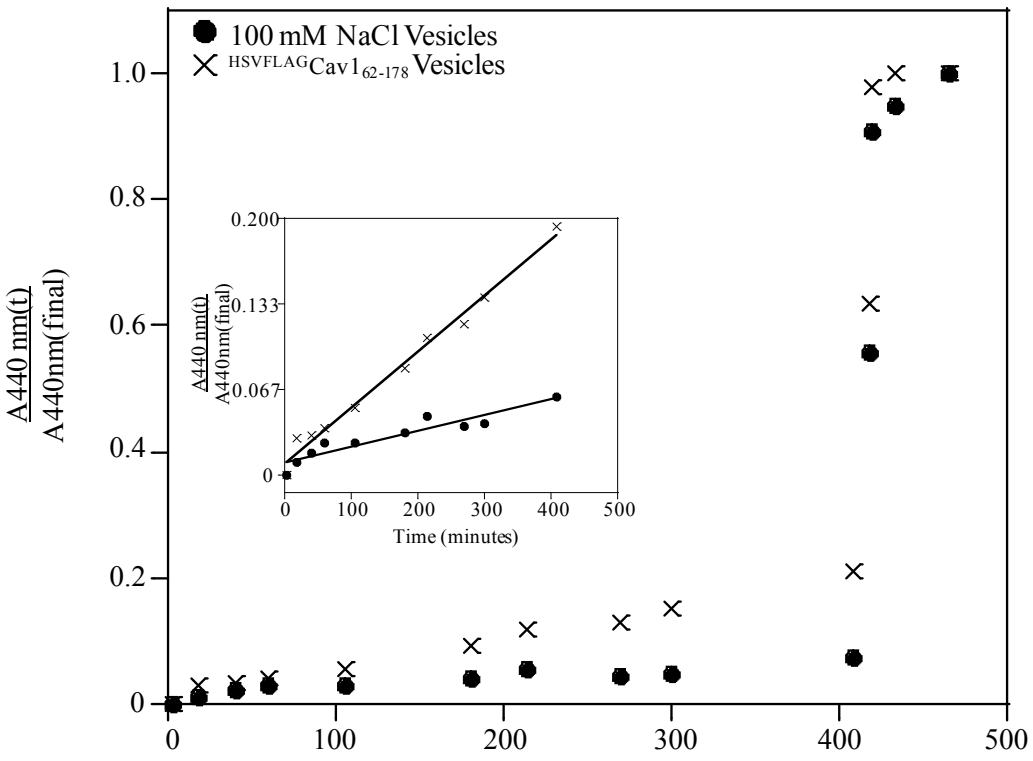

Figure 2-8. Glucose-6-Phosphate is entrapped within the vesicles over a time period of ~400 minutes. The contents are released by the addition of the mild detergent Triton-X-100 proving that the vesicles are static. The inset shows a small difference in the natural leakage rate between protein lacking and protein containing samples.

Reconstitution and Topological Evaluation of $^{HSVFLAG}Cav1_{62-178}$

After first determining that $^{HSVFLAG}Cav1_{62-178}$ was associated with the vesicle containing faction eluting from the gel filtration column by Western blotting, the amount of protein reconstituted into various cholesterol containing vesicles was examined (Figure 2-9). This method shows that $^{HSVFLAG}Cav1_{62-178}$ co-elutes with the vesicle containing fraction (the weak band above the intense band is a small amount of dimer which was frequently observed during SDS-PAGE analysis, Figure 2-9A). Therefore, $^{HSVFLAG}Cav1_{62-178}$ is incorporated into the vesicles using the PFOA method. Interestingly, $^{HSVFLAG}Cav1_{62-178}$ runs higher than the expected molecular weight of 18.2 kD (Figure 2-9A lane 2). This phenomenon has been reported as a property of hairpin structured membrane proteins due to anomalous detergent binding [158]. Next, the amount of $^{HSVFLAG}Cav1_{62-178}$ incorporated into cholesterol containing vesicles (lanes 3 and 4) was compared relative to the amount of $^{HSVFLAG}Cav1_{62-178}$ incorporated into non-cholesterol containing vesicles (lane 2) and yielded values of 1.0, 0.91, and 1.11 for 0, 5, and 20% cholesterol respectively. This analysis was undertaken because caveolin putatively binds cholesterol in the 94-101 region and an earlier study where caveolin was reconstituted into vesicles found that the protein required cholesterol to achieve significant amounts of reconstituted protein [19,159,160]. This analysis determined that there was no difference in $^{HSVFLAG}Cav1_{62-178}$ incorporation into the vesicles due to cholesterol. Therefore, it appears that caveolin does not strictly require cholesterol to partition into membranes. However, it cannot be discounted that the facile reconstitution of $^{HSVFLAG}Cav1_{62-178}$ into vesicles may be enhance by the presence of the protease cleavage sites engineered to the ends of the protein that were required for a topological evaluation.

To better understand if the $^{HSVFLAG}Cav1_{62-178}$ protein used in these studies was behaving as an integral membrane protein and not just as a peripherally bound or a vesicle entrapped species, a sodium carbonate extraction method was utilized [161]. This method uses sodium carbonate at pH 11.5 to linearize the vesicles into membrane sheets as well as to break up electrostatic interactions between peripherally bound proteins and the membrane surface. The membrane sheets are then collected by ultracentrifugation, and if a membrane protein is incorporated into the bilayer it will be localized to the pellet. Figure 2-9B shows the result of this study. Lane 1 and 2 represent pre- and post-carbonate extraction samples of the same vesicle preparation loaded to the same final protein concentration (10 μg/mL). Analysis of these species by densitometry shows that there is very little difference in intensity of the bands found at 18.2 kD having relative intensities that are within 30% of one another, providing evidence that the $^{HSVFLAG}Cav1_{62-178}$ construct used in these studies is behaving as an integral membrane protein and is not superficially absorbed to the vesicles surface due to electrostatic interactions.

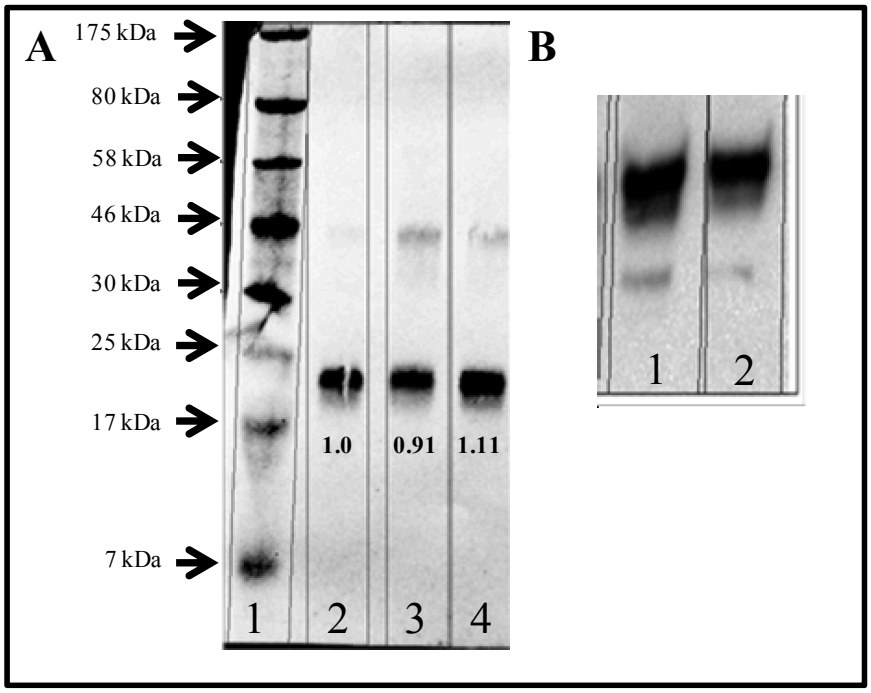

Figure 2-9. A) Western blot analysis of caveolin-1 reconstituted into vesicles of varied cholesterol composition. Lane 1 is a molecular weight ladder. Lane 2, 3, and 4 represent reconstitution of $^{HSVFLAG}Cav1_{62-178}$ into vesicles with a lipid composition of 0, 5, and 20% cholesterol by mol respectively. Each lane was quantified relative to the $^{HSVFLAG}Cav1_{62-178}$ band in lane 2 using densitometry. **B)** Western blot analysis of pre and post carbonate extraction of caveolin-1 from vesicles indicating that caveolin-1 is integrated into the hydrophobic matrix of the vesicles. Bands were quantified relative to the amount of $^{HSVFLAG}Cav1_{62-178}$ in lane 1 by densitometry.

A protease protection assay was used to determine if the protein had been integrated into vesicles in a native 'horseshoe' orientation. Two enterokinase restriction sites were placed on each flank of the transmembrane region, that if solvent accessible, would be cleaved by the protease. It is unlikely that enterokinase would be able to cross bilayers due to its large size (26 kD) and soluble nature, therefore it was an excellent way to probe exposure of the $^{HSVFLAG}Cav1_{62-178}$ termini upon reconstitution. Furthermore, the prior result showing that glucose-6-phosphate dehydrogenase (67 kD) cannot process the majority of entrapped glucose-6-phosphate until vesicle permeabilization by detergent adds support to the notion that enterokinase would not be able to access the interior of the

vesicles. Preceding the N-terminal FLAG site and after the C-terminal FLAG site, are HSV antibody recognition epitopes, which were added to enhance molecular weight changes upon enterokinase cleavage (Figure 2-10).

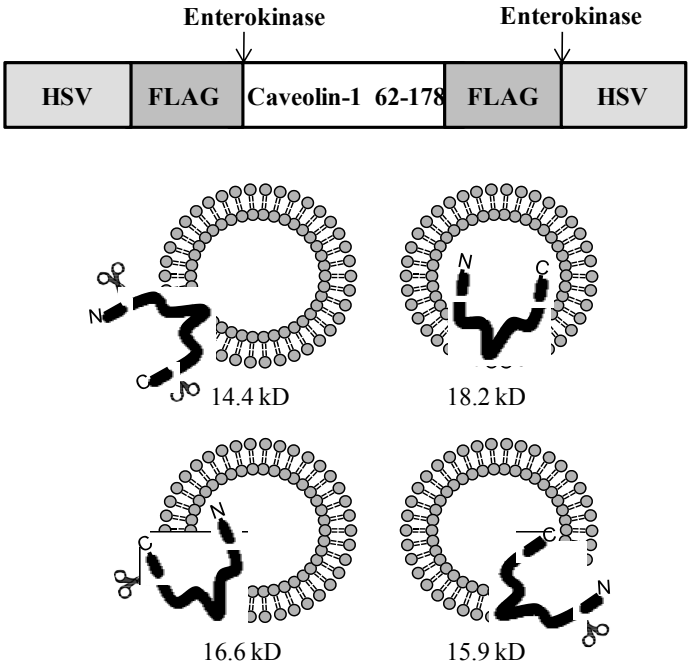

Figure 2-10. Graphic representation of the limited proteolysis assay principle performed on $^{HSVFLAG}Cav1_{62-178}$. The bar diagram on top shows the construct layout with different cleavage possibilities and their expected molecular weight shifts shown below.

Using this construct, four cleavage products were possible, each indicating a different topological orientation within the vesicles. The four predicted molecular weights upon enterokinase treatment are 18.2 kD (uncleaved), 16.6 kD (C- terminal only cleavage), 15.9 kD (N- terminal only cleavage), and 14.4 kD (both termini cleaved). Two possibilities correspond to caveolin-1's natively folded orientation (18.2 kD and 14.4 kD) and two possibilities correspond to a non-biologically relevant transmembrane orientation (16.6 kD and 15.9 kD). The result of the cleavage reaction performed on $^{HSVFLAG}Cav1_{62-178}$ reconstituted into vesicles formed using the PFOA detergent dialysis technique is shown in Figure 2-11. The molecular weight markers generated from making truncations

of $^{HSVFLAG}Cav1_{62-178}$ (Figure 2-11 lane 1) are run side by side with the enterokinase treated and untreated vesicles (Figure 2-11 lanes 2 and 3). Clearly, the four possibilities can be resolved using SDS-PAGE. The cleavage pattern after five hours of allowing the vesicles to interact with enterokinase is shown in lane 3 and resulted in the appearance of two major bands. These cleavage products correspond to the fully cleaved product (14.4 kD) as well as the C-terminally cleaved product (16.6 kD). Using densitometry to compare relative amounts of the cleavage product to the uncleaved parent band showed that although a fraction $^{HSVFLAG}Cav1_{62-178}$ is integrated with both N- and C- termini facing the exterior of the vesicle (32 ± 5%, n=3), most of the protein is present in a misfolded ($N_{interior}$, $C_{exterior}$) transmembrane orientation (60 ± 2% , n=3, Figure 2-11, lane 3).

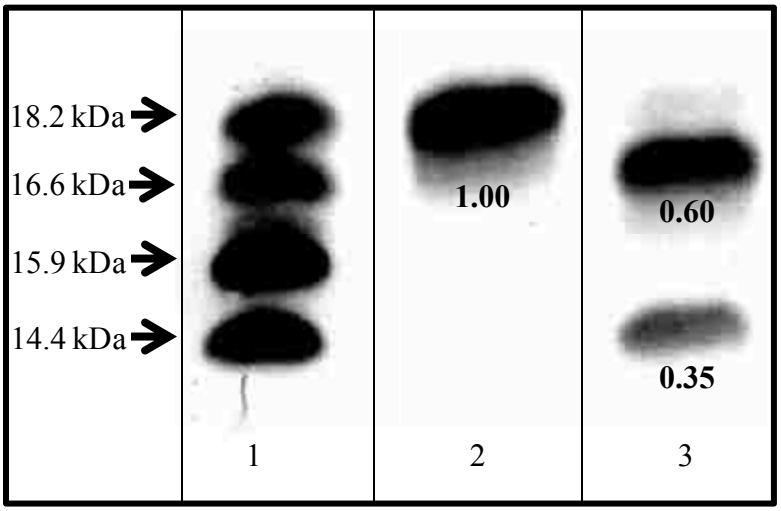

Figure 2-11. Typical results of limited proteolysis assay performed on $^{HSVFLAG}Cav1_{62-178.}$ Lane 1 shows a home-made molecular weight marker that is used to track the cleavage pattern (all four possibilities). Lane 2 shows $^{HSVFLAG}Cav1_{62-178}$ prior to the addition of enterokinase. Lane 3 shows the post enterokinase cleavage product which resulted in the appearance of two major bands. The cleavage products are quantified relative to the parent band in lane 2 by densitometry.

It is worth mentioning that changes in the ionic strength of the formation buffer (leading to a size change in the vesicles) did not have an effect on the observed cleavage pattern, downplaying any significance of vesicle curvature. The result from the cleavage study is surprising for two reasons: One is that the transmembrane conformation would require a significant tilt of the protein to provide hydrophobic coverage of the intramembrane domain and the other is that the protein seems to preferentially orient with the C-terminus on the exterior or with both termini facing the exterior indicating specific topologies were preferred. It would be expected that if the protein weren't refolded properly, a mixture of all four topologies would be observed, however, this was not the case. This leads to the interesting idea that there is an equilibrium between the native topology and the transmembrane topology which would be controlled biologically. It also leads to the possibility that the natively folded population positions its termini on the side of less curvature through a biophysical mechanism as only small amounts of uncleaved species were observed (usually below the detection limit of the assay). It is possible that the tags at the termini or the N-terminal truncation alter the proteins topological behavior. It has been demonstrated that residues flanking the transmembrane region of caveolin have lead to differences in its membrane orientation when translated in the presence of dog pancreas microsomes. Specifically, it was found that a full length caveolin construct with glycosylation epitopes at its termini could be not be glycosylated at either termini ($N_{cytoplasmic}$, $C_{cytoplasmic}$), in line with the study discussed in chapter 1. However, a construct in which N-terminal residues 1-95 were removed could be glycosylated at the N-terminus ($N_{luminal}$, $C_{cytoplasmic}$), and the removal of C-terminal residues 140-178 resulted in a construct that could be glycosylated at its C-terminus ($N_{cytoplasmic}$, $C_{luminal}$) [76]. Finally,

in a construct where the removal of all portions of the protein except the intramembrane domain (construct: 96-139), a mixture of topologies was observed. Removal of the termini changes the net charge of the wild-type caveolin molecule. In the $^{HSVFLAG}Cav1_{62-178}$ construct, both termini have a negative net charge yielding a possible parallel between our studies and the aforementioned study where a fine balance of charged residues may be required to uphold caveolins specific membrane orientation. Therefore the construct used in these studies may not necessarily capture the true nature of the native caveolin-1 given that the addition of a *single* residue flanking a transmembrane sequence has been shown to alter its topology [162].

Another possibility exists that although the insertion of our polypeptide into the bilayer is controlled thermodynamically by lipid-protein interactions (therefore correct hydrophobic coverage is obtained, as evidenced by carbonate extraction), a specific orientation is controlled biologically by the cellular machinery which inserts membrane proteins into the lipid bilayer (such as the Sec61 translocon complex) [163]. Interestingly, the Sec61 translocon often places termini of transmembrane sequences that are preceded by positively charged residues on the cytoplasmic side of the membrane, and the caveolin TMD is flanked by a lysine at position 96 and a lysine at position 136 [164]. Nonetheless it is still very interesting to consider that caveolin-1 may orient with a preference outside of a biological system but more studies will be needed to determine what drives this preference.

It is also known that refolding proteins using fluorous surfactants, such as PFOA, results in the formation of non-native α-helices [143]. These non-native helices could be stable after the detergent has left resulting in the improperly folded transmembrane

orientation. Therefore, it is possible that PFOA is too harsh or too exotic to result in properly folded material. Clearly, other approaches will need to be explored to natively fold caveolin-1 *in vitro*.

CONCLUSIONS

In this chapter, a method of forming lipid vesicles by detergent dialysis of PFOA-EYPC mixtures was demonstrated. This expands upon the limited number of detergents that have properties that facilitate membrane protein reconstitution into vesicles by detergent dialysis (high CMS and can solubilize membrane proteins at high concentrations). Important properties of the vesicles were confirmed including the size, shape, homogeneity, and the ability to entrap solutes included in the formation buffer. It was found that NaCl can be used to control the size of the vesicles formed and that cholesterol can be incorporated into the vesicles in biologically relevant quantities. A novel assay for examining the permeability of the polar solute glucose-6-phosphate was demonstrated and could be useful for studies examining the effects of proteins, detergents, or small molecules on the integrity of vesicles. The reconstitution of a functional construct of the integral membrane protein caveolin-1 was proven by co-elution with vesicles on a gel filtration column. Caveolin-1 was shown to be reconstituted into the bilayer as an integral membrane protein by the carbonate extraction method. Interestingly the $^{HSVFLAG}Cav1_{62\text{-}178}$ construct used in the studies was found to increase vesicle size and permeability slightly. A limited proteolysis assay was presented and it was shown that the majority (60 %) of the protein adopted a non-native fold, possibly due to alterations to the constructs termini, detergent mediated formation of non-native α-helices, or the need for a protein chaperone to mediate the insertion. The remaining population was found to have both termini exposed, indicating that a small fraction could be refolded in a directional fashion. The methodologies presented here may be useful for reconstituting extremely hydrophobic membrane proteins that have

limited solubility in commonly used detergents used for vesicles formation by detergent dialysis.

Appendix 2-1. Sequence of Protein Constructs Utilized

Construct	Protein Sequence
$^{HSVFLAG}Cav1_{62-178}$ Full Length	QPELAPEDPEDDYKDDDDKDVV KIDFEDVIAEPEGTHSFDGIWK ASFTTFTVTKYWYRLLSALFGI P**L**ALIWGIYFAILSFLHIWAVV P**S**IKSFLIEIQ**S**ISRVYSIYVH TV**S**DPLFEAVGKIFSNVRINLQ KEIDYKDDDDKDGIQPELAPED PED
$^{HSVFLAG}M_{ins}Cav1_{62-178}$ N-Terminal Cleavage	QPELAPEDPEDDYKDDDDKMDV VKIDFEDVIAEPEGTHSFDGIW KASFTTFTVTKYWYRLLSALFG IP**L**ALIWGIYFAILSFLHIWAV VP**S**IKSFLIEIQ**S**ISRVYSIYV HTV**S**DPLFEAVGKIFSNVRINL QKEIDYKDDDDKDGIQPELAPE DPED
$^{HSVFLAG}Cav1_{62-178}Stop_{ins}$ C-Terminal Cleavage	QPELAPEDPEDDYKDDDDKDVV KIDFEDVIAEPEGTHSFDGIWK ASFTTFTVTKYWYRLLSALFGI P**L**ALIWGIYFAILSFLHIWAVV P**S**IKSFLIEIQ**S**ISRVYSIYVH TV**S**DPLFEAVGKIFSNVRINLQ KEIDYKDDDDK
$^{HSVFLAG}M_{ins}Cav1_{62-178}Stop_{ins}$ N/C-Terminal Cleavage	QPELAPEDPEDDYKDDDDKMDV VKIDFEDVIAEPEGTHSFDGIW KASFTTFTVTKYWYRLLSALFG IP**L**ALIWGIYFAILSFLHIWAV VP**S**IKSFLIEIQ**S**ISRVYSIYV HTV**S**DPLFEAVGKIFSNVRINL QKEIDYKDDDDK

Appendix 2-2. Mutagenesis primers utilized

Construct	Primer Sequence
$^{HSVFLAG}M_{ins}Cav1_{62-178}$ N-Terminal Cleavage	5'- CAAAGACGACGACGACAAAATGGACGTTGTT AAAATCGACTTC-3'
$^{HSVFLAG}Cav1_{62-178}Stop_{ins}$ C-Terminal Cleavage	5'- CGACGACGACAAAGACTAAATCCAGCCGGAA CTGG-3'

Appendix 2-3. PCR Cycling Conditions

Reaction Component	Volume
Sterile ddH2O	13.3 µL
10X Pfu Turbo Buffer	2.5 µL
10X 9N° Ligase Buffer	2.5 µL
DMSO	0.2 µL
dNTPS (25 mM)	2.5 µL
Template DNA (30 ng/µL)	1.0 µL
Forward (5'-3') Quikchange primer (10 µM)	1.0 µL
Pfu Turbo Polymerase	1.0 µL
9N° Ligase	1.0 µL

PCR Cycling Conditions		
Number of Cycles	Temperature	Time
1	95°C	30 seconds
30 Step1	95°C	30 seconds
Step2	55°C	1 minute
Step3	68°C	6 minutes
Storage	4°C	∞

Appendix 2-4. Transformation Protocols

General Transformation Protocol XL-1 Blue/BL21DE3 *E. coli*

1. Pre-chill a culture tube and thaw 50 µL of cells on ice
2. Add cells and DNA to the culture tube according to the following table:

Application	Cell Type	Amount DNA
Standard Transformation	XL-Blue/BL21DE3 (Subcloning Grade)	1µL of 20 ng/µL plasmid DNA
Mutagenesis	XL-Blue (Ultra-competent)	1µL of post PCR reaction/post DpnI treated mixture
Ligation	XL-Blue (Subcloning Grade)	1µL of post ligation mixture

3. Incubate reaction mixture on ice for 30 minutes.
4. Heat shock the cells at 42°C for 90 seconds.
5. Place the culture back on ice for two minutes.
6. Add 300 µL of SOC media to the culture.
7. Incubate at 37°C for 1 hour with shaking at 250 rpm.
8. Plate various dilutions on LB (XL-1 Blue) or MDAG (BL21DE3) agar plates supplemented with the appropriate antibiotic and allow to grow over night.
9. Pick a single colony for desired downstream application.

Appendix 2-5. Starter and Media Recipes

MDG Starter Recipe (5 mL)		**MDAG Starter Recipe (5 mL)**	
Reagent	Volume	Reagent	Volume
ddH2O	4.8 mL	ddH2O	4.7 mL
1M $MgSO_4$	10 µL	1M $MgSO_4$	10 µL
1000× Trace Metals	1 µL	1000× Trace Metals	1 µL
25% (*w/v*) Aspartate	50 µL	25% (*w/v*) Aspartate	20 µL
40% (*w/v*) Glucose	62.5 µL	40% (*w/v*) Glucose	43.8 µL
50×M	100 µL	50× M	100 µL
17 Amino Acids	None	17 Amino Acids	100 µL
40 mg/mL Methionine	None	40 mg/mL Methionine	40 µL
1000 × Kanamycin	5 µL	1000 × Kanamycin	5 µL

ZYM-5052 Recipe (2L)	
Reagent	Amount
ddH2O	1916 mL
NZ Amine	20 grams
Yeast Extract	10 grams
1M $MgSO_4$	4 mL
1000X Trace Metals	400 µL
50×M	40 mL
50×5052	40 mL

Appendix 2-6. Auto-Induction Growth Protocol

1. Add either a fresh colony or a crystal from a 15% glycerol cell stock to 1-5 mL of MDG supplemented with antibiotic and shake on a platform shaker at 250 rpm at 37℃ for 16-20 hours.
2. Dilute starter culture into ZYM-5052 at a 1:1000 culture to ZYM-5052 ratio and shake on a platform shaker at 250 rpm at 37℃ for 10-14 hours.
3. Harvest by centrifugation at 5000 *x g* for 30 minutes at 4℃.
4. Wash pellets with 0.9 % (*w/v*) NaCl at 1/5 the original culture volume.
5. Centrifuge 5000 *x g* for 30 minutes at 4℃.
6. Cell pellets can be stored short term (days) at -20℃ or long term (months) at -80℃ before protein preparation.

Chapter 3. Does Caveolin-1 Contain a Membrane Embedded Turn?

ABSTRACT

Caveolin-1 is critical in many cellular functions that are localized within caveolae. It is thought that caveolin induces membrane curvature and drives the formation of caveolae, although the mechanism remains elusive. However, caveolins unique topology could be key in understanding the structural role that leads to its bilayer bending predilection. The membrane interacting portion of caveolin-1 is comprised of two α-helical segments, (H1 and H2) connected by a three-residue unstructured break with both N- and C-termini exposed to the cytoplasm. A U-shaped configuration is assumed based on its inaccessibility to extracellular matrix probes, however, both the structure and *exact* topology of caveolin within a bilayer remains elusive. This chapter aims to characterize the structure, depth, and conformation of the core membrane interacting region of caveolin-1 residues 82-136 ($Cav1_{82\text{-}136}$) in a DMPC bilayer using NMR, fluorescence emission measurements, and molecular dynamics simulations. The secondary structure of $Cav1_{82–136}$ from NMR chemical shift index analysis serves as a guideline for generating initial structural models for molecular dynamics simulations (MD). Fifty independent molecular dynamics simulations (100 ns each) were performed to identify the favorable conformation and orientation of $Cav1_{82\text{-}136}$ in the bilayer. A representative configuration was chosen from these multiple simulations and was simulated for 1 μs to further explore the stability and dynamics of $Cav1_{82\text{-}136}$. The results of the simulations agreed strongly with tryptophan fluorescence measurements (i.e., $Cav1_{82–136}$ insertion depth in the bilayer). These data work together to corroborate that $Cav1_{82–136}$ inserts in the membrane with a U-shaped conformation, and that the angle between H1 and H2 is

dynamic and ranges from 35 - 69°. The overall tilt of the $Cav1_{82–136}$ molecule was found to be 27 ± 6°, and it was observed that H1 and H2 tilt differentially to provide lipid coverage of their hydrophobic segments. Additionally, the simulations also reveal that specific faces of H1 and H2 prefer to interact with each other and with lipid molecules and these interactions may help stabilize the membrane-embedded U-shaped conformation.

INTRODUCTION

Despite great gains in the characterization of the secondary structure of caveolin, there are still major questions in terms of its *exact* membrane topology which need to be addressed in order to better understand the proteins tertiary structure in the context of the lipid bilayer. One major question that has brought controversy is what is the structure and orientation of caveolin-1 in a bilayer? Another is the question of the existence of specific intramolecular caveolin helix-helix or intermolecular caveolin-lipid interactions that would help dictate caveolin structure and orientation. This chapter tackles these provocative and critical questions using molecular dynamics (MD) simulations guided and supported by NMR and tryptophan fluorescence emission data. NMR experiments were performed to determine the secondary structure of a caveolin-1 construct consisting of the CSD and IMD (residues 82–136: $Cav1_{82–136}$). NMR experiments employing chemical shift index analysis indicates that residues A87–F107 form helix 1 (H1) and L111–A129 form helix 2 (H2) which are separated by a three residue break spanning from G108 to P110. This data provided a template for starting conformations in molecular dynamics simulations. The short simulations were employed to sample a large conformational space by generating 50 × 100 ns trajectories of $Cav1_{82–136}$ embedded in a lipid bilayer with various starting angles between H1 and H2, different initial H1 and H2 interfaces, and different initial insertion depths. Next, a simulation that best represented the averaged parameters from the short simulations was utilized for an extended conformational evolution over a 1 μs time period to further explore dynamics, stability, and protein-lipid interactions.

The simulation results provide evidence that a U-shaped conformation for $Cav1_{82–136}$ embedded in the lipid bilayer is stable over the course of the simulations. The tilt of the overall $Cav1_{82–136}$ molecule was determined to be 27 ± 6°, revealing a nearly vertical disposition for the protein. The angle between the two helices was dynamic but maintained an average of 53 ± 5°. Interestingly, side-chain interactions between the two helices near the three residue break were evident and may be at play in helping the protein maintain its conformation. Depth measurements revealed that the turn residues were buried within the hydrophobic core of the membrane. The depth was corroborated with tryptophan fluorescence experiments examining the Stoke's shift data obtained for $Cav1_{82–136}$ single tryptophan mutants. Simulations examining the interaction between $Cav1_{82–136}$ and lipids showed that residues in both leaflets of the bilayer can interact with lipid headgroups *via* water mediated hydrogen-bonding. These interactions likely play an important role in the topological and conformational preferences of caveolin-1 within the bilayer. Overall, this chapter helps provide a better understanding of caveolin-1 structure and behavior within the lipid bilayer.

MATERIALS AND METHODS

NMR spectroscopy

Isotopically labeled $Cav1_{82–136}$ and $Cav1_{82–136}$(W85F, W98F, W115F, W128F) were prepared according to protocols described by Lee et al [70]. Lyophilized $Cav1_{82–136}$ constructs were dissolved into a buffer containing 100 mM 1-myristoyl-2-hydroxy-sn-Glycero-3-[Phospho-rac-(1-glycerol)] (sodium salt) (LMPG, Avanti Polar Lipids, Alabaster, AL), 100 mM NaCl, 20 mM phosphate at pH 7, and 10% D_2O for a final protein concentration of ~1.0 mM. This mixture was vortexed vigorously until a clear homogeneous solution resulted. The sample was then passed through a 0.2-μm regenerated cellulose spin filter. NMR spectra were acquired at 310 K using a 600 MHz Avance II spectrometer (Bruker, Billerica, MA) equipped with a cryoprobe. For analysis and backbone assignments, the following transverse relaxation optimized spectroscopy based [165] pulse sequences were utilized: HSQC [166], HNCA [167], HNCACB [168], HN(CO)CA [169], and HNCO [170]. The spectra were processed using NMRPIPE and SPARKY software [171,172]. For the generation of the chemical shift index plot, the observed Cα chemical shifts were subtracted from their corresponding random coil chemical shifts as described by Wishart and Sykes [173]. To aid in backbone assignments, specific amino-acid labeling was employed (Gly, Phe, Tyr, Leu, Ile, and Val).

Single Tryptophan Mutant Cloning, Expression, and Reconstitution into Bicelles

$Cav1_{82–136}$ was cloned, expressed, and purified according to protocols described in Chapter 2 [146]. $Cav1_{82–136}$ contains four tryptophan residues: W85, W98, W115, and W128. Single tryptophan mutant constructs were prepared using the Quick-change site-directed mutagenesis kit (Agilent, Santa Clara, CA). In each mutant, one of the four

native tryptophan residues was retained and the other three were mutated to phenylalanine. Primers were designed using the free web-based primerX program (Bioinformatics.org). See Appendix 2-3 for PCR reaction and cycling conditions. A TROSY-HSQC spectrum was obtained for the most dramatic mutant ($Cav1_{82–136}$(W85F, W98F, W115F, W128F)) to confirm that these mutations were not significantly altering the structure of the native $Cav1_{82–136}$.

$Cav1_{82–136}$ was reconstituted into 4% (*w/w*) lipid, ***q***= 0.5 DMPC/CHAPSO (1,2 dimyristoylphosphatidylcholine (Avanti Polar Lipids, Alabaster, AL)/3-[(3-cholamidopropyl)dimethylammonio]-2-hydroxy-1-propane sulfonate) (Anatrace, Maumee, OH) bicelles at a protein concentration of 30 μM. To achieve this, $Cav1_{82–136}$ was first reconstituted into DMPC vesicles by dissolving the protein and lipid to 30 μM and 20 mM, respectively, in a buffer containing 300 mM PFOA and 20 mM Tris-HCl pH 8.0. This solution was then dialyzed (three 24-h exchanges) against 1 L buffer (20 mM Tris-HCl pH 8.0 and 50 mM NaCl). The vesicle containing solution was centrifuged at 10,000 *x g* for 20 minutes at room temperature. The supernatant collected and centrifuged at 366,613 *x g* for 2 h at 4°C to pellet the vesicles. The pelleted vesicles were then converted into 4% (*w/w*) lipid, ***q*** = 0.5 bicelles by adding ice-cold buffer components (2.704 mL 20 mM phosphate pH 7.0 and 296 μL 25% (*w/w*) CHAPSO) and slowly mixing on ice over the course of 30–60 minutes. The bicelles were then centrifuged at 10,000 *x* g for 20 minutes at room temperature to remove protein and lipid aggregates that may have formed during the reconstitution process. The supernatant was used for fluorescence measurements.

Determination of λ_{max} for Single Tryptophan Mutants

Three separately prepared samples were used to determine λ_{max} for each single tryptophan mutant. Bicelles were used because they scatter very little light, and contain a planar DMPC bilayer, which closely mimics the environment employed in the simulations [116]. Fluorescence emission spectra were acquired using a 1 × 1 cm quartz cuvette held at 310 K with an Eclipse fluorometer (Agilent, Santa Clara, CA). The excitation wavelength used was 295 nm to avoid unwanted tyrosine excitation [127]. Both the excitation and emission slit widths were set to 5 nm. The emission spectra were measured from 315 to 500 nm with a scan speed of 1 nm/s and 0.5 nm data point increments. Four scans were averaged for each construct. A blank solution containing only bicelles was used to subtract background fluorescence. The λ_{max} values were obtained by fitting the spectra to a log-normal distribution using Igor Pro 6.22A software (Wavemetrics, Portland, OR) [133].

Building a Structural Model for *In Silico* Analysis of Caveolin-1

The characterization of the structure and dynamics of $Cav1_{82\text{-}136}$ on a quantitative level required that a model be generated that describes parameters which define its intramolecular fold and topological disposition with respect to the bilayer. To define the intramolecular fold of $Cav1_{82\text{-}136}$ with respect to the bilayer, four parameters are needed: the angle between the two helical axes of H1 and H2 (θ), the angle of rotation for H1 (ρ_1) and H2 (ρ_2), and the distance between a pair of residues that are in close contact (Res_{ij}, the residues are on different helices). To define the rotation, two vectors in the plane perpendicular to the helical axis of rotation are used. One of these vectors is the fifth Cα from the N-terminus of the helix, the other is one drawn connecting the centers of the two

helices, both of which are in structured spots that do not have conformational floppiness that would cause difficulties in interpreting the data to arise (Figure 3-1).

A description of the topology requires four additional parameters: the $Cav1_{82-136}$ tilt angle (φ), which is the angle between the molecular plane of caveolin and the membrane normal, the individual helical tilts of H1 (α) and H2 (β) in the $Cav1_{82-136}$ molecular plane (the least squares plane through all of the Cα atoms which define helices H1 and H2), and the insertion depth of the protein in the bilayer (Z_{COM}), which is defined as the center of mass of the Z position (distance from the bilayer center in Å) of residues at the break (G108-P110). Although it may not be clear, the individual tilt angles of the helices are necessary for an unambiguous description of the $Cav1_{82-136}$ fold in the bilayer. This is because the helices sometimes deviate from the molecular plane of caveolin in the simulations, however, the two individual tilt angles are a good approximation of θ when the two helices are within the same plane (α-β≈θ).

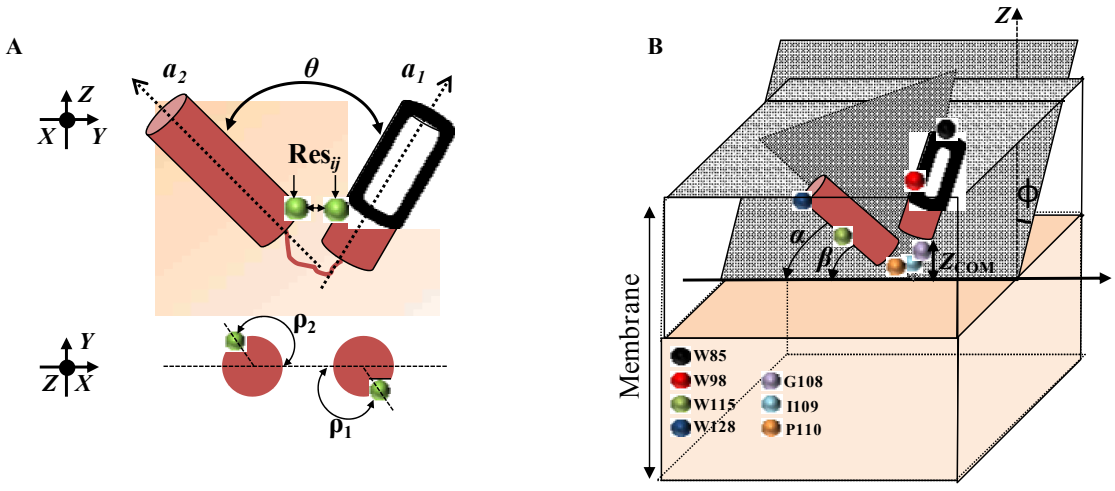

Figure 3-1. A) Parameters used to define the intramolecular fold of $Cav1_{82–136}$ and B) Parameters used to define the orientation of the $Cav1_{82–136}$ molecule with respect to the lipid bilayer. Spheres show the approximate location of residues of interest in terms of their burial within the bilayer.

Multiple 100 ns and 1 μs caveolin-1 simulations in DMPC bilayers

A $Cav1_{82–136}$ model was first generated using the IC BUILD command in CHARMM [174]. Based on the secondary structure assignments from the chemical shift index plot, residues A87–F107 (H1) and L111–A129 (H2) were modeled as ideal α-helices with their Φ- and Ψ- angles assigned to -57.8° and -47°, respectively; the other residues were modeled with their Φ - and Ψ- angles in the CHARMM residue topology file. The Φ- and Ψ- angles of G108 were varied randomly to generate initial structures of $Cav1_{82–136}$ with different angles between the helical axes of H1 and H2 (θ). These structures were then placed into five categories ($\theta_{initial}$=45°, 55°, 65°, 75°, and 85°), with 10 replicas in each set, all of which have θ within ± 5° of $\theta_{initial}$. Prior to inserting caveolin models into the bilayer, the protein was oriented so that its principle axis (the vector sum of the axis of H1 and H2) coincided with the membrane normal (Z). As there is no concrete depth measurement in existence for caveolin, the insertion depth of the model in each replica system was initially positioned along the Z axis by randomly placing the break residues' centers of mass (COM) between -5 Å and 5 Å; by definition Z=0 corresponds to the bilayer center.

After the generation of these initial models, each one was embedded in a DMPC bilayer, solvated by 0.15 M KCl. The system was composed of ~52,000 atoms and had a size of 75 × 75 × 90 $Å^3$. Every system was individually constructed using the MEMBRANE BUILDER module [175,176] in CHARMM-GUI [177]. Each short simulation was ascribed a reference code in the form of cav1_P_Q, with P and Q corresponding to the value of $\theta_{initial}$ and the replica index (cav1_45_5 corresponds to the fifth replica with $\theta_{initial}$=45°). Each system was allowed to equilibrate for 225 ps to allow initially

uncorrelated system components to relax. After this short time period, 100 ns second simulations were performed for each of the 50 systems. For the first 50 ns of each simulation the dihedral restraints of H1 and H2 backbone atoms were not allowed to float in order to maintain their secondary structure according to the chemical shift index analysis. This was designated as an equilibrium time period and was not utilized in the final trajectory analysis. For the final 50 ns, these restraints were taken away and the system was allowed to explore the conformational preferences of $Cav1_{82\text{-}136}$.

All calculations were performed with the constant particle number, pressure, and temperature (NPT) ensemble [178] using CHARMM [174]. The temperature was maintained at 310 K using Nosé-Hoover temperature control [179,180] and the extended system algorithm was employed to maintain a pressure of 1 atm along the membrane normal [178]. The C27 all-atom force field [181] with a modified version of dihedral cross-term correction [182] was used for the protein. In addition to the protein force field, the C36 lipid force field [183] was used for DMPC and the TIP3P water model [184] was employed for water molecules. A time step of 2 fs was enabled with the SHAKE algorithm [185]. Because of the U-shaped conformation of caveolin-1 and potential changes in the protein cross-sectional area in both lipid leaflets during the simulation, the P21image transformation [186] was applied to allow the variation in the number of lipids at the top and bottom leaflets during the simulation. The non-bonded and dynamics options were kept the same as in the MEMBRANE BUILDER input; the van der Waals interactions were smoothly switched off at 10–12 Å by a force-switching function [187] and the electrostatic interactions were calculated using the particle-mesh Ewald method [188] with a mesh size

of ~1 Å for fast Fourier transformation, κ=0.34 Å^{-1}, and a sixth-order B-spline interpolation.

After allowing $Cav1_{82–136}$ to explore conformational and structural preferences in a DMPC bilayer using the multiple 100 ns simulations, the distribution of final structural parameters (θ, φ, α, β, $\rho1$, $\rho2$, Z) for each set was analyzed to ascertain the most probable values. A snapshot from one of the short simulations, cav1_65_3 at 85 ns had structural parameters that met the criteria of being a near mimic of the most probable values from the 50 simulations. This system was employed for a 1-μs simulation using ANTON, a supercomputer designed for long timescale MD simulations. As prior, a constant particle number, volume, and temperature (NVT) ensemble was employed with the Nosé-Hoover temperature coupling scheme (310 K).

The lengths of all bonds involving hydrogen atoms were constrained using M-SHAKE [189]. The cutoff of the van der Waals and short-range electrostatic interactions was set to 10.06 Å. Long-range electrostatic interactions were evaluated with the *k*-space Gaussian split Ewald method [190] and a 64 × 64 × 64 mesh. The integration time step was 2 fs. The r-RESPA integration method [191] was employed and long-range electrostatics were evaluated every 6 fs.

RESULTS AND DISCUSSION

Probing the secondary structure of $Cav1_{82–136}$

A combination of HSQC, HNCA, HNCACB, HNCO, and HN(CO)CA experiments, in conjunction with selective amino-acid labeling, were employed to give definitive backbone assignments for $Cav1_{82–136}$. The HSQC obtained for $Cav1_{82–136}$ revealed excellent chemical shift dispersion, which was indicative of a well structured protein, adding strength to using the secondary structure assignments obtained as a starting point for *in silico* analysis. Using the aforementioned methods, nearly all of the backbone residues (96%) were assigned and all of the Cα values were obtained. Figure 3-2 shows a chemical shift index plot of $Cav1_{82–136}$. Consistently positive stretches of ΔCα values indicate that residues 87–107 (H1) and 111–129 (H2) are α-helical [172]. In line with NMR studies on a shorter construct, (residues 96-136), there is a break between the two helices at residues 108–110, which most likely is the site of a turn between the helices, that returns the polypeptide chain to the same side of the membrane [70]. Regions flanking the helix-break-helix structural core (residues 82–86 and 130–136) show a random pattern of ΔCα values which is indicative of unstructured or dynamic regions of the protein. Importantly, TALOS+ which requires much more data input (Cα, Cβ, CO, N, and NH) is in agreement with the secondary structure assignment given to $Cav1_{82–136}$, confirming that the scaffolding domain and intramembrane domain have a helix-break-helix motif [192]. This expands upon what is known about caveolin-1 secondary structure in this region as it is in contrast to the model put forth by Parton et al. [66], which is based on primary sequence analysis, and predicts three distinct helical regions for residues 82–

136 (i.e., 81–92, 97–107, and 112–128). Therefore, it appears that $Cav1_{82-136}$ is composed of two helices that are roughly equal in length.

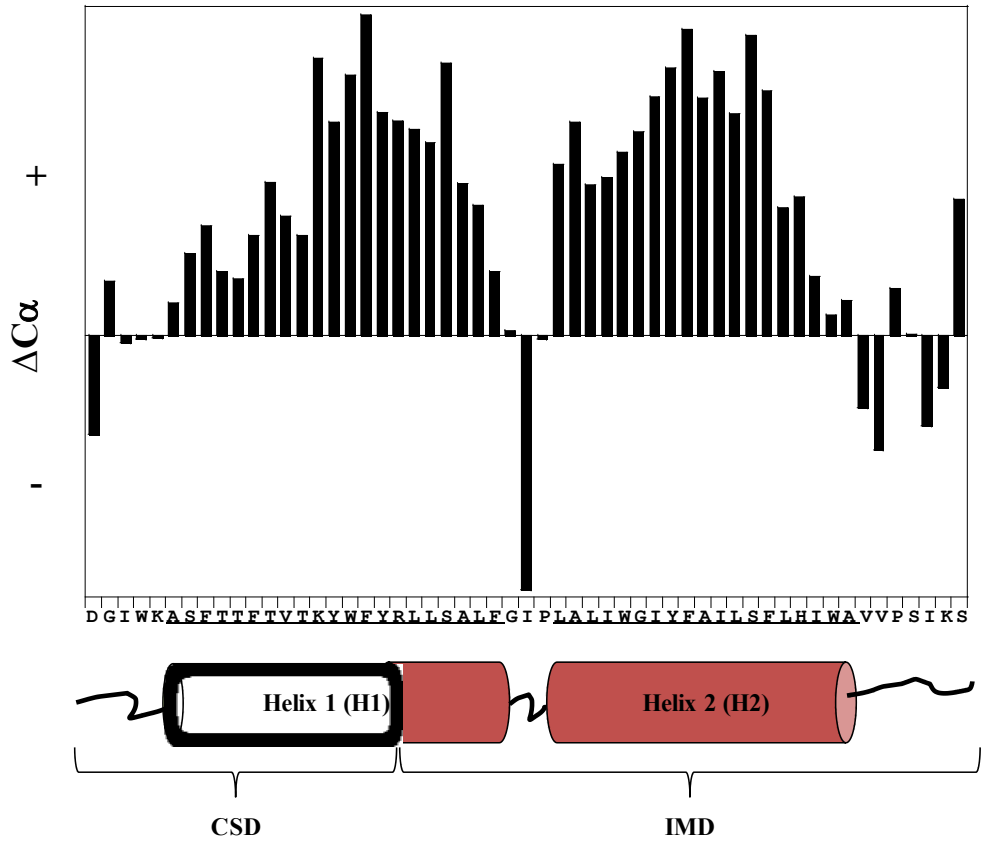

Figure 3-2. Chemical shift index plot of $Cav1_{82-136}$. The secondary structure is that of a helix-break-helix motif as consecutive positive ΔCα values are indicative of α-helical structure, consecutive negative values are consistent with β-strand structure, and mixtures are dynamic regions.

Defining the $Cav1_{82-136}$ Intramolecular Fold in a Lipid Bilayer

The most distinct structural feature of caveolin-1 is its unusual U-shaped conformation shown by *in vivo* studies, where the N- and C- termini rest on the same side of the membrane and there is no portion of the protein accessible to extracellular probes [71,74]. The current topological model places the portion of the protein that makes this dramatic turn to the same face of the bilayer from which it entered within the hydrophobic core of the bilayer. Combining this with the NMR studies, it is clear that

this U-shaped model is made up of a helix-break-helix motif, likely implicating residues 108-110 as the turn residues. Even with this information in hand, it is unclear how the helices would be separated – for instance, is caveolin forming a tight hairpin conformation or does the protein adopt a wide angle in which the protein is linear and rests on the surface of the inner leaflet? The angle between these helices also will likely play a large role in determining which residues pack together and their packing may give information in how a specific angle is stabilized by H1-H2 contacts.

Simulations were set up to examine this question in depth and help determine which angle between the two helices is energetically favorable. Simulation sets ranged with initial H1-H2 angles from 45-85° that were allowed to move into stable conformations over the timescale of the simulation. Figure 3-3 shows the distribution of θ for all simulations. It was found that U-shaped conformation is stable in 98% of the short simulations having θ<90°. Over the course of the longer simulation, the protein had a θ_{final}= 53 ± 5° which lent additional support to the stability of the U-shaped motif. This indicates that, within the timescale explored by the simulation, the U-shape conformation is stable within the bilayer. Significantly, this result shows that the protein is not linear and likely does not lay on the surface of the bilayer, which appears to be very unfavorable. This finding is in-line with carbonate extraction studies which have shown caveolin-1 as an integral membrane protein [71,72]. This important piece of data will aid further refining the proposed mechanism of caveolin induced membrane curvature. Interestingly this finding may eliminate a BAR-domain type mechanism which requires the protein to lay on the surface of the bilayer acting as a scaffold that stabilizes membrane curvature [80,193].

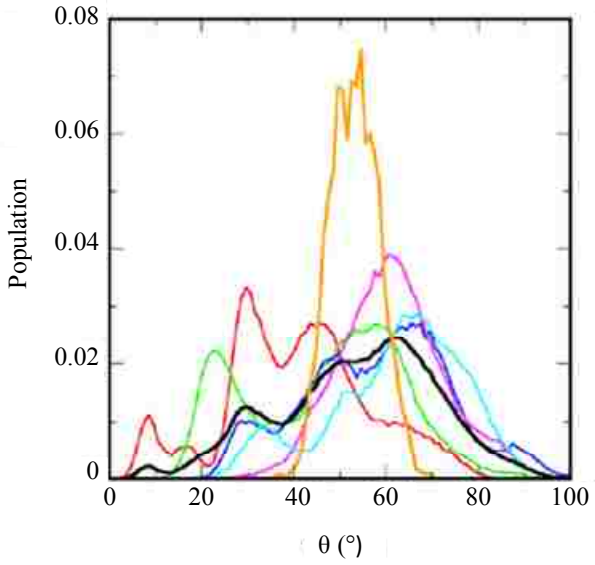

Figure 3-3. Population distributions of θ in all systems. Colors distinguish different simulation sets: cav1_45 (*red*); cav1_55 (*green*); cav1_65 (*blue*); cav1_75 (*magenta*); cav1_85 (*cyan*). Additionally, the 1 μs simulation is indicated (*orange*) along with the average of all the 100 ns systems (*black)*.

Interestingly, the $Cav1_{82\text{-}136}$ molecule displayed a dynamic fluctuation in its θ value in the 1 μs simulation where θ ranged from 35-69°. This fluctuation happened on a time scale in the tens of nanoseconds and was usually accompanied by the diffusion of lipids between the two helices. Lipid headgroup or tail intercalation between the two helices was observed the majority of the time, and their presence often persisted over the course of the entire simulation. The appearance of lipids between H1 and H2 limited the protein from sampling angles below 30°, as angles beneath this limit were coincident with absence of lipids between the two helices. Therefore, caveolin-lipid interactions are critical to the proteins maintenance of a specific fold in the bilayer.

Aside from lipid interactions, specific H1-H2 interactions could be at play in determining the fold of $Cav1_{82\text{-}136}$. Therefore, it was pertinent to determine if there were specific packing interactions between the faces of H1-H2 that could help explain the adoption of a θ value that holds $Cav1_{82\text{-}136}$ in its U-shape. The rotation angle (ρ_1, ρ_2) that

was varied randomly in the beginning of each simulation, the terminal position after the simulations is shown in Figure 3-4 as a cross plot.

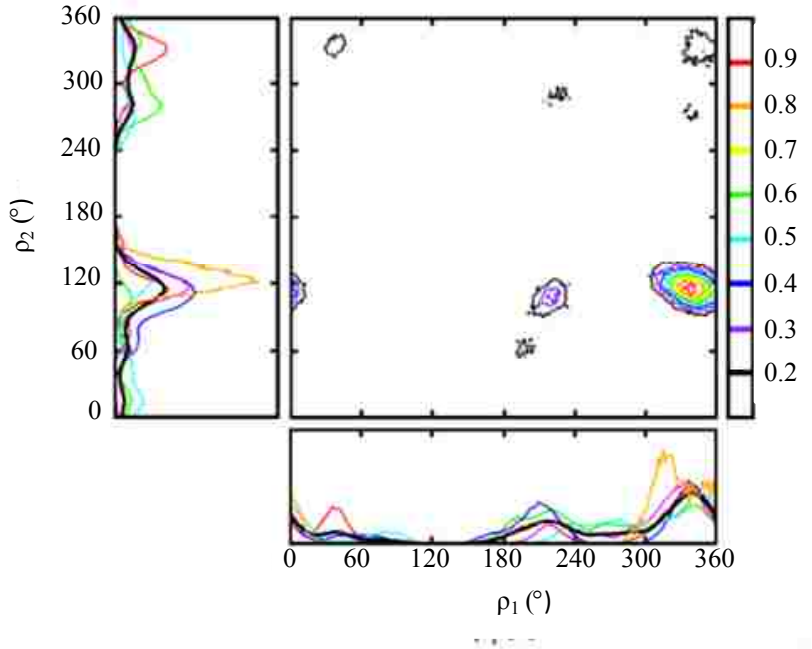

Figure 3-4. The average two dimensional rotation angle distribution for H1 (ρ_1) and H2 (ρ_2) shown as a contour map. Level of the contours are indicated going from low (*black*) to high (*red*) probability. The one-dimensional distributions of each individual helix are shown with each different simulation set distinguished by different colors with cav1_45 (*red*); cav1_55 (*green*); cav1_65 (*blue*); cav1_75 (*magenta*); cav1_85 (*cyan*). Additionally, the 1 μs simulation is indicated (*orange*) along with the average of all the 100 ns systems (*black).*

Although the values were initially randomized, they clearly collapsed upon a favorable orientation by the end of the short and 1 μs simulations of ρ_1=337°, ρ_2=115° and of ρ_1=331°, ρ_2=124° respectively. The closeness between long and short simulations in terms of their ρ_1, ρ_2 pair values, indicates that the helical contacts form quickly, therefore they are likely very stable and are not highly promiscuous. Specific interactions that were observed were van der Waals packing interactions near the turn as the helices come close together (Figure 3-5). Specifically, these packing interactions were between A105 and L106 of H1, I109 of the break, and I114 of H2. This result helps explain both the

biological conservation of a β-branched amino acid at position 109 across species and caveolin isoforms (Figures 1-3 and 1-4), and NMR structural studies that showed only β-branched amino acids are tolerated at this position for proper structuring. I109 is likely very important in mediating interactions between the two helices [70]. Diverging from the turn region, hydrogen bonding interactions between R101 and Y118 to lipid headgroups were observed. For R101 this interaction was electrostatic whereas for Y118 the interaction was due to hydrogen bonding. The positively charged amino acid at position 101 also represents a strongly conserved site among species and isoforms. Therefore, the combination of these interactions may be crucial in generating and holding the U-shaped conformation. It appears that short distance hydrophobic interactions are important at the point of the turn but longer distance hydrogen bonding interactions become dominant at the ends of the helices. Interestingly, in a short simulation in which the U-shape was not maintained, these interactions were not present, strengthening the case for a specific packing interface between H1 and H2.

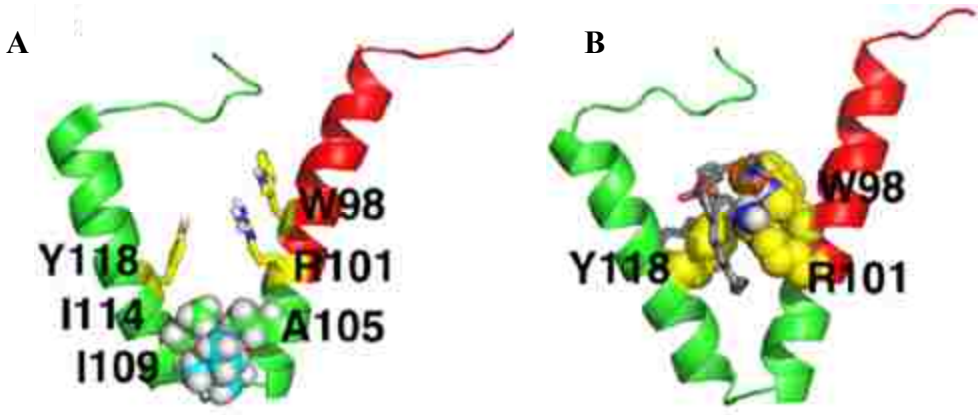

Figure 3-5. A) Residues that are found to interact at the Cav1$_{82\text{-}136}$ H1-H2 interface and **B)** Lipid-protein interactions through specific residues between H1 and H2. This is a cartoon representation and the caveolin-1 scaffolding domain (*red*) and intramembrane domain (*green*) are indicated. Lipids are indicated with phosphate atoms of the headgroups as *orange spheres* and tails as *grey* chains. Both snapshots were taken from the 1-μs simulation.

Evaluation of the Orientation and Membrane Depth of $Cav1_{82\text{-}136}$ in a DMPC Bilayer

The interplay between the hydrophobic length of transmembrane helices and the hydrophobic thickness of the lipid bilayer leads to tilting in membrane proteins. In $Cav1_{82–136}$, the helices have the additional complexity of being tethered together at the break region, which likely would have a role in determining the overall tilt of the caveolin molecule. Additionally, the two helices diverge in their physiochemical properties, therefore the tilts of each independent helix could modulate how the overall caveolin molecule tilts with respect to the membrane. Defining the way the protein tilts in the membrane will undoubtedly yield fruitful insight into caveolins structure-function relationship in a variety of biological contexts.

Over the course of the short simulations the tilt of the molecular plane of $Cav1_{82–136}$ (φ) was examined and fell to an average value of 21 ± 12°, indicating that the protein was near vertical with respect to the plane of the bilayer (Figure 3-6). This again points to a non-peripheral conformation of $Cav1_{82–136}$, otherwise much greater φ values approaching 90° would have been observed. This value varied greatly when comparing simulation sets, but over the longer time course fell to a more discrete value of 27.5 ± 6°, as indicated by the decrease in error in the simulation. Therefore, this result suggests that φ is a slow converging property and requires a longer time scale to obtain a suitable disposition in the bilayer, or is highly sensitive to the starting conformational parameters.

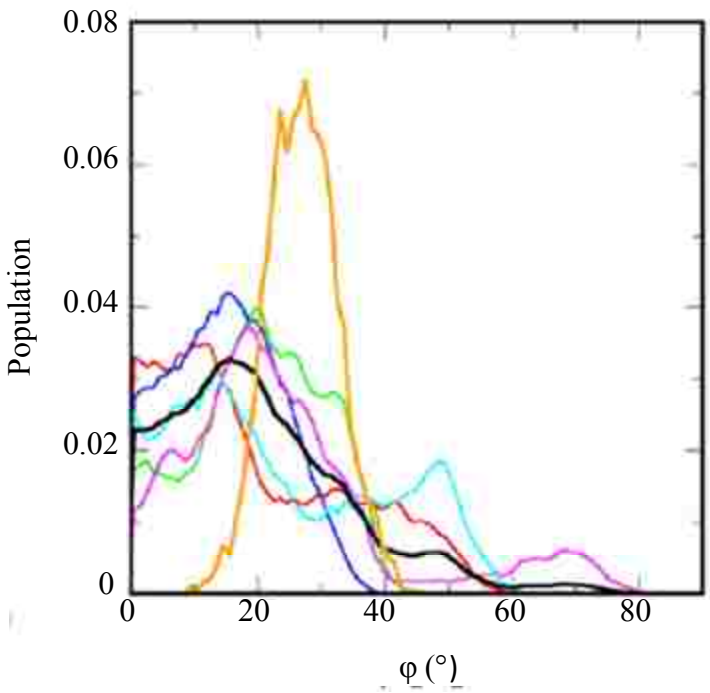

Figure 3-6. The population distribution of φ for all systems simulated. Different simulation sets are indicated by color: cav1_45 (*red*); cav1_55 (*green*); cav1_65 (*blue*); cav1_75 (*magenta*); cav1_85 (*cyan*). Additionally, the 1 μs simulation is indicated (*orange*) along with the average of all the 100 ns systems (*black)*.

With the overall tilt of $Cav1_{82–136}$ being described, there is still the possibility that H1 and H2 can lie somewhat outside the molecular plane of the overall caveolin molecule. This required the determination of individual tilt angles for H1 (α) and H2 (β) with respect to the plane of the bilayer (Figure 3-7).

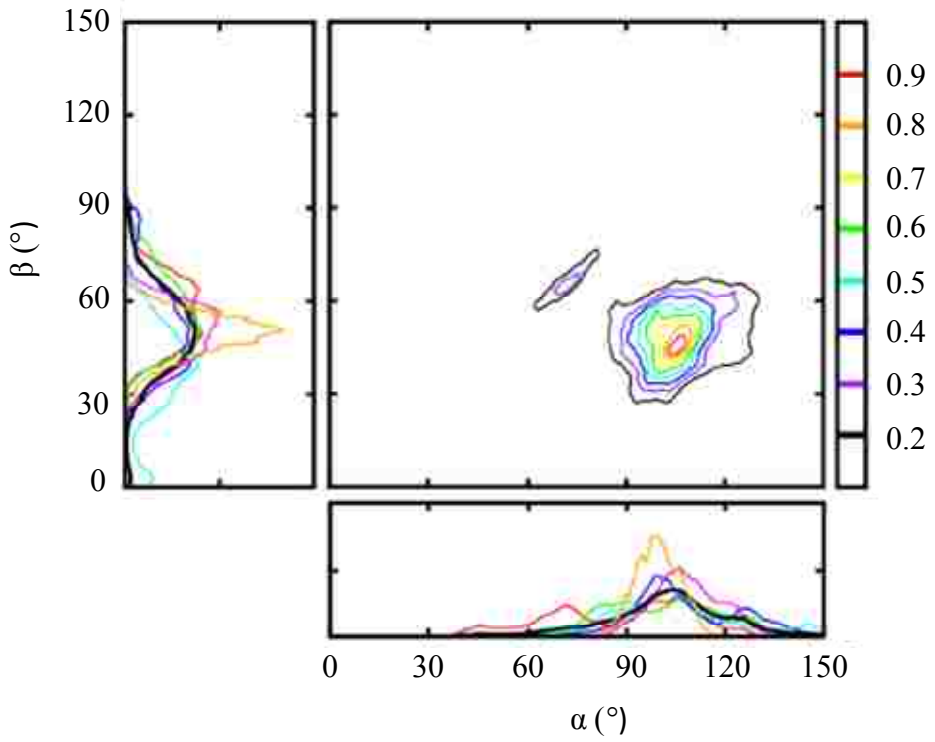

Figure 3-7. The average two-dimensional tilt angle distribution of individual helices H1(α) and H2(β) shown as a contour map. The contour levels are indicated by color going from low (*black*) to high (*red*) probability. The one-dimensional distributions of each individual helix are shown with each different simulation set distinguished by different colors with cav1_45 (*red*); cav1_55 (*green*); cav1_65 (*blue*); cav1_75 (*magenta*); cav1_85 (*cyan*). Additionally, the 1 μs simulation is indicated (*orange*) along with the average of all the 100 ns systems (*black).*

The position of α was found to range between 90-120° in nearly all of the short simulations, and fell to 99° for the 1 μs simulation, indicating a near vertical orientation for H1. For H2, a much greater tilt was observed having a value between 40-60° in the majority of short simulations and rested at 49° for the 1-μs time course. From a physiochemical standpoint these findings make sense with the sequences of H1 and H2. The value of 90° represents the minimum amount of coverage of an α-helix would have at a given depth within the bilayer. Examination of the primary sequence of H1 reveals that the first 2/3 of the helix are populated with a number of polar uncharged and charged

amino acids and does not become markedly hydrophobic until after R101. It is likely that $Cav1_{82–136}$ remains vertical to avoid the energetic penalty of removing the solvation shell from charged residues approaching its turn region such as K96 or R101. On the other hand, the second helix contains no charged amino acids and only a few polar uncharged amino acids, and is mostly comprised of hydrophobic amino acids that would prefer lipid bilayer coverage. Therefore, α and β strongly reflect the matching of the hydrophobic portions of the protein to the thickness of the bilayer.

The postulation of an intramembrane turn for $Cav1_{82–136}$ has remained a controversy as it is not typical for membrane proteins where the N- and C- termini rest upon the same side of the membrane. This is because it would require the breaking of *i* to *i+4* hydrogen bonds that are very stable within the bilayer due to a lack of competition with water molecules [194]. The simulation results show that the three residue break between helices is located within the hydrophobic core in both the short and the 1 μs simulation sets (Figure 3-8). The average Z values for each of the break residues for the short and long simulations are -5.1 ± 2.9 Å (G108), -5.4 ± 2.5 Å (I109), and -6.3 ± 3.0 Å (P110) and -5.9 ±1 .7 Å (G108), -6.8 ± 1.6 Å (I109), and -9.3 ± 1.3 Å (P110) respectively (Table 3-1). Clearly, the short simulations are much wider in their distributions and the longer simulation allows the protein to fall upon a more discrete depth for the break region. It is also important to note that the break residues are on average found in the second leaflet as the starting conditions placed the break randomly from -5 Å to 5 Å. This indicates that there is indeed a preference for these residues to be localized within the second leaflet and the final position is not biased by the starting position.

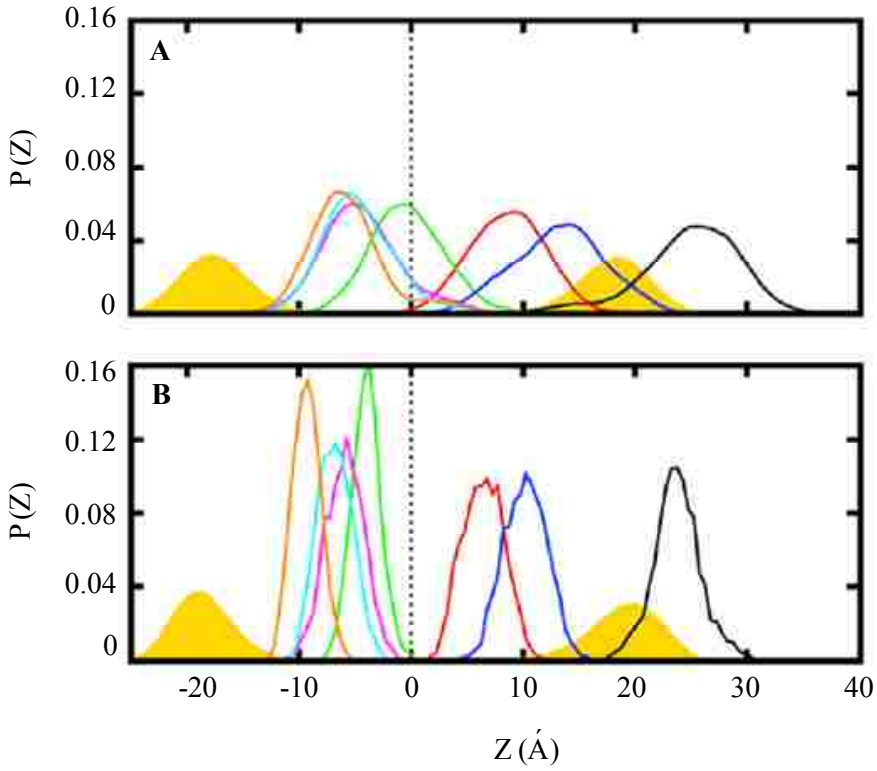

Figure 3-8. Distance from the bilayer center (Z) distributions for key residues in the $Cav1_{82-136}$ sequence. Tryptophan residues W85 (*black*), W98 (*red*), W115 (*green*), and W128 (*blue)* as well as break residues G108 (*magenta*), I109 (*purple*), and P110 (*orange*) are shown in both **A)** Multiple 100 ns simulations and **B)** The 1 μs simulation. The distance of the phosphate atoms of the lipid headgroup are indicated by yellow Gaussian distributions located at approximately 20 and -20 Å form the bilayer center indicated by the dashed line.

The residues are shown to penetrate deeper in the longer simulation and are therefore closer to the lipid headgroup of the second leaflet indicating that a distinct depth in the membrane may important in stabilizing $Cav1_{82–136}$. Importantly, in the snapshots taken, the backbone atoms of the turn residues were found to hydrogen bond to lipid headgroups of the second leaflet, which can be another stabilizing force in controlling the caveolin topology. The break region clearly is shown to be stable in these simulations indicating that a membrane buried turn is energetically possible for caveolin.

The residues in the break region cannot be mutated out without dire consequences to the caveolin structure and therefore cannot be probed directly. However, with such a controversial motif, experimental evidence was needed to validate the simulation results. The four native tryptophan residues in $Cav1_{82–136}$ can be used to indicate its membrane location by examining the emission maximum (λ_{max}) after selectively exciting tryptophan by irradiation at 295 nm. In general, the λ_{max} values are divided into three classes, each related to the degree of exposure to water. Tryptophan residues with λ_{max} in Class I (330-333 nm) are generally solvent-inaccessible because they are tucked away within the bilayer. Class II (340-344 nm) tryptophan residues are usually found at the bilayer/aqueous interface (headgroup region of the bilayer). A Class III (346-350 nm) λ_{max} value is indicative of a tryptophan residue that is fully exposed to high mobile water molecules. Therefore it was desirable to examine the fluorescence emission profiles of single tryptophan mutants reconstituted into phospholipid bicelles to see how the polarity of the sequence changes along the helices. This analysis was highly relevant because bicelles contain a planar bilayer to mimic the simulation conditions. Bicelles also scatter much less light than vesicles, a property which can lead to spectroscopic artifacts that make data interpretation more difficult. Due to the extreme hydrophobicity of $Cav1_{82-136}$, a method was developed to reconstitute the protein into bicelles. This was accomplished using a vesicle to bicelle transition. This method was developed because direct reconstitution of the protein into bicelles by adding bicelles to lyophilized material, or co-lyophilizing the protein with DMPC followed by a rehydration step with DHPC and buffer components was resulting in aggregation of the protein giving very low fluorescence signals that were unsuitable for λ_{max} analysis. Once the protein had been

associated with vesicles by detergent dialysis using the methodologies described in Chapter 2 except in place of EYPC, DMPC was used, the reconstitution into bicelles was facile and protein loss was minimized. This process is detailed in Figure 3-9 and represents a very novel use the PFOA detergent dialysis method.

Figure 3-9. Procedure for vesicle to bicelle transition technique. The PFOA detergent dialysis technique described in Chapter 2 is used to form vesicles. These vesicles are then spun to remove lipid and protein aggregates using a low centrifugal force. The vesicles are then pelleted using a very high gravitational force and the resulting pellet is solubilized using ice-cold buffer containing the rim-forming detergents. This technique was crucial in obtaining high reconstitution yields of $Cav1_{82\text{-}136}$ into phospholipid bicelles.

Figure 3-10 shows the λ_{max} values from the fluorescence emission spectra of each tryptophan after reconstitution into bicelles and are 344.4 ± 2.4 nm (W85), 334.4 ± 0.2 nm (W98), 330.2 ± 1.0 nm(W115), and 338.2 ± 0.6 nm (W128). The data indicated that W85 is a class II/class III hybrid and is likely found in the headgroup region of the bilayer. The λ_{max} value of W98 is between Classes I and II, placing it below the headgroup region and possibly near the aqueous-hydrophobic core interface. The λ_{max} value of W115 is consistent with a class I tryptophan that is in a deeply buried position, possibly near the bilayer center. This tryptophan position is only one helical turn from the break region and is likely the best indicator as to the turn's environment. The final tryptophan, W128, has a λ_{max} value that places it between class I and class II, and therefore is probably located in the hydrophobic core of the first leaflet but is getting close to the lipid headgroup region.

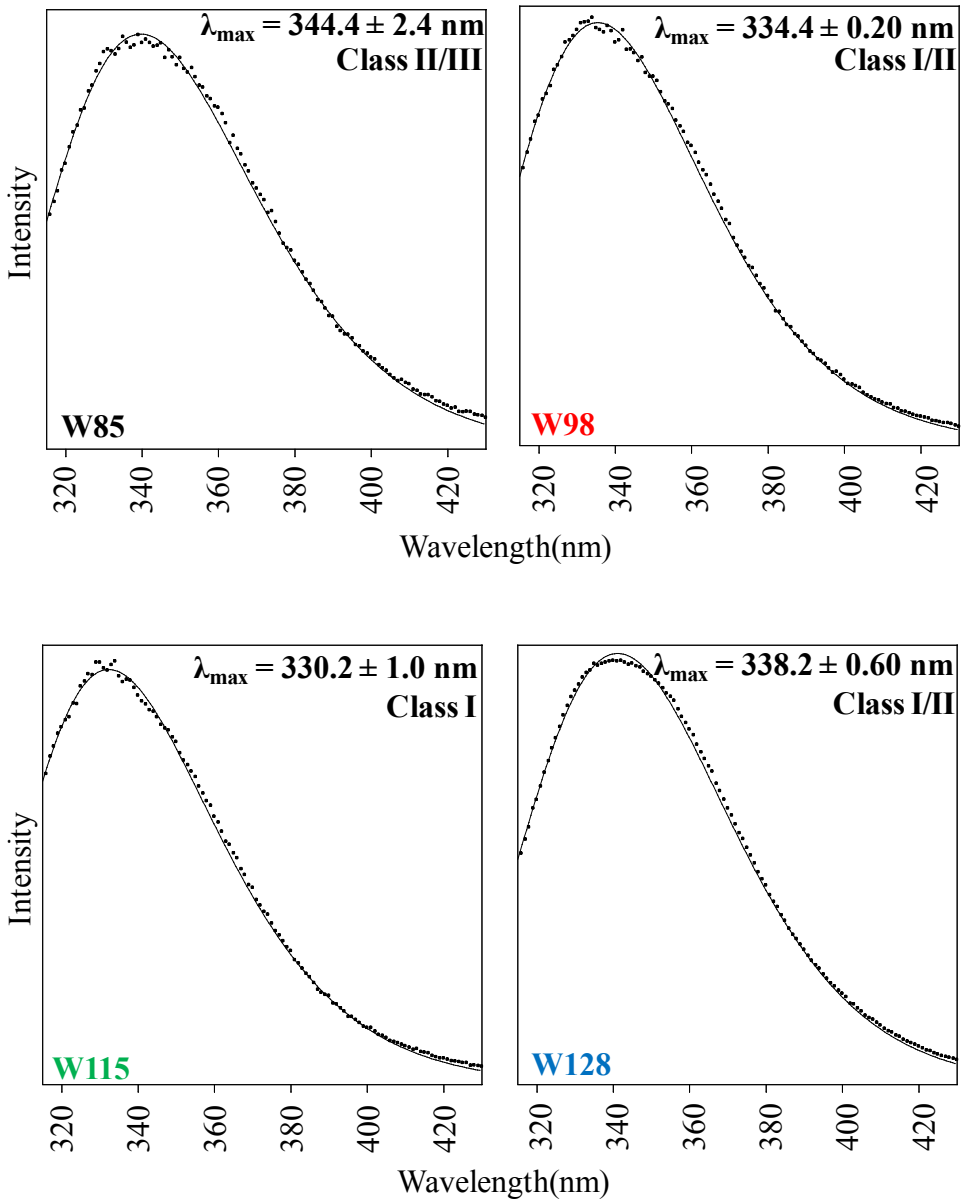

Figure 3-10. Fluorescence emission spectra for $Cav1_{82-136}$ single tryptophan mutants reconstituted into ***q***=0.50 4.0% (*w/w*) DMPC/CHAPSO bicelles. Each spectrum indicates the identity of the mutant, the raw data is shown as points and the fits are shown as solid lines. The λ_{max} from fits are indicated for each mutant.

In order to validate that these single tryptophan mutants were not impacting the structure and/or dynamics of $Cav1_{82-136}$, an HSQC spectrum was obtained to compare ^{15}N labeled $Cav1_{82-136}$ with all four tryptophans and $Cav1_{82-136}$(4F) (a construct where all four

tryptophan residues were mutated to phenylalanine). The spectrum of $Cav1_{82\text{-}136}$(4F) had good chemical shift dispersion and showed only minor changes in its peaks location compared to $Cav1_{82\text{-}136}$ (Figure 3-11).

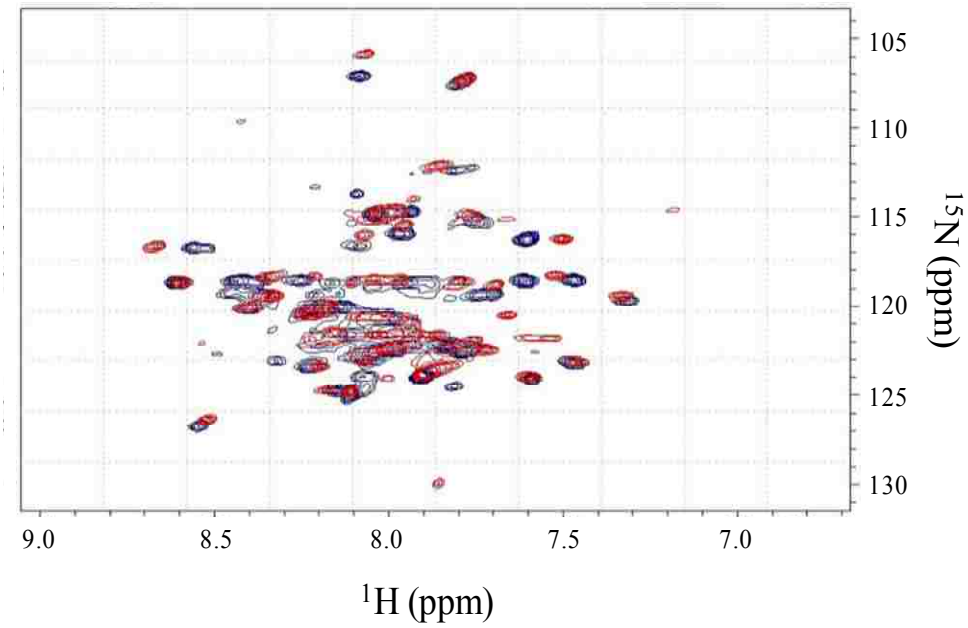

Figure 3-11. Overlay of TROSY-HSQC spectra of $Cav1_{82\text{-}136}$ (*red*) and $Cav1_{82\text{-}136}$(4F) (*blue*).

The relationship between the λ_{max} and water exposure was interrogated further by looking at the relative percentage of water molecules associated with the indole side chain versus the percentage of lipid contacts (Trp-water/(Trp-Water+Trp-lipid)) during the course of the simulation. From lowest exposure of the tryptophan residues to water to the highest exposure, the calculated values are, 2 ± 4% (W115), 22 ± 10% (W128), 32 ± 22% (W98), and 83 ± 14% (W85) for the short simulations and 5 ± 10% (W115), 23 ± 18% (W128), 42 ± 26% (W98), and 89 ± 8% (W85) for the 1 μs simulation. The large change in water contacts observed between the short and long timescales likely indicates that the interplay between hydrophobic coverage and aqueous exposure is a slow converging parameter for the $Cav1_{82\text{-}136}$ molecule. The Z_{COM} values for each tryptophan

were also determined and are shown in Figure 3-8. Akin to the distributions of the break residues, the distributions of the tryptophans were broader for the short simulations than they were for the long simulations. The average values for the 100 ns simulations were 23.4 ± 4.2 Å (W85), 7.5 ± 2.5 Å (W98), -1.1 ± 2.7 Å (W115), and 11.8 ± 2.9 Å (W128). For the 1 μs simulation, the values were 23.7 ± 2.2 Å (W85), 6.5 ± 1.8 Å (W98), -4.0 ± 1.3 Å (W115), and 10.2 ± 2.0 Å (W128). Interestingly, W85 changed the least when comparing the short and long time course showing that its conformational flexibility (not in a helix) allows it to find a favorable position sooner than the other tryptophan sites. These values are strongly correlated with tryptophan emission measurements, as in the simulations W85 is at the top of the first leaflet, W128 is at the interface between the acyl chain-headgroup border, W98 is slightly buried within the lipid bilayer, and W115 is deeply buried in the hydrophobic core. Clearly the simulations are yielding relevant information as to the actual bilayer depth of the break residues which cannot be probed using experimental techniques directly. A cartoon representation of the protein embedded within the DMPC bilayer is shown in figure 3-12. All values for all parameters obtained from the simulations are available in Appendix 3-1.

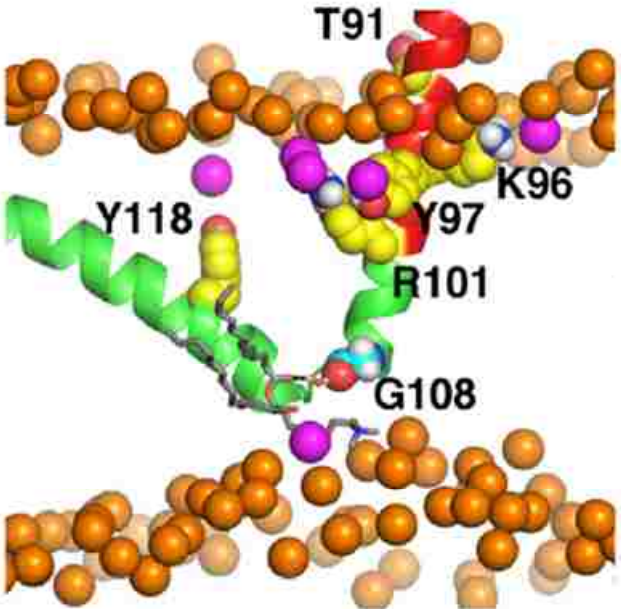

Figure 3-12. Topological disposition of $Cav_{82\text{-}136}$ in a DMPC bilayer. Key residues in H1 (T91, K96, Y97, and R101), the break region (G108), and H2 (Y118) involved in hydrogen bonding and electrostatic interactions with the surrounding lipids are indicated. Phosphate atoms that are within 4.5 Å of Cav182-136 are shown in *magenta*, phosphate atoms in the bulk bilayer are shown in *orange*. A water bridge between the backbone atoms of G108 (*cyan spheres*) and a lipid headgroup to the bottom leaflet is shown and may help stabilize the loss of breaking of H1.

CONCLUSIONS

Caveolins are critical to proper caveolae function and appearance, and are intricately linked to a variety of diseased states. For this reason, significant efforts have been undertaken to better understand the structure and function of caveolin. In this chapter, significant strides have been made in elucidating the membrane bound structure and topology of caveolin-1 residues 82-136, which represents the structural core of the membrane interacting portion of the polypeptide.

Using MD simulations which used NMR secondary structure data of $Cav1_{82-136}$ as a starting point, it was demonstrated that a U-shape conformation in the bilayer was energetically favorable. It also was shown that the structure of $Cav1_{82-136}$ was dynamic showing fluctuations in its angle between the two helices that were largely due to lipid-protein interactions. However, this angle was consistent with a H1-H2 angle that was between 40 and 60°. This analysis rules out caveolin having a transmembrane orientation or a fully extended peripheral orientation, as either of these models would require a very wide H1-H2 angle (θ>90°). This also indicates that caveolin does not likely curve membranes by the same mechanism that other membrane curving proteins use (i.e. BAR domain proteins which rest on the surface of membranes to mediate curvature); therefore the findings presented in this chapter may serve as important advancement in directing future hypotheses attempting to elucidate the mechanism of caveolin-1 induced membrane curvature.

Importantly, the break between the two helices was placed within the second leaflet of the hydrophobic core, indicating that caveolin does not completely transit the bilayer before it makes a dramatic turn. Although this motif would appear to be

unfavorable due to a loss of intra-helical hydrogen bonds, the energetic penalty was likely compensated for by hydrogen bonding between the break residue G108 and lipid headgroups. The placement of the break residues in the second leaflet as well as the overall depth profile in the simulations was strongly supported using tryptophan fluorescence experiments performed in bicelles. The simulations also revealed that a specific orientation of the helices with respect to one another was favored (ρ_1=343°, ρ_2=111°) where residues in and around the break interact via van der Waals forces. It was observed that residues towards the termini of the helices interact with lipids intercalated between them through hydrogen bonding. The sum of these interactions may be critical to upholding the U-shaped motif in the membrane.

It cannot go without mention, however, that these studies were performed in DMPC bilayers without the presence of cholesterol, which is a major component of caveolae. Therefore it is critical that the next steps taken probe the possible role that the sterol has on these structural parameters. Furthermore, the construct lacks 70% of the total protein, including three sites of cysteine palmitoylation. Although the core membrane interacting segment has been investigated, a longer construct would help determine if distant regions of the protein are involved in defining the structural parameters that were obtained through the MD simulations. Finally, it is known that caveolin oligomerizes and these simulations were performed using monomeric conditions. Although it is not yet known how the protein oligomerizes, it will be of interest to determine how the oligomerization process changes the binding mode of caveolin in the bilayer.

Appendix 3-1. Average Values of Parameters for $Cav1_{82\text{-}136}$ from MD Simulations

Replicate	θ	ϕ	ρ_1	ρ_2	Z G108[Å]	Z I109[Å]	Z P110[Å]	α	β
45_1	44°±4°	39°±6°	353°±14°	325°±11°	-6.0±2.1	-7.5±2.3	-9.7±2.1	101°±5°	63°±6°
45_2	63°±11°	14°±7°	334°±17°	116°±10°	-6.5±2.0	-7.1±1.9	-8.3±1.9	109°±7°	51°±9°
45_3	34°±3°	24°±8°	34°±10°	330°±9°	0.7±2.3	-0.4±2.1	2.0±2.2	49°±7°	46°±7°
45_4	12°±5°	28°±7°	327°±14°	328°±12°	-5.4±2.6	-7.7±2.7	-8.8±2.7	76°±6°	66°±5°
45_5	44°±5°	45°±6°	197°±13°	61°±11°	-7.8±1.9	-4.8±1.8	-6.2±1.7	115°±7°	71°±10°
45_6	62°±6°	6°±4°	324°±23°	137°±20°	-6.4±1.9	-7.0±2.0	-8.1±1.8	109°±6°	49°±6°
45_7	30°±3°	7°±5°	41°±9°	341°±9°	-5.0±2.0	-4.7±2.0	-5.1±2.0	64°±6°	60°±6°
45_8	45°±5°	6°±4°	335°±16°	288°±13°	-5.3±2.2	-8.0±2.3	-8.7±2.2	96°±5°	52°±4°
45_9	47°±9°	14°±6°	347°±15°	111°±12°	-5.4±1.9	-6.1±1.8	-8.8±1.8	90°±11°	45°±5°
45_10	29°±3°	13°±4°	217°±28°	112°±8°	-5.5±1.6	-4.7±1.6	-4.5±1.6	73°±6°	68°±6°
Avg±S.E.	41°±15°	20°±13°	251°±118°	215°±109°	-5.3±2.1	-5.8±2.2	-6.6±3.3	88°±21°	57°±9°
55_1	66°±12°	18°±6°	262°±19°	308°±13°	-5.2±2.0	-7.3±1.8	-8.0±1.9	121°±9°	55°±8°
55_2	27°±5°	22°±5°	318°±10°	17°±11°	-8.9±1.9	-6.8±1.9	-7.7±2.0	84°±5°	63°±5°
55_3	51°±5°	31°±5°	282°±15°	278°±9°	-5.8±1.6	-6.3±1.7	-5.5±1.8	120°±6°	73°±7°
55_4	59°±6°	25°±8°	354°±14°	334°±14°	-3.4±2.0	-4.0±1.8	-5.0±1.7	106°±5°	47°±5°
55_5	59°±7°	26°±9°	204°±16°	76°±25°	-9.4±2.3	-7.1±2.4	-7.6±2.2	115°±10°	56°±9°
55_6	26°±7°	10°±6°	218°±14°	293°±18°	-6.9±2.3	-7.1±2.1	-6.2±2.0	80°±9°	55°±8°
55_7	45°±7°	5°±4°	231°±18°	294°±12°	-6.5±2.0	-7.6±2.0	-7.8±2.0	98°±8°	54°±6°
55_8	61°±8°	23°±5°	191°±16°	103°±15°	-7.2±1.8	-5.6±2.2	-6.4±2.3	105°±10°	45°±9°
55_9	51°±9°	27°±8°	343°±13°	345°±12°	-2.8±2.2	-3.6±2.1	-4.7±1.9	96°±7°	45°±6°
55_10	23°±4°	17°±5°	344°±17°	274°±12°	-5.0±1.9	-7.1±2.0	-7.3±2.1	84°±7°	74°±7°
Avg±S.E.	47°±15°	20°±7°	275°±59°	232°±113°	-6.1±2.0	-6.3±1.3	-6.6±1.2	101°±14°	57°±10°
65_1	67°±6°	19°±7°	331°±13°	121°±10°	-6.4±2.0	-7.0±1.8	-9.5±1.9	108°±8°	42°±8°
65_2	67°±7°	21°±6°	343°±13°	104°±11°	-7.7±1.9	-7.3±2.1	-8.5±2.1	132°±8°	65°±5°
65_3	63°±10°	19°±10°	331°±12°	121°±11°	-6.8±2.1	-7.6±2.1	-9.3±1.9	103°±6°	44°±9°
65_4	84°±8°	13°±6°	202°±13°	76°±12°	-5.2±1.7	-3.5±1.7	-5.6±1.6	126°±5°	43°±8
65_5	47°±6°	7°±5°	344°±14°	108°±11°	-3.9±1.8	-4.3±1.6	-6.7±1.6	97°±6°	51°±6°
65_6	49°±7°	16°±6°	59°±19°	61°±12°	-2.8±2.4	-3.7±2.2	-6.9±2.1	92°±12°	43°±11°
65_7	66°±6°	12°±7°	221°±12°	133°±10°	-9.0±2.0	-7.1±2.0	-6.6±1.7	123°±10°	59°±8°
65_8	45°±7°	21°±8°	182°±18°	112°±15°	-5.7±2.6	-2.9±2.6	-3.9±2.3	92°±8°	51°±7°
65_9	30°±4°	18°±6°	215°±18°	96°±8°	-8.8±2.0	-6.5±1.9	-6.2±1.9	99°±10°	82°±6°
65_10	61°±7°	6°±4°	350°±15°	108°±10°	-4.5±1.9	-5.2±1.9	-7.7±1.8	101°±5°	40°±7°
Avg.±S.E.	58°±14°	15°±5°	257°±93°	104°±20°	-6.1±2.0	-5.5±1.7	-7.1±1.6	107°±14°	52°±13°
75_1	68°±7°	28°±10°	39°±19°	77°±11°	-2.9±2.2	-3.3±2.2	-6.4±2.2	107°±8°	39°±6°
75_2	58°±5°	12°±6°	339°±13°	122°±10°	-4.5±2.7	-5.1±2.8	-7.0±2.4	106°±8°	51°±7°
75_3	58°±7°	15°±8°	229°±12°	108°±12°	-8.5±1.7	-6.9±1.8	-7.3±1.8	108°±7°	51°±6°
75_4	63°±7°	24°±8°	288°±14°	322°±15°	-4.6±1.8	-7.0±2.0	-7.6±2.1	120°±7°	57°±6°
75_5	45°±6°	13°±7°	336°±18°	117°±13°	-3.5±1.9	-4.1±2.0	-5.7±1.9	97°±6°	55°±5°
75_6	65°±8°	65°±7°	323°±13°	340°±21°	3.9±3.1	2.4±2.4	4.1±2.6	105°±14°	41°±15°
75_7	53°±7°	9°±5°	229°±29°	286°±13°	-11.0±2.4	-9.7±2.4	-7.8±2.8	108°±11°	55°±8°
75_8	57°±10°	19°±6°	337°±18°	120°±14°	-5.3±2.2	-5.9±2.0	-7.5±2.0	109°±8°	55°±5°
75_9	66°±5°	27°±6°	318°±13°	124°±10°	-5.3±1.6	-6.7±1.4	-8.8±1.5	104°±6°	42°±5°
75_10	79°±8°	29°±6°	353°±13°	118°±14°	-4.1±2.8	-4.5±2.7	-7.2±2.5	116°±9°	38°±6°
Avg.±S.E.	61°±9°	24°±15°	279°±90°	173°±95°	-4.6±3.7	-5.1±3.0	-6.1±3.5	108°±6°	48°±7°
85_1	73°±6°	20°±10°	347°±16°	16°±12°	-4.5±2.2	-5.3±1.9	-5.8±1.7	100°±7°	27°±4°
85_2	58°±7°	10°±6°	236°±13°	278°±17°	-9.1±2.2	-7.5±2.2	-6.6±2.3	107°±6°	49°±9°
85_3	68°±9°	10°±5°	350°±16°	111°±13°	-4.3±2.2	-4.5±2.0	-6.5±2.2	104°±9°	37°±5°
85_4	75°±9°	49°±4°	280°±12°	6°±13°	1.3±1.6	-2.4±1.6	-4.1±1.5	126°±6°	52°±9°
85_5	143°±9°	27°±11°	260°±15°	44°±37°	1.7±2.4	-0.6±2.4	2.1±2.4	145°±6°	6°±5°
85_6	74°±7°	37°±6°	310°±15°	128°±11°	-4.6±2.0	-5.8±1.8	-8.7±1.7	113°±9°	41°±6°
85_7	61°±5°	8°±5°	350°±18°	121°±10°	-3.8±2.7	-3.8±2.3	-5.5±2.1	104°±5°	45°±5°
85_8	68°±7°	46°±6°	336°±26°	266°±15°	0.2±2.8	2.8±2.2	1.8±1.8	93°±9°	27°±8°
85_9	33°±4°	13°±7°	358°±14°	316°±15°	-8.0±2.1	-9.3±2.1	-10.2±2.0	88°±5°	57°±5°
85_10	48°±5°	18°±6°	79°±17°	43°±17°	-3.5±2.0	-5.6±1.9	-8.6±1.8	80°±10°	35°±8°
Avg.±S.E.	70°±27°	24°±15°	291°±81°	133°±109°	-3.5±3.4	-4.2±3.3	-5.2±4.0	106°±18°	38°±14°
Total Avg.	55°±20°	21°±12°	271°±92°	171°±109°	-5.1±2.9	-5.4±2.5	-6.3±3.0	102°±17°	50°±13°
1-μs Simulation	53°±5°	27°±6°	331°±22°	124°±12°	-5.9±1.7	-6.8±1.6	-9.3±1.3	99°±7°	49°±7°

Appendix 3-2. Sequences of Protein Constructs Utilized

Construct	Protein Sequence
$Cav1_{82-136}$	DGI**W**KASFTTFTVTKY**W**YRLLSALFGIP**L**ALI**W**GIYFAILSFLHI **W**AVVP**S**IKS
$Cav1_{82-136}$ (4F)	DGI**F**KASFTTFTVTKY**F**YRLLSALFGIP**L**ALI**F**GIYFAILSFLHI **F**AVVP**S**IKS
$Cav1_{82-136}$ (W85)	DGI**W**KASFTTFTVTKY**F**YRLLSALFGIP**L**ALI**F**GIYFAILSFLHI **F**AVVP**S**IKS
$Cav1_{82-136}$ (W98)	DGI**F**KASFTTFTVTKY**W**YRLLSALFGIP**L**ALI**F**GIYFAILSFLHI **F**AVVP**S**IKS
$Cav1_{82-136}$ (W115)	DGI**F**KASFTTFTVTKY**F**YRLLSALFGIP**L**ALI**W**GIYFAILSFLHI **F**AVVP**S**IKS
$Cav1_{82-136}$ (W128)	DGI**F**KASFTTFTVTKY**F**YRLLSALFGIP**L**ALI**F**GIYFAILSFLHI **W**AVVP**S**IKS

Appendix 3-3. Mutagenesis Primers Utilized

Construct	Primer Sequence
F85W	5'-GGATCCATGGACGGTATCTGGAAAGCGTCTTTCACCAC-3'
F98W	5'-CACCGTTACCAAATACTGGTTCTACCGTCTGCTGTC-3'
F115W	5'-CTGGCGCTGATCTGGGGTATCTACTTCGC-3'
F128W	5'-CTTTCCTGCACATCTGGGCGGTTGTTCCGTC-3'

Chapter 4. Cysteine Scanning Mutagenesis of Full Length Caveolin-1 Helps to Explain Its Multi-Faceted Interactome

ABSTRACT

Caveolin-1 is critical in modulating the architecture and engineering the functions of caveolae. At the heart of its functional role is the scaffolding domain (CSD, residues 82-101), which is thought to be involved both signal transduction and cholesterol transport. However, the *exact* topology of the CSD is unknown, and is unpredictable due to its unusual amino acid composition. Additionally, it is unknown how cholesterol may modulate the topology of caveolin-1. To elucidate the CSD topology with respect to the membrane, the accessibilities of single cysteine mutants (spanning residues 82-111) to the membrane impermeant reagent biotin-maleimide was probed after reconstituting the protein into phospholipid bicelles. These mutants were confirmed to have not caused major perturbations to the wild-type caveolin structure by probing the secondary structure of the protein using far UV circular dichroism measurements. The protein was then gently reconstituted in phospholipid bicelles using a native preparation method. In bicelles where the planar region was composed purely of DMPC, it was determined that residues 82-87 were in an aqueous exposed region, whereas residues 88-111 were either in a dynamic or a membrane buried environment. Interestingly, the inclusion of a cholesterol analog, cholesteryl hemisuccinate (CHS) at a biologically relevant concentration modulated the overall topology of the protein by increasing the exposure of the 90-95 region. The findings in this chapter support the multi-faceted nature proposed for the CSD in terms of binding signaling molecules and interacting with cholesterol simultaneously.

INTRODUCTION

The caveolin-1 scaffolding domain is thought to mediate many of the important functions of caveolae (Figure 4-1). In particular, the CSD plays an outsized role as it interacts with a number of cell signaling proteins (Src-like kinases, Ha-Ras, endothelial nitric-oxide synthase (eNOS), and G protein α-subunits), associates with cholesterol, and has been shown to be important for caveolin-1 oligomerization *in vivo* [16-21]. For example, this region has been implicated in the negative regulation of eNOS activity where mutations in the CSD resulted in a significant to total loss of inhibitory activity [195]. Additionally, cholesterol binding is thought to be mediated through residues 94-101 which contain a cholesterol recognition/interaction amino acid consensus (CRAC) motif (sequence VTKYWFYK) [159,196]. Importantly, this stretch of the protein has been demonstrated to be necessary and sufficient for membrane binding [72].

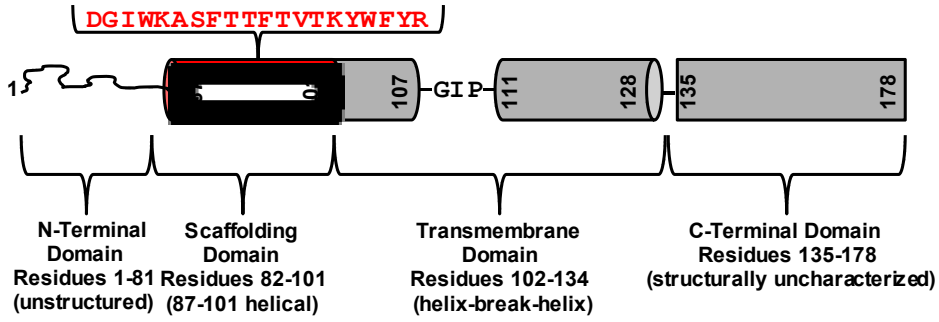

Figure 4-1. Domain map highlighting the sequence of the caveolin-1 scaffolding domain. The amphipathic nature of the sequence (*red*) makes CSD burial difficult to predict.

Despite the diversity in the physiochemical properties of ligands that the CSD is purported to interact with, its degree of exposure with respect to the bilayer remains unverified, and therefore it is unclear how this region can bind to soluble proteins and cholesterol simultaneously. To date, there have been a number of inquiries into the

topological disposition of the CSD. A study by Epand et al examining the fluorescence emission of two tryptophan residues, W85 and W98, within water-soluble CSD based peptides (construct caveolin-1 82-103) found that there was little change in their emission properties when mixed with multilamellar vesicles, indicating that there was not a strong affinity of these peptides to bind to membranes. In the same study, two-dimensional ^{1}H magic angle spinning nuclear Overhauser enhancement spectroscopy (NOESY) experiments examined the interaction of these peptides with multilamellar vesicles [159]. The NOESY experiments supported an interaction between the peptide and the lipid headgroups but did not suggest a specific orientation or topology of the peptides with respect to the membrane. A study by Aoki et al employed molecular dynamics simulations to compare the topology of two caveolin-1 constructs, one encompassing part of the intramembrane domain (residues 103-122) and one encompassing part of the scaffolding and intramembrane domains (residues 94-122) [77]. This simulation showed that caveolin-1 adopted a U-shape conformation within the bilayer when the CSD portion of the polypeptide was included but not in its absence. This simulation revealed that the CSD was critical to the U-shape conformation. The simulation placed half of the residues of the CSD within the headgroup region and the other half within the hydrophobic core of the membrane. A later simulation study examining the same stretch of the protein (residues 94-122) embedded in lipid bilayers found that tryptophan residue 98 was found within 0 ± 2.5 Å of the phosphate headgroup and the depth was dependent on the amount of phospholipid unsaturation and the presence of cholesterol [46]. In this study it was found that cholesterol changed the topology by giving the protein a more interfacial, surface orientation. Finally, the studies in Chapter 3, which are based on most

of the CSD being part of a helical region, showed that the CSD enters the membrane in a near vertical fashion and that residue 96 is likely where the protein enters the hydrophobic core of the membrane. These studies support the scaffolding domain as being the portion of caveolin-1 which first enters the hydrophobic core of the bilayer but have not pinpointed a specific residue experimentally. Although these studies have been very insightful most of them have lacked the entire CSD, utilize short caveolin-1 peptides, and are based on simulations. Therefore it is still an open question as to the topology of the CSD in the context of the full-length caveolin-1 protein, where other regions of the protein could have an effect on the burial of this crucial region. It is also unclear as to how the exposure of the protein to cholesterol would modulate the accessibility of the CSD.

To definitively characterize the membrane topology of the CSD, cysteine scanning mutagenesis was utilized, which has been used extensively to elucidate the topology of membrane proteins [197-202]. Using this approach, single cysteine mutants of a full length caveolin-1 construct ($^{mychis}Cav1_{1-178}$) scanning the entire scaffolding domain (residues 82-101) and a portion of the intramembrane domain (residues 102-111) were generated. Next, fluorescence anisotropy studies were utilized to determine at which $\boldsymbol{q}$ value (ratio of DMPC to DHPC) bicelles began to take on properties similar to that of pure lipid vesicles (T_m measurements). Each mutant was then purified into 2.3% (*w/v*) $\boldsymbol{q_{eff}}$ = 1.0, DMPC/DHPC bicelles using nickel affinity chromatography and their secondary structure was evaluated using far-UV circular dichroism spectroscopy by comparison to the wild-type (cysteine lacking) control to identify any sites which disrupted caveolin structure. For cysteine accessibility studies, the protein was isolated

out of *E coli* membranes to ensure only properly folded and trafficked mutants were analyzed [29]. These membranes were then solubilized into 2.3% (*w/v*) q_{eff} = 1.0, DMPC/DHPC bicelles or 2.3% (*w/v*) q_{eff} = 1.0, DMPC (80%)/cholesteryl hemisuccinate (CHS) (20%)/DHPC bicelles. Using reactivity to a membrane impermeant biotin-maleimide reagent as a measure of accessibility, it was found that in both bicelle systems the accessibility of $^{mychis}Cav1_{1\text{-}178}$ changed dramatically over the sequence of the CSD. This study pinpointed the CSD as being the portion of the polypeptide which first enters the hydrophobic core of the bilayer. Interestingly, it was found that the $^{mychis}Cav1_{1\text{-}178}$ construct was more deeply buried in pure DMPC bilayers compared to a more realistic environment which contained the CHS. This result suggested that various factors limit the penetration depth of caveolin into the lipid bilayer and this may have implications on caveolin's degree of exposure *in vivo*.

MATERIALS AND METHODS

Determination of gel (liquid ordered) to fluid (liquid disordered) transition temperatures for bicellar solutions

For fluorescence anisotropy experiments, 2.3% (*w/w*) DMPC–DHPC mixtures having q_{eff} values ranging from 0.05 to 1.50 (0.05, 0.30, 0.50, 0.75, 1.00, 1.50) were prepared on a 3 gram scale using the following method (For an explanation of q_{eff} see Chapter 1). DMPC in chloroform (50 mg/mL) was added (83, 370, 510, 630, 720, and 827 μL respectively) to a 2 mL microcentrifuge tube. After this, 1,6-Diphenyl-1,3,5-hexatriene (DPH, Sigma Aldrich, St. Louis, MO) dissolved in methanol was added to each tube to give a final concentration of 6 μM once resuspended in the final volume. The samples were then dried under vacuum overnight. The samples were then hydrated by the addition of 2.78 mL of water, and 75 μL of 40× buffer (400 mM HEPES, 4.0 M NaCl pH 7.4). Finally, DHPC was added as a 25% (*w/w*) stock (in water) to achieve clear homogeneous solutions (250, 196, 169, 146, 129, and 107 μL respectively). These solutions were used directly for anisotropy measurements. DMPC vesicles were prepared by the addition of 16 mg of DMPC in 600 μL of chloroform with DPH dissolved in methanol (1:500 DPH to lipid molar ratio). The sample was then dried under vacuum overnight and rehydrated using 2.78 mL of water and 75 μL of 40× buffer (400 mM HEPES, 4.0 M NaCl pH 7.4). This solution was sonicated for 5 minutes using a Branson sonifier (Danbury, CT) equipped with a microtip to generate small unilamellar vesicles. The solution became translucent and was then centrifuged at 20,000 *x g* for 5 minutes at

room temperature to remove titanium particles and non-vesicular lipid aggregates. The supernatant was diluted 4-fold for the fluorescence experiments.

Fluorescence emission spectra were acquired with magnetic stirring using a 1 × 1 cm quartz cuvette on an Agilent Eclipse fluorometer (Santa Clara, CA). The excitation and emission slit widths were both set to 5 nm. The fluorescence emission intensity was measured with excitation (355 nm) and emission (430 nm) with polarizers parallel to each other (both oriented at 0° from vertical) and repeated in the perpendicular configuration (excitation 0° and emission 90°). The correction factor for emission monochromator transmission efficiency was obtained from the ratio of emission intensity at 0° and 90° with the excitation polarizer oriented at 90°. Melting curves were generated for both pure DMPC vesicles and DMPC/DHPC bicelles by examining the change in DPH anisotropy as a function of temperature over the range of 2-36 °C.

Cloning and Construction of Caveolin-1 Mutants

A construct encompassing the full-length caveolin-1 ($^{mychis}Cav1_{1\text{-}178}$, Appendix 4-1, underlined portion denotes CSD) was purchased from Genscript (Piscataway, NJ). This construct contained three mutations where cysteines 133, 143, and 156 were mutated to serine in order to avoid labeling of these positions (Appendix 4-1, bolded). These mutations have been shown to be non-disruptive for caveolin-1 trafficking to caveolae *in vivo* [35]. To the C-terminus, a myc antibody epitope tag and 6× polyhistidine tag were included for immuno-detection and affinity purification respectively (Appendix 4-1, myc epitope is in blue, histidine tag is in red). Single cysteine mutants were generated from residues 82-111 using the Agilent quick change mutagenesis kit (Santa Clara, CA) for a total of 30 mutants (See Appendix 4-1 for full length and mutant constructs). Primers

were designed using the free web-based primerX program, see Appendix 4-2 (Bioinformatics.org). See Appendix 2-3 for PCR reaction and cycling conditions. The construct DNA was sub-cloned into the multiple cloning site of the pET 24a vector (Novagen, La Jolla, CA) between the NdeI and XhoI restriction sites for expression in *E. coli* (strain BL21DE3). Transformation protocols are described in Appendix 2-4.

Protein Expression

Expression of the protein of interest was accomplished using the auto induction method developed by Studier et al [147]. Briefly, starter cultures were grown with rapid shaking (250 rpm) at 37°C in MDG media supplemented with kanamycin for 24 hours. After this time period, a 1:100 dilution of this culture was made into 3 mL of ZYM-5052 media and the growth was harvested after 12 hours by centrifugation at 20,000 *x g* for 5 minutes followed by removal of the supernatant and storage of the bacterial pellet at -80°C until use. For large scale growths the procedure was performed exactly the same except a 1:1000 dilution of the culture was made into 1 L of ZYM-5052 media. It was determined that growth dynamics were very similar under both conditions.

Non-denaturing Purification of $^{mychis}Cav1_{1-178}$ into Phospholipid Bicelles using Mini-Nickel Spin Column for Circular Dichroism Spectroscopy Measurements

All steps of the preparation were performed at 4°C. Cell pellets were resuspended into 600 µL of lysis buffer (1 mg/mL lysozyme, 5 mM β-mercaptoethanol, 10 mM imidazole, 50 mM phosphate pH 8.0, 50 mM Empigen BB®detergent (Sigma Aldrich, St. Louis, MO), and 300 mM NaCl). Next, the suspension was gently mixed over the course

of 30 minutes. This step was followed by disruption of the bacterial membranes using a Branson sonifier (Danbury, CT) equipped with a microtip. The suspension was then spun at 20,000 *x g* for 20 minutes to pellet insoluble cellular debris. The protein was purified using a nickel-NTA spin column (Qiagen, Valencia, CA) according to the manufacturer's instructions. The wash buffer was composed of 5 mM β-mercaptoethanol, 40 mM imidazole, 50 mM phosphate pH 8.0, 50 mM Empigen BB® detergent, and 300 mM NaCl. The detergent was then exchanged for bicelles by washing the column with 2.3% (*w/w*) q_{eff} = 1.0 DMPC/DHPC bicelles, 5 mM β-mercaptoethanol, 40 mM imidazole, 50 mM phosphate pH 8.0, and 100 mM NaCl. The elution buffer was composed of 2.3% (*w/w*) q_{eff} = 1.0 DMPC/DHPC bicelles, 5 mM β-mercaptoethanol, 500 mM imidazole, 5 mM phosphate pH 8.0, and 100 mM NaCl. Samples were eluted into 100 μL of bicelles and imidazole was removed using Zeba® spin desalting columns equilibrated with 7 mM DHPC in 10 mM phosphate pH 7.0 supplemented with 0.5 mM *tris*(2-carboxyethyl)phosphine (TCEP). Total protein levels were normalized by determining the concentration spectroscopically by measuring the absorbance at the 280 nm wavelength and diluting the samples to the same concentration (roughly 20 μM) using a bicellar solution.

Circular Dichroism Spectroscopy Measurements

Circular dichroism measurements were performed on all mutants using a JASCO CD Spectrophotometer (Easton, MD) held at 25°C. A 0.1 mm path length quartz cuvette containing a sample volume of 50 μL was utilized for measurements. Data were collected by scanning every wavelength from 260-190 nm in continuous scan mode at a

speed of 200 nm/minute taking 16 accumulations for signal averaging. A background spectrum of 2.3% (*w/w*) q_{eff} = 1.0 DMPC-DHPC bicelles was used as a blank. The data were converted from machine units (θ) to delta epsilon units (Δε) using the following equation:

$$\Delta\varepsilon = \theta \times \frac{(0.1 \times MRW)}{(P \times C) \times 3298}$$

Here, MRW is the mean residue weight (protein MW/number of residues in the protein), P is the pathlength in cm, and C is the protein concentration in mg/mL yielding units of $M^{-1}cm^{-1}$.

Large Scale Preparation of $^{mychis}Cav1_{1\text{-}178}$ into Phospholipid Bicelles for Analytical Ultracentrifugation Experiments

Cells from a 1 L growth were harvested by centrifugation at 5,000 *x g* and were washed with 0.9% (*w/v*) NaCl. The pellet was then resuspended in 120 mL of a lysis buffer containing 50 mM phosphate pH 8.0, 300 mM NaCl, and 2% (*v/v*) Empigen BB® detergent by stirring for 10 minutes at 4℃. The Sample was then sonicated using a Branson sonifier for a period of 15 minutes total, holding the temperature below 8℃. After this time period, the supernatant was cleared by centrifugation at 50,000 *x g* for 1 hour at 4℃. The sample was passed through a 0.2 µm syringe filter and was then bound to a Ni-Sepharose column. The bound protein was washed using a gradient going from 0-50 mM imidazole over a 125 mL volume, with buffer A being composed of 50 mM phosphate pH 8, 300 mM NaCl, and 50 mM Empigen BB®, and buffer B being composed of 50 mM phosphate pH 8, 300 mM NaCl, 250 mM imidazole, and 50 mM Empigen

BB®. After weakly bound species were removed the protein was eluted in a buffer containing 50 mM phosphate pH 8, 300 mM NaCl, 200 mM imidazole, and 50 mM Empigen BB®. The protein-containing fractions were pooled and the sample was concentrated to ~ 10 mL using ultrafiltration. This sample was then filtered through a 0.2 μm syringe filter and was injected onto a Sephacryl 300 HR 16/60 column (GE Healthcare, Piscataway, NJ) equilibrated with a buffer comprised of 50 mM phosphate pH 7.4, 150 mM NaCl, 10 mM Empigen BB® and was isolated from other species remaining in the sample. The sample was quantified by examining the absorbance at the 280 nm wavelength.

To incorporate $^{mychis}Cav1_{1\text{-}178}$ into bicelles, an appropriate amount of the gel filtration fraction was bound to a Ni-NTA spin column. The detergent was then exchanged for bicelles by washing the column twice with 300 μL of a buffer containing 2.3% (*w/w*) $\boldsymbol{q_{eff}}$ = 1.0 DMPC/DHPC bicelles, 250 mM imidazole, 10 mM HEPES pH 7.4, and 100 mM NaCl. The imidazole was removed using Zeba® spin desalting columns equilibrated with 7 mM DHPC in 10 mM HEPES pH 7.4, and 100 mM NaCl with D_2O at 71.7% (*v/v*) (density matched conditions). The samples were then diluted to 30 ± 2 μM, 15 ± 2 μM, and 7.5 ± 2 μM for analytical ultracentrifugation experiments by dilution of the desalted eluant with a bicellar solution.

Sedimentation Equilibrium Experiments of $^{mychis}Cav1_{1\text{-}178}$

Sedimentation equilibrium experiments were performed at 25°C using a Beckman XL-A analytical ultracentrifuge and a 4-hole AnTi-60 rotor. Samples were loaded into a 6-channel charcoal-filled epon centerpiece and a reference solution containing only

buffer was included. An equilibration time of 24 hours at 10,000 rpm was given before scans were taken. Equilibrium measurements (280 nm) were taken from 10,000 rpm to 35,000 rpm with 1000 rpm steps. The bicellar $^{mychis}Cav1_{1\text{-}178}$ solution was analyzed at three speeds (25,000, 30,000, and 35,000 rpm) and at three concentrations. These experiments were carried out at 25°C. The data were fit to a single-species model using a non-linear least squares approach with the software Heteroanalysis (version 1.1.0.58, University of Connecticut Storrs, CT). The molecular weight, baseline, and reference concentrations were allowed to float during the fitting process.

Native Membrane Preparation from E. coli and Reconstitution into q_{eff} = 1.0 Bicelles

Unless otherwise noted, all steps of the preparation were performed at 4°C. Cell pellets were resuspended into 1000 µL of Tris-Acetate EDTA pH 8.0 buffer supplemented with 100 mM β-mercaptoethanol by a briefly vortex mixing. This step was followed by disruption of the bacterial membranes using a Branson sonifier (Danbury, CT) equipped with a microtip for 96 seconds in an ice bath. The suspension was then spun at 5,800 *x g* for 15 minutes to pellet insoluble cellular debris. The supernatant was then spun at 20,000 *x g* for 2 hours to pellet bacterial membranes. The supernatant was removed and the pelleted membranes were then washed using 100 mM phosphate buffered saline (PBS) pH 7.4 supplemented with 0.5 mM TCEP and the previous centrifugation step was repeated. Next, the supernatant was removed and the bacterial membranes were solubilized by adding 30 µL of 2.3% (*w/w*) q_{eff} = 1.0 DMPC-DHPC bicelles prepared in 100 mM PBS and 0.15 mM TCEP or the same buffer except 2.3% (*w/w*) q_{eff} = 1.0 DMPC/DHPC bicelles contained 20% CHS (Anatrace, Muamee, OH) in

terms of the total lipid mol %. Solubilization required 2 minutes of vortex mixing. Insoluble material was then pelleted by centrifugation of the sample at 20,000 *x g* for 1 hour at 25°C. After this step, 25 µL of the supernatant was removed for analysis.

Bicelles that contained CHS had to be prepared using a specialized protocol. Briefly, the requisite amounts of CHS (10.65 mg, CHS-TRIS salt) and DMPC (47.53 mg) for 5 g of 2.3 % (*w/w*) $\boldsymbol{q_{eff}}$ = 1.0 DMPC/CHS/DHPC bicelles were co-dissolved in a 2:1 mixture of chloroform (1 mL) and were then dried down under vacuum. This solution was then reconstituted into a buffer containing all the final components, (i.e. 215 µL 25% (*w/*v) DHPC, 500 µL 1 M PBS, 4.22 mL H_2O) which was subsequently lyophilized for 24 hours. This mixture was then taken into water for a second round of lyophilization before use in experiments.

Chemical Accessibility Assays

After purification, a Western blot was performed by diluting 5µL of the reconstituted material five fold into SDS-PAGE sample buffer in order to estimate the $^{mychis}Cav1_{1\text{-}178}$ concentrations using densitometry. The samples were then diluted to a similar level using a bicellar solution before the labeling reaction was performed. This step was performed in order to avoid cysteine labeling rate differences that would come from differences in the total level of protein between each single cysteine mutant. After dilution of samples to the same level, 20 µL of a $^{mychis}Cav1_{1\text{-}178}$ construct was added to a tube containing 200 nL of 20 mM N^{α}-(3-Maleimidylpropionyl)Biocytin (biotin-maleimide, Invitrogen, Carlsbad, CA) dissolved in dimethylsulfoxide for a final concentration of 0.2 mM biotin maleimide. The sample was briefly mixed and then the biotin-maleimide reaction was allowed to continue for 10 minutes at 21°C. The reaction

was quenched by the addition of β-mercaptoethanol to a concentration of 100 mM and incubation for 10 minutes. After this time period, the sample was diluted to 100 μL using SDS-PAGE sample buffer and was used for Western analysis. This process was repeated three times each for both lipid systems using different membrane preparations to account for culture to culture and run to run variability.

SDS-PAGE and Immunoblotting

Protein samples were resolved on 15% polyacrylamide gels and transferred to a PVDF membrane. The blots were blocked with 0.5% (*w/v*) casein in TBST, and probed using avidin-alkaline phosphatase conjugate (BioRad, Hercules, CA). Next, the blots were stripped, blocked with 5% (*w/v*) powdered milk in TBST and re-probed using the anti-myc primary antibody (Sigma Aldrich, St. Louis, MO) and anti-mouse alkaline-phosphatase conjugate secondary antibody (Thermofisher Corporation, Rockford, IL). Signals were detected using ECL reagent (BioRad, Hercules, CA).

Image and Data Analysis

Immuno-blots and biotinylation blots were imaged and quantified using a BioRad ChemiDoc XRS+ system and Image Lab software (BioRad, Hercules, CA). Biotinylation and total protein levels were estimated by densitometry where the % Biotinylation of a given mutant was calculated as the Biotin signal/Protein signal. The data set was normalized with respect to the most effectively labeled mutant on the blot and the relative biotinylation was plotted versus the cysteine replacement. Relative biotinylation signals for each position were averaged with the maximum number of neighbor relative biotinylation signals within ± one residue to generate average relative

biotinylation plots. Igor Pro 6.22A (WaveMetrics, Inc., Lake Oswego, OR) was used to fit the data (for both fluorescence anisotropy and relative biotinylation data) to a sigmoidal function of the form:

$$y = base + \left\{ \frac{max}{\left(1 + e^{\left(\frac{(xhalf - x)}{rate}\right)}\right)} \right\}$$

RESULTS AND DISCUSSION

Construction of Helix-1 Cysteine Mutants and Chemical Accessibility Assay Principle

The CSD topology is intriguing; there evidence suggesting that there are an almost inconceivable number of ligands which are both soluble and membrane bound in nature [159,203,204]. The sequence of the CSD is rich with charged and polar uncharged amino acids and this makes the prediction of this region's burial difficult to ascertain. There have been a number of inquiries into the exposure of this region but they have been inconclusive due to the use of short peptide-based constructs which lack either portions or entire domains of caveolin [159,205,206]. To tackle the question of CSD burial to better understand how the protein would be able to bind a diverse variety of ligands, the well established method of cysteine scanning mutagenesis strategy was utilized [197-202]. In this method, constructs are generated which lack native cysteines and have a single cysteine replacement site introduced in a one by one fashion along the length of the sequence under investigation. The single cysteine mutant is then subjected to a water soluble cysteine reactive probe which can only react with de-protonated (aqueous located) cysteines (Figure 4-2). Advantageously, this approach gives residue by residue information on the degree of aqueous exposure and yields information in the broader trend in accessibility along the protein sequence. Therefore, 30 single cysteine mutant constructs of full length caveolin were generated replacing every individual amino acid within the scaffolding domain and part of the intramembrane domain (82-111) (see Appendix 4-1) to examine the exposure along the sequence to a water soluble cysteine reactive probe, biotin-maleimide. Additionally, an anti-myc epitope and 6×

polyhistidine tag were added to the C-terminus for immunodetection and nickel affinity purification respectively. It has been shown that the addition of a 6× polyhistidine tag to the C-terminus does not affect caveolin's ability to form caveolae, bolstering the argument that the C-terminal tags do not significantly impact caveolin's native activity[29].

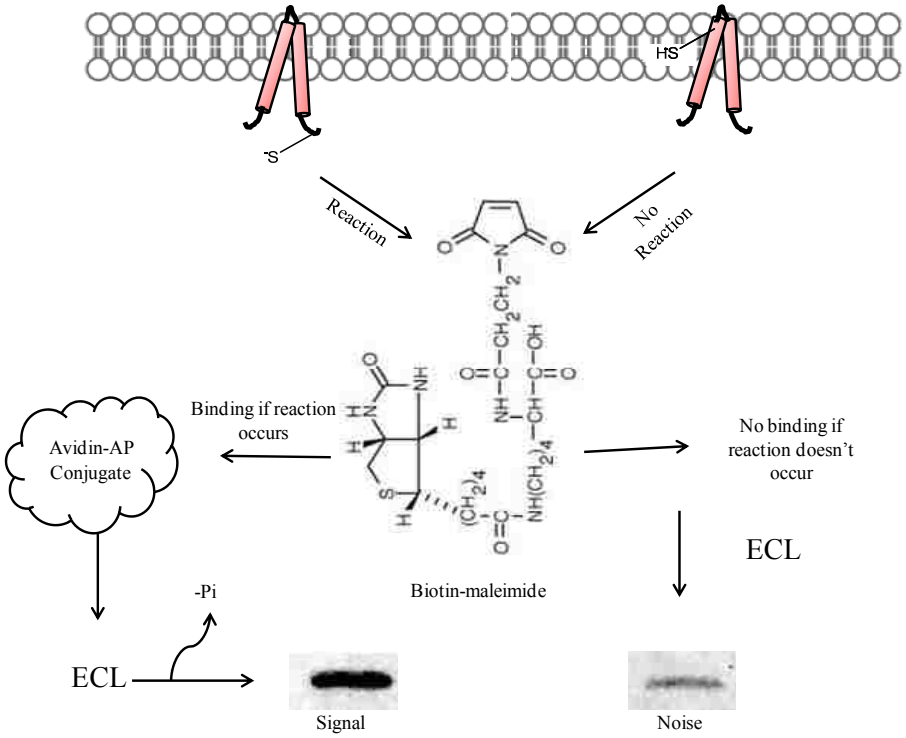

Figure 4-2. Assay principle for cysteine scanning mutagenesis. Caveolin-1 single cysteine mutants (*red*) that are de-protonated will react with maleimides. In the aqueous environment cysteines have a p*Ka* of ~8.5 and will be de-protonated to a significant extent at physiological pH. The p*Ka* in the hydrophobic core of the bilayer is raised to ~14 due to the low dielectric of the membrane environment, and therefore these cysteines will not be able to react.

Validation of Bicelles using Fluorescence Anisotropy Measurements

A key aspect of this experimental strategy is the need for an actual lipid bilayer in which the protein can be embedded into natively, which rules out the use of detergent micelles. However, *E. coli* membranes alone are not ideal because they are comprised mainly of phosphatidylethanolamine (PE) (mammalian cells have a roughly equal mixture of phosphatidylethanolamine and phosphatidylcholine) and there is no control

over the membrane composition (i.e. the introduction of cholesterol). This can hinder studies that examine how different lipids present in the environment play a role in modulating membrane protein burial. Liposomes are also an option but due to the length of time that is required to form them by detergent dialysis; they are not viable as cysteine oxidation and heterogeneity in the topologies of reconstituted protein can complicate the analysis of these studies. Bicelles, on the other hand, have the advantage of being easy to produce, usable in high throughput purification, and also have a bilayered region which membrane proteins can bury their hydrophobic portions into natively. Additionally the membrane environment of the bicelles can be modulated with a variety of different lipid species [119,120].

Bicelles can be prepared at different q ratios, however, it is not clear at which q the bicelle begins taking on properties less akin to that of a mixed micelle and more like those of a pure bilayer as the physical properties of the bicelle are linked to its size. Therefore, the transition temperature of bicelles (T_m) was examined at various q_{eff} values (Figure 4-3). This was achieved by incorporating a small amount of the DPH fluorophore into the samples and measuring the anisotropy as a function of temperature. It has been well established that DPH anisotropy is quite sensitive to the amount of lipid order in a system [207]. When DPH was incorporated into pure DMPC bilayers, the anisotropy ranges from 0.340 (highly ordered) at 2°C to 0.085 (low degree of order) at 36°C. Importantly, sigmoidal behavior was observed which is indicative of a cooperative phase transition of the lipid going through a liquid ordered to liquid disordered transition. As one may expect, although the T_m approached that of the pure DMPC bilayer, phase transitions did tend to be broader with lower degrees of anisotropy in the gel phase. This

can likely be attributed to the presence of the detergent which will have a finite presence in the bilayered region, disrupting gel phase packing of the DMPC. Analysis of the melting curve gave a T_m of 23.1±0.4°C, in agreement with measurements performed on DMPC bilayers using other techniques [121]. These studies were then carried out for bicelles for a range of q_{eff} values (0.05-1.5). For the lowest q_{eff} examined (0.05), the anisotropy value ranged from 0.08 at 2°C to 0.03 at 36°C, and the T_m could not be evaluated because it was outside of the range of temperatures used in the experiment (well below the freezing point of water). However, it was observed as q increased, the phase behavior of the bicelles became more like that of a pure DMPC bilayer. For example, q_{eff} = 1.5 bicelles have a T_m of 24.4 ± 0.2 °C with an anisotropy ranging from 0.310 to 0.090. Therefore a q = 1.0 was chosen for these studies because it was the lowest q that had a T_m within 1 degree of a pure DMPC bilayer and did not have a significant increase in viscosity that would make these solutions difficult to work with. Also, it appeared that the anisotropy value was similar in magnitude when pure DMPC vesicles and q_{eff} = 1.0 bicelles were around the T_m, suggesting that the detergent levels did not significantly alter the degree of disorder for the lipids fluid phase (this was more so the case for higher q_{eff} values). Importantly, this study cautions against the use of bicelles with very low q values as they may behave as mixed micelles and will not likely capture the essence of a true bilayer. Low q bicelles will likely subject proteins to detergent effects that could disrupt their topological analysis.

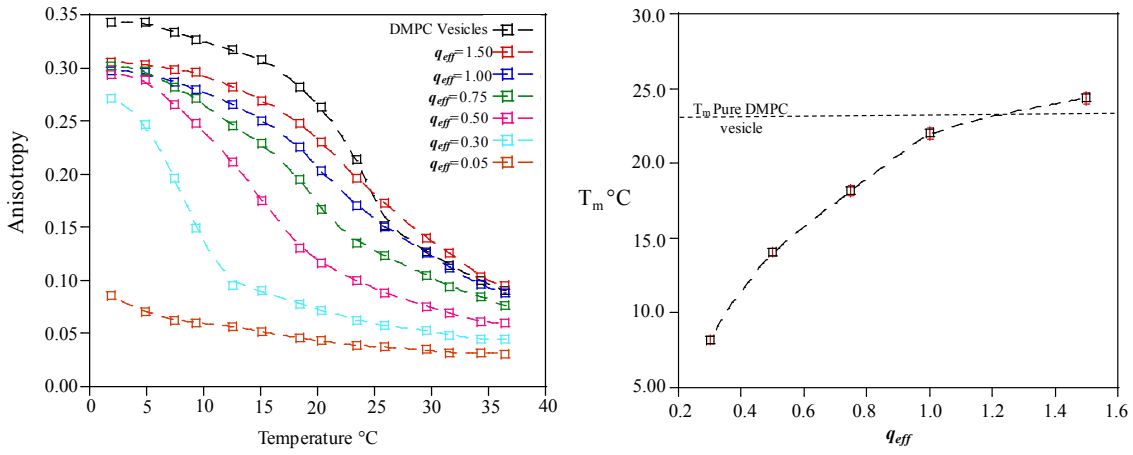

Figure 4-3. Left) Anisotropy for various q_{eff}*'s* as a function of temperature. **Right)** The T_m derived from fitting the melting curves to a sigmoidal equation shows that as q increases, the T_m approaches the transition temperature for a pure DMPC bilayer hyperbolically.

Evaluation of the $^{mychis}Cav1_{1\text{-}178}$ Oligomeric State in Bicelles

As caveolin-1 is known to behave as a high order oligomer *in vivo*, it was desirable to know if the protein employed in these studies would have this behavior. Oligomeric activity could influence the interpretation of the accessibility assays by blocking sites that would be exposed if not for being part of an aggregate. However, it had been shown previously that caveolin-1 residues 62-178 did not aggregate *in vitro*, and was in fact monomeric [43]. Therefore the protein was expressed and purified on a large scale by nickel affinity and gel filtration chromatography, re-bound onto a mini-nickel spin column for exchange into bicelles, and then once reconstituted into bicelles, the protein was desalted into a buffer containing D_2O under a density matched condition for q_{eff}= 1.0 bicelles (previously determined in the lab of KJG), (Figure 4-4 shows purification traces).

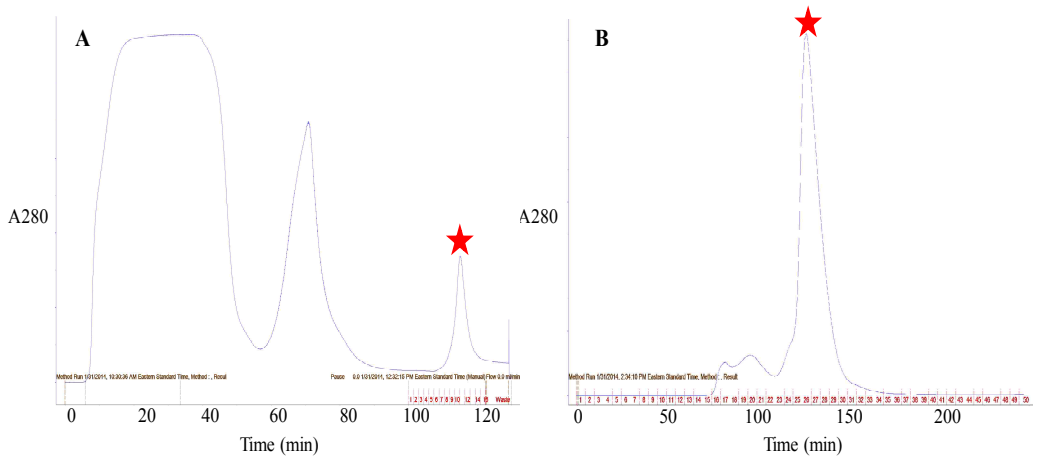

Figure 4-4. Purification traces for large scale expression of $^{mychis}Cav1_{1\text{-}178}$. **A)** Nickel affinity chromatogram. **B)** Gel filtration chromatogram. Red star denotes peaks that were collected.

Using this approach the reconstituted protein was subjected to a sedimentation equilibrium study in the AUC. In a sedimentation equilibrium study, the protein travels down the solution column until sedimentation and diffusion are in equilibrium. Once the species has come to equilibrium, absorbance optics measure the concentration profile of the protein across the analytical ultracentrifuge sample cell, and this profile gives information on the protein's molecular weight. The experiment was performed with bicelles under a "density matched" condition, which means that the density of the buffer and the partial specific volume of the bicelles are the same. Therefore, bicelles will no longer sediment and the concentration profile will allow the extraction of a molecular weight of only the protein and not the protein-detergent aggregate. The molecular weight of the protein was analyzed at three different speeds and three different concentrations (see methods). When the data were fit to an ideal single species model, a molecular weight of 22,961 ± 103 Da was obtained, which compares nicely to the calculated molecular weight of 22,674 Da (Figure 4-5). Therefore, the protein is behaving as a monomer, which greatly reduces the complexity of accessibility analysis in these studies.

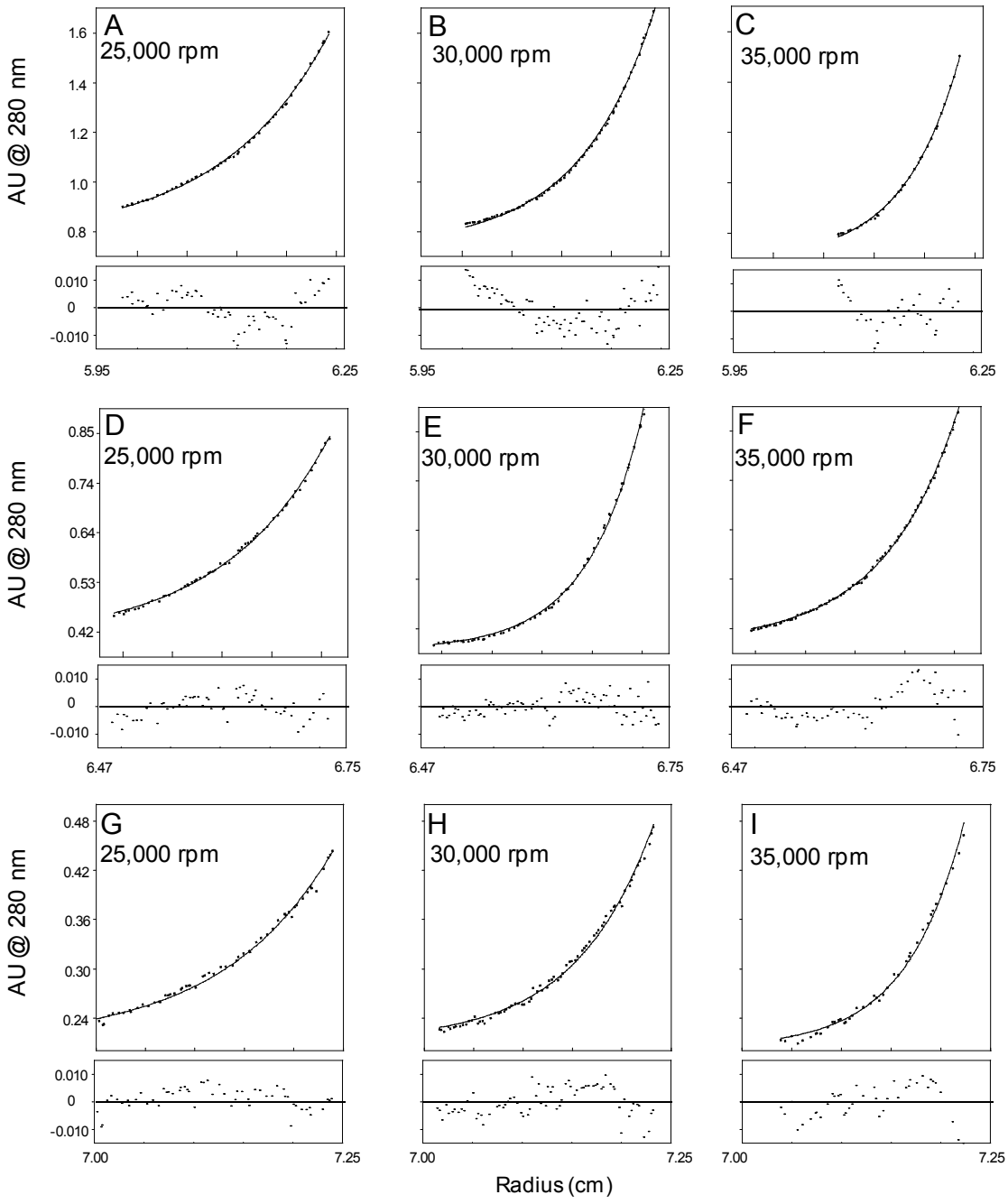

Figure 4-5. Sedimentation equilibrium profiles for $^{mychis}Cav1_{1\text{-}178}$ in bicelles. Panels **A-C** represent a concentration of 30 μM, **D-F** a concentration of 15 μM, and **G-I** a concentration of 7.5 μM. Residuals are displayed underneath each equilibrium profile.

Evaluation of Single Cysteine Mutants Effect on $^{mychis}Cav1_{1-178}$ Secondary Structure

One of the benefits of cysteine scanning mutagenesis studies is that it requires only a single site of cysteine replacement to be introduced, making it a mild way to probe protein topology. However, it is still important to evaluate what effect the mutation will have on the proteins structure and function. Although caveolin-1 is involved in a myriad of cellular processes, there is no clear assay to evaluate the correctness of the protein's fold. Therefore, a comparative study was performed utilizing far UV circular dichroism spectroscopy. In this study the closeness of each single cysteine mutant in terms of its secondary structure was compared to that of the cysteine lacking control, which contains all the native caveolin-1 residues in the 82-111 stretch.

For these studies the over-expressed $^{mychis}Cav1_{1-178}$ had to be purified away from endogenous *E. coli* proteins which would add a large bias to circular dichroism spectra. A non-denaturing strategy was employed using the mild detergent Empigen BB® to bind the protein to a mini nickel spin column. Once the background proteins were eliminated by washes with a low concentration of imidazole, $^{mychis}Cav1_{1-178}$ was exchanged into bicelles and eluted as shown in Figure 4-6.

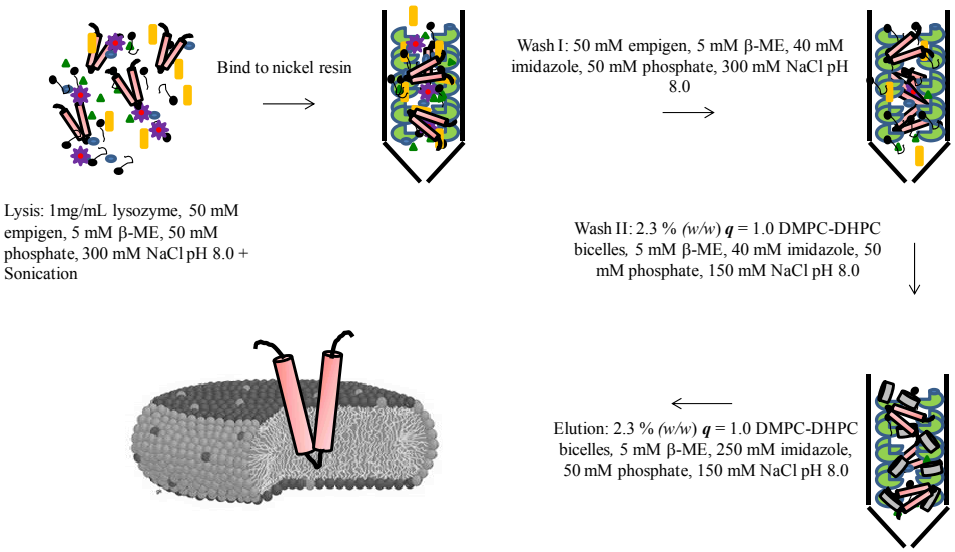

Figure 4-6. Reconstitution strategy for obtaining highly pure $^{mychis}Cav1_{1\text{-}178}$ in bicelles.

Using this method the protein was purified in high yields. Examination of each mutant using CD spectroscopy by scanning the 190-240 nm region revealed the global secondary structure of the single cysteine mutants (Figure 4-7). Although it has been shown in a number of membrane mimetic systems that the caveolin-1 is predominantly α-helical, there are no reports of its secondary structure in bicelles. It appears that in agreement with many studies in other detergent systems, the protein has considerable α-helical character [68,75,208]. Each mutant overlay shows that no major disruption of the native structure was caused by cysteine replacement with each spectrum showing the characteristic 190 nm maxima and 208 and 222 nm minima. Although intensity differences were present, it should be noted that the Zeba® desalting columns used to remove imidazole lose their effectiveness at high concentrations of salts and may result in differences from the bicelle blank that could cause these small variations. Therefore, these data are only to be used qualitatively.

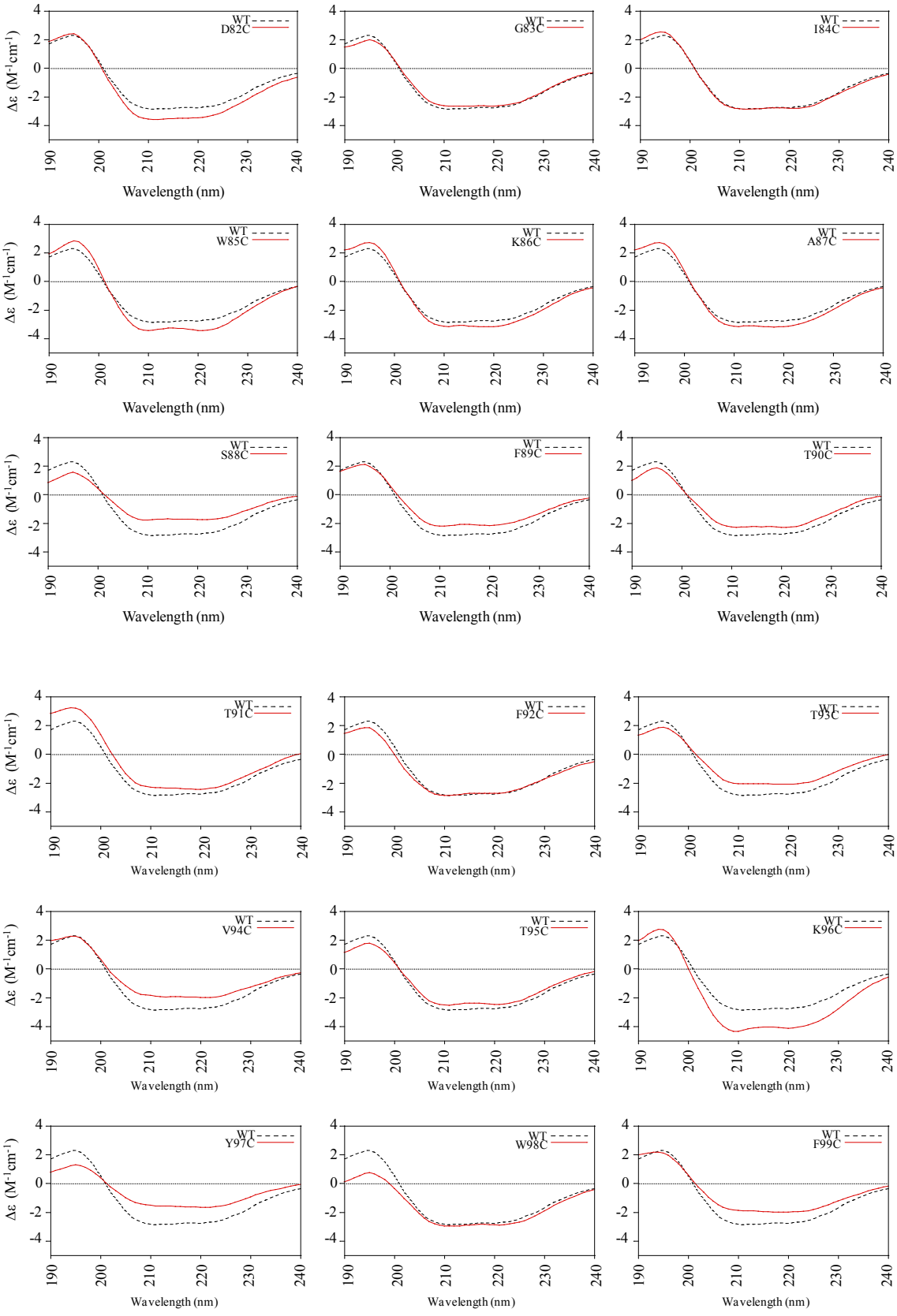
WT
D82C
G83C
I84C
W85C
K86C
A87C
S88C
F89C
T90C
T91C
F92C
T93C
V94C
T95C
K96C
Y97C
W98C
F99C
Δε (M-1cm-1)
Wavelength (nm)

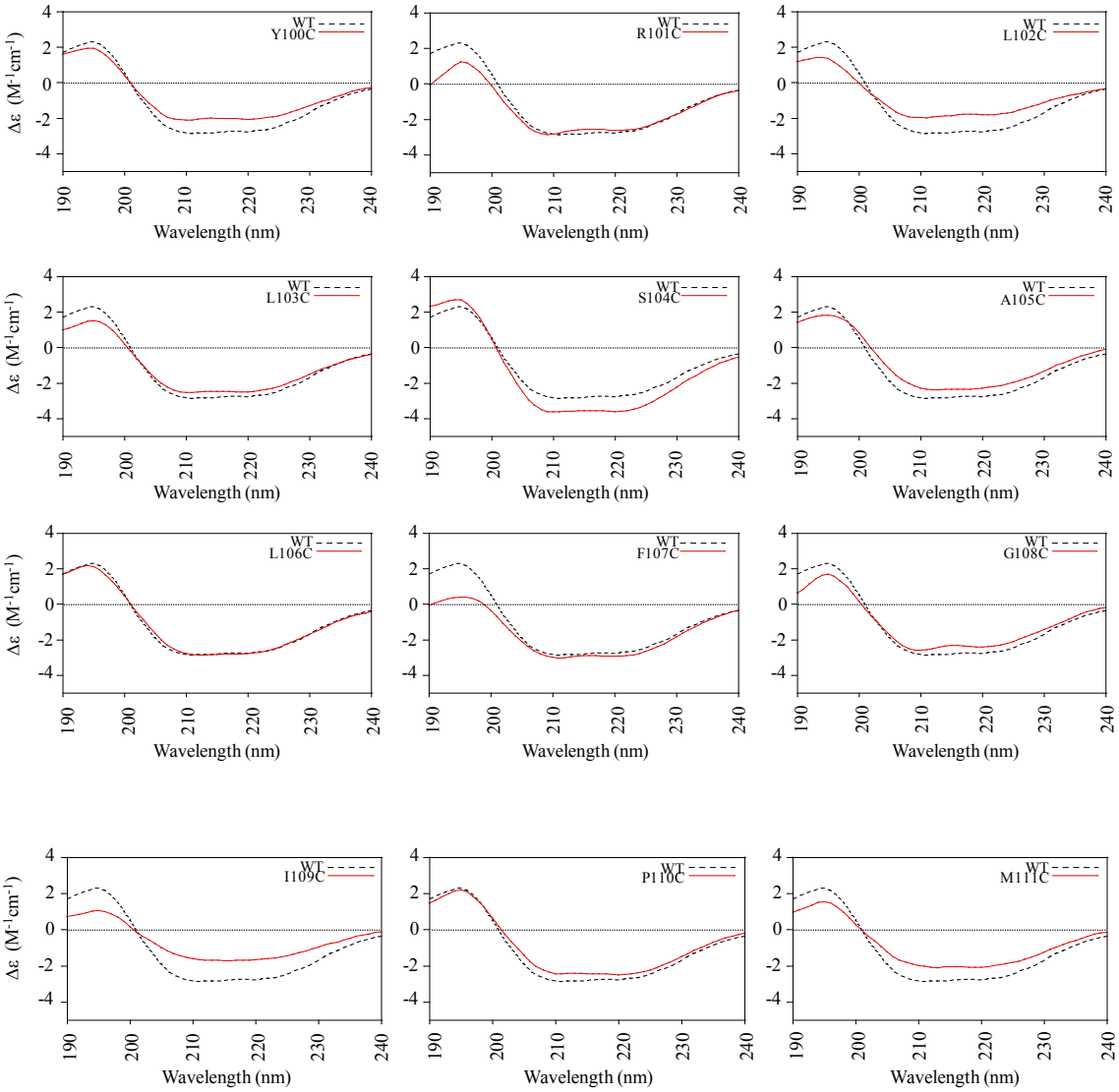

Figure 4-7. Far UV CD spectra of single cysteine mutants (*red*) compared to the wild-type protein (*dashed*).

Analysis of the CSD Topology Using Cysteine Scanning Accessibility Studies

To examine the topology of $^{mychis}Cav1_{1\text{-}178}$, a native preparation strategy was utilized which entailed isolating protein from *E. coli* membranes. This was undertaken because the protein associated with the *E. coli* plasma membrane would have been reconstituted into the membrane by the bacterial translocon, giving it a native fold. Cryo-electron microscopy studies have shown that caveolae can be formed in *E. coli* by the

expression of caveolin [29]. From these bacterial systems it was also shown that the behavior of caveolin was identical to that of the protein in mammalian systems. For instance, the topology was as predicted (N- and C- termini were on the same side of the membrane), isoforms that typically cannot form caveolae did not result in heterogeneous formation (*C. elegans* caveolin-1 and caveolin-2), and a S80E mutation, that results in Golgi retention of the protein in mammalian cells, was sufficient to disrupt caveolae formation [29]. All constructs expressed in this study were found to be localized to the *E. coli* membrane fraction (Figure 4-8). After isolation of the membranes through a series of centrifugation steps and washes, the membrane pellet was flooded with bicelles; bicelles do not likely cause disruption of the protein's topology/fold as they are very mild. Importantly it was found that TCEP had to be present during the purification steps to keep the cysteine residues from oxidizing.

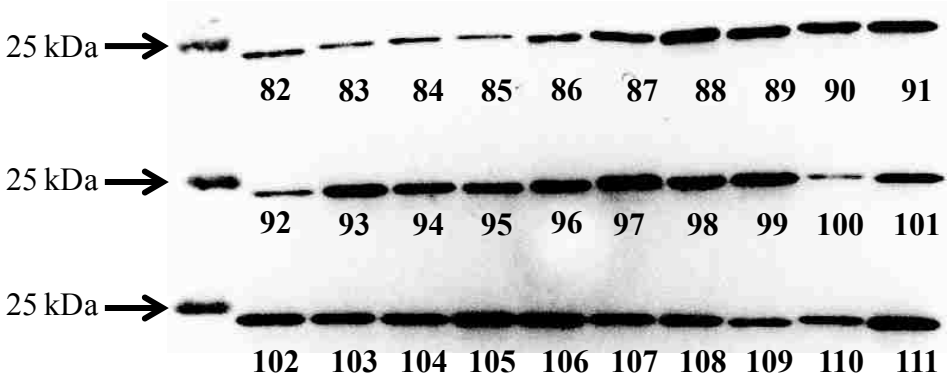

Figure 4-8. Western blot showing that $^{mychis}Cav1_{1-178}$ single cysteine mutants (residue replacement site identified by number under the band) are localized to the membrane fraction of *E. coli*. Levels of protein were somewhat variant; however, this reflected the expression difference and not the difference in trafficking to the membrane. The band at 25 kD is a molecular weight marker.

As mentioned, *E. coli* membranes do not natively contain cholesterol. This approach allowed a comparative study to be undertaken to investigate the impact a

cholesterol-like analogue (CHS) would have in determining the protein's topology once reconstituted into the bicelles (Figure 4-9).

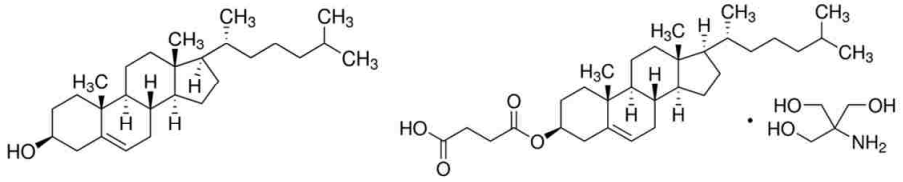

Cholesterol **Cholesteryl Hemisuccinate**

Figure 4-9. Comparison of cholesterol and cholesteryl hemisuccinate. Cholesteryl hemisuccinate has a negative charge at neutral pH whereas cholesterol is neutral.

Cholesterol is not amenable to incorporation into bicelles at ambient temperatures when it is at concentrations above 5% by mol. The cholesterol analog CHS was used because bicelles can be prepared with 20% by mol which is the concentration of cholesterol that is natively found in mammalian cells. Therefore the CHS containing bicelles should be a very good mimic of caveolae which are mainly composed of saturated phospholipids in a cholesterol rich environment [26]. Additionally, CHS confers a negative charge to the bicelles and at 20% by mol it would give a similar charge to that of the inner leaflet of the plasma membrane which has a phosphatidylserine and phosphatidylinositol concentration approaching 15% by mol [210]. This approach also allowed the probing of what role cholesterol would have on CSD topology as caveolin is thought to bind cholesterol through an interaction with residues 94-101 (VTKYWFR) [140,159].

Before subjecting the mutants to a reaction with biotin-maleimide, a gel was run on the reconstituted material to evaluate the total protein levels. In these experiments, the total protein concentration needed to be similar to avoid rate differences (i.e. if a particular mutant was expressed 10 times greater than others, it may appear to get labeled to a greater extent but in reality this may result from more reactants being present). Once

the relative amounts were determined, all samples are diluted to a similar concentration using bicelles.

A time course was run to evaluate the degree of background labeling of the wild-type compared to a construct positioned at the beginning of the CSD (W85C) and a construct predicted to be buried in the intramembrane domain (L106C) (Figure 4-10). This time course showed low background labeling of the cysteine lacking control and a persistent low level of biotinylation for L106C compared to W85C. For practical reasons, the 10 minute time course was chosen as the point to quench the reaction in subsequent experiments.

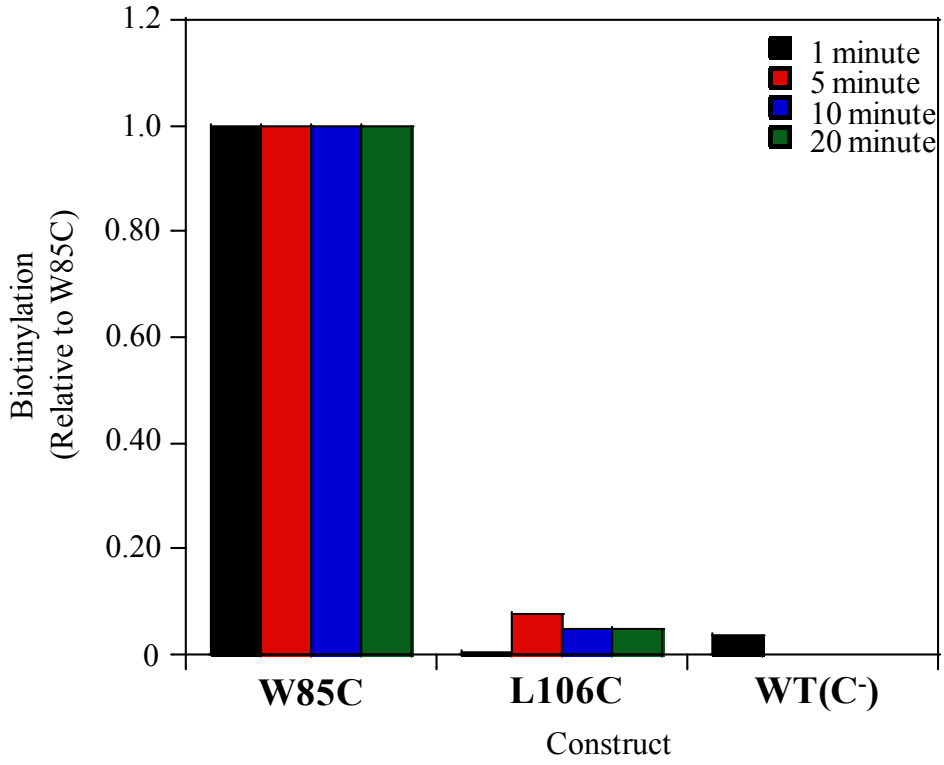

Figure 4-10. Time course evaluation of single cysteine mutants located in the CSD (W85C) and intramembrane domain (L106C). Additionally the cysteine lacking control was evaluated. Legend indicates the time point where the reaction was quenched and subsequently analyzed by Western blotting. Clearly, there is little change in the extent of relative biotinylation over the time course investigated. Low levels of relative biotinylation (0-5%) were observed for the cysteine lacking control.

After all 30 of the reconstituted mutants were reacted with biotin-maleimide and quenched, a gel was run to quantify the degree of biotinylation for each replacement site. Mutants that have cysteine residues outside the bilayer (accessible) will show high reactivity towards biotin-maleimide, whereas those with their cysteine replacement site within the bilayer (inaccessible) will show low reactivity. Each mutant was evaluated for its degree of biotinylation on a per protein basis by Western blot analysis. Figure 4-11 shows total protein amounts as indicated by blotting the anti-myc antibody after solubilization in membranes and dilution to a similar level based on densitometry for 2.3 % (*w/w*) $\boldsymbol{q}$ = 1.0 DMPC/DHPC bicelles (Panel A) and DMPC/CHS/DHPC bicelles (Panel B). Clearly, all the levels are similar during the reaction, which discounts labeling rate enhancements brought on by differentials in the amount of protein (levels were within a factor of 10).

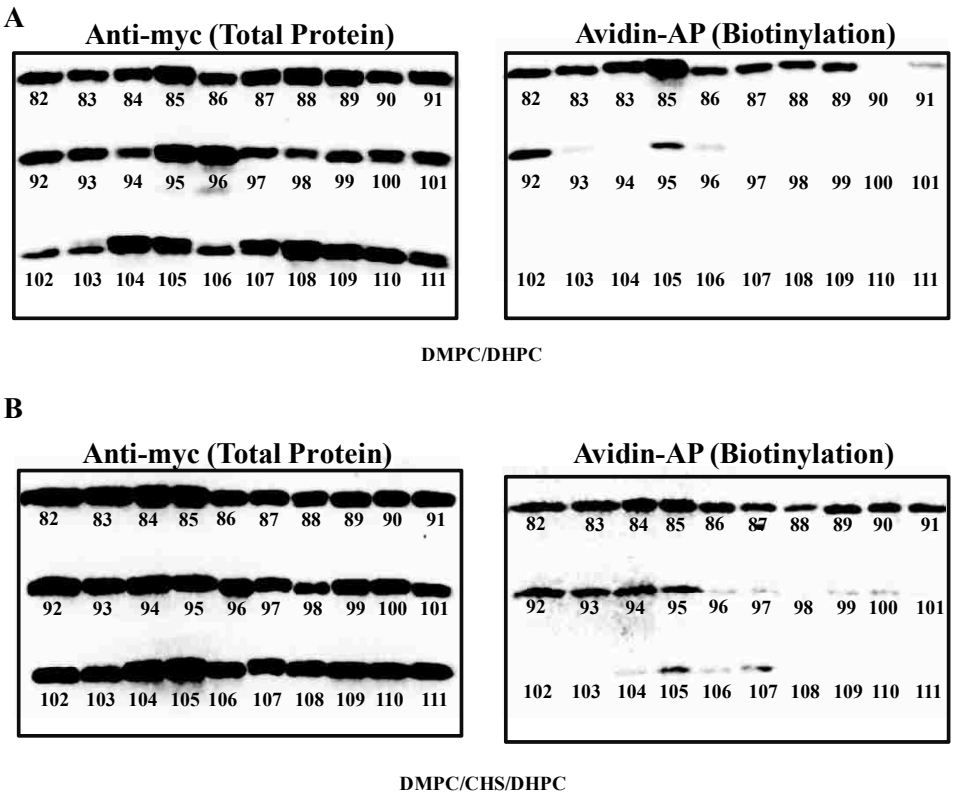

Figure 4-11. Representative Western blots for biotinylation experiments of $^{mychis}Cav1_{1-178}$ in bicelles. **A)** Anti-myc (*left*) and Avidin-AP (*right*) blots for DMPC/DHPC bicelles. **B)** Anti-myc (*left*) and Avidin-AP (*right*) for DMPC/DHPC/CHS bicelles. Note that in the Avidin-AP blot for DMPC/DHPC bicelles, it appears that residue 95 would be strongly labeled. However, if one is to look at the total protein blot, it appears that there is more material deposited during Western blotting and therefore, this residue has low labeling.

Figure 4-11 also shows blots probing for biotinylation using the avidin-AP conjugate for q_{eff} = 1.0 DMPC/DHPC bicelles (Panel A) and DMPC/CHS/DHPC bicelles (Panel B). There is a noticeable difference in the magnitude of the signal between cysteines that could be labeled and those that were inaccessible to the reagent. However, these differences must be evaluated on a per protein basis as differences in transfer can be a large source of error. To account for this issue, a plot of relative biotinylation versus cysteine replacement site was prepared for both data sets (Figure 4-12). The data showed that for q = 1.0 DMPC/DHPC bicelles there is strong labeling with the biotin-maleimide

reagent for residues 82-89. In the 90-96 region, the labeling appears to be dynamic (typically less than 40% of the highest labeled residue on the blot) and is very low for residues 97-111 (typically less than 15% of the highest labeled residue on the blot). Interestingly, F92C is an outlier where it shows a very high relative accessibility compared to surrounding residues. Due to outliers such as F92C, biotinylation is best evaluated as a ***trend*** in the accessibility of the CSD by making a plot of the cysteine replacement site versus the averaged local accessibility (Figure 4-12, average local accessibility denotes the relative biotinylation of the position indicated plus the relative biotinylation of the two flanking sites on either side, see methods). Here a sigmoidal function can be fitted to the data and shows that the accessibility changes dramatically over the CSD region where residue A87C is the inflection point.

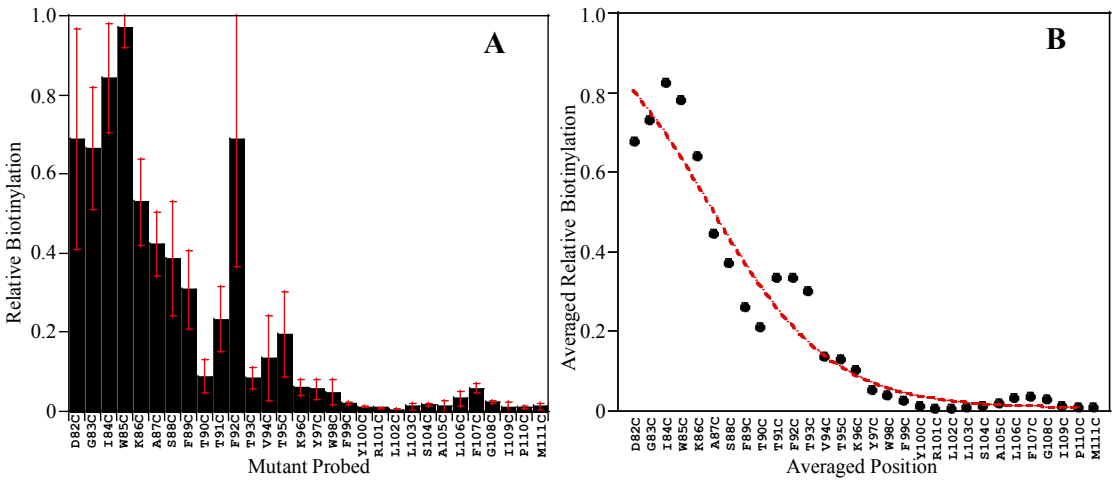

Figure 4-12. A) Relative biotinylation values for each of the 30 constructs reconstituted into DMPC/DHPC bicelles. Note that the residue with the highest degree of biotinylation varied blot to blot, and therefore no individual residue has a value of 1. Error bars represent the average of 3 experiments. The amount of error in these experiments is large (for labeled residues its ~10-20%, for unlabeled residues this error is *much* lower) but there is a statistically significant difference in the regions of high and low degrees of labeling. **B)** Averaged relative biotinylation values for each position were used to examine the overall trend in accessibility, and helps to interpret how the accessibility of $^{mychis}Cav1_{1\text{-}178}$ changes along the length of the sequence.

This position has an averaged accessibility of 0.42 and could represent a position that would be exposed and buried an equal amount of the time, giving it a position that could be somewhere within the headgroup region of the bilayer. It appears that the CSD has a dichotic position in the membrane where residues from 82-95 would be at least partially exposed and residues 96-111 would be buried. Data from the fluorescence studies presented in Chapter three indicated that tryptophan 85 and 98 are located in the headgroup (accessible) and the hydrophobic core (inaccessible) regions of the bilayer respectively when reconstituted into DMPC/DHPC bicelles and are therefore consistent with this analysis of the cysteine scanning mutagenesis study [208]. These accessibility data are also in agreement with the molecular dynamics simulation work in chapter three indicating that in pure DMPC bilayers residues 91 - 95 are located around and within the headgroup region. Therefore, residues in this stretch may show heterogeneous burial that would be somewhere between that of an exposed and that of an unexposed region's burial [208].

Figure 4-11 shows that for $\boldsymbol{q}$ = 1.0 DMPC/CHS/DHPC bicelles there is strong labeling for the first 14 residues which drops off starkly at position 96. These data are somewhat different than the data for the pure DMPC bicelles as they show that in the presence of CHS, $^{mychis}Cav1_{1\text{-}178}$ seems to have more even labeling across the CSD and a more dramatic drop off in accessibility that occurs between positions 93 and 98 (Figure 4-13). Fitting of the averaged relative accessibility data to a sigmoidal function extracts an inflection point of T95C, which has an averaged accessibility of 0.35 (Figure 4-13). Although in both lipid environments the accessibility to the water soluble probe changes

rapidly in the CSD region, pinpointing it as the likely region of membrane entrance, the appearance of the averaged relative biotinylation plots are quite different.

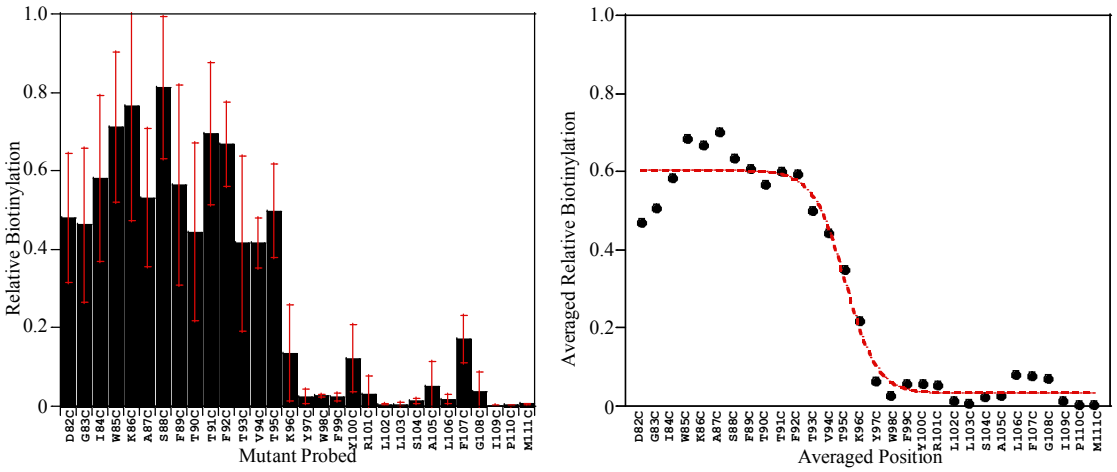

Figure 4-13. A) Relative biotinylation values for each of the 30 constructs reconstituted into DMPC/DHPC/CHS bicelles. As was the case for DMPC/DHPC bicelles, the residue with the highest degree of biotinylation varied blot to blot, and therefore no individual residue has a value of 1. Error bars represent the average of 3 experiments. **B)** Averaged relative biotinylation values for each position were used to examine the overall trend in accessibility. It appears that CHS promoted a more even degree of biotinylation across the CSD and a considerably more distinct drop off in accessibility.

Residues 97-111 are poorly accessible in both of the lipid systems. A deeper look at the difference between the two lipid systems by examining which residues were statistically different in terms of their relative biotinylation indicated that scaffolding domain residues T90, T91, T93, V94, and T95 and the intramembrane domain residue F107 were more accessible when CHS was included (Table 4-1). It should be noted that F107 was an outlier compared to residues surrounding it. Therefore CHS appears to be adjusting the exposure of the CSD such that the residues 90-95 are sampling an environment with a higher degree of water penetration on average. This result could be indicating that CHS has decreased the depth of bilayer penetration or tilt of the CSD.

As both lipid systems should be in the gel phase at the temperature employed (T_m= 22.00±0.27℃ for DMPC/DHPC bicelles and sterols broaden the T_m), it appears that the sterols presence or the surface charge that CHS imparts on the bicelles could be impacting the protein's topology. This is in agreement with a number of studies investigating the response of caveolin-1 topology to the inclusion of the sterol in bilayers. For instance, a molecular dynamics simulation of residues 94-122 embedded in bilayers showed that the protein was much deeper in pure DPPC bilayers than it was in 70:30 DPPC:cholesterol bilayers [46]. Additionally, tryptophan fluorescence quenching studies on a caveolin-1 intramembrane peptide (residues 103-122) showed that acrylamide was able to quench tryptophan residues within the protein more effectively when reconstituted into membranes composed of POPC/DPPC/Cholesterol versus those composed of purely POPC suggesting that cholesterol limits the proteins insertion into bilayers.

Single Cysteine Position	Relative Biotinylation DMPC/DHPC	Relative Biotinylation DMPC/DHPC/CHS
82	0.69 ± 0.28	0.48 ± 0.17
83	0.67 ± 0.15	0.46 ± 0.20
84	0.84 ± 0.14	0.58 ± 0.21
85	0.97 ± 0.05	0.71 ± 0.19
86	0.53 ± 0.11	0.77 ± 0.29
87	0.42 ± 0.08	0.53 ± 0.18
88	0.39 ± 0.14	0.81 ± 0.18
89	0.31 ± 0.10	0.56 ± 0.25
90	0.09 ± 0.04	0.44 ± 0.23
91	0.23 ± 0.08	0.70 ± 0.18
92	0.69 ± 0.32	0.67 ± 0.11
93	0.09 ± 0.03	0.42 ± 0.22
94	0.14 ± 0.11	0.42 ± 0.06
95	0.20 ± 0.11	0.50 ± 0.12
96	0.06 ± 0.02	0.14 ± 0.12
97	0.06 ± 0.03	0.03 ± 0.02
98	0.05 ± 0.03	0.03 ± 0.01
99	0.02 ± 0.01	0.02 ± 0.01
100	0.01 ± 0.01	0.12 ± 0.09
101	0.01 ± 0.01	0.03 ± 0.05
102	0.00 ±0.01	0.01 ± 0.01
103	0.01 ± 0.01	0.01 ± 0.01
104	0.02 ± 0.01	0.01 ± 0.01
105	0.01 ± 0.01	0.05 ± 0.06
106	0.03 ± 0.02	0.02 ± 0.01
107	0.06 ± 0.01	0.17 ± 0.06
108	0.02 ± 0.01	0.04 ± 0.05
109	0.01 ± 0.01	0.00 ± 0.01
110	0.01 ± 0.01	0.00 ± 0.01
111	0.01 ± 0.01	0.01 ± 0.01

Table 4-1. Table of relative biotinylation value averages of three trials for both bicelle types employed in this study. Residues that had statistically significant differences in accessibility have been highlighted in *orange*.

The relationship between caveolin-1 and cholesterol is very intimate and caveolin-1 is considered to be a cholesterol binding protein [19]. Residues (94-101) in the CSD form a putative CRAC motif [159,196]. The disposition of cholesterol within bilayers places its hydroxyl moiety in the headgroup region and the sterol portion within the

hydrophobic core of the bilayer [210]. The accessibility data show that in the presence of CHS, the CRAC motif would be partially exposed and partially buried and could facilitate the interaction with both the headgroup and ring regions of cholesterol. Interestingly, the CHS seems to cause an increase in the exposure of the CRAC motif residues 94 and 95; however, it is unclear how this would enhance the proposed interaction between the protein and cholesterol. Taken together, our accessibility data clearly show that the CSD could simultaneously interact with cholesterol and be available for binding to soluble proteins. These studies rationalize how the CSD can interact with both signaling proteins and cholesterol simultaneously.

Using a residue by residue approach, these data have revealed that the CSD topology is even more complicated than originally thought and is highly dependent on the lipid environment. To complicate this matter further, there is no consensus as the two dimensional structure of the CSD. Our circular dichroism data suggest that the protein is indeed highly α-helical in bicelles. Bioinformatic and structural studies that have been performed have suggested that the stretch of residues in the 82-111 region is composed of two α-helices, one amphipathic, and one transmembrane (residues 81-92 and residues 97-107) [66,68,75]. However, the structural studies performed in Chapter 3 indicated that the region is comprised of a single transmembrane α-helix (residues 87-107) [208]. Although the former model of two α-helices is difficult to project, the depth of a single α-helix ranging from residues 87-111 can be estimated. A pure DMPC bilayer is roughly 40 Å thick, with a single headgroup region having a thickness of ~10 Å [208]. If A87C (inflection point of sigmoidal fit in pure DMPC bilayers) is in the center of the headgroup region, there is about 5 Å between this residue and the borderline of the hydrophobic

core. If one assumes that the protein does not tilt at all, this helix would extend 31.5 Å placing the C-terminus of the helix into the center of the opposing headgroup region. However, if that was the case, labeling of F107C-M111C would have been observed, therefore it is likely that if this protein was behaving as a single membrane spanning α-helix, A87C would be above the center of the headgroup region or the protein would be tilted to account for the results of this study (Figure 4-14). This model places the turn residues within the second leaflet, near the interface between the headgroup and the hydrophobic core regions of the bilayer. This is consistent with the simulation data presented in Chapter 3. However, due to the nature of these studies (i.e. relative scale), the only definitive statement that can be made is between an intramembrane region versus an exposed region [211]. The assumption that A87 would be in the center of the headgroup region may be incorrect. Therefore it is unclear how the protein would enter the bilayer, although the averaged relative biotinylation data could be consistent with a large degree of tilt.

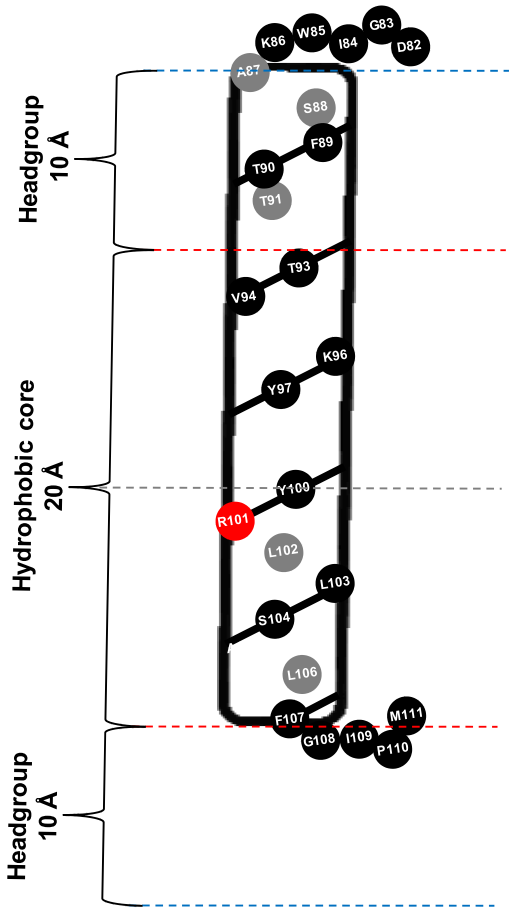

Figure 4-14. Speculative cartoon of the topology of caveolin-1 residues 82-111 in DMPC/DHPC bicelles based on biotinylation data. This analysis is based on residues 87-107 being α-helical, residues 93-111 being intramembrane (less than 20% relative biotinylation), A87 being positioned somewhere within the headgroup region. The ability of arginine 101 (*red*) to reach the headgroup region of the bilayer to avoid desolvation of the positive charge is likely key in determining the degree of tilt. Gray circles are going away from the viewer whereas black circles are coming towards the viewer.

The addition of cholesterol to a pure DMPC bilayer at 20% by mol increases the bilayer thickness by about 1-2 Å, however, the thickness increase is due to the rigidifying of the acyl chains, therefore the headgroup region likely remains a similar thickness [212,213]. With T95C being buried close to the headgroup-hydrophobic core border, a model assuming a single transmembrane α-helix model (residues 87-107) would place F107C

~7 Å short of the opposite leaflet's headgroup region assuming a tilt angle of zero. This model would be consistent with the topological data presented here, however the burial of the arginine would likely have to be compensated for by the protein having to tilt somewhat to avoid shedding its hydration layer (Figure 4-15).

When examining the primary sequence of the 82-111 region, it is interesting to speculate as to the rationale of why caveolin may prefer cholesterol rich bilayers compared to the bulk membrane. There are a number of charged residues in the CSD, two of which are expected to be in inaccessible regions in both lipid systems employed that could be key in maintaining the depth of caveolin-1 in the bilayer (K96 is completely across species and isoforms and R101 is positive charge conserved). The more deeply buried DMPC model shows that K96 and R101 would have to extend their aliphatic chains significantly to secure the charges outside of the bilayer. In the presence of cholesterol the protein is less deeply buried and charged residues would be closer to the bilayer surface. This position could allow snorkeling of these residues out of the hydrophobic core to avoid desolvation of the guanidino/lysine moieties more readily. This hypothesis will likely need experimental validation to gain stronger support. Additionally, it will be worthwhile to examine the trend of labeling in bicelles composed of negatively charged lipids to determine if the sterol's presence changes the topology or if the presence of a negative charge on the CHS moiety could bring on topological differences (perhaps by electrostatic interactions with K96 and R101). If the assumption that the inflection point is not within the headgroup region, these models become less constrictive, nonetheless, it is clear that the 96-111 region seems to be inaccessible and these residues would be positioned within the hydrophobic core of the membrane.

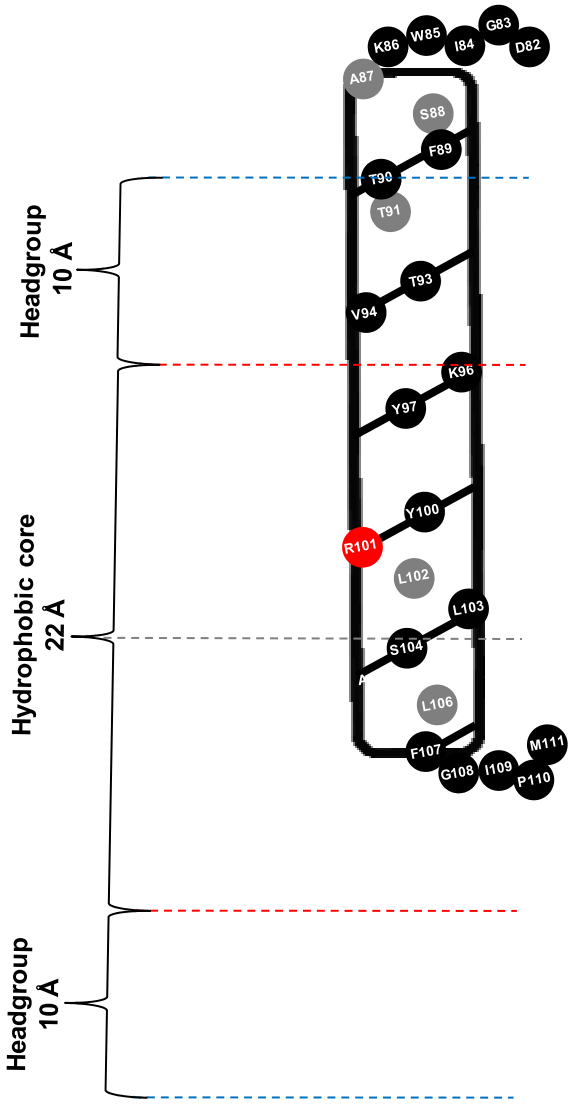

Figure 4-15. Speculative cartoon of the topology of caveolin-1 residues 82-111 in a DMPC/DHPC/CHS bicelles based on biotinylation data. This analysis is based on residues 87-107 being α-helical, residues 96-111 being intramembrane (less than 10% relative biotinylation), T95 being positioned somewhere within the headgroup region. As was the case for caveolin in DMPC/DHPC bicelles, the ability of arginine 101 (*red*) to reach the headgroup region of the bilayer to avoid desolvation of the positive charge will likely affect the way the protein tilts. Gray circles are residues going away from the viewer whereas black circles are residues coming towards the viewer.

The data corroborate other studies that probed binding of caveolin-1 to some of its partners. For example, eNOS binding to caveolin-1 has been shown to be dependent on a triplet of residues (T90, T91, and F92), which according to the accessibility data, would

be exposed and available for binding in cholesterol rich bilayers but less exposed in pure DMPC bilayers [195]. Clearly this interaction is occurring outside of the hydrophobic core of the bilayer, with the more exposed portion of the CSD. This is a reasonable location for CSD-protein interactions considering that many of the caveolin-1 interaction partners such as eNOS, Src kinases, and G proteins are soluble proteins which are held proximal to the membrane surface by acylation [17,215]. It seems that cholesterol could optimize the CSD interactions with soluble ligands.

The uniform inaccessibility of residues 96-111 in both cases supports a variety of tilts but doesn't support a horizontal surface orientation (as some models predict [66]), as this would give an oscillating accessible/non-accessible pattern [215,216]. Therefore, this result places the putative loop formed by the intramembrane domain in the hydrophobic core as has been suggested by others in the field [66,75-77]. The accessibility data corroborate the intramembrane turn location that has been proposed in Chapter 3. However, due to the scale being relative, a more concrete experimental metric will likely be needed to fully corroborate this assertion.

CONCLUSIONS

In this chapter, single cysteine mutants of caveolin-1 were reconstituted into biologically relevant (in terms of T_m) DMPC/DHPC bicelles and DMPC/CHS/DHPC bicelles for secondary structure evaluation using circular dichroism and topological evaluation using chemical accessibility assays. This is the first example of cysteine scanning studies employing biotin-maleimide having been performed on over-expressed membrane proteins natively reconstituted into bicelles. The accessibility studies showed a clear trend in labeling, where the residues become decreasingly accessible as the position of the mutation approaches the putative turn region of caveolin-1 in both membrane environments. This data provides a strong indication that the CSD is likely the portion of the protein which first enters the bilayer. Importantly, the entrance point into the hydrophobic core can now be more confidently positioned to residue 96, which is buried in both model systems. The postulation of a membrane embedded turn seems to be reasonable as evidenced by the lack of labeling in the 108-110 region, however, one must err caution as these residues have been shown to be sensitive to substitution [70]. In any case, it appears that the studies employed have lead to a refinement of the topology model of caveolin-1. This study also showed that CHS, which closely resembles cholesterol and imparts negative charge, modifies the CSD topology by increasing its exposure one helical turn. Structural data will likely be critical in deciphering how this interaction changes caveolins membrane positioning on the molecular level. In the future, the examination of the remainder of the intramembrane domain (residues 112-134) using the same technique will be important for determining the overall burial and exit point from the membrane. This chapter presents clear topological data which help

explain the multi-faceted functionality of the CSD and shed light on the role that the lipid environment plays in determining the proteins aqueous exposure.

Appendix 4-1. Sequences of Protein Constructs Utilized

$^{mychis}Cav1_{1-178}$	MSGGKYVDSE GHLYTVPIRE QGNIYKPNNK AMADELSEKQ VYDAHTKEID LVNRDPKHLN DDVVKIDFED VIAEPEGTHS FDGIWKASFT TFTVTKYWFY RLLSALFGIP MALIWGIYFA ILSFLHIWAV VP**S**IKSFLIE IQ**S**ISRVYSI YVHTV**S**DPLF EAVGKIFSNV RINLQKEIEQ KLISEEDLLE HHHHHH

Construct	Sequence of 82-111 Portion
Wild-Type	N-DGIWKASFTTFTVTKYWFYRLLSALFGIPM-C
D82C	N-**C**GIWKASFTTFTVTKYWFYRLLSALFGIPM-C
G83C	N-D**C**IWKASFTTFTVTKYWFYRLLSALFGIPM-C
I84C	N-DG**C**WKASFTTFTVTKYWFYRLLSALFGIPM-C
W85C	N-DGI**C**KASFTTFTVTKYWFYRLLSALFGIPM-C
K86C	N-DGIW**C**ASFTTFTVTKYWFYRLLSALFGIPM-C
A87C	N-DGIWK**C**SFTTFTVTKYWFYRLLSALFGIPM-C
S88C	N-DGIWKA**C**FTTFTVTKYWFYRLLSALFGIPM-C
F89C	N-DGIWKAS**C**TTFTVTKYWFYRLLSALFGIPM-C
T90C	N-DGIWKASF**C**TFTVTKYWFYRLLSALFGIPM-C
T91C	N-DGIWKASFT**C**FTVTKYWFYRLLSALFGIPM-C
F92C	N-DGIWKASFTT**C**TVTKYWFYRLLSALFGIPM-C
T93C	N-DGIWKASFTTF**C**VTKYWFYRLLSALFGIPM-C
V94C	N-DGIWKASFTTFT**C**TKYWFYRLLSALFGIPM-C
T95C	N-DGIWKASFTTFTV**C**KYWFYRLLSALFGIPM-C
K96C	N-DGIWKASFTTFTVT**C**YWFYRLLSALFGIPM-C
Y97C	N-DGIWKASFTTFTVTK**C**WFYRLLSALFGIPM-C
W98C	N-DGIWKASFTTFTVTKY**C**FYRLLSALFGIPM-C
F99C	N-DGIWKASFTTFTVTKYW**C**YRLLSALFGIPM-C
Y100C	N-DGIWKASFTTFTVTKYWF**C**RLLSALFGIPM-C
R101C	N-DGIWKASFTTFTVTKYWFY**C**LLSALFGIPM-C
L102C	N-DGIWKASFTTFTVTKYWFYR**C**LSALFGIPM-C
L103C	N-DGIWKASFTTFTVTKYWFYRL**C**SALFGIPM-C
S104C	N-DGIWKASFTTFTVTKYWFYRLL**C**ALFGIPM-C
A105C	N-DGIWKASFTTFTVTKYWFYRLLS**C**LFGIPM-C
L106C	N-DGIWKASFTTFTVTKYWFYRLLSA**C**FGIPM-C
F107C	N-DGIWKASFTTFTVTKYWFYRLLSAL**C**GIPM-C
G108C	N-DGIWKASFTTFTVTKYWFYRLLSALF**C**IPM-C
I109C	N-DGIWKASFTTFTVTKYWFYRLLSALFG**C**PM-C
P110C	N-DGIWKASFTTFTVTKYWFYRLLSALFGI**C**M-C
M111C	N-DGIWKASFTTFTVTKYWFYRLLSALFGIP**C**-C

Appendix 4-1. Mutagenesis Primers Utilized

Construct	Primer Sequence
D82C	5’-GAAGGTACCCACTCTTTCTGTGGTATCTGGAAAGCGTC-3’
G83C	5’-CCCACTCTTTCGACTGTATCTGGAAAGCG-3’
I84C	5’-CCACTCTTTCGACGGTTGTTGGAAAGCGTCTTTCAC-3’
W85C	5’-CTTTCGACGGTATCTGTAAAGCGTCTTTCACC-3’
K86C	5’-CTTTCGACGGTATCTGGTGTGCGTCTTTCACCACCTTC-3’
A87C	5’-CTTTCGACGGTATCTGGAAATGTTCTTTCACCACCTTCACCG-3’
S88C	5’-GTATCTGGAAAGCGTGTTTCACCACCTTCAC-3’
F89C	5’-GTATCTGGAAAGCGTCTTGTACCACCTTCACCGTTAC-3’
T90C	5’-GTATCTGGAAAGCGTCTTTCTGTACCTTCACCGTTACCAAATAC-3’
T91C	5’-CTGGAAAGCGTCTTTCACCTGTTTCACCGTTACCAAATAC-3’
F92C	5’-GCGTCTTTCACCACCTGTACCGTTACCAAATACTG-3’
T93C	5’-GCGTCTTTCACCACCTTCTGTGTTACCAAATACTGGTTC-3’
V94C	5’-CTTTCACCACCTTCACCTGTACCAAATACTGGTTC-3’
T95C	5’-CTTTCACCACCTTCACCGTTTGTAAATACTGGTTCTACCGTC-3’
K96C	5’-CCACCTTCACCGTTACCTGTTACTGGTTCTACCGTC-3’
Y97C	5’-CTTCACCGTTACCAAATGTTGGTTCTACCGTCTGC-3’
W98C	5’-CGTTACCAAATACTGTTTCTACCGTCTGCTG-3’
F99C	5’-CGTTACCAAATACTGGTGTTACCGTCTGCTGTCTG-3’
Y100C	5’-CAAATACTGGTTCTGTCGTCTGCTGTCTGCG-3’
R101C	5’-CAAATACTGGTTCTACTGTCTGCTGTCTGCGC-3’
L102C	5’-CCAAATACTGGTTCTACCGTTGTCTGTCTGCGCTGTTCGGTATC-3’
L103C	5’-GTTCTACCGTCTGTGTTCTGCGCTGTTC-3’
S104C	5’-GTTCTACCGTCTGCTGTGTGCGCTGTTCGGTATC-3’
A105C	5’-CTACCGTCTGCTGTCTTGTCTGTTCGGTATCCCG-3’
L106C	5’-CGTCTGCTGTCTGCGTGTTTCGGTATCCCGATG-3’
F107C	5’-CTGTCTGCGCTGTGTGGTATCCCGATGG-3’
G108C	5’-GTCTGCGCTGTTCTGTATCCCGATGG-3’
I109C	5’-CTGCGCTGTTCGGTTGTCCGATGGCGCTGATC-3’
P110C	5’-GCGCTGTTCGGTATCTGTATGGCGCTGATCTGG-3’
M111C	5’-CTGCGCTGTTCGGTATCCCGTGTGCGCTGATCTGGGGTATCTAC-3’

Chapter 5. The Lipid Environment and Proline at Position 110 Modulate the Aqueous Exposure of Caveolin-1

ABSTRACT

The hallmark conformational feature of caveolin-1 is that it has an unusual topology where both N- and C- termini are cytoplasmic as a result of a membrane-embedded turn. Recent biophysical studies have revealed that a highly conserved proline residue located at position 110 (P110) and the protein's association with cholesterol are critical to the structure and topology of caveolin. Some studies have suggested that the protein is dramatically altered and becomes linearized upon the substitution of proline 110 to alanine, whereas others suggested that there is very little change in the proteins conformation. There have been reports that cholesterol results in secondary structure changes to the protein (increased β-strand character) and also causes global topological changes. This work utilizes a functional construct of caveolin-1 ($Cav1_{62-178}$) reconstituted into DPC micelles to characterize structural and accessibility changes that occur upon the P110A substitution ($Cav1_{62-178}$(P110A)). Additionally, cholesterol's effect on determining the protein's exposure was examined by reconstituting the protein in micelles composed of both DPC and cholesterol-PEG600. To unveil global and local changes in the environment of the protein upon alanine substitution and the presence of cholesterol, four evenly-spaced tryptophan residues native to the caveolin-1 protein were utilized as fluorescent reporters. Near and far UV circular dichroism spectroscopy experiments were used to examine changes in aromatic residue packing and global secondary structure between constructs. Next, fluorescence λ_{max} and Stern-Volmer quenching analysis were used to examine global (all tryptophan residues present) and

local (single tryptophan mutants) accessibility differences. Fluorescence λ_{max} and Stern-Volmer quenching analysis revealed that upon mutation and inclusion of cholesterol, local changes in tryptophan accessibility occurred. Additionally, a fluorescence resonance energy transfer experiment was used to further examine conformational changes that may be occurring in the presence of the cholesterol mimic. This study supports the structural importance of P110 in maintaining a specific caveolin-1 fold, but downplays pervious inquiries that suggested an over-arching topological role. This study also indicates that cholesterol may cause small changes in the protein's fold but large changes in the proteins aqueous exposure.

INTRODUCTION

Caveolins are found within cholesterol rich domains in the bilayer called caveolae. They all contain a highly conserved 33 amino acid long intramembrane domain (residues 102-135 in caveolin-1) that has been postulated to form an unusual re-entrant loop within the hydrophobic core of the lipid bilayer resulting in a cytoplasmic location for both the N- and C- termini [42,66,71,74]. The position of this loop within the intramembrane domain of caveolin-1 was suggested to be comprised of four amino acids located at positions 108-111 based on primary sequence analysis [66].

In Chapter 3, nuclear magnetic resonance spectroscopy (NMR) experiments performed on a caveolin-1 construct containing the entire intramembrane domain and the N-terminal flanking region (residues 82-136) revealed that the secondary structure of this region was comprised of two helices, each containing ~20 amino acids (residues 87-107 and residues 111-128) separated by a three residue break in helicity (residues 108-110) [208]. The three amino acids in the unstructured region are glycine 108, isoleucine 109, and proline 110 and are thought to form a re-entrant loop structure. Mutagenesis experiments employing NMR revealed that the identities of the amino acids in this region were critical to the caveolin-1 structure [70]. It was found that positions 108 and 109 could only tolerate conservative amino acid substitutions and that proline at position 110 appeared to be central to maintaining the proper structuring of the protein. Based on this result, it has been postulated that P110 is a critical residue for forming the hallmark intramembrane loop configuration. However, the exact nature of the disruption following P110 mutation could not be inferred from analysis of the NMR spectra alone.

Interestingly, the degree of α-helical character in the 82-101 region has been disputed. Some studies have suggested that there may be a propensity for anti-parallel β-strand formation in the 84-94 region of the protein [31]. When residues 76-109 of caveolin-1 were examined using Fourier transform infrared spectroscopy, circular dichroism spectroscopy, and solid-state NMR, it was shown that substantial portions of the protein remained non-helical in the presence of cholesterol [69]. The β-strand character was observed specifically in the region of alanine 87 to lysine 96, with the 99-109 region showing α-helical character. However, no insight was given in how this change in the secondary structure would play into caveolin's topology.

A number of investigations that attempted to shed light on the role of the conserved proline on the structure and topology of caveolin-1 have used a proline 110 to alanine mutant (P110A). An *in vivo* immuno-fluorescence study performed on an N-terminally FLAG-tagged caveolin-1 construct showed that wild-type caveolin-1 could not bind FLAG-antibodies unless the cells were permeabilized [77]. However, upon the P110A mutation, FLAG-antibody binding was observed in non-permeabilized cells. This study indicated that a topological change occurred but, only the location of the N- terminus was probed. Therefore, it was not clear whether this change was due to the linearization of the peptide (one long transmembrane helix) or a less dramatic orientation change (N- and C- termini both oriented extracellularly). Interestingly, this study also indicated that the P110A impacts the protein functionally as the mutant could not form caveolae. In the same study, the effect of the P110A mutation on a truncated intramembrane construct (residues 94-122) embedded in a lipid bilayer was evaluated using molecular dynamics simulations and supported a linear conformation for the mutant protein. A tryptophan

fluorescence study that employed truncated wild-type and P110A N- and C-terminally lysinated intramembrane-domain constructs (residues 103-122) reconstituted into vesicles showed that the mutant was less solvent accessible than the wild-type protein. However, these constructs were soluble in the absence of lipid mimics, did not contain the entire intact intramembrane domain, and included more than a single tryptophan. Therefore the data were unable to give conclusive information pertaining to structural and topological changes that occurred upon the mutation [75]. Additionally, an *in vitro* study employing a full-length caveolin-1 construct containing two glycosylation sites at both the N- and C-termini reconstituted into dog pancreas microsomes showed that neither the wild-type or the P110A mutant could be glycosylated, pointing to a cytoplasmic disposition for the termini [76]. This result showed that wild-type and mutant constructs had the same orientation; casting doubt on the over-arching role that proline had been posited to play in determining caveolins configuration. However, the interpretation of these data was based on a negative result, and therefore conclusions from these experiments must be taken with pause because not all sequences containing a glycosylation epitope are necessarily glycosylated. Clearly, there is still a need to address the role that proline plays in modulating the structure and topology of caveolin-1.

Although chapter 4 indicated that a closely related cholesterol mimic (CHS) increases the exposure of the CSD by one helical turn, the results could not differentiate if the change was related to the presence of the sterol or the negative charge of the molecule. Additionally, the study does not indicate how other portions of the protein that are predicted to be membrane embedded (residues 112-134) would change in response to the sterol. There have been attempts to gain insight into how cholesterol may play into

caveolin topology. In a study by Epand et al utilizing small peptidic mimics of residues in the 83-101 region reconstituted into POPC or POPC/Cholesterol (1:1) multilamellar vesicles, it was found that these peptides showed a deeper position within the membrane when cholesterol was present [159]. Conversely, in another study by Aoki et al, a lysinated caveolin analogue containing half the intramembrane domain (residues 103-122 flanked by four and five lysine residues at the N- and C- termini respectively) reconstituted into POPC/DPPC/Cholesterol 1:1:1 vesicles showed higher accessibility to the collisional quencher acrylamide compared to when it was reconstituted into vesicles composed purely of POPC. A molecular dynamics study of caveolin-1 residues 94-122 embedded in various bilayer types attempted to reconcile the topological difference in response to the sterol by providing evidence that the depth of tryptophan residues was more affected by the removal of cholesterol from DPPC bilayers than they were from POPC bilayers [46]. Nonetheless, it remains to be shown how a longer construct of caveolin-1 containing the entire intramembrane domain and flanking regions would respond to the presence of the sterol.

The importance of the proline at position 110 and cholesterol represent two key topological parameters that haven't been addressed in the context of a caveolin-1 construct that accurately captures the essence of the full-length protein. In this chapter, a functional caveolin-1 construct (traffics correctly to caveolae *in vivo*) containing residues 62-178 ($Cav1_{62-178}$) was employed to probe structural and accessibility differences between the wild-type and the P110A mutant reconstituted into dodecylphosphocholine (DPC) micelles and DPC:cholesterol-PEG600 (a cholesterol analog) micelles [145]. Circular dichroism measurements in the far and near UV regions indicated a preservation

of secondary structure but a major change in the tertiary fold between the wild-type and mutant construct. These studies also indicated a possible increase in β-strand character when the protein was in DPC:cholesterol-PEG600 micelles. The fluorescence properties of the four native tryptophan residues in caveolin-1 (W85, W98, W115, and W128), which are exquisitely evenly spaced throughout the structural core of the protein, were used advantageously to shed light on the exposure of the intramembrane domain upon the P110A mutation and cholesterol-PEG600 inclusion. The tryptophan residues in both wild-type and the P110A mutant were probed in aggregate by examining tryptophan λ_{max} of emission and fluorescence quenching and did not indicate dramatic changes in accessibility were occurring upon proline replacement. In contrast, the inclusion of cholesterol-PEG600 into the micelles caused major changes in the accessibility of $Cav1_{62\text{-}178}$. To definitively and precisely evaluate the specific modulation of the local tryptophan environments by the P110A mutation and inclusion of the sterol into micelles, four single tryptophan mutant constructs were generated for both the wild-type and P110A $Cav1_{62\text{-}178}$ for a total of 8 constructs. The conformation and secondary structure of each was probed using CD spectroscopy in the near and far ultraviolet regions and the exposure of each was probed using λ_{max} and Stern-Volmer quenching analysis. Near and far UV circular dichroism experiments on the mutants indicated that there were slight changes in the tryptophan packing environment but the secondary structure was largely maintained between the wild-type and the P110A single tryptophan mutants. Fluorescence studies indicated that modest changes in the local environment of tryptophan residues at positions 85, 98, and 115 occurred upon the mutation of P110A, with tryptophans within the center of the intramembrane domain becoming more shielded

from the aqueous environment. These findings show that the P110A mutation leads to significant alterations in the fold and minor changes in the aqueous accessibility of caveolin-1. On the other hand, the same suite of studies performed on single tryptophan mutants (WT and P110A) in the presence of the sterol indicated that minor changes occurred in the protein's fold but major changes were observed in the local accessibility of the protein to iodide. Additionally, a fluorescence resonance energy transfer (FRET) experiment looking at how the distance between a dansyl moiety covalently attached at position 133 and all four tryptophan residues in aggregate changed in response to the sterol. The FRET study supported the near UV CD studies that indicated cholesterol-PEG600 causes a minor change in the conformation of caveolin-1.

MATERIALS AND METHODS

Protein Expression and Purification

DNA for wild-type $Cav1_{62-178}$, was synthesized by Genscript Corporation (Piscataway, NJ). Caveolin-1 has three native cysteines that are palmitoylated *in vivo* (C133, C143, C156), and these residues were shown to be not critical to caveolin-1 trafficking to caveolae [35]. Therefore, these sites were mutated to serine to avoid unwanted disulfide bond formation. The $Cav1_{62-178}$ gene was cloned, over-expressed, and purified according to previously reported protocols (See chapter 2) [146]. After purification using high performance liquid chromatography, the identity of the protein was confirmed using MALDI-TOF mass spectrometry. Next, purified $Cav1_{62-178}$ was aliquoted and lyophilized using protocols described by Rieth et al [43]. Mutant constructs were prepared using the Agilent Quik change mutagenesis kit (Santa Clara, CA) for a total of ten constructs (see Appendix 2-3 for PCR conditions). For labeling of the protein with dansyl aziridine which reacts specifically with cysteines, a construct was generated where S133 was changed to the native cysteine ($Cav1_{62-178}$(C133)). $Cav1_{62-178}$ contains four tryptophan residues: W85, W98, W115, and W128 that can be used to explore the exposure of the protein along the sequence. For single tryptophan mutants, one of the four native tryptophan residues was retained and the other three were mutated to phenylalanine to generate the following constructs: $Cav1_{62-178}$(W85), $Cav1_{62-178}$(W98), $Cav1_{62-178}$(W115), and $Cav1_{62-178}$(W128). Additionally proline 110 of $Cav1_{62-178}$ was mutated to alanine for wild-type and each of the four single tryptophan mutants to generate the following constructs: $Cav1_{62-178}$ P110A, $Cav1_{62-178}$(W85) P110A, $Cav1_{62-178}$(W98) P110A, $Cav1_{62-178}$(W115) P110A, and $Cav1_{62-178}$(W128) P110A (see

Appendices 5-1 and 5-2 for construct sequences and mutagenesis primers respectively). Unless otherwise noted, all mutants were expressed and purified according to protocols described in Chapter 2.

Labeling of Cav1$_{62-178}$(C133) with Dansyl Aziridine

For purification of Cav162-178(C133), the protocol described by Diefenderfer et al was employed with some minor differences [146]. Cav1$_{62-178}$(C133) was purified by nickel-NTA chromatography by first dissolving the post Triton-X-100 pellet in a binding buffer comprised of 8% (*w/v*) PFOA, 0.5 mM TCEP, 50 mM phosphate pH 8.0, washing the bound protein with a buffer comprised of 1% (*w/v*) PFOA, 0.5 mM TCEP, and 50 mM phosphate pH 8.0. The protein was eluted with a buffer comprised of 1% (*w/v*) PFOA, 250 mM imidazole, 0.5 mM TCEP, and 50 mM phosphate pH 8.0. The eluted protein was quantified by measuring the absorbance at 280 nm and then rapidly desalted using sephadex G-25 resin equilibrated with a buffer containing 1% PFOA (*w/v*), 50 mM phosphate pH 8.0. The desalted protein was then treated with a 50 fold molar excess of dansyl aziridine (generously synthesized by Dr. Larry Courtney, dissolved in DMOS at 100 mg/mL). The solution was then covered in foil and was allowed to react for 18 hours. Excess dansyl aziridine was quenched by the addition of β-mercaptoethanol added to a concentration of 10 mM. The protein was then precipitated by dialysis against 20 L of 50 mM ammonium sulfate. The precipitate was then subjected to cyanogen bromide cleavage, purified using reverse phase HPLC, and aliquoted out of HFIP [146]. The percent labeling of the protein was estimated by measuring the absorbance at 340 nm (dansyl peak absorbance) using an extinction coefficient of 3980 $M^{-1}cm^{-1}$ for dansyl and the

absorbance at 280 nm for the protein (22% of the dansyl absorbance at 340 nm was subtracted from the absorbance at 280 nm to account for its lower wavelength absorption) [217,218]. Only 100% labeled material was utilized for fluorescence resonance energy transfer experiments. The protein was reconstituted as described in proceeding sections.

Protein Reconstitution

To 1.2 mg of lyophilized $Cav1_{62-178}$, 3 mL of ice-cold buffer comprised of 20 mM phosphate pH 7.0, 100 mM NaCl, and 50 mM DPC (Anatrace, Maumee, OH) was added to reconstitute the protein to a final protein concentration of 30 μM. After vortex mixing until clarification, each sample was filtered using a 0.2 μm filter to remove particulates. All mutants were reconstituted in an identical manner.

For samples containing cholesterol-PEG600 (Sigma Aldrich, St. Louis, MO), $Cav1_{62-178}$ constructs were first dissolved into HFIP at a concentration of 2 mg/mL. A 1.2 mg quantity of protein was added to a 3 mL solution of 60 mM phosphate pH 7.0, 300 mM NaCl, 60 mM cholesterol-PEG600, and 90 mM DPC. The HFIP concentration was adjusted to 50% (*v/v*) and the solution was lyophilized over night. The solution was then rehydrated and subsequently lyophilized for 15 hours to remove all traces of HFIP. The powder was then taken up into 9 mL of H_2O to yield a solution which was 20 mM phosphate pH 7.0, 100 mM NaCl, and 20 mM cholesterol-PEG600 and 30 mM DPC for a final protein concentration of 30 μM. This solution was then reconstituted by incubation on ice for 1-2 hours with occasional gentle mixing. The solutions were filtered through a 0.2 μm filter before use.

Far and Near UV Circular Dichroism Spectroscopy

Circular dichroism experiments were performed using a JASCO circular dichroism spectrophotometer (Easton, MD). The experiments were carried out at 298 K using a quartz cuvette with a 0.1 mm path length and a 1 cm path length for far and near UV experiments respectively.

For far UV experiments, spectra were obtained from 260 to 190 nm with a 1 nm data point interval in step mode accumulating 16 scans. For near UV experiments, spectra were obtained from 350 to 250 nm with a 0.5 nm data point interval in step mode accumulating 16 scans. In each case, a background spectrum of buffer without reconstituted $Cav1_{62\text{-}178}$ was subtracted from the protein containing spectra. Circular dichroism experiments were performed for $Cav1_{62\text{-}178}$ and $Cav1_{62\text{-}178}$(P110A) constructs twice. For far UV experiments, machine units (θ) were converted to mean residue ellipticity [θ] using the following equation:

$$[\theta] = \theta \times \frac{(0.1 \times MRW)}{(P \times C)}$$

Here, MRW is the mean residue weight (protein MW/number of residues in the protein), P is the path length in cm, and C is the protein concentration in mg/mL yielding units of $deg \times cm^2 \times dmol^{-1}$. Far UV spectra were decomposed to reveal their secondary structure characteristics using the CDSTR algorithm with basis set 7 (optimized for 240-190 nm wavelength range) in dichroweb [224]. For near UV experiments, machine units (θ) were converted to mean protein ellipticity [θ] using the following equation:

$$[\theta] = \theta \times \frac{(0.1 \times MW)}{(P \times C)}$$

Here, MW is the molecular weight of the protein, P is the path length in cm, and C is the protein concentration in mg/mL yielding units of deg×cm^2×dmol^{-1}.

Tryptophan λ_{max} Determination and Fluorescence Quenching

Steady-state fluorescence emission spectra were acquired at 298 K with an Eclipse fluorometer (Agilent, Santa Clara, CA) using a 1 × 1 quartz cuvette. The excitation wavelength chosen was 295 nm which selectively excites tryptophan residues [127]. Both excitation and emission slits were set to 5 nm. The emission spectrum was measured from 315-500 nm with a scan speed of 1 nm/s and 0.5 nm data point increments, averaging four scans. The λ_{max} values for all constructs used in the study were determined by fitting the data to a log-normal distribution using Igor Pro 6.22A (WaveMetrics, Inc., Lake Oswego, OR) [133]. The error in λ_{max} values were assigned from the average of separate reconstitution experiments and was roughly ± 1 nm.

Fluorescence quenching experiments were performed directly after λ_{max} determinations utilizing a kinetic mode of data acquisition. First, freshly prepared dithiothreitol was added to a final concentration of 1 mM. The sample was then continuously excited at the 295 nm wavelength and the fluorescence intensity at the λ_{max} of emission was monitored at a rate of 1 measurement/s. Initially the sample's fluorescence intensity was monitored for 3 minutes to ensure the sample was at equilibrium and accurately determine the unquenched intensity. After this time period, an 18 µL aliquot of 20 % (*w/w*) potassium iodide in 1 mM dithiothreitol was added to 2.58 mL of reconstituted Cav1$_{62\text{-}178}$ and the intensity was monitored for one minute before the next addition of quencher. Addition of the quencher was repeated to obtain

quenching data in the 10-100 mM range. Intensity averages at each potassium iodide concentration were fit to the modified Stern-Volmer equation to determine tryptophan fractional accessibilities [127].

$$\frac{I_0}{I_0 - I} = \frac{1}{f_a K_a [Q]} + \frac{1}{f_a}$$

All fluorescence experiments were repeated three times for the following constructs, $Cav1_{62\text{-}178}$, $Cav1_{62\text{-}178}$(W85), $Cav1_{62\text{-}178}$(W98), $Cav1_{62\text{-}178}$(W115), $Cav1_{62\text{-}178}$(W128), $Cav1_{62\text{-}178}$(P110A), $Cav1_{62\text{-}178}$(P110A/W85), $Cav1_{62\text{-}178}$(P110A/W98), $Cav1_{62\text{-}178}$(P110A/W115), and $Cav1_{62\text{-}178}$(P110A/W128).

Fluorescence Resonance Energy Transfer Experiments

The samples were diluted to the same concentration (~30 μM) using either a buffer comprised of 20 mM phosphate pH 7.0, 100 mM NaCl, and 50 mM DPC or 20 mM phosphate pH 7.0, 100 mM NaCl, and 20 mM cholesterol-PEG600 and 30 mM DPC. Steady-state fluorescence emission spectra were acquired at 298 K with an Eclipse fluorometer (Agilent, Santa Clara, CA) using a 1 × 0.1 cm quartz cuvette. The excitation wavelength chosen was 295 nm which selectively excites tryptophan residues [127]. Both excitation and emission slits were set to 2.5 nm. The emission spectrum was measured from 315-595 nm with a scan speed of 1 nm/s and 0.5 nm data point increments, averaging ten scans. Three experiments were performed for both micellar environments. Intensities at the λ_{max} were used directly for fluorescence resonance energy transfer efficiency determination in equation 1-6:

$$E = 1 - \frac{F_{DA}}{F_D}$$

For the distance calculation, an R_0 of 21 Å [127] for the tryptophan-dansyl pair was utilized in equation 1-7:

$$E = \frac{R_0^6}{R_0^6 + r^6}$$

RESULTS AND DISCUSSION

Construct Design and Protein Reconstitution

In order to characterize the structural and accessibility changes occurring upon the caveolin-1 P110A mutation, a construct that encompassed residues 62-178 ($Cav1_{62-178}$) was chosen. This portion of the protein was selected because it has been shown to capture the behavior of the full-length protein in terms of trafficking to caveolae [145]. Therefore, the structural core that is critical for the protein's function is intact in the $Cav1_{62-178}$ construct. In order to exhaustively characterize accessibility changes imparted by the P110A mutation along the sequence of the protein, single tryptophan mutants of the four native tryptophan residues in caveolin-1 were generated for both the wild-type and the mutant construct for a total of 8 mutants. Importantly, the tryptophan residues are reasonably spaced across the intramembrane domain (roughly every 14 amino acids from residues 85-128), providing complete coverage of the environment that the structural core of the protein experiences. In each of these constructs, one tryptophan was maintained while the others were mutated to phenylalanine. Phenylalanine was chosen because of its similarity to tryptophan in terms of hydrophobicity and size. All constructs were reconstituted in DPC micelles. DPC micelles were chosen because they are native-like and have been widely utilized in biophysical studies of membrane proteins (For chemical structure see Figure 1-11) [219-222]. To determine how the protein would change conformation in response to the inclusion of cholesterol, a detergent-like cholesterol mimic was utilized (cholesterol-PEG600) (Figure 5-1) as pure cholesterol has poor micelle solubility. This molecule was chosen because it can be incorporated at 40%

by mol within the micelle, which is the concentration of cholesterol natively found within caveolae. Additionally, this reagent, like cholesterol, is not charged.

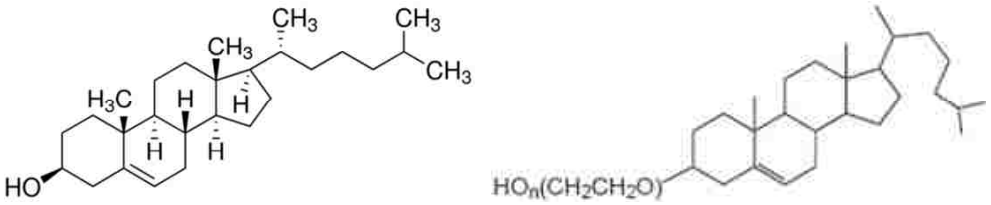

Cholesterol **Cholesterol-PEG600**

Figure 5-1. Comparison of cholesterol and cholesterol-PEG600. The PEG moiety allows for a high degree of cholesterol incorporation into micelles. The mass that the PEG unit adds to cholesterol is roughly 600D on average.

Far and near UV Circular Dichroism Spectroscopy

Circular dichroism spectroscopy was used to compare the secondary and tertiary structural changes that occur upon the P110A mutation. Figure 5-2 shows the far UV circular dichroism spectra for $Cav1_{62-178}$ and $Cav1_{62-178}$(P110A) constructs. When reconstituted into DPC, the far UV spectra of both the wild-type and mutant protein had a very similar appearance and showed two distinct minima at 208 and 222 nm, which is a signature of α-helical secondary structure. However, a close examination of the spectra indicated that there may be a slight increase in helicity upon the P110A mutation (~15%, see table 5-1) [223]. This small increase could be due to the turn region becoming helical as alanine does not have the helix-breaking properties of proline [224,225]. Therefore, the loss of proline does not result in a major change in the secondary structure of caveolin-1, as its mutation to alanine only resulted in slight changes to the far UV circular dichroism spectra. All single tryptophan mutants were also examined. In DPC micelles, the secondary structures of the single tryptophan mutants compared nicely to that of the constructs where all four tryptophans were present as α-helical character was the major

contributor to the secondary structure (Figure 5-2, Table 5-1). Interestingly, in some of the single tryptophan mutants made for the wild-type construct, increased α-helical character was observed relative to the wild-type that was of the same magnitude as the increase caused by the P110A mutation. However, it appeared that the increase in helicity for the P110A mutant was more consistent, as the percentage of helicity between P110A mutants had a much smaller error (60 ± 1%) than that for wild-type mutants (54 ± 8%).

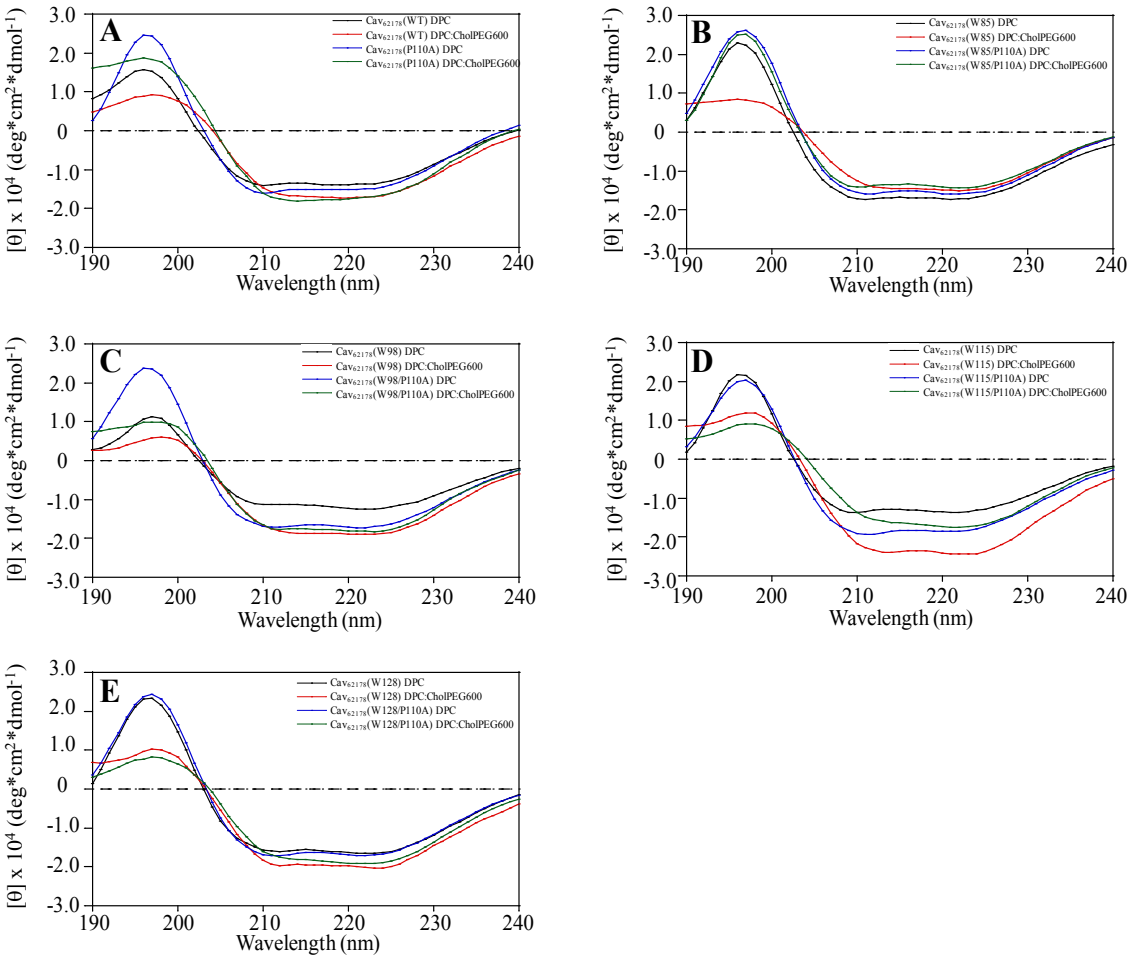

Figure 5-2. Comparison of far UV circular dichroism spectra of $Cav1_{62\text{-}178}$ constructs reconstituted in DPC micelles (*black*) or DPC:cholesterolPEG600 micelles (*red*) and $Cav1_{62\text{-}178}$ P110A constructs reconstituted into DPC micelles (*blue*) or DPC:cholesterolPEG600 micelles (*green*). Panels **A-E** represent $Cav1_{62\text{-}178}$ constructs with all tryptophans present, W85 present, W98 present, W115 present, and W128 present respectively. The value [θ] is calculated for the mean residue ellipticity.

Comparison of the different micelle environments also indicated that there was little difference between the protein reconstituted into DPC or DPC:CholesterolPEG600 micelles. Morphologically, the CD spectra of cholesterolPEG600 samples always had somewhat less defined minima (208 and 222 nm) and maxima (195 nm). This could be due to the appearance of β-strand character which has a minima at 215 nm and a less intense maxima at 195. Analysis of the spectra using dichroweb indicated that there was

on average about 19.0 ± 2.0% β-strand character for $Cav1_{62-178}$ constructs reconstituted into DPC:CholesterolPEG600 micelles versus 11.0 ± 3.0% β-strand character for $Cav1_{62-178}$ constructs reconstituted into micelles composed of DPC only. It appears that there is a statistically significant increase in the amount of β-strand character, in agreement with studies by others who have suggested that the sterol modifies caveolin's secondary structure. The increase was also observed when comparing $Cav1_{62-178}$ P110A constructs in the different micelle environments (Table 5-1). Therefore it appears that the DPC:cholesterol-PEG600 micelle increases β-sheet character for the constructs used in this study. More data will be required to definitively prove where this increase is localized, as dichroweb can only give a very rough estimate of such structural data.

Construct and Micelle System	α-Helix (%)	β-Strand (%)	Turns (%)	Disordered (%)
$Cav1_{62-178}$ Wild-Type (DPC)	0.45	0.13	0.17	0.25
$Cav1_{62-178}$ Wild-Type (DPC:Cholesterol-PEG600)	0.48	0.22	0.12	0.17
$Cav1_{62-178}$ P110A (DPC)	0.59	0.12	0.18	0.12
$Cav1_{62-178}$ P110A (DPC:Cholesterol-PEG600)	0.49	0.20	0.12	0.20
$Cav1_{62-178}$(W85) (DPC)	0.60	0.10	0.14	0.16
$Cav1_{62-178}$(W85) (DPC:Cholesterol-PEG600)	0.43	0.20	0.17	0.20
$Cav1_{62-178}$(W85) P110A (DPC)	0.60	0.10	0.16	0.14
$Cav1_{62-178}$(W85) P110A (DPC:Cholesterol-PEG600)	0.59	0.08	0.21	0.11
$Cav1_{62-178}$(W98) (DPC)	0.44	0.14	0.2	0.22
$Cav1_{62-178}$(W98) (DPC:Cholesterol-PEG600)	0.51	0.19	0.13	0.16
$Cav1_{62-178}$(W98) P110A (DPC)	0.62	0.09	0.14	0.15
$Cav1_{62-178}$(W98) P110A (DPC:Cholesterol-PEG600)	0.49	0.21	0.14	0.16
$Cav1_{62-178}$(W115) (DPC)	0.57	0.07	0.21	0.15
$Cav1_{62-178}$(W115) (DPC:Cholesterol-PEG600)	0.57	0.18	0.11	0.13
$Cav1_{62-178}$(W115) P110A (DPC)	0.61	0.12	0.15	0.14
$Cav1_{62-178}$(W115) P110A (DPC:Cholesterol-PEG600)	0.51	0.21	0.15	0.13
$Cav1_{62-178}$(W128) (DPC)	0.61	0.09	0.15	0.15
$Cav1_{62-178}$(W128) (DPC:Cholesterol-PEG600)	0.53	0.16	0.15	0.16
$Cav1_{62-178}$(W128) P110A (DPC)	0.59	0.12	0.14	0.14
$Cav1_{62-178}$(W128) P110A (DPC:Cholesterol-PEG600)	0.49	0.23	0.13	0.15
AVG $Cav1_{62-178}$ (DPC)	0.54 ± 0.08	0.11 ± 0.03	0.17 ± 0.03	0.19 ± 0.05
AVG $Cav1_{62-178}$ (DPC:Cholesterol-PEG600)	0.50 ± 0.05	0.19 ± 0.02	0.14± 0.02	0.16 ± 0.03
AVG $Cav1_{62-178}$ P110A (DPC)	0.60 ± 0.01	0.11 ± 0.01	0.15 ± 0.02	0.14 ± 0.03
AVG $Cav1_{62-178}$ P110A (DPC:Cholesterol-PEG600)	0.51 ± 0.04	0.19 ± 0.06	0.15 ± 0.04	0.15 ± 0.03

Table 5-1. Percentages of different secondary structure components for each mutant from Dichroweb analysis. Averaged values show that the secondary structure between different mutants is very similar and that the type of micelle is important in determining the amount of β-strand character.

Near UV circular dichroism, which gives information about the unique environment that phenylalanine (255-270 nm), tyrosine (275-282 nm), and tryptophan (290-305 nm) are sampling, was used to examine differences in the tertiary fold between the wild-type and mutant proteins [126]. When all tryptophans were present in aggregate, the appearance of the near UV circular dichroism spectra for wild-type and P110A mutant proteins in DPC micelles were very different, especially in the 290-305 nm region (Figure 5-3). There is a large negative peak centered on 298 nm that was not present for $Cav1_{62-178}$ but was observed for $Cav1_{62-178}$(P110A). The spectra also differed somewhat in their magnitude but had a similar morphology in the 285-250 nm region. Although tryptophan and tyrosine overlap significantly in this region, there are no mutations to tyrosine residues; therefore, the decrease in signal in this region could indicate changes in tryptophan packing. These differences indicate that the structure of the protein has changed. Therefore it is plausible that the mutation of P110A has decreased helical packing within the transmembrane region. Additionally, the appearance of the large negative peak in the near UV spectrum of $Cav1_{62-178}$(P110A) is indicative of a dramatic environmental change around one or more of the four tryptophan residues. To try to link these changes to a particular tryptophan residue, each single tryptophan mutant was examined using near UV circular dichroism.

Interestingly, when comparing the $Cav1_{62-178}$ and $Cav1_{62-178}$(W85) spectra, it appears that W85 contributes strongly to the peak centered on 290 nm, implicating this tryptophan in being in a unique fold of the protein. When examining the single tryptophan mutants in which P110 is present the spectra always have a larger signal in the 295-275 nm region. The most significant case of this change is in comparing $Cav1_{62-}$

$_{178}$(W98) and Cav1$_{62\text{-}178}$(W98) P110A. In the Cav1$_{62\text{-}178}$(W98) spectrum the CD signal increases over the 290-270 region whereas in the Cav1$_{62\text{-}178}$(W98) P110A spectrum the CD signal decreases dramatically. In chapter 3, W98 was observed to be on the face of helix-1 that would be involved in helix-helix packing with helix-2. Therefore, the change in the morphology of the Cav1$_{62\text{-}178}$(W98) P110A far UV trace could reflect alterations in this interaction. All other single tryptophan mutant traces looked similar in terms of their morphology between the wild-type and P110A mutants. Curiously, the large negative peak that appeared at 298 nm in the Cav1$_{62\text{-}178}$ P110A spectrum could not be linked to any of the single tryptophan mutants. This observation possibly implicates a unique tryptophan-tryptophan interaction within the P110A mutant. Proline is a special amino acid in terms of its structural effect on proteins as it has a narrow range of obtainable Φ and Ψ angles on the Ramachandran plot. Therefore, the replacement of this residue with an alanine greatly opens the allowed number of Φ and Ψ angle combinations around the turn region. This less stringent angle around position 110 may result in different rotations of either of the helical regions within the structural core of the protein. A change in the rotation of the helical regions would result in a different environment for amino acids around and within them, and explains the differences observed in the near UV circular dichroism plot. Regardless of the nature of the structural change, it is evident that proline 110 plays an important role in maintaining the proper fold of the protein.

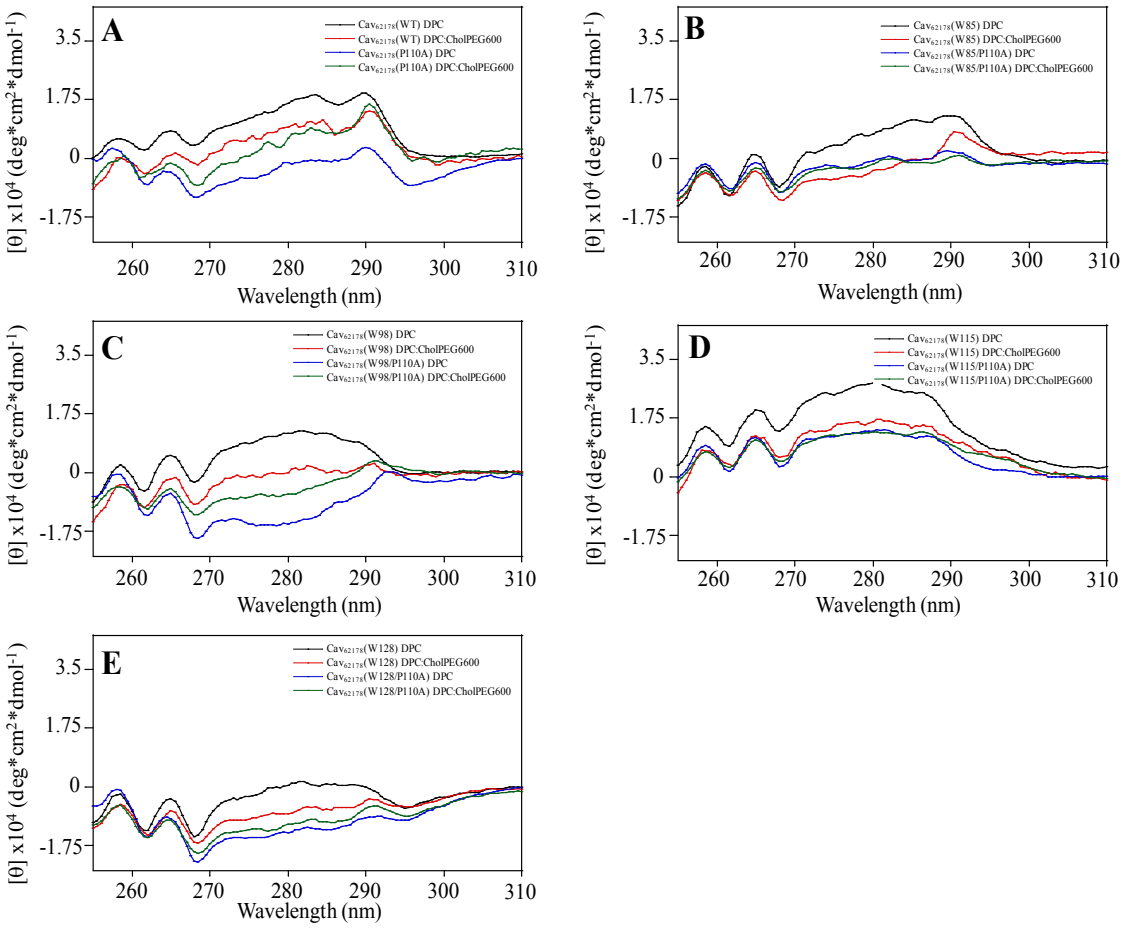

Figure 5-3. Comparison of near UV circular dichroism spectra of Cav1$_{62\text{-}178}$ constructs reconstituted in DPC micelles (*black*) or DPC:cholesterolPEG600 micelles (*red*) and Cav1$_{62\text{-}178}$ P110A constructs reconstituted into DPC micelles (*blue*) or DPC:cholesterolPEG600 micelles (*green*). Panels **A-E** represent Cav1$_{62\text{-}178}$ constructs with all tryptophans present, W85 present, W98 present, W115 present, and W128 present respectively. The value [θ] is calculated for the mean protein ellipticity.

Examination of the differing micelle environments shows that the inclusion of cholesterol-PEG600 caused a decrease in the intensity of the near UV circular dichroism spectra but does not significantly change the morphology compared to DPC only micelles for both wild-type and P110A spectra when all tryptophan residues are present (Figure 5-3). In agreement with the observation that W85 contributes strongly to the signal positioned around 290 nm, this peak is very strong in the case of the Cav1$_{62\text{-}178}$(W85)

spectrum. This lack of dramatic changes in the near UV spectra leads to the conclusion that cholesterol may not change the conformation of caveolin significantly around the tryptophan groups. The lack of appearance of any "new" peaks likely indicates that cholesterol would not be locked in place through a specific interaction; such has been suggested to occur between cholesterol and the 94-101 region of the protein. This finding corroborates simulation studies which failed to see a specific cholesterol packing interface [46]. This also downplays the increased β-strand character in having a role in changing the conformation of the protein.

Tryptophan λ_{max} Determination and Fluorescence Quenching: Comparison of $Cav1_{62-178}$ and $Cav1_{62-178}$ P110A Constructs

The tryptophan residues native to $Cav1_{62-178}$ can act as reporters of solvent exposure by analyzing their fluorescence emission maximum (λ_{max}) [133]. Analysis of the change in λ_{max} ($\Delta\lambda_{max}$) can be used to compare the degree of aqueous exposure between $Cav1_{62-178}$ mutants and different micellar environments (here $\Delta\lambda_{max}$ will be from the reference point of going from the wild-type to the P110A mutant, or going from DPC to DPC:cholesterol-PEG). Generally, a blue shift in the λ_{max} value is indicative of greater membrane burial or tertiary structure associated shielding from the aqueous environment [130,134-136]. In these studies, a negative value of $\Delta\lambda_{max}$ will be indicative of a blue shift (decrease in accessibility) and a positive value of $\Delta\lambda_{max}$ will be indicative of a red shift (increase in accessibility) compared to the reference point. Steady-state Fluorescence emission spectra for all constructs used in the study in both DPC and DPC:cholesterolPEG600 micelles are shown in figure 5-4.

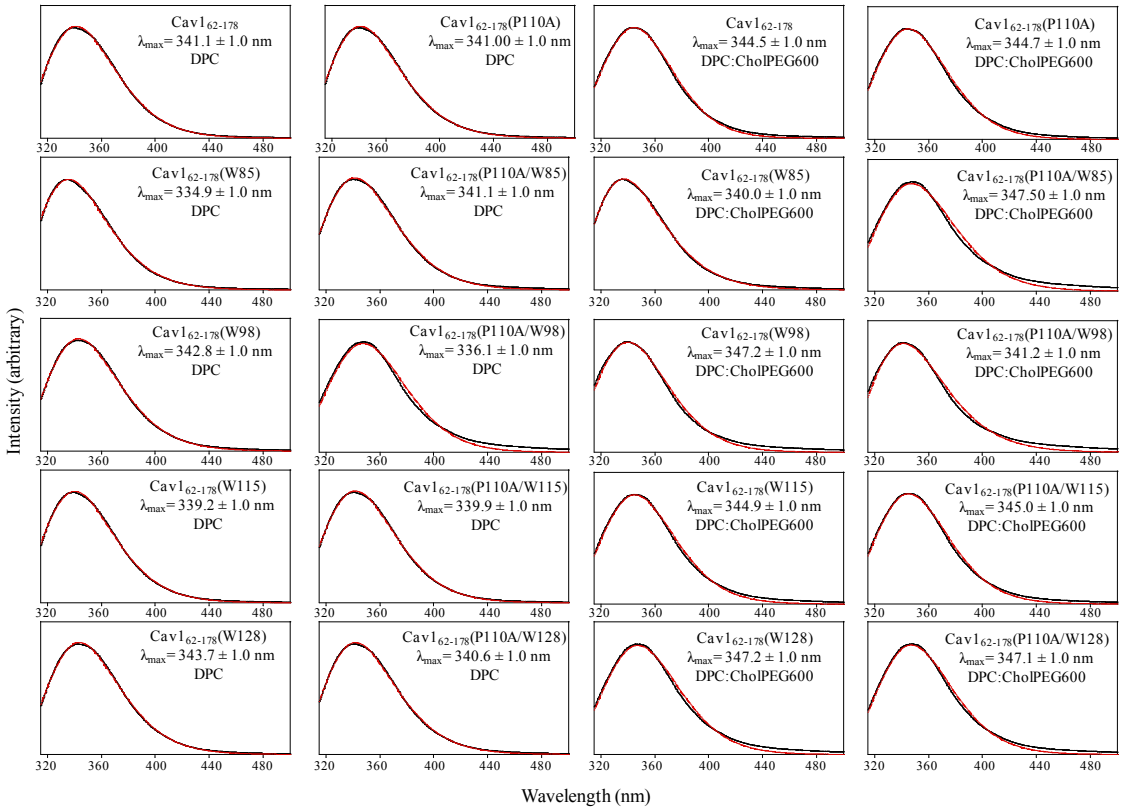

Figure 5-4. Steady state tryptophan emission profiles for $Cav1_{62\text{-}178}$ and $Cav1_{62\text{-}178}$ P110A constructs in DPC or DPC:cholPEG600 micelles. Raw data (*black*) and fits (*red*) are indicated. Fits were used to obtain λ_{max} values, hence determining the wavelength that would be monitored for fluorescence quenching experiments. Experiments were repeated three times to ensure λ_{max} values were consistent. An error of ± 1 nm was assigned to all peaks as this reflected the variance in different preparations.

To further probe accessibility changes upon the P110A mutation of caveolin-1, tryptophan fluorescence quenching experiments employing iodide were performed [127]. Quenching of tryptophan fluorescence by the soluble quencher iodide is greater for residues that are exposed to the aqueous environment (large fractional accessibility, f_a) than for those buried within a membrane. Modified Stern-Volmer quenching curves for all constructs utilized in the study in both DPC and DPC:cholesterol-PEG600 micelles are shown in figure 5-5. Importantly, quenching experiments add a second technique that

can compare and contrast with λ_{max} information, which can be subject to influences from the local environment of the tryptophan residue (i.e. polarity of neighboring residues, degree of hydrogen bonding available in the environment) and not necessarily differences in aqueous exposure. Similar to $\Delta\lambda_{max}$ analysis, Δf_a values can be used to compare differences in the exposure due to environment or mutation (Here, Δf_a will be from the reference point of going from the wild-type to the P110A mutant, or going from DPC to DPC:cholesterol-PEG). In these studies, a negative Δf_a will be indicative of a more shielded environment and a positive Δf_a will be indicative of a less shielded environment than the reference point.

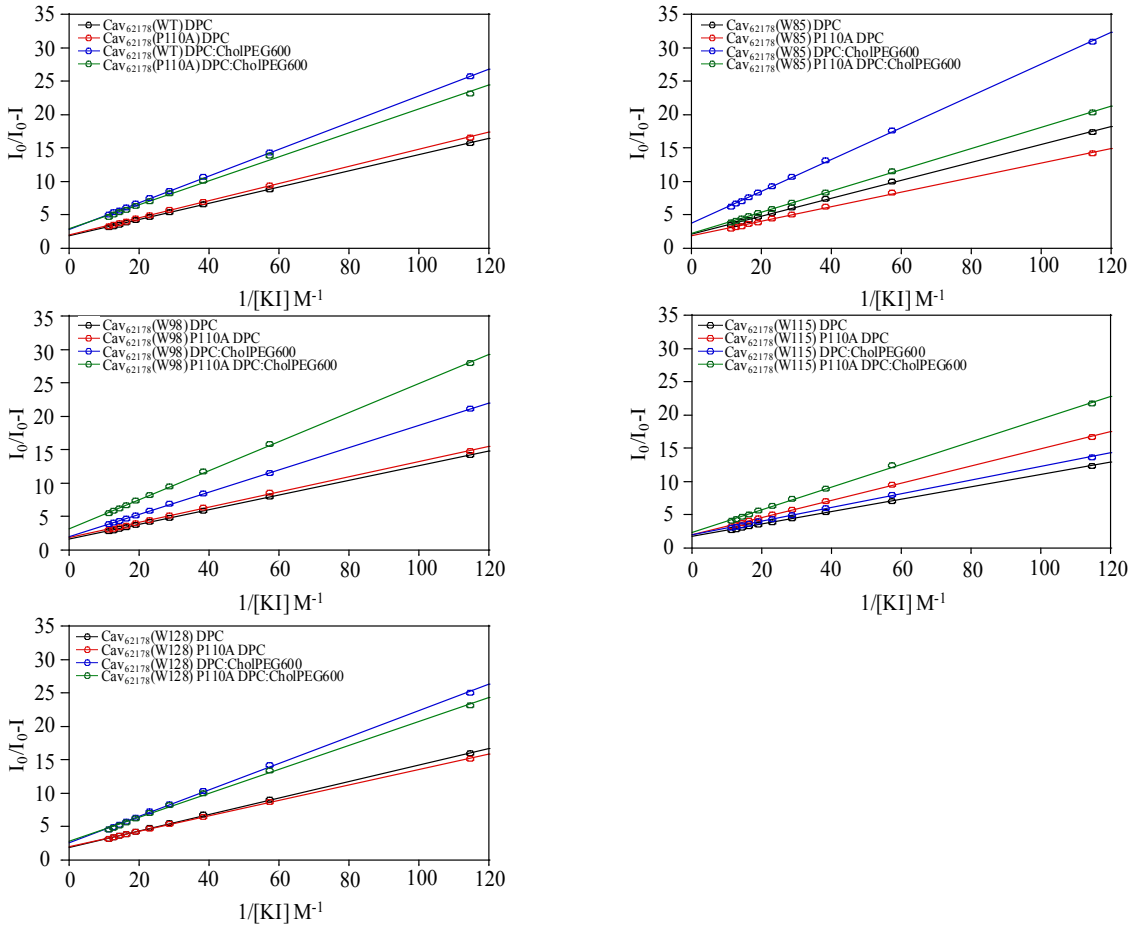

Figure 5-5. Representative modified Stern-Volmer quenching curves for all Cav1$_{62\text{-}178}$ constructs. Plots showed very linear behavior and extrapolation to the y-intercept yielded f_a values.

Both wild-type and the P110A mutant that contained all tryptophans were probed to determine if there were major changes in accessibility between constructs. Analysis of both Cav1$_{62\text{-}178}$ and Cav1$_{62\text{-}178}$ P110A emission spectra yielded λ_{max} values of 341 nm ($\Delta\lambda_{max}=0$), indicating that in aggregate, the tryptophan residues appeared to be sampling a similar environment (Figure 5-6). Next, Cav1$_{62\text{-}178}$ and Cav1$_{62\text{-}178}$ P110A were quenched using iodide and both yielded linear modified Stern-Volmer quenching curves (Figure 5-5). Extrapolation of the best fit line in modified Stern-Volmer plots to the y-intercept yielded fractional accessibility (f_a) values of 0.55 ± 0.02 and 0.54 ± 0.01 respectively

(Δf_a=0) (Figure 5-7). The determined λ_{max} and f_a values indicate that tryptophan residues in $Cav1_{62\text{-}178}$ and $Cav1_{62\text{-}178}$ P110A do not seem to have appreciably different accessibilities. However, the CD data implicated changes in the tryptophan environment upon the P110A mutation (large negative peak at 298 nm). This result suggested that the behavior of the tryptophans in aggregate was masking changes that may be occurring for each tryptophan individually (i.e. as one tryptophan becomes more exposed, another becomes less exposed). In order to definitively probe changes that may be occurring local to each tryptophan residue, the four single tryptophan mutants generated for both $Cav1_{62\text{-}178}$ and $Cav1_{62\text{-}178}$ P110A were subjected to the same analysis.

The first tryptophan in the caveolin sequence is at position 85 and is a few amino acids prior to the start of the structural core of the protein. Analysis of the single tryptophan mutant spectra for $Cav1_{62\text{-}178}$(W85) and $Cav1_{62\text{-}178}$(W85) P110A yielded λ_{max} values of 334.86 ± 1.0 nm and 341.12 ± 1.0 nm respectively. Therefore, the $\Delta\lambda_{max}$ going from $Cav1_{62\text{-}178}$(W85) to $Cav1_{62\text{-}178}$(W85) P110A was 6.3 ± 1.4 nm, consistent with a less hydrophobic environment for the mutant (Figure 5-6). Fluorescence quenching analysis yielded very linear modified Stern-Volmer plots that had f_a values of 0.53 ± 0.01 and 0.59 ± 0.02 for $Cav1_{62\text{-}178}$(W85) and $Cav1_{62\text{-}178}$(W85) P110A respectively (Figures 5-7). The Δf_a value obtained was 0.06 ± 0.01, confirming that W85 became more accessible to iodide quenching upon the mutation. Tryptophan 85 is 25 amino acid residues away from position 110 and, remarkably, sensed a different environment when the P110A mutation was made. Therefore, this finding lends extremely strong support to the hypothesis that P110 is required for maintenance of the global caveolin fold.

The next tryptophan in caveolin is at position 98 is centered within the protein's structural core (helix-break-helix region). Analysis of the single tryptophan mutant spectra for Cav1$_{62\text{-}178}$(W98) and Cav1$_{62\text{-}178}$(W98) P110A yielded λ_{max} values of 342.78 ± 1.0 nm and 336.08 ± 1.0 nm respectively. The $\Delta\lambda_{max}$ value obtained was -6.7 ± 1.4 nm, which indicates that the proline replacement results in greater micelle coverage of this region of the helix (Figure 5-6). Modified Stern-Volmer plots for both constructs were linear and gave f_a values of 0.63 ± 0.02 and 0.58 ± 0.01 for Cav1$_{62\text{-}178}$(W98) to Cav1$_{62\text{-}178}$(W98) P110A respectively (Figure 5-7). The Δf_a value of -0.06 ± 0.02 agrees with λ_{max} data, therefore it is clear that the proline substitution resulted in a significantly more buried environment for the W98. Therefore, proline 110 is *absolutely critical* to maintaining a specific depth of caveolin in the micelle.

The second tryptophan resident to the structural core of the protein is W115. This position should serve as a reporter for the putative turn region as it is located one helical turn from position 110. Analysis of the single tryptophan mutant spectra for Cav1$_{62\text{-}178}$(W115) and Cav1$_{62\text{-}178}$(W115) P110A yielded λ_{max} values of 339.33 ± 1.0 nm and 339.86 ± 1.0 nm respectively. The $\Delta\lambda_{max}$ value obtained, 0.5 ± 1.40 nm, is small in magnitude, which correlates with a relatively miniscule difference between wild-type and mutant environments around W115 (Figure 5-6). Quenching of both wild-type and mutant W115 constructs again yielded very linear modified Stern-Volmer plots and gave f_a values of 0.60 ± 0.01 and 0.52 ± 0.01 for Cav1$_{62\text{-}178}$(W115) to Cav1$_{62\text{-}178}$(W115) P110A respectively (Figure 5-7). Interestingly, this yields a Δf_a of -0.08 ± 0.01, which is the largest fold change in iodide accessibility between any of the single tryptophan mutants between WT and P110A single tryptophan mutants. It appears that the two methods are

not in agreement in terms of the effect that the proline replacement causes. As mentioned previously, λ_{max} values are subject to factors other than micelle coverage. One such factor is hydrogen bonding from the indole to the surrounding amino acids or other molecules in the local environment of the tryptophan, which causes red shifts in emission spectra [226]. Therefore, the lack of blue shift in the spectra of $Cav1_{62\text{-}178}$(W115) P110A coincident with a decrease in iodide accessibility could be due to the formation of a unique hydrogen bond between tryptophan 115 and the surrounding environment. Although this is a plausible explanation for the discrepancy between methods, more experiments will be needed to confirm this hypothesis.

The final tryptophan at position 128 is the terminal residue of the second helix within the structural core of the protein. Analysis of the single tryptophan mutant spectra for $Cav1_{62\text{-}178}$(W128) and $Cav1_{62\text{-}178}$(W128) P110A yielded λ_{max} values of 343.65 ± 1.0 nm and 340.59 ± 1.0 nm respectively. This gives a small $\Delta\lambda_{max}$ value of -3.1 ± 1.4, indicating that W128 was only slightly more buried in the case of the mutant (Figure 5-6). Modified Stern-Volmer plots were linear and yielded f_a values of 0.57 ± 0.01and 0.55 ± 0.01 for $Cav1_{62\text{-}178}$(W128) and $Cav1_{62\text{-}178}$(W128) P110A respectively. Clearly, the $\Delta\lambda_{max}$ was strongly supported by the small Δf_a value of -0.02 ± 0.02 (Figure 5-7). Therefore it can be concluded that the P110A mutation only slightly modifies the depth of the C-terminal end of the structural core of the protein.

With this combined fluorescence data, conclusions as to how the intramembrane domain and flanking regions are modulated by the presence of proline at position 110 can be drawn. The decrease in accessibility of tryptophan residues within the intramembrane domain points to a role of proline 110 in altering the penetration depth of the protein in

micelles. This effect seems to be more dramatic for residues within the center of the intramembrane domain, as the decrease in accessibility was less significant for W128 than it was for W98 and W115. Interestingly, it seems that the deeper burial of the intramembrane domain within the hydrophobic core of the micelles comes at the cost of greater exposure for W85. Therefore, proline 110 also has a role in orienting regions flanking the intramembrane domain. All data for the single tryptophan mutants are reported in tables 5-1 and 5-2.

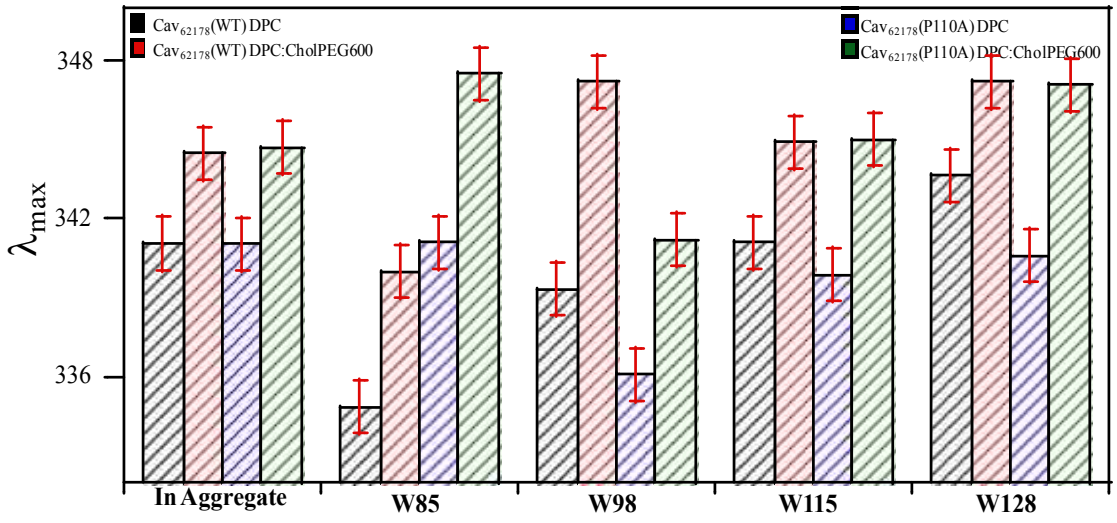

Figure 5-6. Comparison of λ_{max} values obtained from tryptophan emission profile fits.

Tryptophan Position	DPC micelles			DPC with Cholesterol:PEG600 micelles		
	λ_{max} (nm)		$\Delta\lambda_{max}$ (nm) (P110A – WT)	λ_{max} (nm)		$\Delta\lambda_{max}$ (nm) (P110A – WT)
	$Cav1_{62-178}$	$Cav1_{62-178}$ P110A		$Cav1_{62-178}$	$Cav1_{62-178}$ P110A	
W85	334.9 ± 0.8	341.1 ± 0.2	6.3 ± 0.8	340.0 ± 0.2	347.5 ± 0.1	7.5 ± 0.2
W98	342.8 ± 0.3	336.1 ± 1.0	-6.7 ± 1.0	347.2 ± 0.1	341.2 ± 0.1	-6.0 ± 0.1
W115	339.2 ± 0.6	339.9 ± 1.5	-0.5 ± 1.6	344.9 ± 0.1	345.0 ± 0.1	0.1 ± 0.1
W128	343.7 ± 0.3	340.6 ± 1.4	-3.1 ± 1.4	347.2 ± 0.1	347.1 ± 0.2	-0.1 ± 0.2

Table 5-2. λ_{max} and $\Delta\lambda_{max}$ values obtained for single tryptophan mutants of $Cav1_{62-178}$ and $Cav1_{62-178}$ P110A.

Tryptophan λ_{max} Determination, and Fluorescence Quenching of $Cav1_{62-178}$ Constructs: a Comparison of Micellar Environments

Minor changes in the secondary and tertiary structure of $Cav1_{62-178}$ were observed in the near and far ultraviolet regions when the micellar environment was loaded with cholesterol-PEG600 at 40% by mol. Specifically, the amount of β-sheet character increased and the appearance of the near UV CD spectra showed a decrease in signal intensity. To evaluate if these changes were also coincident with changes in protein accessibility, the changes in λ_{max} ($\Delta\lambda_{max}$) and f_a (Δf_a) were used to compare the degree of aqueous exposure between $Cav1_{62-178}$ in micelles composed purely of DPC and those composed of DPC:cholesterol-PEG600.

First, the $Cav1_{62-178}$ that contained all tryptophans was probed to determine if there were major changes in accessibility between micellar environments. Analysis of $Cav1_{62-178}$ reconstituted into either DPC or DPC:cholesterol-PEG600 spectra yielded λ_{max} values of 341.1 ± 1.0 nm and 344.5 ± 1.0 nm respectively, indicating that in aggregate, the tryptophan residues appeared to be sampling a similar environment as the magnitude of the red shift was minor (~3.4 nm, Figure 5-4 and Figure 5-6). Next, $Cav1_{62-178}$ was quenched using iodide and gave linear modified Stern-Volmer quenching curves for both micelle types (Figure 5-7). Extrapolation of the best fit line in modified Stern-Volmer plots to the y-intercept yielded fractional accessibility (f_a) values of 0.55 ± 0.02 and 0.34 ± 0.01 for $Cav1_{62-178}$ in DPC and $Cav1_{62-178}$ in DPC:CholesterolPEG600 respectively (Δf_a=-0.21 ± 0.02) (Figure 5-7). This result was very surprising as there was little difference between the emission maxima but a very large decrease in iodide accessibility. To better characterize how this change in accessibility translates across the

intramembrane domain, the individual tryptophan mutants were examined using the same approach.

Analysis of the single tryptophan mutant spectrum for $Cav1_{62\text{-}178}$(W85) reconstituted into DPC:cholesterolPEG600 yielded a λ_{max} value of 340.0 ± 1.0 nm. Therefore, the $\Delta\lambda_{max}$ going to a cholesterol rich environment from DPC was 5.1 ± 1.4 nm, a fairly large red shift (Figure 5-6). Fluorescence quenching analysis yielded very linear modified Stern-Volmer plot and gave a f_a value of 0.34 ± 0.01 for $Cav1_{62\text{-}178}$(W85) in the sterol rich environment (Figures 5-7). The Δf_a value obtained was -0.26 ± 0.01, confirming that the W85 became much less susceptive to iodide quenching upon translocation to a cholesterol rich environment. This is not in agreement with the small magnitude in the change of the emission maximum.

Analysis of the single tryptophan mutant spectrum for $Cav1_{62\text{-}178}$(W98) reconstituted into DPC:cholesterol-PEG600 yielded a λ_{max} value of 347.2 ± 1.0 nm (Figure 5-5). Going from pure DPC micelles to the DPC:cholesterol-PEG600 micelles yields a $\Delta\lambda_{max}$ of 4.4 ± 1.4 nm, indicating a red shift for W98 (Figure 5-6). The modified Stern-Volmer plot gave a f_a value of 0.48 (Figure 5-7). The Δf_a value between DPC micelles and those containing cholesterol-PEG600 was -0.15 ± 0.02, again pointing to increase shielding of the tryptophan environment from the aqueous milieu due to the sterol.

The next tryptophan examined in DPC:cholesterol-PEG600 micelles, $Cav1_{62\text{-}178}$(W115), gave a λ_{max} value of 344.9 ± 1.0 nm (Figure 5-5). The $\Delta\lambda_{max}$ value was 5.7 ± 1.4 nm, revealing a dramatic change in the accessibility or hydrogen bonding environment due to the sterol (Figure 5-6). A significant change in the f_a value was again

observed, where a modified Stern-Volmer plot yielded an accessibility of 0.50 ± 0.01 (Δf_a = -0.10 ± 0.02) (Figure 5-7). Again, the change in the emission maximum (red shift) and the change in iodide accessibility were not in strong agreement.

The final tryptophan site examined in DPC:cholesterol-PEG600 micelles, $Cav1_{62-178}$(W128), gave a λ_{max} value of 347.2 ± 1.0 nm (Figure 5-5). Again, there was a red shift in the emission maximum compared to that of the protein incorporated into pure DPC micelles ($\Delta\lambda_{max}$ = 4.2 nm). However, as has been the case with the other mutants, the modified Stern-Volmer plot yielded a f_a = 0.38± 0.01, giving a Δf_a = -0.20 ± 0.02 which again points to the protein being shielded from the aqueous phase to a greater degree when in the presence of cholesterol (Figure 5-7). It is clear that the micelle environment is causing drastic changes in the accessibility of the protein in terms of the fraction accessible to iodide quenching, where all constructs are less exposed to the aqueous environment.

It appears that the inclusion of cholesterol-PEG600 results in the protein being much less accessible to the water soluble quencher iodide without leading to a significant blue shift in the observed spectra. This same trend was observed when comparing $Cav1_{62-178}$ P110A constructs reconstituted into the differing micelle environments. Therefore, it is likely that the shift in the emission maximum may be the result of increased hydrogen bonding between the tryptophan residues and polyethylene glycol moieties hanging off the cholesterol molecule. In the case of this study, the $\Delta\lambda_{max}$ only appears to be useful in comparing different constructs in the same type of micelle as the values tracked with the change in the fractional accessibility in a more consistent manner.

There were some significant differences when comparing $Cav1_{62\text{-}178}$ and $Cav1_{62\text{-}178}$ P110A constructs reconstituted into DPC:CholPEG600 micelles. The $\Delta\lambda_{max}$ value between $Cav1_{62\text{-}178}$ and $Cav1_{62\text{-}178}$ P110A with all four tryptophan residues in aggregate was roughly zero. The f_a values were roughly the same as well (~0.34), yielding a Δf_a of zero. Interestingly, there was a very significant red shift going from $Cav1_{62\text{-}178}$(W85) to $Cav1_{62\text{-}178}$(W85) P110A of 7.5 ± 1.4 nm. The Δf_a was found to be 0.19 ± 0.02, in agreement with the change in the emission maximum, indicating a significant decrease in shielding of W85 upon the P110A mutation. This change was much more dramatic than that observed between $Cav1_{62\text{-}178}$(W85) to $Cav1_{62\text{-}178}$(W85) P110A in pure DPC micelles. For $Cav1_{62\text{-}178}$(W98) and $Cav1_{62\text{-}178}$(W98) P110A, it was found that the $\Delta\lambda_{max}$ and Δf_a values were -6.0 ± 1.4 nm and -0.15 ± 0.02 respectively. This indicates that there was a significant increase in shielding from the aqueous environment. For $Cav1_{62\text{-}178}$(W115) and $Cav1_{62\text{-}178}$(W115) P110A, it was found that the $\Delta\lambda_{max}$ and Δf_a values were -0.1 ± 1.4 nm and -0.07 ± 0.01 respectively. This indicates that there was increased shielding of W115 in response to the P110A mutation that was not strongly reflected by the change in emission maximum. For $Cav1_{62\text{-}178}$(W128) and $Cav1_{62\text{-}178}$(W128) P110A, it was found that the $\Delta\lambda_{max}$ was -0.1 ± 1.4 nm and the Δf_a was roughly zero. Therefore, it seems that accessibility of W128 remains unchanged. These data mirrors the changes in the pure DPC micelles indicating that P110A mutation alters the accessibility of the caveolin-1 protein in a predictable way, where W85 is more exposed, W98 and W115 are less exposed, and W128 is unaffected (Figure 5-7). Although three tryptophan residues decrease in their accessibility going from wild-type to P110A $Cav1_{62\text{-}178}$, the two tryptophan residues that are on the N-terminal side are much more affected. This result

could indicate that there is a significant amount of play between the cholesterol-PEG600 and the protein, and that P110 helps to position the protein for this putative interaction.

Cholesterol has been suggested in some studies on caveolin to be a factor causing aggregation of the protein into 200, 400, and 600 kD oligomers *in vivo* [74]. Therefore protein oligomerization could also be at play in shielding tryptophan residues from quenching. Of course, more conclusive evidence (possibly analytical ultracentrifugation) will be needed to support this conclusion. Therefore, in the context of the construct used for these studies, it seems that cholesterol leads to a decreased aqueous accessibility in this system. This result may need visitation in a more relevant system that has a bilayer to examine if cholesterol indeed imparts a topological change as these results could be artifacts from differential micelle coverage of the protein in the DPC:cholesterol-PEG600 mixture that may not be related to the protein's burial. In contrast to P110A which caused changes in the tertiary fold of the protein and does not impart significant changes in the secondary structure and only modest alterations to the degree of micelle coverage, it appears that cholesterol inclusion causes the opposite, where large changes were observed for the degree of burial but slight changes were observed in regards to the tertiary fold of the protein.

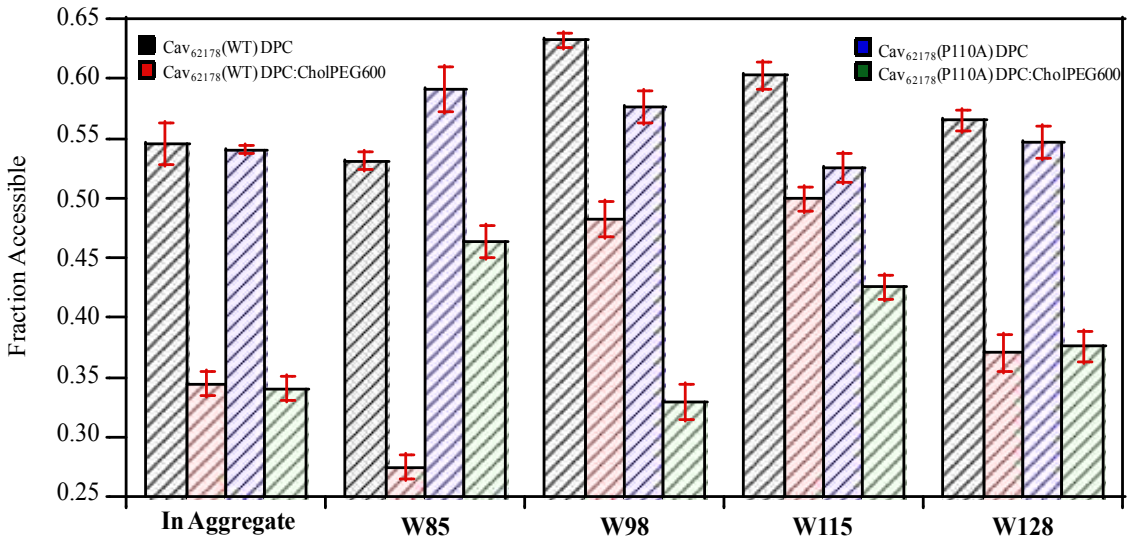

Figure 5-7. Comparison of f_a values obtained from modified Stern-Volmer plots.

Tryptophan Position	DPC micelles			DPC with Cholesterol-PEG600 micelles		
	f_a (%)		Δf_a (%) (P110A – WT)	f_a (%)		Δf_a (%) (P110A – WT)
	$Cav1_{62-178}$	$Cav1_{62-178}$ P110A		$Cav1_{62-178}$	$Cav1_{62-178}$ P110A	
W85	53 ± 1	59 ± 2	6 ± 1	27 ± 1	46 ± 1	19 ± 1
W98	63 ± 1	58 ± 1	-5 ± 1	48 ± 1	33 ± 2	-15 ± 2
W115	60 ± 1	53 ± 1	-7 ± 1	50 ± 1	43 ± 1	-7 ± 1
W128	57 ± 1	55 ± 1	-2 ± 1	37 ± 1	38 ± 2	1 ± 2

Table 5-3. f_a and Δf_a values obtained for single tryptophan mutants of $Cav1_{62-178}$ and $Cav1_{62-178}$ P110A.

Fluorescence Resonance Energy Transfer Experiments: Comparison of Differing Micelle Environments

The near UV circular dichroism experiments suggested that there was not a major change in tryptophan packing when the protein was reconstituted into cholesterol-PEG600 micelles. However, far UV experiments seemed to suggest a more dramatic change in the secondary structure of the protein that could impact the fold. To examine the impact of the sterol on the fold of the intramembrane domain and flanking regions, a fluorescence resonance energy transfer experiment was devised. In this experiment, a cysteine native to position 133 was re-introduced and was labeled using dansyl-aziridine (Figure 5-8). Once covalently attached, the dansyl can be excited by

tryptophan's emission and this requires close contact of the fluorophores in space for the energy transfer event to occur. Upon excitation, changes in the tryptophan distances due to the micellar environment will be evidenced by increases or decreases in the efficiency of the energy transfer (increase in dansyl emission at the cost of a decrease in tryptophan emission, (Figure5-9)). $R_{0,}$ the radius of 50% transfer efficiency is 21 Å for the tryptophan-dansyl FRET pair. This distance would be appropriate to examine changes in the average distance of this position from nearby tryptophan residues as W128 is only 5 residues away from the labeled position and W115 is ~20 Å away from W128 (assuming they are within the same helix as suggested in chapter 3). Assuming a static triangle shaped, helix-break-helix motif with an intra-helical angle 53° (see Chapter 3), there would be an average distance of 24 Å between the heads of the helices. Therefore, the dansyl group could also report on changes in the distance to tryptophans W85 and W98.

Getting the protein labeled to 100% is critical for this experiment because unlabeled material will not contribute to the FRET process. It was found that the protein had to be kept completely reduced until moments before the addition of the reagent using TCEP because caveolin-1 has a strong disulfide bond forming tendency that results in protein dimerization.

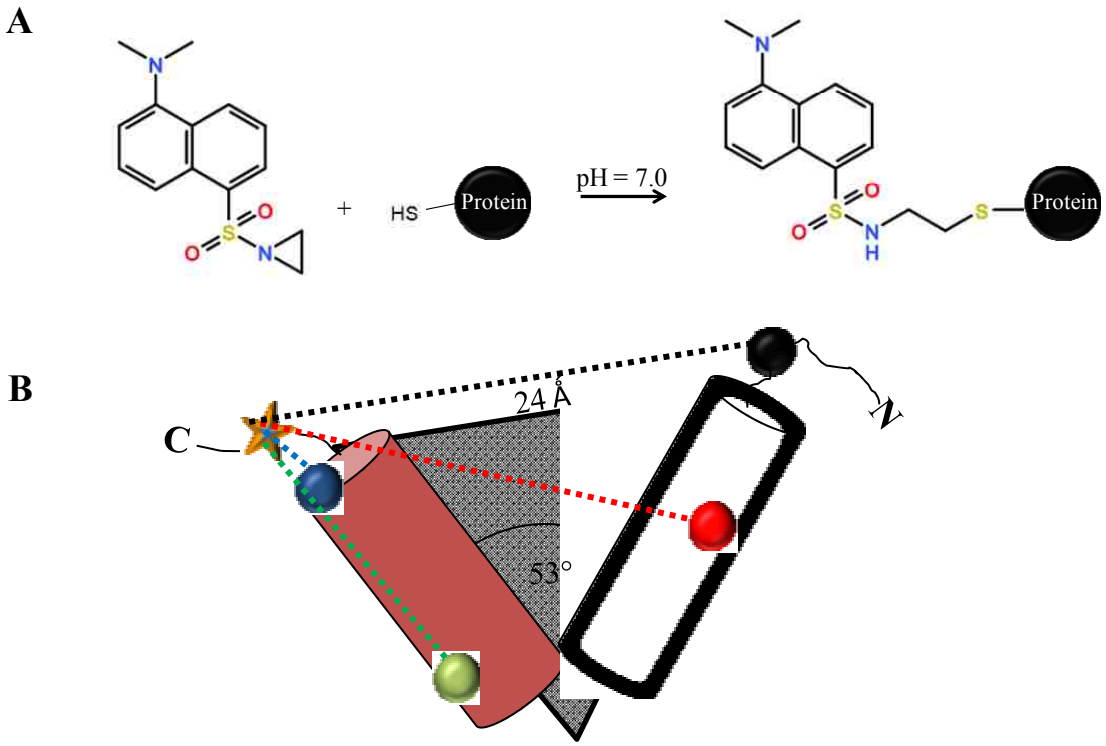

Figure 5-8. A) The dansyl-aziridine moiety is highly reactive due to ring strain and can be attached to sulfhydryl groups on proteins at a physiological pH. **B)** FRET assay principle. The hypothesis is that changes in the micelle environment will cause differences in the dansyl-tryptophan distance. The dansyl label is denoted as a star and tryptophan residues 85, 98, 115, and 129 are show as circles in *black*, *red*, *green*, and *blue* respectively. The "fixed" distance between the top of the two helices is based on geometric arguments assuming the helices form a co-planar triangle with one helix being 27 Å and the other being 28.5 Å and the intra-helical angle is 53° based on MD simulations (see Chapter 3).

However, if the TCEP was left in solution, only 50% of the protein was labeled on average. Once the protein was purified by nickel affinity chromatography, it was desalted and the reagent was added as fast as possible. This reaction had to be quenched after about 18 hours as incubation times greater than 24 hours resulted in over-labeling. This is because the aziridine can react with other nucleophiles on the protein (i.e. lysine). Over-labeling is undesirable because it can complicate FRET analysis. The absorbance spectrum of the labeled $Cav1_{62\text{-}178}$ is shown in figure 5-9.

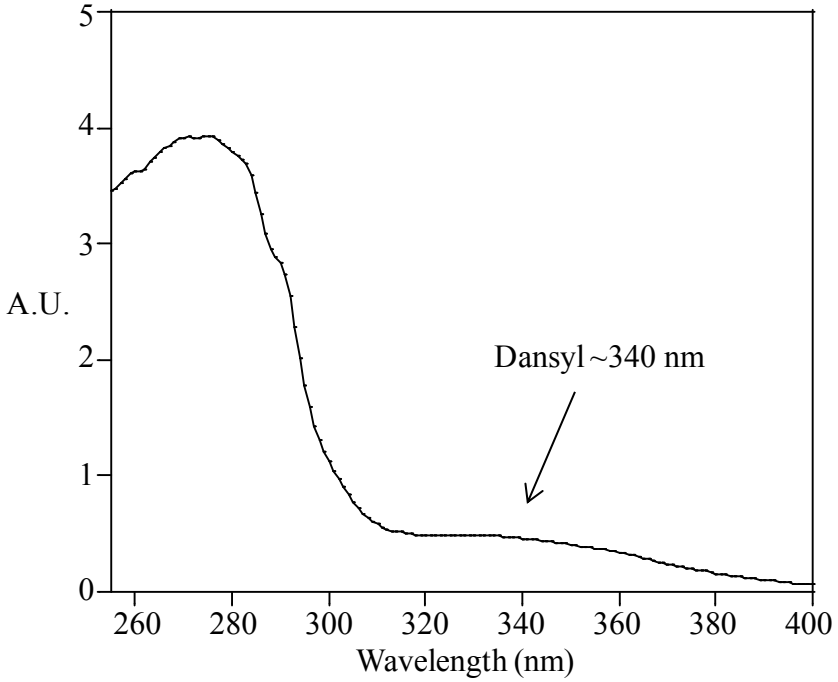

Figure 5-9. Post HPLC purified $Cav1_{62\text{-}178}$ UV-VIS absorbance profile. The peak absorbance at 340 nm is due to the covalently attached dansyl label.

The FRET experiment showed that there were significant differences (~20%) in the energy transfer efficiency between the dansyl moiety and the tryptophan groups when going from pure DPC micelles to DPC:cholesterol-PEG600 micelles (0.64 ± 0.01 and 0.43 ± 0.01 respectively) (Figure 5-10). When using an R_0 of 21 Å, the average donor-acceptor distance translates to 19.04 ± 0.10 Å and 22.00 ± 0.10 Å for $Cav1_{62\text{-}178}$(C133)

reconstituted in DPC and DPC:cholesterol-PEG600 micelles respectively. This is in agreement with a simulation study which showed that there was an increase the average radius of gyration for caveolin residues 94-122 in the presence of cholesterol, suggesting that the sterol promotes open conformations of caveolin [46]. This change is very slight in terms of intramolecular distance, and agrees with the near UV CD data which pointed to very little change in tryptophan packing in micelles composed of DPC:cholesterol-PEG600. These data cannot say how the conformation changed, only that there was a change in the average distance between the donor and acceptor pair. For this reason, the exact nature of the distance change could not be evaluated. The use of single tryptophan mutants may give more specific information of how each tryptophan environment changes when the sterol is included in the micelles, and could clarify the exact nature of the change observed. It is also possible that the distance between the dansyl moiety and some of the tryptophan residues would be greater than $2R_0$, and therefore this would not yield any relevant information to changes that are occurring with cholesterol being present ($E=1.56\%$ at $r=2R_0$). In this case it may be necessary to label many more sites to completely understand how or if the conformation is changing with the inclusion of cholesterol.

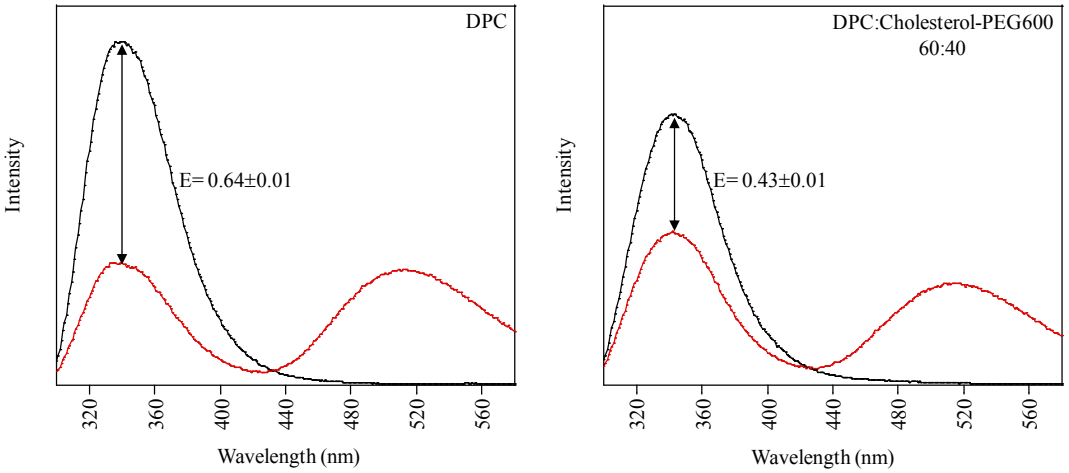

Figure 5-10. Comparison of dansyl-tryptophan FRET for $Cav1_{62\text{-}178}$ reconstituted into either DPC micelles (*left*) or DPC:cholesterol-PEG600 micelles (*right*). The unlabeled species emission profile is in *black* and the dansyl-labeled species is in *red*. Total amounts of protein were the same as assessed by measuring the absorbance at 280 nm and diluting each sample using the appropriate micelle blank. Therefore differences in the emission intensity between the unlabeled spectra are due to environmental effects of the different types of detergent micelles.

CONCLUSIONS

Recent biophysical studies revealed that the highly-conserved P110 of caveolin-1 is critical to its structure and topology. Importantly, this residue is thought to be vital to the appearance of a membrane-embedded helix-break-helix motif that gives caveolin-1 its hallmark topology and the loss of this residue is sufficient to disrupt caveolae formation. Despite many investigations into the part that P110 plays in caveolin-1 topology, results have been inconclusive in determining the exact magnitude of its role in modulating the structure and aqueous accessibility of the protein. In previous NMR studies, high quality hetero-nuclear single quantum correlation spectra were not obtainable for the caveolin-1 P110A mutant, indicative of a poorly structured protein. In this chapter, the data have linked this poor structuring to changes within the tertiary structure rather than the secondary structure using near and far circular dichroism spectroscopy [70]. It was found that the examination of each tryptophan individually was critical to observe changes in the proteins micellar coverage as the behavior of tryptophans in aggregate masked the accessibility changes that occurred upon the P110A mutation. Specifically, the P110A mutation slightly decreased the accessibility of tryptophan mutants within the structural core of the protein (residues 87-128), confirming that the proline is playing a role in modulating the caveolin topology. However, the magnitudes of these changes were not dramatic, therefore the mutation leads to only a modest difference in tryptophan accessibility and not major changes (i.e. the translocation of a tryptophan from a fully buried to a fully exposed environment.). The proline also plays a role in determining the global fold as W85 showed an increased accessibility upon mutation. This study lends support to *in vitro* glycosylation studies which failed to see very drastic changes in the

topology of caveolin-1 upon proline substitution [76]. To date, this body of work represents the most in-depth study of structural and accessibility changes that occur from the substitution of caveolin's critical proline residue.

In this study, cholesterol (in the context of a pegylated micellar analogue) was shown to result in very slight changes in helical packing, and promoted β-strand character. The FRET experiments showed that there is a slight increase in the average distance between a dansyl moiety placed at position 133 and the tryptophan residues within the 85-128 region, possibly indicating a more open conformation of the protein. On the other hand, quenching data suggested that there is a significant decrease in aqueous accessibility of the tryptophans in the presence of the sterol (these data were not at all consistent with λ_{max} data). These data are at odds with the findings in chapter 4 in regards to the sterol's effect on the burial of the scaffolding domain and reports in the literature which indicated that the protein became more accessible in the presence of cholesterol. Interestingly, when the P110A mutant was probed in DPC:cholesterol-PEG600 micelles, it showed the same trend in accessibility changes that was observed between the wild-type and mutant in pure DPC micelles, where residue 85 became more exposed and residues 98 and 115 became more buried. Interestingly, the accessibility of the two tryptophan residues that were on the N-terminal side of the P110 residue were much more affected by its mutation to alanine. It was found that shits in λ_{max} did not strongly agree with the degree of quenching when comparing different micelle types. However, the λ_{max} and quenching studies were generally in agreement when comparing proteins within the same micellar environment (i.e. blue shift in λ_{max} was coincident with a decrease in the fraction accessible). Therefore it is with great caution that λ_{max} should

be used alone in comparing the hydrophobic coverage of a protein in different types of micelles. It is difficult to glean topological information in a micellar environment and these studies will need to be performed in a bilayered mimic for stronger validation of trends observed upon P110A mutation and cholesterol inclusion. Nonetheless this chapter has utilized the most native-like construct to date to try to answer questions of how the accessibility of the entire intramembrane domain is linked to the proline at position 110 and cholesterol. Future work will be needed to place these accessibility changes into the context of conformational changes within a lipid bilayer.

Appendix 5-1. Sequences of Protein Constructs Utilized

Construct	Protein Sequence
$Cav1_{62-178}$ Wild-Type	DVVKIDFEDVIAEPEGTHSFDGI**W**KASFTTFTVTKY**W**YRLLSA LFGI**PL**ALI**W**GIYFAILSFLHI**W**AVVP**S**IKSFLIEIQ**S**ISRVY SIYVHTV**S**DPLFEAVGKIFSNVRINLQKEI
$Cav1_{62-178}$ Wild-Type C133	DVVKIDFEDVIAEPEGTHSFDGI**W**KASFTTFTVTKY**W**YRLLSA LFGI**PL**ALI**W**GIYFAILSFLHI**W**AVVP**C**IKSFLIEIQ**S**ISRVY SIYVHTV**S**DPLFEAVGKIFSNVRINLQKEI
$Cav1_{62-178}$(W85)	DVVKIDFEDVIAEPEGTHSFDGI**W**KASFTTFTVTKY**F**YRLLSA LFGI**PL**ALI**F**GIYFAILSFLHI**F**AVVP**S**IKSFLIEIQ**S**ISRVY SIYVHTV**S**DPLFEAVGKIFSNVRINLQKEI
$Cav1_{62-178}$(W98)	DVVKIDFEDVIAEPEGTHSFDGI**F**KASFTTFTVTKY**W**YRLLSA LFGI**PL**ALI**F**GIYFAILSFLHI**F**AVVP**S**IKSFLIEIQ**S**ISRVY SIYVHTV**S**DPLFEAVGKIFSNVRINLQKEI
$Cav1_{62-178}$(W115)	DVVKIDFEDVIAEPEGTHSFDGI**F**KASFTTFTVTKY**F**YRLLSA LFGI**PL**ALI**W**GIYFAILSFLHI**F**AVVP**S**IKSFLIEIQ**S**ISRVY SIYVHTV**S**DPLFEAVGKIFSNVRINLQKEI
$Cav1_{62-178}$(W128)	DVVKIDFEDVIAEPEGTHSFDGI**F**KASFTTFTVTKY**F**YRLLSA LFGI**PL**ALI**F**GIYFAILSFLHI**W**AVVP**S**IKSFLIEIQ**S**ISRVY SIYVHTV**S**DPLFEAVGKIFSNVRINLQKEI
$Cav1_{62-178}$ P110A	DVVKIDFEDVIAEPEGTHSFDGI**W**KASFTTFTVTKY**W**YRLLSA LFGI**AL**ALI**W**GIYFAILSFLHI**W**AVVP**S**IKSFLIEIQ**S**ISRVY SIYVHTV**S**DPLFEAVGKIFSNVRINLQKEI
$Cav1_{62-178}$ P110A(W85)	DVVKIDFEDVIAEPEGTHSFDGI**W**KASFTTFTVTKY**F**YRLLSA LFGI**AL**ALI**F**GIYFAILSFLHI**F**AVVP**S**IKSFLIEIQ**S**ISRVY SIYVHTV**S**DPLFEAVGKIFSNVRINLQKEI
$Cav1_{62-178}$ P110A(W98)	DVVKIDFEDVIAEPEGTHSFDGI**F**KASFTTFTVTKY**W**YRLLSA LFGI**AL**ALI**F**GIYFAILSFLHI**F**AVVP**S**IKSFLIEIQ**S**ISRVY SIYVHTV**S**DPLFEAVGKIFSNVRINLQKEI
$Cav1_{62-178}$ P110A(W115)	DVVKIDFEDVIAEPEGTHSFDGI**F**KASFTTFTVTKY**F**YRLLSA LFGI**AL**ALI**W**GIYFAILSFLHI**F**AVVP**S**IKSFLIEIQ**S**ISRVY SIYVHTV**S**DPLFEAVGKIFSNVRINLQKEI
$Cav1_{62-178}$ P110A(W128)	DVVKIDFEDVIAEPEGTHSFDGI**F**KASFTTFTVTKY**F**YRLLSA LFGI**AL**ALI**F**GIYFAILSFLHI**W**AVVP**S**IKSFLIEIQ**S**ISRVY SIYVHTV**S**DPLFEAVGKIFSNVRINLQKEI

Appendix 5-2. Mutagenesis Primers Utilized

Construct	Primer Sequence
F85W	5'-GGATCCATGGACGGTATCTGGAAAGCGTCTTTCACCAC-3'
F98W	5'-CACCGTTACCAAATACTGGTTCTACCGTCTGCTGTC-3'
F115W	5'-CTGGCGCTGATCTGGGGTATCTACTTCGC-3'
F128W	5'-CTTTCCTGCACATCTGGGCGGTTGTTCCGTC-3'
P110A F115F	5'-CTGTCTGCGCTGTTCGGTATCGCACTGGCGCTGATCTTCGGTATC-3'
P110A F115W	5'-CTGTCTGCGCTGTTCGGTATCGCACTGGCGCTGATCTGGGGTATC-3'

Chapter 6. Applications of Indole-PE: A Novel Lipid with a Tryptophan Headgroup for Use in Quenching Studies

ABSTRACT

Fluorescence quenching studies are routinely employed to estimate the burial of tryptophans within the tertiary folds of soluble proteins. Fluorescence quenching of tryptophan residues within membrane proteins embedded in micelles, bicelles, and vesicles has also become a standard method to evaluate the protein's degree of burial. The quenching of membrane proteins tends to be more complex because the barrier effect of the membrane mimetic on quenchers is not precisely known. To help with the interpretation of quenching studies, a novel lipid with an indole headgroup, dubbed "indole-PE", was synthesized by coupling 3-iodoacetic acid and DMPE *via* peptide bond formation. This chapter describes the purification and characterization of the fluorescence properties of indole-PE. Additionally, the utility of indole-PE as a molecular ruler was examined in two cases. In the first case it is shown that indole-PE can be used to investigate the permeability of commonly used quenchers across lipid vesicles. In the second example, it is shown that indole-PE serves as a tool to help interpret fluorescence λ_{max} measurements and iodide fluorescence quenching experiments performed on thirteen single tryptophan mutant constructs of caveolin-1 reconstituted into phospholipid bicelles.

INTRODUCTION

Tryptophan fluorescence is highly useful in the structural probing of proteins. For instance the λ_{max} of a residue's emission can often be linked to different degrees of exposure to water and therefore can be an analytical tool to study protein folding or in the case of membrane proteins, an estimation of their burial within phospholipid bilayers. Additionally, tryptophan can be quenched by a number of different small molecules. These molecules can carry different charges or vary in their degree of polarity and therefore their usage in combination can yield a rich amount of information about the environment of a given residue. In the study of membrane proteins, soluble probes are often used which have limited aces sot the membrane matrix. To what degree these different probes cross or diffuse into bilayers to cause differential quenching is not known. A common technique used is comparing the degree of quenching of the free amino acid tryptophan to that of the protein of interest. This approach can be complicated as free tryptophan can interact with membranes and cannot help with finer levels of differentiation (i.e. burial at aqueous headgroup interface or within the hydrophobic core of the bilayer).

In this study, a novel lipid which contains the indole moiety as its headgroup, indole-PE, was synthesized to provide a more accurate molecular ruler for comparison in λ_{max} and quenching studies of tryptophan residues. Herein, the synthetic approach and purification of the lipid is described. The product was confirmed by MALDI-TOF mass spectrometry and NMR. Additionally the fluorescent properties were probed. It was found that indole-PE incorporated into liposomes provides a good marker to determine if the polar tryptophan quenching reagents can permeate across bilayers. It is also shown to

be useful in quenching studies when reconstituted into phospholipid bicelles. Specifically it was utilized as a metric for a tryptophan scanning mutagenesis study on caveolin-1 residues 62-178. In this study, 13 single tryptophan mutants were generated for the protein by mutating all native tryptophans to phenylalanine and then replacing aromatic positions or non-conserved positions with tryptophan in the 85-133 region. It was found that these positions were less accessible to iodide quenching than indole-PE indicating that this region of the protein is buried beneath the aqueous headgroup interface.

MATERIALS AND METHODS

$^{HSVFLAG}Cav1_{62\text{-}178}$ Single Tryptophan Mutant Cloning, Expression, and Reconstitution into Bicelles

$^{HSVFLAG}Cav1_{62\text{-}178}$ was cloned, expressed, and purified according to protocols described in chapter 2 and Appendices 2-3 through 2-6. $Cav1_{62–178}$ contains four tryptophan residues: W85, W98, W115, and W128. The original gene had all four native tryptophan residues replaced with phenylalanine. After this, 13 constructs were generated with a single tryptophan re-introduced at a native site (W85, W98, W115, W128), a site that contained an aromatic residue (F89, F99, F107, Y118, F124), or a site that was not highly conserved across isoforms (L102, M111, I117, C133) (See Appendix 6-1) using the Quik-change site-directed mutagenesis kit (Agilent, Santa Clara, CA). Additionally native cysteines were mutated to serine in order to avoid any biologically irrelevant disulfide bond formation and are justified by reasons discussed in previous chapters. Primers were designed using the free web-based primerX program (Bioinformatics.org) (See Appendix 6-2). See Appendix 2-4 for PCR reaction and cycling conditions.

$^{HSVFLAG}Cav1_{62\text{-}178}$ was reconstituted into 2.5% (*w/w*) lipid, $\boldsymbol{q}$= 0.5 DMPC/DHPC bicelles at a protein concentration of 30 μM. To achieve this, $^{HSVFLAG}Cav1_{62\text{-}178}$ (1.64 mg) and DMPC (32.8 mg) were dissolved in 3 mL HFIP. Next, 2 mL of water was added and this solution was rapidly frozen and lyophilized for 24 hours. The lyophilized mixture was then converted to bicelles by adding 166 μL 25% (*w/w*) DHPC, 300 μL 200 mM phosphate pH 7.0, and 2500 μL H_2O by vortex mixing. The bicelles were then centrifuged at 10,000 *x* g for 20 minutes at room temperature to remove aggregates that

may have formed during the reconstitution process. The supernatant was used for fluorescence measurements.

Determination of λ_{max} for Single Tryptophan Mutants

Two separately prepared samples were used to determine λ_{max} for each single tryptophan mutant. Bicelles were used because they scatter very little light, and contain a planar DMPC bilayer, which avoids orientation differences associated with vesicles. Fluorescence emission spectra were acquired using a 1 × 1 cm quartz cuvette held at 298 K with an Eclipse fluorometer (Agilent, Santa Clara, CA). The excitation wavelength used was 295 nm to avoid unwanted tyrosine excitation [127]. Both the excitation and emission slit widths were set to 5 nm. The emission spectra were measured from 315 to 500 nm with a scan speed of 1 nm/s and 0.5 nm data point increments. Four scans were averaged for each construct. A blank solution containing only bicelles was used to subtract background fluorescence. The λ_{max} values were obtained by fitting the spectra to a log-normal distribution using Igor Pro 6.22A software (Wavemetrics, Portland, OR)[133].

Synthesis and Purification of Indole-PE

In a 20 mL glass scintillation vial, 0.573 mmol (100 μL, neat) of N,N-diisopropylethylamine, 0.044 mmol (7.65 mg, powder) indole-3-acetic acid, 0.20 mmol (30.5 mg, powder) 1-hydroxybenzotriazole hydrate, and 0.050 mmol (9.00 mg, powder) 1-Ethyl-3-(3-dimethylaminopropyl)carbodiimide were dissolved into 2.5 mL of chloroform with stirring. After 1 hour, 0.022 mmol (13.80 mg, powder) of 1,2-dimyristoyl-*sn*-glycero-3-phosphoethanolamine (DMPE) was added with stirring and the

mixture was allowed to react at room temperature overnight in the dark. The mixture was then transferred to a 50 mL glass conical tube and 5 mL of chloroform was added along with 10 mL of 20 mM phosphate pH 7.0 and 9 drops of a saturated NaCl solution. The mixture was vortexed for 5 minutes, and centrifuged at 6000 *x g* for 10 minutes at 4°C. The top layer was disregarded and the bottom layer was washed a second time. The bottom layer was then dried using $MgSO_4$ and the solution was filtered using Whatman No. 2 filter paper. The supernatant was dried under vacuum to a gel. The resulting gel was then taken up into 5 mL of a 50:50 solution of ammonium acetate buffer pH 8.0 and methanol by vortexing. The reconstituted material was then passed through a 0.2 μm regenerated cellulose filter. The sample was then injected onto a 250 x 21.20 mm C4 reverse phase column with a 15 μm particle packing having a 300 Å pore size at 10 mL/min. The lipid was eluted using a 1.25 %/ minute gradient starting at 50 % buffer A (ammonium acetate buffer pH 8.0) 50 % buffer B (methanol) and going to 100 % buffer B. After drying down the isolated product, the stock was kept in chloroform at -80°C until usage. The purification gave rise to a well resolved species having an ^1H NMR (500 MHz, $CDCl_3$)δ 0.87(t, 6H), 1.2-1.32(m, 36H), 1.53(m, br, 4H), 2.00(s, 3H), 2.20(q, 3H), 3.30(br, 2H), 3.60(s, 2H), 3.70(br, 3H), 4.0(q, 1H), 4.2(d, 1H), 5.18(m, 1H), 6.88(t, 1H), 7.06(t, 1H), 7.1(m, 2H), 7.27(d, 3H), 7.33(d, 1H), 7.5(d, 1H), 9.507(s, 1H). Additionally, MALDI-TOF mass spectrometry was utilized by drying the product down in an Eppendorf tube and then resuspension of the film in a solution containing saturated sinnipinic acid in 1:1:2 0.1% trifluoroacetic acid:acetonitrile:acetic acid yielding a HR-MALDI MS for $C_{43}H_{72}O_9N_2P$ ($[M+Na]^+$) Calcd.: 816.037 D. Found: 815.969 D.

Reconstitution of Indole-PE into Vesicles and Bicelles

For reconstitution into vesicles, 180 µl of a 2.5 mM stock (450 nmol) of indole-PE in chloroform was co-mixed with 46.62 mg of egg yolk phosphatidylcholine dissolved in chloroform at 50 mg/mL. The mixture was then dried down using N_2(g) and the resultant film was placed under vacuum for 4 hours. The film was then dissolved in a buffer containing 300 mM PFOA (Oakwood Products, West Columbia, SC), 10 mM Tris-HCl pH 8.0 to the egg PC to achieve a final lipid concentration of 20 mM. The mixture was then heated until it became transparent. The resulting solution was then added to a 10 kD MWCO slide-a-lyzer G2 dialysis cassette and was dialyzed against 2 L of 10 mM Tris-HCl pH 8.0, 100 mM NaCl. The mixture was dialyzed for three days with exchanges every 24 hours to ensure complete removal of PFOA and resulted in the formation of vesicles. The vesicles were spun at 12,000 *x g* for 20 minutes to remove any aggregated material. The supernatant was used for fluorescence quenching experiments.

For reconstitution into bicelles, 36 µl of a 2.5 mM stock (90 nmol) of indole-PE in chloroform was co-mixed with 32.8 mg of DMPC dissolved at 50 mg/mL in chloroform. This solution was then dried down using N_2(g) and the resultant film was hydrated with 166 µL 25% (*w/w*) DHPC, 300 µL 200 mM phosphate pH 7.0, and 2500 µL H_2O by vortex mixing. Once homogeneous, the solution was frozen and lyophilized for 24 hours. The lyophilized material was then reconstituted using 2925 µL H_2O to generate 2.5% (*w/w*) $\boldsymbol{q}$=0.5 DMPC/Indole-PE/DHPC bicelles. The sample was then utilized in fluorescence quenching experiments and λ_{max} determinations.

Measurement of Indole-PE Excitation and Emission Spectra

This measurement was performed on indole-PE reconstitute into bicelles. Fluorescence excitation and emission spectra were acquired using a 1 × 0.1 cm quartz cuvette held at 298 K with an Eclipse fluorometer (Agilent, Santa Clara, CA). The excitation and emission slits were set to 2.5 nm. First the absorbance spectra was evaluated using UV-VIS spectroscopy and it was determined that 280 nm was the peak absorption wavelength. This wavelength was used to excite the indole-PE and the emission spectrum was obtained by scanning in the 240-500 nm wavelength range acquiring a total of 50 scans using a scan speed of 1 nm/s with 0.5 nm data point increments. After determination of the maximum wavelength of emission, the excitation spectrum was obtained by scanning in the 240-330 nm wavelength range acquiring a total of 50 scans using a scan speed of 1 nm/s with 0.5 nm data point increments. The λ_{max} of emission was determined by fitting the emission spectrum to a log-normal equation [132,133]. The Stoke's shift was calculated by taking the difference of the emission and excitation maxima in terms of wavenumbers (cm^{-1}).

Measurement of Bilayer Permeability of Iodide and Acrylamide using Large Unilamellar Vesicles with Reconstituted Indole-PE

The vesicles formed were diluted 12.5 fold into 3 mL to a final concentration of 12 μM and 1.6 mM for indole-PE and EYPC, respectively, using the dialysis buffer supplanted with 1 mM DTT at 25℃. Using an excitation wavelength of 280 nm, the emission intensity was recorded at 343 nm (λ_{max}) for 3 minutes using a 1 s averaging time. To determine if KI can cross the bilayer, 60 μL of 1 M KI dissolved in 1 mM DTT

was added with stirring to give a final concentration of 20 mM KI. After monitoring the fluorescence signal for 30 minutes, Triton-X-100 (reduced form) was added to a final concentration of 1 % (*v/v*). The fluorescence signal was monitored for an additional 20 minutes. This addition leads to a signal increase, therefore a control employing only the addition of Triton-X-100 determined that the signal increase was due in part to the addition of the detergent. The data is corrected for before and after permeabilization, and yields data on the unexposed fraction. This experiment was repeated using acrylamide under the same conditions without DTT.

Fluorescence Quenching of Indole-PE and Single Tryptophan Mutants Reconstituted Into DMPC/DHPC Bicelles

The quenching studies were performed on indole-PE and single tryptophan mutants reconstituted into 2.5% (*w/w*) lipid, $\boldsymbol{q}$ = 0.5 DMPC/DHPC bicelles on a 3 mL scale at a concentration of 30 μM. Fluorescence emission spectra were acquired using a 1 × 1 cm quartz cuvette held at 298 K with an Eclipse fluorometer (Agilent, Santa Clara, CA). The excitation wavelength used was 295 nm. Fluorescence emission curves were collected and analyzed using a log-normal equation to determine the λ_{max} of emission for each mutant [132,133]. The λ_{max} of emission was monitored during the quenching experiments. Both the excitation and emission slit widths were set to 5 nm. Four scans were taken for each point. An 18 μL aliquot of 20% (*w/w*) KI in 1 mM DTT was added to the cuvette with rapid stirring for the first point allowing 1 minute before measuring the intensity at λ_{max}. After this, 18 μL aliquots of the quencher were added for each point, allowing 1 minute of mixing before recording the intensity. Stern-Volmer quenching

curves were generated by a plot of $[I^-]$ versus I_0/I and the slope was taken as the K_{SV}. Modified Stern-Volmer quenching curves were generated by plotting $1/[I^-]$ versus I_0/I_0-I and the y intercept was taken as the fractional accessibility of each single tryptophan mutant.

Indole-PE was used in the case of the bicelle studies so that all quenching measurements could be compared to a headgroup located indole group.

RESULTS AND DISCUSSION

Synthesis and Purification of Indole-PE

The generation of lipids with amino acids as their headgroup is not a new idea. This work has been pioneered by Regen and co-workers in his nearest neighbor studies [212]. However, there is no report of an indole moiety having been coupled to a lipid. Such a molecule could serve as a useful standard in evaluations of tryptophan accessibility in a variety of contexts. Therefore, standard peptide bond formation chemistry using HOBt/EDC to couple indole acetic acid and 1,2-dimyristoyl-*sn*-glycero-3-phosphoethanolamine was utilized (Reaction Scheme 6.1).

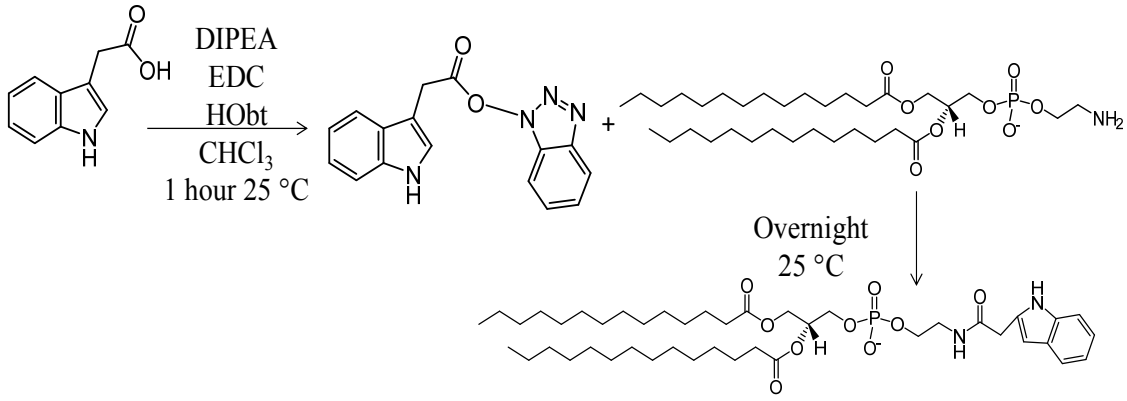

Reaction Scheme 6-1. Synthesis of indole-PE.

This approach resulted in a species that could be isolated using reverse phase HPLC to homogeneity (Figure 6-1). The product migrated to a single spot using thin layer chromatography and was confirmed to have the correct identity by ^{1}H and ^{31}P NMR and MALDI-TOF (Figure 6-1).

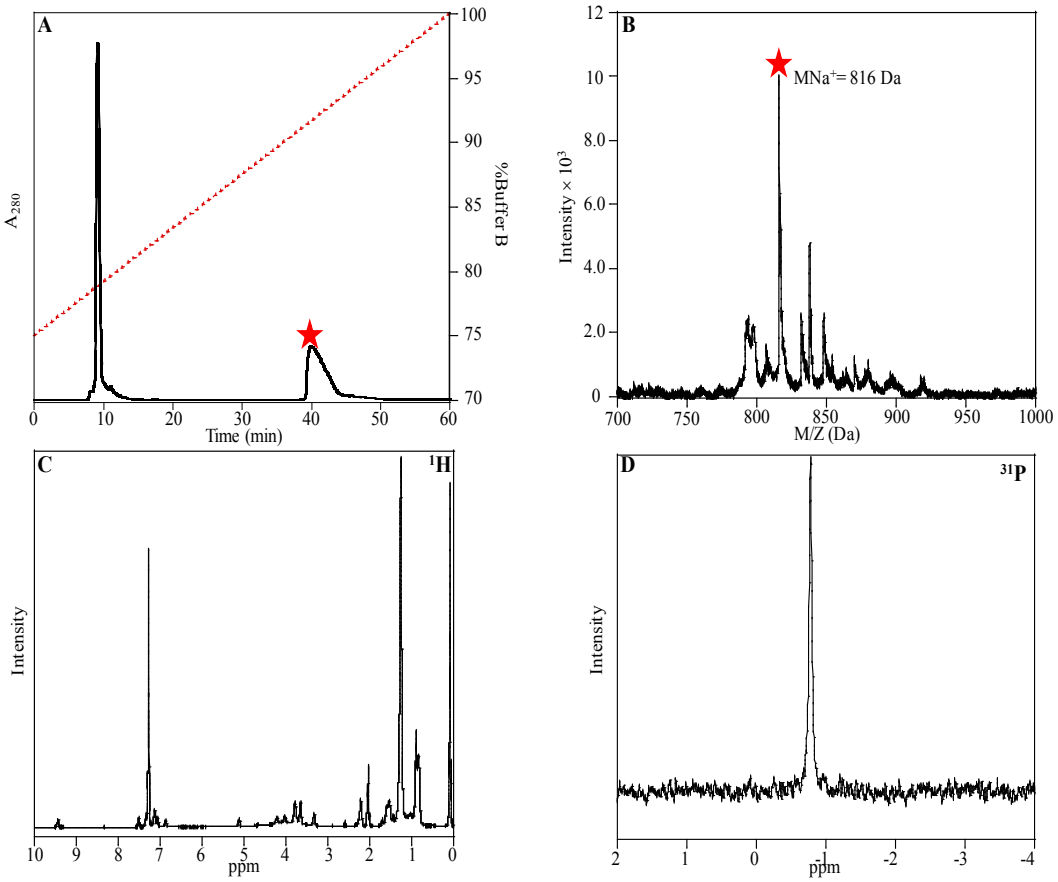

Figure 6-1. Purification trace for indole-PE using reverse phase HPLC. The product is denoted by the red star. **B)** High resolution MALDI-TOF spectrum of indole-PE. The molecular ion appeared to be a sodium adduct denoted by the red star. **C)** Proton NMR of indole-PE. For assignments, see methods section. Resonances in the 1-3 ppm region where indicative of the acyl-chain region of the molecule whereas resonances in the 6-8 ppm region had signatures of the indole moiety. **D)** The presence of the phosphate headgroup was shown using ^{31}P NMR.

Bilayer Permeability of Commonly Used Quenchers

Fluorescence quenching studies are common place in investigations of the aqueous exposure of fluorescent molecules. In the case of species buried within the lipid bilayer, or trapped within vesicles, it is unclear how these quenchers respond to the phospholipid barrier. Prior quenching studies have suggested that potassium iodide and acrylamide, which are soluble quenchers commonly employed in topological investigations, passively diffuses across lipid bilayers [227]. This study was performed by

entrapping tryptophan within the vesicles at an expected concentration of 15 mM. Tryptophan, although zwitterionic, is small and hydrophobic and could have leaked across bilayers causing a false positive for the bilayer crossing of the quenchers. Therefore it is still an open question as to the ability of iodide and acrylamide to cross bilayers. The proposition that these quenchers can cross bilayers, if true, complicates analysis of quenching studies of proteins within lipid vesicles, and can lead to inaccurate data on depth and orientation estimates. This claimed "leakage" of the quenchers was investigated by employing indole-PE incorporated into lipid vesicles formed of roughly 55 nm in diameter. Vesicles of this size have roughly equivalent amounts of the indole-PE distributed in each leaflet (this assumption was based on vesicle size calculations from Huang and Mason [156]). Therefore, it would be expected that only 50 % of the fluorescence that *can* be quenched at a given quencher concentration should be available under non-permeabilized conditions for our vesicles. The addition of acrylamide caused an intense drop in indole-PE fluorescence directly after the reagent was added. The fluorescence then remained relatively constant over the course of 30 minutes (0.05%/minute decrease, Figure 6.2). After the addition of Triton-X-100, the fluorescence signal of the indole-PE was quenched further, consistent with acrylamide being able to access the tryptophan headgroup on the inner leaflet of the vesicle under permeabilized conditions. The magnitude of the drop in fluorescence after permeabilization was roughly equal to that of the non-permeabilized sample (14% and 11% of the total signal, respectively). This result agrees with the expected distribution of indole-PE being equal in the inner and outer leaflets. When added to the external environment of the vesicles, iodide also quenched indole-PE fluorescence (Figure 6-2).

Interestingly, after a short period of a relatively steady signal, the fluorescence began to decay linearly, possibly indicating that the iodide indeed was crossing the bilayer, which is consistent with reports in the literature [227]. Addition of Triton-X-100 caused a further drop in the intensity. The drops in intensity before and after permeabilization were again consistent with an equal distribution of indole-PE on either side of the bilayer (8% and 7% of the total signal respectively). When considering the properties of the two quenchers utilized, it is unusual that negatively charged iodide would permeate across the bilayer more readily than acrylamide. Therefore, the smaller size of the iodide ion compared to that of the acrylamide molecule could result in iodides enhanced permeability into vesicles. It seems that acrylamide may be a better choice when evaluating the distribution of tryptophan groups that are exposed on different sides of the bilayer. Additionally, it was observed that the magnitude of the quencher's effect on the indole-PE fluorescence was different with acrylamide being twice as potent of a quencher versus iodide. This could be explained by the negative charge on indole-PE that would repulse other negatively charged species. This study therefore shows the benefit of using quenchers that vary in their properties to obtain as much information on a fluorophores location as possible.

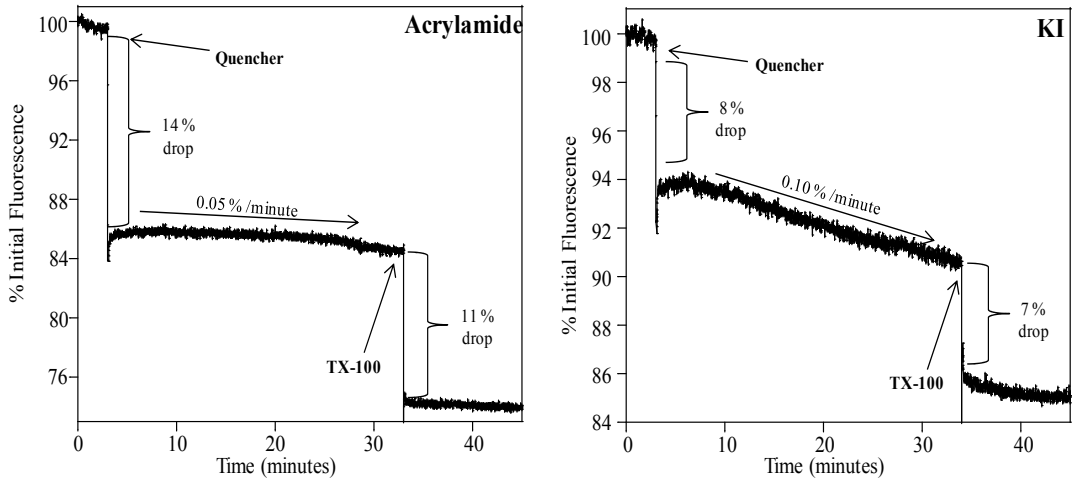

Figure 6-2. Acrylamide and iodide were evaluated for their ability to quench indole-PE located within different leaflets of vesicles. The results are consistent with an equal distribution of the fluorophore in each leaflet of the large unilamellar vesicles. The smaller ionic quencher, iodide, had enhanced permeability into these vesicles compared to the larger polar quencher, acrylamide. Experiments were repeated twice and showed similar results.

Tryptophan Scanning of Caveolin-1 in Bicelles Using Indole-PE as a Molecular Ruler

One advantage of bicelles in terms of investigating absolute exposure of reconstituted membrane proteins using fluorescence quenching is that they do not have an interior compartment that can complicate quenching analysis. However, differences in quenching efficiencies that would be observed between tryptophans within the aqueous, headgroup, and bilayer regions are not clear for bicelles as there are a limited number of reports where the quenching of proteins reconstituted within them has been investigated. In particular, it is unclear if tryptophans located within the headgroup and bilayer region would show differences in quenching efficiency, due to the increased water penetration brought about by the detergent in the bicelle. Therefore, it seemed necessary to have a molecular ruler in order to allow stronger conclusions to be drawn on membrane protein quenching experiments performed in bicelles.

First, the excitation and emission spectra were acquired for the indole-PE molecule reconstituted into bicelles. The indole-PE was found to have a λ_{max} of excitation and emission of 280 nm and 343.47 ± 0.93 nm respectively giving a Stoke's shift value of 6389 cm^{-1}. Next, the indole-PE exposure was probed using iodide (Figure 6-3).

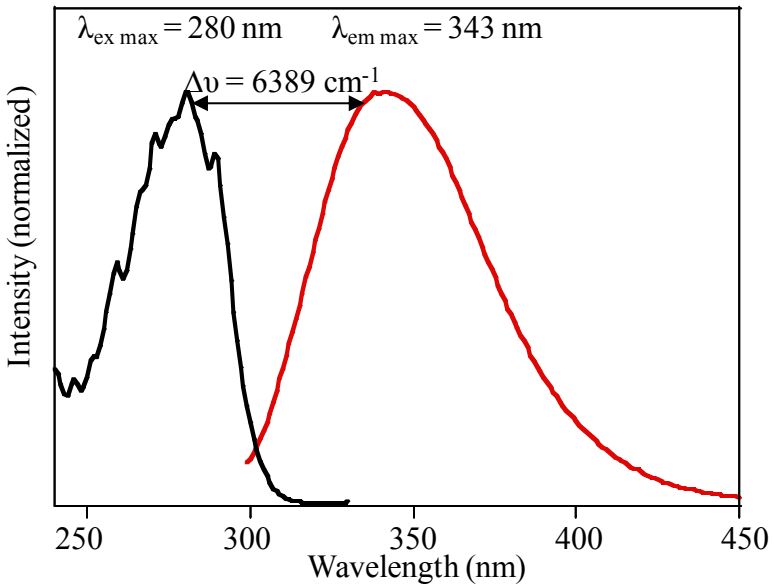

Figure 6-3. Normalized excitation (*black*) and emission (*red*) spectra for indole-PE reconstituted into phospholipid bicelles.

Quenching curves were very linear and highly reproducible and were analyzed using both Stern-Volmer plots and the modified Stern-Volmer plot in order to obtain both K_{SV} (average collisional quenching constant) and the fractional accessibility (Figure 6-4). From the slope of the Stern-Volmer plot, the K_{SV} was determined to be 4.40 M^{-1}, which is much less accessible than tryptophan in buffer that has a K_{SV} value of ~14.3 M^{-1}, characteristic of an indole group that is shielded from the aqueous environment (Figure 6-4). The fractional accessibility was determined from the intercept of the modified Stern-Volmer plot and gave a value of 0.67 ± 0.03 (Figure 6-4). The value is likely

underinflated due to the negative charge on the indole-PE moiety which, due to electrostatic repulsion, would decrease the apparent fractional accessibility. However, the λ_{max} is consistent with an aqueous-headgroup bordering molecule (~343 nm), and therefore this value is consistent with a species that would not be completely solvent exposed. This molecular ruler is also valid for this comparative study considering that the $^{HSVFLAG}Cav1_{62\text{-}178}$ molecule has an isoelectric point = 4.21 and would also be negatively charged at the pH that these studies were performed at.

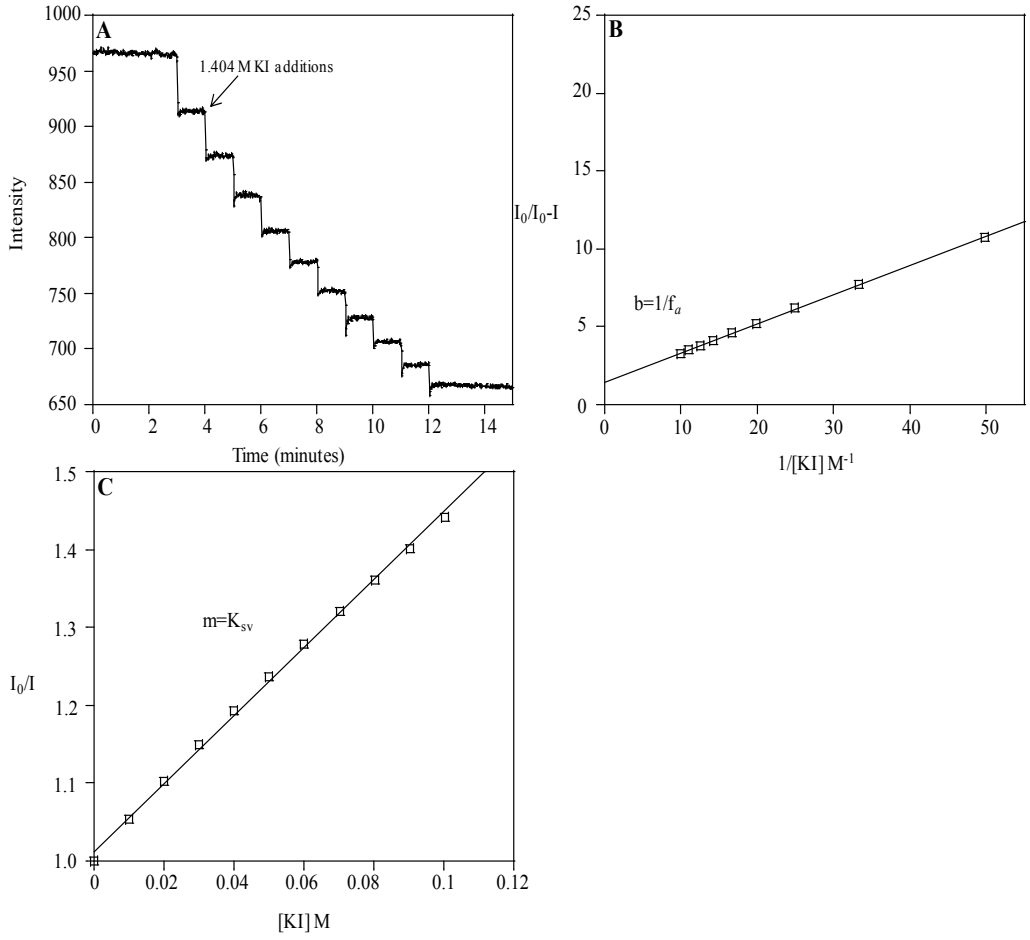

Figure 6-4. Quenching of indole-PE with iodide. **A)** Kinetic quenching plot generated by monitoring the 343 nm wavelength and adding iodide every minute after an initial 3 minute incubation period. **B)** Modified Stern-Volmer plot used to obtain the fractional accessibility of indole-PE. **C)** Stern-Volmer plot used to obtain the K_{SV} value for indole-PE to iodide. Some deviation towards the *x*-axis was observed at high concentrations of iodide.

With the accessibility of indole-PE characterized, the quenching of single tryptophan mutants was undertaken to determine the positioning of the protein within the bicelles. For these studies, a construct which was flanked by highly charged antibody epitopes (HSV and FLAG) at both the N- and C- termini was utilized to facilitate reconstitution into bicelles by classical methods. The addition of charged tags greatly decreased the protein's propensity for aggregation and allowed the time consuming vesicle to bicelle transition method presented in chapter 3 to be circumvented. Thirteen mutants in the 85-133 region were analyzed, thereby giving good coverage of the proposed membrane interacting domains (the scaffolding domain + the intramembrane domain). Importantly, this will give information about the trend in accessibility and may shed light on the burial of the turn region (residues 108-110) as well as the burial of the helical regions. After reconstitution, the mutants were probed by the same methods used for the indole-PE. The λ_{max} of emission, K_{SV}, and the fractional accessibility values were utilized to evaluate the trend in accessibility along the sequence (Table 6.1). From the quenching of the spectra (Figure 6-5 shows un-quenched and partially quenched emission spectra for each mutant), it was clear that there were differences in the burial going along the sequence.

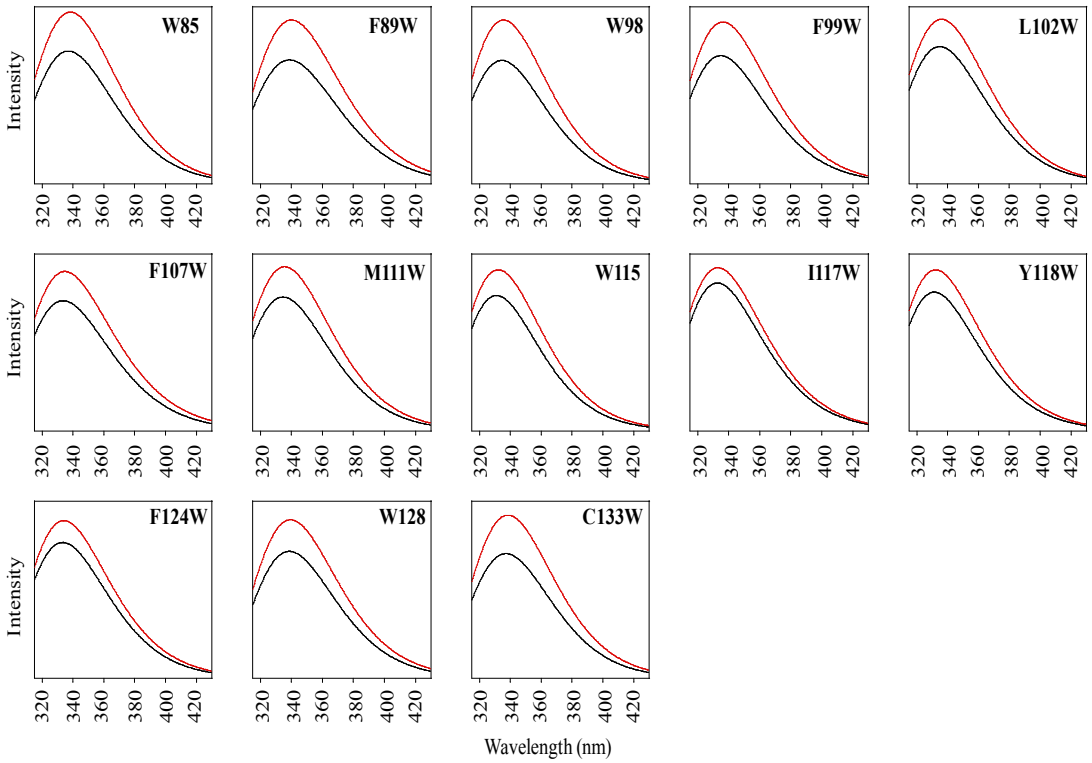

Figure 6-5. Fluorescence emission spectra for each mutant probed in the presence of 0 mM iodide (*red*) and ~110 mM iodide (*black*).

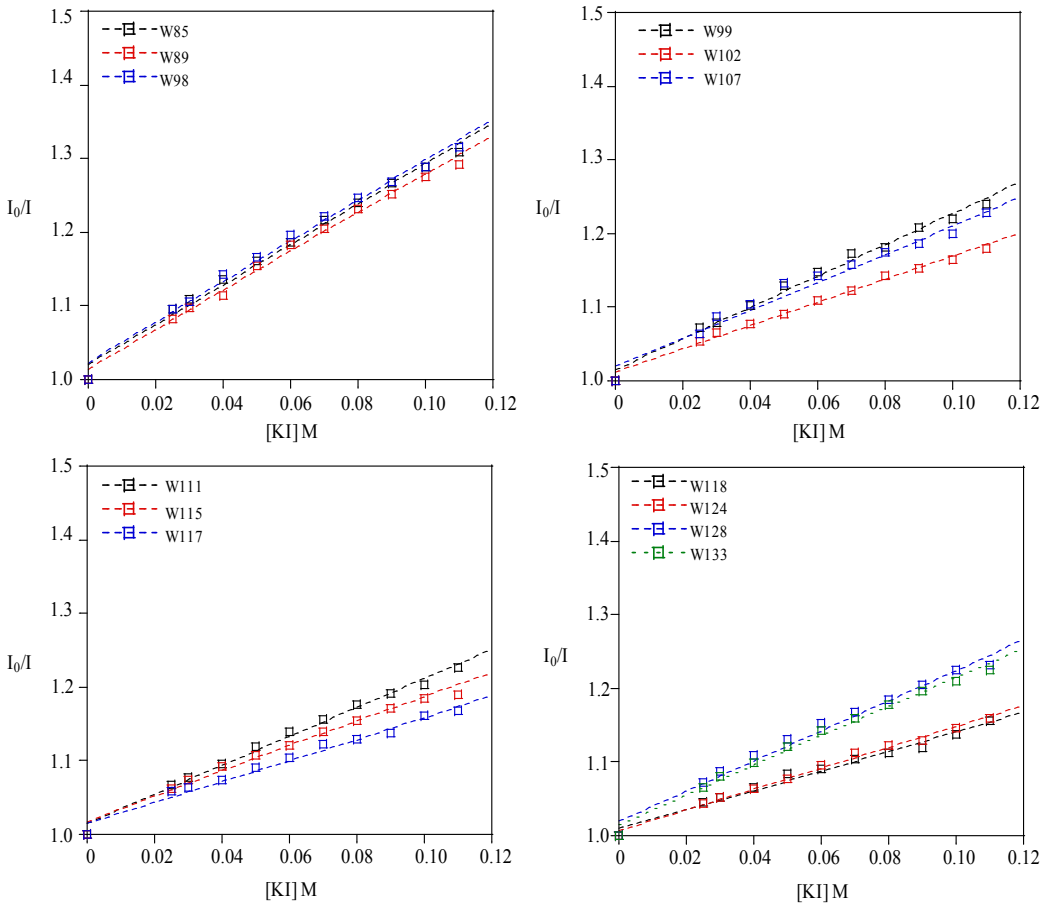

Figure 6-6. Representative Stern-Volmer quenching curves for each single tryptophan mutant used in the study.

Fitting of the λ_{max} of emission data at different iodide concentrations to Stern-Volmer plots (Figure 6-6) showed linear trends with slight curvature towards the *x* axis, which indicates a partially buried fraction. Modified Stern-Volmer plots were very linear which is important for fractional accessibility determination as poorly linear plots tend to have very large error due to extrapolation to an infinite quencher concentration (Figure 6-7). Each parameter determined from the fluorescence experiments was plotted as a function of the position probed to evaluate how the accessibility changes along the length of the 85-133 region of the protein (Figure 6-8, Table 6-1).

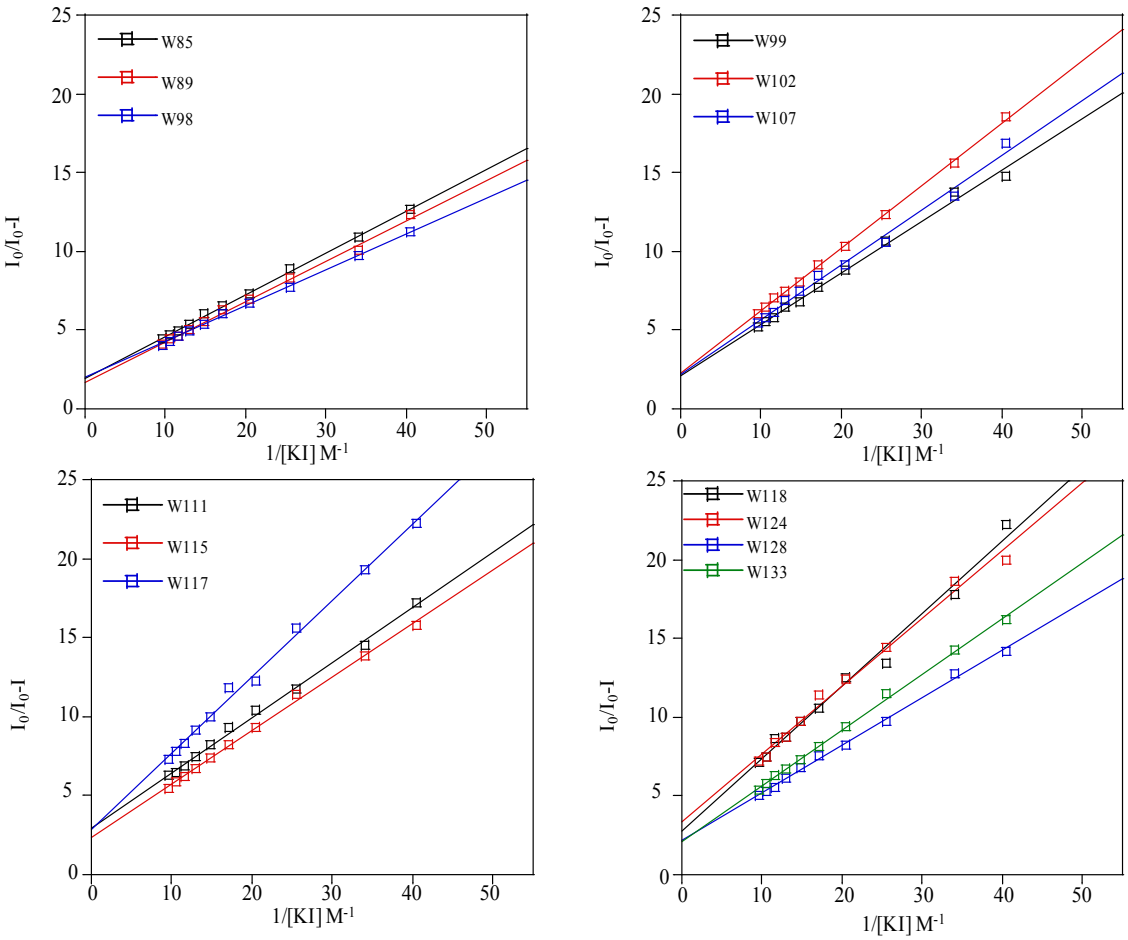

Figure 6-7. Modified Stern-Volmer plot used to evaluate the fractional accessibility of the fluorophore population for each single tryptophan mutant used in the study.

Importantly, the plots have are evaluated with respect to the indole-PE moiety which represents a headgroup accessible species. Clearly there is a similar trend among all determined parameters where there is decrease in the λ_{max}, K_{SV}, and f_a from residues 85-107 consistent with greater burial of the protein approaching the turn region. Interestingly, in both λ_{max} and K_{SV} values, there appears to be an upswing in these values around position 111. This could be indicative of the protein having crossed the bilayer center and started to enter the aqueous-headgroup region of the second leaflet. This would be in agreement with the simulation data from Chapter 3 which positioned the turn residues near the headgroup region of the second leaflet of the bilayer. After residue 111,

the data shows that the accessibility continues to decrease in terms of the λ_{max} and K_{SV}. The values began to increase again after residue 124. These trends are less pronounced in the fractional accessibility data which, due to large error bars show very little difference in accessibility in the 99-133 region. The W-shape of the overall plots is consistent with the horseshoe topology as a straight transmembrane helix would show a simple U-shape. However, it is likely that more evidence would be needed to fully support this conjecture. Importantly, all values probed were *significantly* lower than that determined for the indole-PE molecule. This indicates that the protein is buried at least as deep as the headgroup region from residues 85-133. These data are in agreement with the data in Chapter 3 indicating that the 87-107 region may be overall less buried than the 111-128 region, as the λ_{max} and K_{SV} values appear to be on average lower for region after the turn. Interestingly, W128 has a relatively red shifted λ_{max} in comparison to residues surrounding it (F124W and C133W). However if one looks at the K_{SV} and f_a values, they clearly show accessibilities that are more in line with the surrounding residues (compare this to W85 and F89W which have f_a and K_{SV} values that reflect the λ_{max}). This could be an indication that W128 is involved in a hydrogen bonding interaction. More data will be needed to support this conjecture. It is unlikely that the negatively charged tags would be influencing the quenching data as they are far removed from the sites scanned. The data agree nicely with values obtained on the shorter, tag-less caveolin-1 construct used in chapter 3 (residues 82-136) – with the major difference being W85 that is 8 nm blue shifted in this study. However, it may be that the truncated construct used in Chapter 3 results in improper burial as these data are also consistent with the simulation data. Although interesting, these mutants will need to be evaluated in terms of their ability to

behave like wild-type caveolin *in vivo* to be sure that they are not significantly altering the protein.

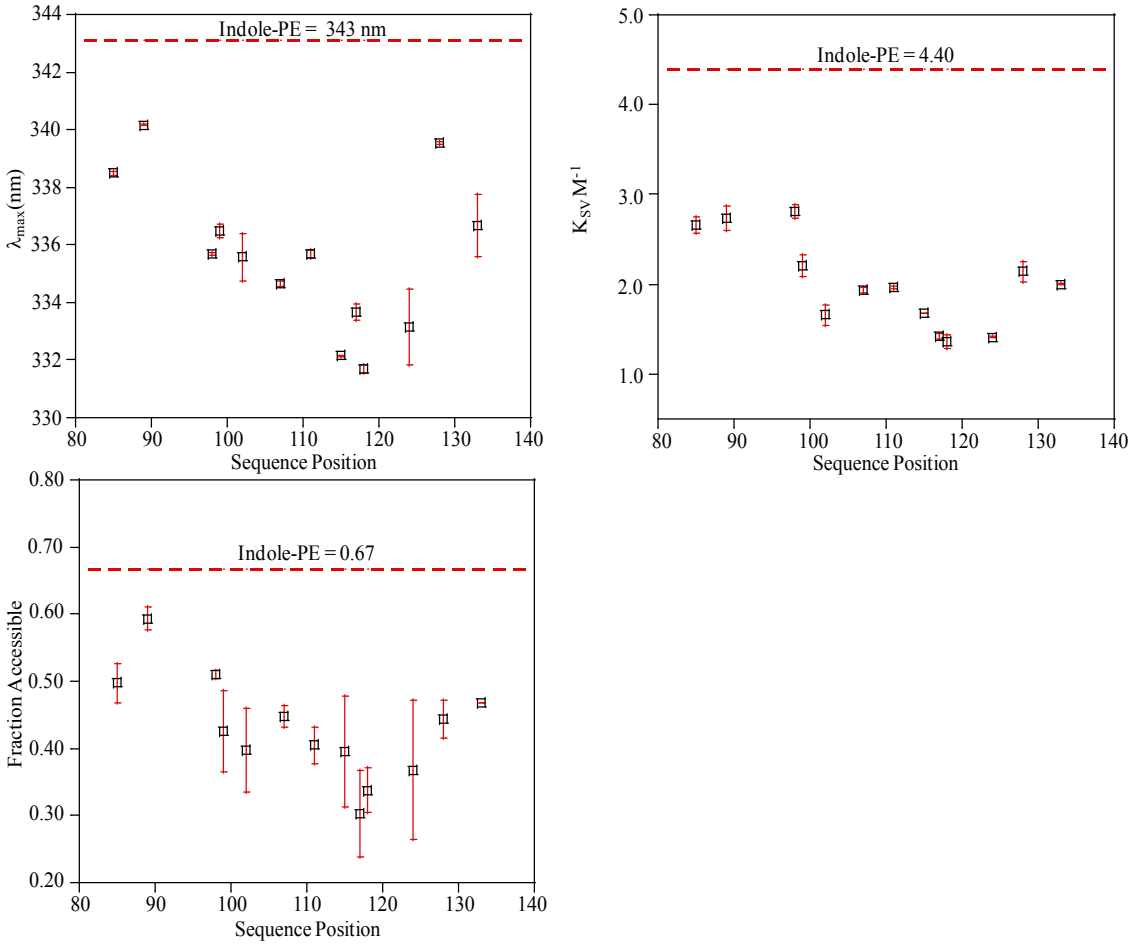

Figure 6-8. Examination of parameters (λ_{max}, K_{SV}, and Fraction accessible) for each mutant along the region of the protein scanned. All plots show similar trends in accessibility. Importantly, parameters determined for indole-PE (*red dashed line*) give an indication that each species is buried beneath the top of the headgroup region of the bicelles.

Construct	λ_{max} (nm)	K_{SV} (M^{-1})	f_a
Indole-PE	343.5 ± 0.9	4.40 ± 0.05	0.667 ± 0.030
W85	338.5 ± 0.1	2.66 ± 0.09	0.497 ± 0.030
F89W	340.2 ± 0.1	2.74 ± 0.13	0.593 ± 0.017
W98	335.7 ± 0.1	2.81 ± 0.07	0.511 ± 0.010
F99W	336.5 ± 0.2	2.21 ± 0.12	0.425 ± 0.060
L102W	335.6 ± 0.8	1.66 ± 0.11	0.398 ± 0.062
F107W	334.7 ± 0.1	1.94 ± 0.03	0.447 ± 0.017
M111W	335.7 ± 0.1	1.96 ± 0.01	0.405 ± 0.027
W115	332.1 ± 0.1	1.67 ± 0.01	0.395 ± 0.082
I117W	333.7 ± 0.3	1.42 ± 0.04	0.303 ± 0.065
Y118W	331.7 ± 0.1	1.36 ± 0.07	0.337 ± 0.033
F124W	333.14 ± 1.3	1.41 ± 0.01	0.368 ± 0.103
W128	339.6 ± 0.1	2.14 ± 0.11	0.443 ± 0.029
C133W	336.7 ± 1.1	2.00 ± 0.01	0.468 ± 0.001

Table 6-1. Averaged values of parameters determined for all fluorophores in the study (n = 2-3).

CONCLUSIONS

This chapter has provided a number of important findings. For the first time a *bonafide* indole-based marker for the headgroup region of the bilayer has been synthesized, purified to homogeneity, and characterized in terms of its usefulness in fluorescence studies of proteins embedded in phospholipid bilayers. Specifically, it was shown that both iodide and acrylamide fluorescence quenchers could be used in examinations of membrane protein burial within phospholipid vesicles but iodide may have to be used on a faster time scale as it diffuses through bilayers more readily. Additionally, the probe helped with interpretation of quenching data in phospholipid bicelles. This is important because, unlike vesicles and micelles, there is a dearth in the literature on the amount quenching that would be expected for a membrane protein with a tryptophan buried within a bicelle's bilayered region. These data showed that for thirteen caveolin-1 single tryptophan mutants, each was buried deeper than the top of the aqueous-headgroup interface, covering a span of 49 residues. This result agrees with the hydropathy plots which predicted this region to be buried in the 102-135 region. These data cannot differentiate between different degrees of membrane burial, this will likely require the synthesis of an indole probe that can be fixed within the center of the bilayer.

Appendix 6-1. Sequences of Protein Constructs Utilized

Construct	Protein Sequence
$^{HSVFLAG}Cav1_{62\text{-}178}$ (W85)	QPELAPEDPEDDYKDDDDKDVVKIDFEDVIAEP EGTHSFDGI**W**KASFTTFTVTKY**F**FYRLLSALFG IP**L**ALI**F**GIYFAILSFLHI**F**AVVPSIKSFLIEI QSISRVYSIYVHTVSDPLFEAVGKIFSNVRINL QKEIDYKDDDDKDGIQPELAPEDPED
$^{HSVFLAG}Cav1_{62\text{-}178}$ (F89W)	QPELAPEDPEDDYKDDDDKDVVKIDFEDVIAEP EGTHSFDGI**F**KAS**W**TTFTVTKY**F**FYRLLSALFG IP**L**ALI**F**GIYFAILSFLHI**F**AVVPSIKSFLIEI QSISRVYSIYVHTVSDPLFEAVGKIFSNVRINL QKEIDYKDDDDKDGIQPELAPEDPED
$^{HSVFLAG}Cav1_{62\text{-}178}$ (W98)	QPELAPEDPEDDYKDDDDKDVVKIDFEDVIAEP EGTHSFDGI**F**KASFTTFTVTKY**W**FYRLLSALFG IP**L**ALI**F**GIYFAILSFLHI**F**AVVPSIKSFLIEI QSISRVYSIYVHTVSDPLFEAVGKIFSNVRINL QKEIDYKDDDDKDGIQPELAPEDPED
$^{HSVFLAG}Cav1_{62\text{-}178}$ (F99W)	QPELAPEDPEDDYKDDDDKDVVKIDFEDVIAEP EGTHSFDGI**F**KASFTTFTVTKY**FW**YRLLSALFG IP**L**ALI**F**GIYFAILSFLHI**F**AVVPSIKSFLIEI QSISRVYSIYVHTVSDPLFEAVGKIFSNVRINL QKEIDYKDDDDKDGIQPELAPEDPED
$^{HSVFLAG}Cav1_{62\text{-}178}$ (L103W)	QPELAPEDPEDDYKDDDDKDVVKIDFEDVIAEP EGTHSFDGI**F**KASFTTFTVTKY**F**FYRL**W**SALFG IP**L**ALI**F**GIYFAILSFLHI**F**AVVPSIKSFLIEI QSISRVYSIYVHTVSDPLFEAVGKIFSNVRINL QKEIDYKDDDDKDGIQPELAPEDPED
$^{HSVFLAG}Cav1_{62\text{-}178}$ (F107W)	QPELAPEDPEDDYKDDDDKDVVKIDFEDVIAEP EGTHSFDGI**F**KASFTTFTVTKY**F**FYRLLSAL**W**G IP**L**ALI**F**GIYFAILSFLHI**F**AVVPSIKSFLIEI QSISRVYSIYVHTVSDPLFEAVGKIFSNVRINL QKEIDYKDDDDKDGIQPELAPEDPED
$^{HSVFLAG}Cav1_{62\text{-}178}$ (M111W)	QPELAPEDPEDDYKDDDDKDVVKIDFEDVIAEP EGTHSFDGI**F**KASFTTFTVTKY**F**FYRLLSALFG IP**W**ALI**F**GIYFAILSFLHI**F**AVVPSIKSFLIEI QSISRVYSIYVHTVSDPLFEAVGKIFSNVRINL QKEIDYKDDDDKDGIQPELAPEDPED
$^{HSVFLAG}Cav1_{62\text{-}178}$ (W115)	QPELAPEDPEDDYKDDDDKDVVKIDFEDVIAEP EGTHSFDGIFKASFTTFTVTKY**F**FYRLLSALFG IP**L**ALI**W**GIYFAILSFLHI**F**AVVPSIKSFLIEI QSISRVYSIYVHTVSDPLFEAVGKIFSNVRINL QKEIDYKDDDDKDGIQPELAPEDPED
$^{HSVFLAG}Cav1_{62\text{-}178}$ (I117W)	QPELAPEDPEDDYKDDDDKDVVKIDFEDVIAEP EGTHSFDGI**F**KASFTTFTVTKY**F**FYRLLSALFG IP**L**ALI**F**G**W**YFAILSFLHI**F**AVVPSIKSFLIEI QSISRVYSIYVHTVSDPLFEAVGKIFSNVRINL QKEIDYKDDDDKDGIQPELAPEDPED

$^{HSVFLAG}Cav1_{62\text{-}178}$ (Y118W)	QPELAPEDPEDDYKDDDDKDVVKIDFEDVIAEP EGTHSFDGI**F**KASFTTFTVTKY**F**FYRLLSALFG IP**L**ALI**F**GI**W**FAILSFLHI**F**AVVPSIKSFLIEI QSISRVYSIYVHTVSDPLFEAVGKIFSNVRINL QKEIDYKDDDDKDGIQPELAPEDPED
$^{HSVFLAG}Cav1_{62\text{-}178}$ (F124W)	QPELAPEDPEDDYKDDDDKDVVKIDFEDVIAEP EGTHSFDGI**F**KASFTTFTVTKY**F**FYRLLSALFG IP**L**ALI**F**GIYFAILS**W**LHI**F**AVVPSIKSFLIEI QSISRVYSIYVHTVSDPLFEAVGKIFSNVRINL QKEIDYKDDDDKDGIQPELAPEDPED
$^{HSVFLAG}Cav1_{62\text{-}178}$ (W128)	QPELAPEDPEDDYKDDDDKDVVKIDFEDVIAEP EGTHSFDGI**F**KASFTTFTVTKY**F**FYRLLSALFG IP**L**ALI**F**GIYFAILSFLHI**W**AVVPSIKSFLIEI QSISRVYSIYVHTVSDPLFEAVGKIFSNVRINL QKEIDYKDDDDKDGIQPELAPEDPED
$^{HSVFLAG}Cav1_{62\text{-}178}$ (C133W)	QPELAPEDPEDDYKDDDDKDVVKIDFEDVIAEP EGTHSFDGI**F**KASFTTFTVTKY**F**FYRLLSALFG IP**L**ALI**F**GIYFAILSFLHI**F**AVVPSIK**W**FLIEI QSISRVYSIYVHTVSDPLFEAVGKIFSNVRINL QKEIDYKDDDDKDGIQPELAPEDPED

Appendix 6-2. Mutagenesis Primers Utilized

Construct	Primer Sequence
W85	5’-CTCTTTCGACGGTATCTGGAAAGCGTCTTTCACCAC-3’
F89W	5’-GTATCTTCAAAGCGTCTTGGACCACCTTCACCGTTAC-3’
W98	5’-CACCGTTACCAAATACTGGTTCTACCGTCTGCTGTC-3’
F99W	5’-CGTTACCAAATACTTCTGGTACCGTCTGCTGTCTG-3’
L102W	5’-CAAATACTTCTTCTACCGTTGGCTGTCTGCGCTGTTCGG-3’
F107W	5’-GCTGTCTGCGCTGTGGGGTATCCCGCTGG-3’
M111W	5’-GCTGTTCGGTATCCCGTGGGCGCTGATCTTCGG-3’
W115	5’-CTGGCGCTGATCTGGGGTATCTACTTCGC-3’
I117W	5’-GCGCTGATCTTCGGTTGGTACTTCGCGATCCTG-3’
Y118W	5’-GCTGATCTTCGGTATCTGGTTCGCGATCCTGTCTTTC-3’
F124W	5’-CGCGATCCTGTCTTGGCTGCACATCTTCGC-3’
W128	5’-GTCTTTCCTGCACATCTGGGCGGTTGTTCCGTCTATC-3’
C133W	5’-CTTCGCGGTTGTTCCGTGGATCAAATCTTTCCTGATC-3’

References

1. Palade GE (1953) Fine structure of blood capillaries. J. Appl. Physiol. 24:1424.

2. Yamada E (1955) The fine structure of the gall bladder epithelium of the mouse. J Biophys. Biochem. Cytol. 1:445-447.

3. Mobley BA, Eisenberg BR (1975) Sizes of components in frog skeletal muscle measured by methods of stereology. J. Gen. Physiol. 66:31-45.

4. Thorn H, Stenkula KG, Karlsson M, Ortegren U, Nystorm F, Gustavsson J, Stralfors P (2003) Cell surface orifices of caveolae and localization of caveolin to the necks of caveolae in adipocytes. Mol. Biol. Cell. 14:3967-3976.

5. Wheaton K, Sampsel K, Boisvert F, Davy A, Robbins S, Riabowol K (2001) Loss of functional caveolae during senescence of human fibroblasts. J. Cell Physiol. 187:226-235.

6. Kirkham M, Nixon SJ, Howes MT, Abi-Rached L, Wakeham DE, Hanzal-Bayer M, Ferguson C, Hill MM, Fernandez-Rojo M, Brown DA, Hancock JF, Brodsky FM, Parton RG (2008) Evolutionary analysis and molecular dissection of caveola biogenesis. J. Cell. Sci. 121:2075-2086.

7. Chang WJ, Ying YS, Rothberg KG, Hooper NM, Turner AJ, Gambliel HA, De Gunzburg J, Mumby SM, Gilman AG, Anderson RG (1994) Purification and characterization of smooth muscle cell caveolae. J. Cell Biol. 126:127-138.

8. Lisanti MP, Scherer PE, Vidugiriene J, Tang ZL, Hermanowskivosatka A, Tu YH, Cook RF, Sargiacomo M (1994) Characterization of caveolin-rich membrane domains isolated from an endothelial-rich source - implications for human-disease. J. Cell Biol. 126:111-126.

9. Liu J, Oh P, Horner T, Rogers RA, Schnitzer JE (1997) Organized endothelial cell surface signal transduction in caveolae distinct from glycosylphosphatidylinositol-anchored protein microdomains. J. Biol. Chem. 272:7211-7222.

10. Parton RG, Joggerst B, Simons K (1994) Regulated internalization of caveolae. J. Cell. Biol. 127:1199-1215.

11. Sinha B, KÃ¶ster D, Ruez R, Gonnord P, Bastiani M, Abankwa D, Stan RV, Butler-Browne G, Vedie B, Johannes L, Morone N, Parton RG, Raposo G, Sens P, Lamaze C, Nassoy P (2011) Cells respond to mechanical stress by rapid disassembly of caveolae. Cell. 144:402-413.

12. Kiss A (2012) Caveolae and the regulation of endocytosis. Adv. Exp. Med. Biol. 729:14-28.

13. Pelkmans L, Puntener D, Helenius A (2002) Local actin polymerization and dynamin recruitment in SV40-induced internalization of caveolae. Science. 296:535-539.

14. Pelkmans L, Kartenbeck J, Helenius A (2001) Caveolar endocytosis of simian virus 40 reveals a new two-step vesicular-transport pathway to the ER. Nat. Cell Biol. 3:473-483.

15. Marjomaki V, Pietiainen V, Matilainen H, Upla P, Ivaska J, Nissinen L, Reunanen H, Huttunen P, Hyypia T, Heino J (2002) Internalization of echovirus 1 in caveolae. J. Virol. 76:1856-1865.

16. Drab M, Verkade P, Elger M, Kasper M, Lohn M, Lauterbach B, Menne J, Lindschau C, Mende F, Luft FC, Schedl A, Haller H, Kurzchalia TV (2001) Loss of caveolae, vascular dysfunction, and pulmonary defects in caveolin-1 gene-disrupted mice. Science. 293:2449-2452.

17. Li SW, Couet J, Lisanti MP (1996) Src tyrosine kinases, G(alpha) subunits, and H-ras share a common membrane-anchored scaffolding protein, caveolin - caveolin binding negatively regulates the auto-activation of src tyrosine kinases. J Biol. Chem. 271:29182-29190.

18. Couet J, Li SW, Okamoto T, Ikezu T, Lisanti MP (1997) Identification of peptide and protein ligands for the caveolin-scaffolding domain - implications for the interaction of caveolin with caveolae-associated proteins. J Biol. Chem. 272:6525-6533.

19. Murata M, Peranen J, Schreiner R, Wieland F, Kurzchalia TV, Simons K (1995) Vip21/Caveolin is a cholesterol-binding protein. Proc. Natl. Acad. Sci. U. S. A. 92:10339-10343.

20. Smart E, Ying Y., Donzell W., Anderson R.G. (1996) A role for caveolin in transport of cholesterol from endoplasmic reticulum to plasma membrane. J Biol. Chem. 271(46):29427-29435.

21. Sargiacomo M, Scherer PE, Tang Z, Kubler E, Song KS, Sanders MC, Lisanti MP (1995) Oligomeric structure of caveolin: Implications for caveolae membrane organization. Proc. Natl. Acad. Sci. U. S. A. 92:9407-9411.

22. Krijnse Locker J, Schmid SL (2013) Integrated electron microscopy: Super-duper resolution. PLoS Biol. 11:e1001639.

23. Stan R (2005) Structure of caveolae. Biochim. Biophys. Acta. 1746:334-348.

24. Sonnino S, Prinetti A (2009) Sphingolipids and membrane environments for caveolin. FEBS Lett. 583:597-606.

25. Ortegren U, Yin L, Ost A, Karlsson H, Nystrom FH, Stralfors P (2006) Separation and characterization of caveolae subclasses in the plasma membrane of primary adipocytes; segregation of specific proteins and functions. FEBS J. 273:3381-3392.

26. Ortegren U, Karlsson M, Blazic N, Blomqvist M, Nystrom FH, Gustavsson J, Fredman P, Stralfors P (2004) Lipids and glycosphingolipids in caveolae and surrounding plasma membrane of primary rat adipocytes. Eur. J. Biochem. 271:2028-2036.

27. Chao WT, Fan SS, Chen JK, Yang VC (2003) Visualizing caveolin-1 and HDL in cholesterol-loaded aortic endothelial cells. J. Lipid Res. 44:1094-9.

28. Frank PG, Cheung MWC, Pavlides S, Llaverias G, Park DS, Lisanti MP (2006) Caveolin-1 and regulation of cellular cholesterol homeostasis. Am. J. Heart Circ.Physiol. 291:H677-H686.

29. Walser PJ , Ariotti N , Howes M , Ferguson C , Webb R , Schwudke D , Leneva N , Cho KJ , Cooper L , Rae J , Floetenmeyer M , Oorschot VM , Skoglund U , Simons K , Hancock JF , Parton RG. (2012) Constitutive formation of caveolae in bacterium. Cell. 150:752-763.

30. Fra AM, Williamson E, Simons K, Parton RG (1995) De novo formation of caveolae in lymphocytes by expression of VIP21-caveolin. Proc. Natl. Acad. Sci. U. S. A. 92:8655-8659.

31. Spisni E, Tomasi V, Cestaro A, Tosatto SC (2005) Structural insights into the function of human caveolin 1. Biochem. Biophys. Res. Commun. 338:1383-1390.

32. Tang ZL, Okamoto T, Boontrakulpoontawee P, Katada T, Otsuka AJ, Lisanti MP (1997) Identification, sequence, and expression of an invertebrate caveolin gene family from the nematode caenorhabditis elegans - implications for the molecular evolution of mammalian caveolin genes. J Biol. Chem. 272:2437-2445.

33. Nixon SJ, Wegner J, Ferguson C, Mery PF, Hancock JF, Currie PD, Key B, Westerfield M, Parton RG (2005) Zebrafish as a model for caveolin-associated muscle disease; caveolin-3 is required for myofibril organization and muscle cell patterning. Hum. Mol. Genet. 14:1727-1743.

34. Scherer PE, Tang ZL, Chun MY, Sargiacomo M, Lodish HF, Lisanti MP (1995) Caveolin isoforms differ in their N-terminal protein-sequence and subcellular-distribution - identification and epitope mapping of an isoform-specific monoclonal-antibody probe. J. Biol. Chem. 270:16395-16401.

35. Dietzen DJ, Hastings WR, Lublin DM (1995) Caveolin is palmitoylated on multiple cysteine residues. palmitoylation is not necessary for localization of caveolin to

caveolae. J. Biol. Chem. 270:6838-6842.

36. Scherer PE, Lewis RY, Volonte D, Engelman JA, Galbiati F, Couet J, Kohtz DS, vanDonselaar E, Peters P, Lisanti MP (1997) Cell-type and tissue-specific expression of caveolin-2 - caveolins 1 and 2 co-localize and form a stable hetero-oligomeric complex in vivo. J. Biol. Chem. 272:29337-29346.

37. Way M, Parton RG (1995) M-caveolin, a muscle-specific caveolin-related protein. . FEBS Lett. 376:108-112.

38. Song KS, Scherer PE, Tang ZL, Okamoto T, Li SW, Chafel M, Chu C, Kohtz DS, Lisanti MP (1996) Expression of caveolin-3 in skeletal, cardiac, and smooth muscle cells - caveolin-3 is a component of the sarcolemma and co-fractionates with dystrophin and dystrophin-associated glycoproteins. J. Biol. Chem. 271:15160-15165.

39. Tang ZL, Scherer PE, Okamoto T, Song K, Chu C, Kohtz DS, Nishimoto I, Lodish HF, Lisanti MP (1996) Molecular cloning of caveolin-3, a novel member of the caveolin gene family expressed predominantly in muscle. J. Biol. Chem. 271:2255-2261.

40. Schlegel A, Lisanti MP (2000) A molecular dissection of caveolin-1 membrane attachment and oligomerization - two separate regions of the caveolin-1 C-terminal domain mediate membrane binding and oligomer/oligomer interactions in vivo. J. Biol. Chem. 275:21605-21617.

41. Das K, Lewis RY, Scherer PE, Lisanti MP (1999) The membrane-spanning domains of caveolins-1 and -2 mediate the formation of caveolin hetero-oligomers. implications for the assembly of caveolae membranes in vivo. J. Biol. Chem. 274:18721-8.

42. Sargiacomo M, Scherer PE, Tang Z, Kübler E, Song KS, Sanders MC, Lisanti MP (1995) Oligomeric structure of caveolin: Implications for caveolae membrane organization. Proc. Natl. Acad. Sci. U. S. A. 92:9407-9411.

43. Rieth MD, Lee J, Glover KJ (2012) Probing the caveolin-1 P132L mutant: Critical insights into its oligomeric behavior and structure. Biochemistry. 51:3911-3918.

44. Hill M, Bastiani M, Luetterforst R, Kirkham M, Kirkham A, Nixon S, Walser P, Abankwa D, Oorschot V, Martin S, Hancock J, Parton R (2008) PTRF-cavin, a conserved cytoplasmic protein required for caveola formation and function. Cell. 132:113-124.

45. Bastiani M, Liu L, Hill MM, Jedrychowski MP, Nixon SJ, Lo HP, Abankwa D, Luetterforst R, Fernandez-Rojo M, Breen MR, Gygi SP, Vinten J, Walser PJ, North KN, Hancock JF, Pilch PF, Parton RG (2009) MURC/Cavin-4 and cavin family

members form tissue-specific caveolar complexes. J. Cell. Biol. 185:1259-1273.

46. Sengupta D (2012) Cholesterol modulates the structure, binding modes, and energetics of caveolin-membrane interactions. J. Phys. Chem. B. 116:14556-14564.

47. Capozza F, Combs TP, Cohen AW, Cho YR, Park SY, Schubert W, Williams TM, Brasaemle DL, Jelicks LA, Scherer PE, Kim JK, Lisanti MP (2005) Caveolin-3 knockout mice show increased adiposity and whole body insulin resistance, with ligand-induced insulin receptor instability in skeletal muscle. Am. J. Physiol. Cell Physiol. 288:C1317-C1331.

48. Capozza F, Combs T, Cho YR, Cohen AW, Jelicks LA, Scherer PE, Kim JK, Lisanti MP (2005) Caveolin-3 KO mice show increased adiposity and whole-body insulin resistance, with impaired insulin signaling in skeletal muscle. Diabetes. 54:A643-A643.

49. Cohen AW, Combs TP, Scherer PE, Lisanti MP (2003) Role of caveolin and caveolae in insulin signaling and diabetes. Am. J. Physiol. Endocrinol. Metab. 285:E1151-E1160.

50. Fernández-Hernando C, Yu J, Dávalos A, Prendergast J, Sessa WC (2010) Endothelial-specific overexpression of caveolin-1 accelerates atherosclerosis in apolipoprotein E-deficient mice. Am. J. Pathol. 177:998-1003.

51. Komers R, Schutzer WE, Reed JF, Lindsley JN, Oyama TT, Buck DC, Mader SL, Anderson S (2006) Altered endothelial nitric oxide synthase targeting and conformation and caveolin-1 expression in the diabetic kidney. Diabetes. 55:1651-1658.

52. Sotgia F, Rui H, Bonuccelli G, Mercier I, Pestell RG, Lisanti MP (2006) Caveolin-1, mammary stem cells, and estrogen-dependent breast cancers. Cancer Res. 66:10647-10651.

53. Weiss N, Couchoux H, Legrand C, Berthier C, Allard B, Jacquemond V (2008) Expression of the muscular dystrophy-associated caveolin-3(P104L) mutant in adult mouse skeletal muscle specifically alters the ca(2+) channel function of the dihydropyridine receptor. Pflugers Arch. 457:361-75.

54. Williams TM, Sotgia F, Lee H, Hassan G, Di Vizio D, Bonuccelli G, Capozza F, Mercier I, Rui H, Pestell RG, Lisanti MP (2006) Stromal and epithelial caveolin-1 both confer a protective effect against mammary hyperplasia and tumorigenesis: Caveolin-1 antagonizes cyclin D1 function in mammary epithelial cells. Am. J. Pathol. 169:1784-1801.

55. Williams TM, Lisanti MP (2005) Caveolin-1 in oncogenic transformation, cancer, and metastasis. Am. J. Physiol. Cell Physiol. 288:C494-C506.

56. Xia H, Khalil W, Kahm J, Jessurun J, Kleidon J, Henke CA (2010) Pathologic caveolin-1 regulation of PTEN in idiopathic pulmonary fibrosis. Am. J. Pathol. 176:2626-2637.

57. Williams TM, Hassan GS, Li JW, Cohen AW, Medina F, Frank PG, Pestell RG, Di Vizio D, Loda M, Lisanti MP (2005) Caveolin-1 promotes tumor progression in an autochthonous mouse model of prostate cancer - genetic ablation of cav-1 delays advanced prostate tumor development in tramp mice. J. Biol. Chem. 280:25134-25145.

58. Sloan EK, Stanley KL, Anderson RL (2004) Caveolin-1 inhibits breast cancer growth and metastasis. Oncogene. 23:7893-7897.

59. Williams TM, Cheung MWC, Park DS, Razani B, Cohen AW, Muller WJ, Di Vizio D, Chopra NG, Pestell RG, Lisanti MP (2003) Loss of caveolin-1 gene expression accelerates the development of dysplastic mammary lesions in tumor-prone transgenic mice. Mol. Biol. Cell. 14:1027-1042.

60. Bonuccelli G, Casimiro MC, Sotgia F, Wang C, Liu M, Katiyar S, Zhou J, Dew E, Capozza F, Daumer KM, Minetti C, Milliman JN, Alpy F, Rio MC, Tomasetto C, Mercier I, Flomenberg N, Frank PG, Pestell RG, Lisanti MP (2009) Caveolin-1 (P132L), a common breast cancer mutation, confers mammary cell invasiveness and defines a novel stem cell/metastasis-associated gene signature. Am J Pathol 174:1650-1662.

61. Mercier I, Bryant KG, Sotgia F, Bonuccelli G, Witkiewicz AK, Dasgupta A, Jasmin JF, Pestell RG, Lisanti MP (2009) Using caveolin-1 epithelial immunostaining patterns to stratify human breast cancer patients and predict the caveolin-1 (P132L) mutation. Cell Cycle 8:1396-1401.

62. Ohsawa Y, Toko H, Katsura M, Morimoto K, Yamada H, Ichikawa Y, Murakami T, Ohkuma S, Komuro I, Sunada Y (2004) Overexpression of P104L mutant caveolin-3 in mice develops hypertrophic cardiomyopathy with enhanced contractility in association with increased endothelial nitric oxide synthase activity. Hum. Mol. Genet. 13:151-157.

63. Stoppani E, Rossi S, Meacci E, Penna F, Costelli P, Bellucci A, Faggi F, Maiolo D, Monti E, Fanzani A (2011) Point mutated caveolin-3 form (P104L) impairs myoblast differentiation via akt and p38 signalling reduction, leading to an immature cell signature. Biochim. Biophys. Acta. 1812:468-479.

64. Fielding PE, Chau P, Liu D, Spencer TA, Fielding CJ (2004) Mechanism of platelet-derived growth factor-dependent caveolin-1 phosphorylation: Relationship to sterol

binding and the role of serine-80. Biochemistry. 43:2578-2586.

65. Fernandez I, Ying Y, Albanesi J, Anderson RG (2002) Mechanism of caveolin filament assembly. Proc. Natl. Acad. Sci. U.S.A. 99:11193-11198.

66. Parton RG, Hanzal-Bayer M, Hancock JF (2006) Biogenesis of caveolae: A structural model for caveolin-induced domain formation. J. Cell Sci. 119:787-796.

67. Le Lan C, Gallay J, Vincent M, Neumann JM, de Foresta B, Jamin N (2010) Structural and dynamic properties of juxta-membrane segments of caveolin-1 and caveolin-2 at the membrane interface. Eur. Biophys. J. 39:307-325.

68. Lan CL, Neumann J, Jamin N (2006) Role of the membrane interface on the conformation of the caveolin scaffolding domain: A CD and NMR study. FEBS Lett. 580:5301-5305.

69. Hoop CL, Sivanandam VN, Kodali R, Srnec MN, van der Wel PC (2012) Structural characterization of the caveolin scaffolding domain in association with cholesterol-rich membranes. Biochemistry. 51:90-99.

70. Lee J, Glover KJ (2012) The transmembrane domain of caveolin-1 exibits a helix-break-helix structure. Biochim. Biophys. Acta. 1818:1158-1164.

71. Dupree P, Parton RG, Raposo G, Kurzchalia TV, Simons K (1993) Caveolae and sorting in the trans-golgi network of epithelial cells. Embo. J. 12:1597-1605.

72. Schlegel A, Schwab RB, Scherer PE, Lisanti MP (1999) A role for the caveolin scaffolding domain in mediating the membrane attachment of caveolin-1 - the caveolin scaffolding domain is both necessary and sufficient for membrane binding in vitro. J. Biol. Chem. 274:22660-22667.

73. Sargiacomo M, Sudol M, Tang Z, Lisanti MP (1993) Signal transducing molecules and glycosyl-phosphatidylinositol-linked proteins form a caveolin-rich insoluble complex in MDCK cells. J. Cell. Biol. 122:789-807.

74. Monier S, Parton RG, Vogel F, Behlke J, Henske A, Kurzchalia TV (1995) VIP21-caveolin, a membrane protein constituent of the caveolar coat, oligomerizes in vivo and in vitro. Mol. Biol. Cell. 6:911-927.

75. Aoki S, Epand RM (2012) Caveolin-1 hydrophobic segment peptides insertion into membrane mimetic systems: Role of proline residue. Biochim. Biophys. Acta. 1818:12-18.

76. Norholm MH, Shulga YV, Aoki S, Epand RM, von Heijne G (2011) Flanking residues help determine whether a hydrophobic segment adopts a monotopic or bitopic topology in the endoplasmic reticulum membrane. J. Biol. Chem. 286:25284-

25290.

77. Aoki S, Thomas A, Decaffmeyer M, Brasseur R, Epand R (2010) The role of proline in the membrane re-entrant helix of caveolin-1. J. Biol. Chem. 285:33371-33380.

78. McMahon HT, Gallop JL (2005) Membrane curvature and mechanisms of dynamic cell membrane remodelling. Nature. 438:590-596.

79. Chen Z, Rand RP (1997) The influence of cholesterol on phospholipid membrane curvature and bending elasticity. Biophys. J. 73:267-276.

80. Zimmerberg J, Kozlov MM (2006) How proteins produce cellular membrane curvature. Nat. Rev. Mol. Cell Biol. 7:9-19.

81. Zurek N, Sparks L, Voeltz G (2011) Reticulon short hairpin transmembrane domains are used to shape ER tubules. Traffic. 12:28-41.

82. Voeltz GK, Prinz WA, Shibata Y, Rist JM, Rapoport TA (2006) A class of membrane proteins shaping the tubular endoplasmic reticulum. Cell. 124:573-586.

83. von Heijne G (2007) The membrane protein universe: What's out there and why bother? J. Intern. Med. 261:543-57.

84. von Heijne G (2007) Membrane proteins up for grabs. Nat. Biotechnol. 25:646-7.

85. Carpenter EP, Beis K, Cameron AD, Iwata S (2008) Overcoming the challenges of membrane protein crystallography. Curr. Opin. Struct. Biol. 18:581-586.

86. Shaul PW, Smart EJ, Robinson LJ, German Z, Yuhanna IS, Ying Y, Anderson RG, Michel T (1996) Acylation targets emdothelial nitric-oxide synthase to plasmalemmal caveolae. J Biol Chem 271:6518-6522.

87. Kiefhaber T, Rudolph R, Kohler HH, Buchner J (1991) Protein aggregation in vitro and in vivo: A quantitative model of the kinetic competition between folding and aggregation. Biotechnology (N Y). 9:825-829.

88. Orsini G, Goldberg ME (1978) The renaturation of reduced chymotrypsinogen A in guanidine HCl. refolding versus aggregation. J. Biol. Chem. 253:3453-3458.

89. Zettlmeissl G, Rudolph R, Jaenicke R (1979) Reconstitution of lactic dehydrogenase. noncovalent aggregation vs. reactivation. 1. physical properties and kinetics of aggregation. Biochemistry. 18:5567-5571.

90. Burgess NK, Dao TP, Stanley AM, Fleming KG (2008) Beta-barrel proteins that reside in the escherichia coli outer membrane in vivo demonstrate varied folding

behavior in vitro. J. Biol. Chem. 283:26748-26758.

91. Tanford C, Reynolds JA (1976) Characterization of membrane proteins in detergent solutions. Biochim. Biophys. Acta. 457:133-70.

92. Chung KY, Kim TH, Manglik A, Alvares R, Kobilka BK, Prosser RS (2012) Role of detergents in conformational exchange of a G protein-coupled receptor. J. Biol. Chem. 287:36305-36311.

93. Whiles JA, Glover KJ, Vold RR, Komives EA (2002) Methods for studying transmembrane peptides in bicelles: Consequences of hydrophobic mismatch and peptide sequence. J. Magn. Reson. 158:149-156.

94. Whiles JA, Deems R, Vold RR, Dennis EA (2002) Bicelles in structure-function studies of membrane-associated proteins. Bioorg. Chem. 30:431-442.

95. Glover KJ, Whiles JA, Vold RR, Melacini G (2002) Position of residues in transmembrane peptides with respect to the lipid bilayer: A combined lipid NOEs and water chemical exchange approach in phospholipid bicelles. J. Biomol. NMR. 22:57-64.

96. Mimms LT, Zampighi G, Nozaki Y, Tanford C, Reynolds JA (1981) Phospholipid vesicle formation and transmembrane protein incorporation using octyl glucoside. Biochemistry. 20:833-40.

97. Oliver RC, Lipfert J, Fox DA, Lo RH, Doniach S, Columbus L (2013) Dependence of micelle size and shape on detergent alkyl chain length and head group. PLoS One. 8:e62488.

98. Moraes I, Evans G, Sanchez-Weatherby J, Newstead S, Stewart PD (2014) Membrane protein structure determination - the next generation. Biochim. Biophys. Acta. 1838:78-87.

99. Ng HQ, Kim YM, Huang Q, Gayen S, Yildiz AA, Yoon HS, Sinner E, Kang C (2012) Purification and structural characterization of the voltage-sensor domain of the hERG potassium channel. Protein. Expr. Purif. 86:98-104.

100. Vukoti K, Kimura T, Macke L, Gawrisch K, Yeliseev A (2012) Stabilization of functional recombinant cannabinoid receptor CB(2) in detergent micelles and lipid bilayers. PLoS One. 7:e46290.

101. Kessi J, Poiree JC, Wehrli E, Bachofen R, Semenza G, Hauser H (1994) Short-chain phosphatidylcholines as superior detergents in solubilizing membrane proteins and preserving biological activity. Biochemistry. 33:10825-10836.

102. Van Horn WD, Ogilvie ME, Flynn PF (2008) Use of reverse micelles in membrane protein structural biology. J. Biomol. NMR. 40:203-211.

103. Sanders CR, Hoffmann AK, Grayn DN, Keyes MH, Ellis CD (2004) French swimwear for membrane proteins. Chembiochem. 5:423-426.

104. Menger, F.M., and Doll, D.W. (1984) On the structure of micelles. J. Am. Chem. Soc. 106:1109-1113.

105. Howell SC, Mittal R, Huang L, Travis B, Breyer RM, Sanders CR (2010) CHOBIMALT: A cholesterol-based detergent. Biochemistry. 49(44):9572-9583.

106. Chou JJ, Baber JL, Bax A (2004) Characterization of phospholipid mixed micelles by translational diffusion. J. Biomol. NMR. 29:299-308.

107. Gutmann DA, Mizohata E, Newstead S, Ferrandon S, Postis V, Xia X, Henderson PJ, van Veen HW, Byrne B (2007) A high-throughput method for membrane protein solubility screening: The ultracentrifugation dispersity sedimentation assay. Protein. Sci. 16:1422-1428.

108. Tonazzi A, Galluccio M, Oppedisano F, Indiveri C (2006) Functional reconstitution into liposomes and characterization of the carnitine transporter from rat liver microsomes. Biochim. Biophys. Acta. 1758:124-131.

109. Read JA, Duncan R (2011) Biophysical and functional assays for viral membrane fusion peptides. Methods. 55:122-126.

110. Hung SC, Wang W, Chan SI, Chen HM (1999) Membrane lysis by the antibacterial peptides cecropins B1 and B3: A spin-label electron spin resonance study on phospholipid bilayers. Biophys. J. 77:3120-3133.

111. Surrey T, Jahnig F (1992) Refolding and oriented insertion of a membrane protein into a lipid bilayer. Proc. Natl. Acad. Sci. U.S.A. 89:7457-61.

112. Zucker SD, Goessling W, Bootle EJ, Sterritt C (2001) Localization of bilirubin in phospholipid bilayers by parallax analysis of fluorescence quenching. J. Lipid. Res. 42:1377-1388.

113. Sanders CR, Prosser RS (1998) Bicelles: A model membrane system for all seasons? Structure. 6:1227-1234.

114. Vold RR, Prosser RS (1996) Magnetically oriented phospholipid bilayered micelles for structural studies of polypeptides. does the ideal bicelle exist? J Magn Reson Ser B. 113:267-271.

115. Whiles JA, Glover KJ, Vold RR, Komives EA (2002) Methods for studying transmembrane peptides in bicelles: Consequences of hydrophobic mismatch and peptide sequence. J. Magn. Reson. 158:149-156.

116. Glover KJ, Whiles JA, Wu G, Yu N, Deems R, Struppe JO, Stark RE, Komives EA, Vold RR (2001) Structural evaluation of phospholipid bicelles for solution-state studies of membrane-associated biomolecules. Biophys. J. 81:2163-71.

117. Struppe J, Whiles JA, Vold RR (2000) Acidic phospholipid bicelles: A versatile model membrane system. Biophys.l J. 78:281-289.

118. Song Y, Hustedt EJ, Brandon S, Sanders CR (2013) Competition between homodimerization and cholesterol binding to the C99 domain of the amyloid precursor protein. Biochemistry. 52:5051-5064.

119. Yuanli Song , Kathleen F. Mittendorf , Zhenwei Lu , and Charles R. Sanders (2014) Impact of bilayer lipid composition on the structure and topology of the transmembrane amyloid precursor C99 protein. J. Am. Chem. Soc. 136 (11):4093-4096.

120. Yamaguchi T, Suzuki T, Yasuda T, Oishi T, Matsumori N, Murata M (2012) NMR-based conformational analysis of sphingomyelin in bicelles. Bioorg. Med. Chem. 20:270-278.

121. Triba MN, Devaux PF, Warschawski DE (2006) Effects of lipid chain length and unsaturation on bicelles stability. A phosphorus NMR study. Biophys. J. 91:1357-1367.

122. Glover KJ, Whiles JA, Vold RR, Melacini G (2002) Position of residues in transmembrane peptides with respect to the lipid bilayer: A combined lipid noes and water chemical exchange approach in phospholipid bicelles. J. Biomol. NMR. 22:57-64.

123. Glover KJ, Whiles JA, Wood MJ, Melacini G, Komives EA, Vold RR (2001) Conformational dimorphism and transmembrane orientation of prion protein residues 110-136 in bicelles. Biochemistry. 40:13137-42.

124. Whiles JA, Brasseur R, Glover KJ, Melacini G, Komives EA, Vold RR (2001) Orientation and effects of mastoparan X on phospholipid bicelles. Biophys. J. 80:280-293.

125. Dror RO, Green HF, Valant C, Borhani DW, Valcourt JR, Pan AC, Arlow DH, Canals M, Lane JR, Rahmani R, Baell JB, Sexton PM, Christopoulos A, Shaw DE (2013) Structural basis for modulation of a G-protein-coupled receptor by allosteric drugs. Nature. 14;503(7475):295-299.

126. Kelly SM, Price NC (2000) The use of circular dichroism in the investigation of protein structure and function. Curr. Protein. Pept. Sci. 1:349-384.

127. Lakowicz JR. Principles of fluorescence spectroscopy. 3rd ed. New York: Springer; 2006.

128. Asuncion-Punzalan E, Kachel K, London E (1998) Groups with polar characteristics can locate at both shallow and deep locations in membranes: The behavior of dansyl and related probes. Biochemistry. 37:4603-4611.

129. Volonte D, Galbiati F, Lisanti MP (1999) Visualization of caveolin-1, a caveolar marker protein, in living cells using green fluorescent protein (GFP) chimeras - the subcellular distribution of caveolin-1 is modulated by cell-cell contact. FEBS Lett. 445:431-439.

130. Burstein EA, Vedenkina NS, Ivkova MN (1972) Fluorescence and the location of tryptophan residues in protein molecules. Photochem. Photobio. 18:263-279.

131. Nilsson L, Halle B (2005) Molecular origin of time-dependent fluorescence shifts in proteins. Proc. Natl. Acad. Sci. U.S.A. 102:13867-13872.

132. Moon CP, Fleming KG (2011) Using tryptophan fluorescence to measure the stability of membrane proteins folded in liposomes. Methods. Enzymol. 492:189-211.

133. Ladokhin AS, Jayasinghe S, White SH (2000) How to measure and analyze tryptophan fluorescence in membranes properly, and why bother? Anal. Biochem. 285:235-245.

134. Burstein EA, Abornev SM, Reshetnyak YK (2001) Decomposition of protein tryptophan fluorescence spectra into log-normal components. I. decomposition algorithms. Biophys. J. 81:1699-1709.

135. Reshetnyak YK, Burstein EA (2001) Decomposition of protein tryptophan fluorescence spectra into log-normal components. II. the statistical proof of discreteness of tryptophan classes in proteins. Biophys. J. 81:1710-1734.

136. Reshetnyak YK, Koshevnik Y, Burstein EA (2001) Decomposition of protein tryptophan fluorescence spectra into log-normal components. III. correlation between fluorescence and microenvironment parameters of individual tryptophan residues. Biophys. J. 81:1735-1758.

137. Shinitzky M, Rivnay B (1977) Degree of exposure of membrane proteins determined by fluorescence quenching. Biochemistry. 16:982-986.

138. Holt A, Almeida R, Nyholm T, Loura L, Daily A, Straffhorst R, Rijkers D, Koeppe R, Prieto M, Killian JA (2008) Is there a preferential interaction between cholesterol and tryptophan residues in membrane proteins? Biochemistry. 47:2638-2649.

139. Hope MJ, Ball MB, Mayer LD, Janoff AS, Cullis PR (1986) Generation of multilamellar and unilamellar phospholipid vesicles. Chem. Phys. Lipids. 40:89-90-107.

140. Epand RM (2006) Cholesterol and the interaction of proteins with membrane domains. Progr. Lipid Res. 45:279-294.

141. Helenius A, Fries E, Kartenbeck J (1977) Reconstitution of semliki forest virus membrane. J. Cell. Biol. 75:866-880.

142. Shepherd FH, Holzenburg A (1995) The potential of fluorinated surfactants in membrane biochemistry. Anal. Biochem. 224:21-7.

143. Singh R, Flowers RA,2nd (2010) Efficient protein renaturation using tunable hemifluorinated anionic surfactants as additives. Chem. Commun. (Camb). 46:276-278.

144. Lu RC, Guo XR, Jin C, Xiao JX (2009) NMR studies on binding sites and aggregation-disassociation of fluorinated surfactant sodium perfluorooctanoate on protein ubiquitin. Biochim. Biophys. Acta. 1790:134-140.

145. Machleidt T, Li W, Liu P, Anderson RGW (2000) Multiple domains in caveolin-1 control its intracellular traffic. J. Cell. Biol. 148:17-28.

146. Diefenderfer C, Lee J, Mlyanarski S, Guo Y, Glover KJ (2009) Reliable expression and purification of highly insoluble transmembrane domains. Anal. Biochem. 384:274-8.

147. Studier FW (2005) Protein production by auto-induction in high density shaking cultures. Protein. Expr. and Purif. 41:207-34.

148. Stewart JC (1980) Colorimetric determination of phospholipids with ammonium ferrothiocyanate. Anal. Biochem. 104:10-14.

149. Zhu A, Romero R, Petty HR (2011) An enzymatic colorimetric assay for glucose-6-phosphate. Anal. Biochem. 419:266-270.

150. Schlaad H, You L, Sigel R, Smarsly B, Heydenreich M, Mantion A, Masic A (2009) Glycopolymer vesicles with an asymmetric membrane. Chem. Commun. (Camb). (12):1478-80. doi:1478-1480.

151. Parmar MM, Edwards K, Madden TD (1999) Incorporation of bacterial membrane proteins into liposomes: Factors influencing protein reconstitution. Biochim. Biophys. Acta. 1421:77-90.

152. Greenhut SF, Bourgeois VR, Roseman MA (1986) Distribution of cytochrome b5 between small and large unilamellar phospholipid vesicles. J. Biol. Chem. 261:3670-3675.

153. Ollivon M, Lesieur S, Grabielle-Madelmont C, Paternostre M (2000) Vesicle reconstitution from lipid-detergent mixed micelles. Biochim. Biophys. Acta. 1508:34-50.

154. Chattopadhyay A, London E (1984) Fluorimetric determination of critical micelle concentration avoiding interference from detergent charge. Anal. Biochem. 139:408-412.

155. Gent MP, Prestegard JH (1974) Cholesterol-phosphatidylcholine interactions in vesicle systems. implication of vesicle size and proton magnetic resonance line-width changes. Biochemistry. 13:4027-4033.

156. Huang C, Mason JT (1978) Geometric packing constraints in egg phosphatidylcholine vesicles. Proc. Natl. Acad. Sci. U.S.A. 75:308-310.

157. Zhu A, Romero R, Petty HR (2011) An enzymatic colorimetric assay for glucose-6-phosphate. Anal. Biochem. 419:266-270.

158. Rath A, Glibowicka M, Nadeau VG, Chen G, Deber CM (2009) Detergent binding explains anomalous SDS-PAGE migration of membrane proteins. Proc. Natl. Acad. Sci. U.S.A. 106:1760-1765.

159. Epand RM, Sayer BG, Epand RF (2005) Caveolin scaffolding region and cholesterol-rich domains in membranes. J. Mol. Biol. 345:339-350.

160. Li SW, Song KS, Lisanti MP (1996) Expression and characterization of recombinant caveolin - purification by polyhistidine tagging and cholesterol-dependent incorporation into defined lipid membranes. J. Biol. Chem. 271:568-573.

161. Fujiki Y, Hubbard AL, Fowler S, Lazarow PB (1982) Isolation of intracellular membranes by means of sodium carbonate treatment: Application to endoplasmic reticulum. J. Cell. Biol. 93:97-102.

162. Cymer F, von Heijne G, White SH (2015) Mechanisms of integral membrane protein insertion and folding. J. Mol. Biol. 427:999-1022.

163. Higy M, Junne T, Spiess M (2004) Topogenesis of membrane proteins at the endoplasmic reticulum. Biochemistry. 43:12716-12722.

164. Lerch-Bader M, Lundin C, Kim H, Nilsson I, von Heijne G (2008) Contribution of positively charged flanking residues to the insertion of transmembrane helices into the endoplasmic reticulum. Proc. Natl. Acad. Sci. U.S.A. 105:4127-4132.

165. Pervushin K, Riek R, Wider G, Wuthrich K (1997) Attenuated T2 relaxation by mutual cancellation of dipole-dipole coupling and chemical shift anisotropy indicates an avenue to NMR structures of very large biological macromolecules in solution. Proc. Natl. Acad. Sci. U.S.A. 94:12366-12371.

166. Salzmann M, Pervushin K, Wider G, Senn H, Wuthrich K (1998) TROSY in triple-resonance experiments: New perspectives for sequential NMR assignment of large proteins. Proc. Natl. Acad. Sci. U.S.A. 95:13585-13590.

167. Kay LE, Ikura M, Tschudin R, Bax A (2011) Three-dimensional triple-resonance NMR spectroscopy of isotopically enriched proteins. 1990. J. Magn. Reson. 213:423-441.

168. Grzesiek S, Bax A (1992) An efficient experiment for sequential backbone assignment of medium-sized isotopically enriched proteins. J. Magn. Reson. 99:201-207.

169. Bax A, Ikura M (1991) An efficient 3D NMR technique for correlating the proton and 15N backbone amide resonances with the alpha-carbon of the preceding residue in uniformly 15N/13C enriched proteins. J. Biomol. NMR. 1:99-104.

170. Stephan Grzesiek AB (1992) Improved 3D triple-resonance NMR techniques applied to a 31 kDa protein. J. Magn. Reson. 96:432-440.

171. Delaglio F, Grzesiek S, Vuister GW, Zhu G, Pfeifer J, Bax A (1995) NMRPipe: A multidimensional spectral processing system based on UNIX pipes. J. Biomol. NMR. 6:277-293.

172. Goodard, TD, and Kneller, DG Sparky 3. University of California, San Francisco.

173. WISHART D, SYKES B (1994) The C-13 chemical-shift index - a simple method for the identification of protein secondary structure using C-13 chemical-shift data. J. Biomol. NMR. 4:171-180.

174. Brooks BR, Brooks CL,3rd, Mackerell AD,Jr, Nilsson L, Petrella RJ, Roux B, Won Y, Archontis G, Bartels C, Boresch S, Caflisch A, Caves L, Cui Q, Dinner AR, Feig M, Fischer S, Gao J, Hodoscek M, Im W, Kuczera K, Lazaridis T, Ma J, Ovchinnikov V, Paci E, Pastor RW, Post CB, Pu JZ, Schaefer M, Tidor B, Venable RM, Woodcock HL, Wu X, Yang W, York DM, Karplus M (2009) CHARMM: The

biomolecular simulation program. J. Comput. Chem. 30:1545-1614.

175. Jo S, Kim T, Im W (2007) Automated builder and database of protein/membrane complexes for molecular dynamics simulations. PLoS One. 2:e880.

176. Jo S, Lim JB, Klauda JB, Im W (2009) CHARMM-GUI membrane builder for mixed bilayers and its application to yeast membranes. Biophys. J. 97:50-58.

177. Jo S, Kim T, Iyer VG, Im W (2008) CHARMM-GUI: A web-based graphical user interface for CHARMM. J. Comput. Chem. 29:1859-1865.

178. Jakobsen AF (2005) Constant-pressure and constant-surface tension simulations in dissipative particle dynamics. J. Chem. Phys. 122:124901.

179. Hoover WG (1985) Canonical dynamics: Equilibrium phase-space distributions. Phys. Rev. A 31:1695-1697.

180. Nosé S, Klein ML (1983) Constant pressure molecular dynamics for molecular systems. Mol. Phys. 50:1055-1076.

181. MacKerell AD, Bashford D, Bellott M, Dunbrack RL, Evanseck JD, Field MJ, Fischer S, Gao J, Guo H, Ha S, Joseph-McCarthy D, Kuchnir L, Kuczera K, Lau FT, Mattos C, Michnick S, Ngo T, Nguyen DT, Prodhom B, Reiher WE, Roux B, Schlenkrich M, Smith JC, Stote R, Straub J, Watanabe M, Wiorkiewicz-Kuczera J, Yin D, Karplus M (1998) All-atom empirical potential for molecular modeling and dynamics studies of proteins. J. Phys. Chem. B. 102:3586-3616.

182. Mackerell AD,Jr, Feig M, Brooks CL,3rd (2004) Extending the treatment of backbone energetics in protein force fields: Limitations of gas-phase quantum mechanics in reproducing protein conformational distributions in molecular dynamics simulations. J. Comput. Chem. 25:1400-1415.

183. Klauda JB, Venable RM, Freites JA, O'Connor JW, Tobias DJ, Mondragon-Ramirez C, Vorobyov I, MacKerell AD,Jr, Pastor RW (2010) Update of the CHARMM all-atom additive force field for lipids: Validation on six lipid types. J. Phys. Chem. B. 114:7830-7843.

184. Jorgensen WL, Chandraskhar J, Madura JD, Impey RW, Klein ML (1983) Comparison of simple potential functions for simulating liquid water. J. Chem. Phys. 79:926-935.

185. Ryckaert J, Ciccotti G, Berendsen HJC (1977) Numerical integration of the cartesian equations of motion of a system with constraints: Molecular dynamics of n-alkanes. J. Comp. Phys. 23:327-341.

186. Dolan EA, Venable RM, Pastor RW, Brooks BR (2002) Simulations of membranes and other interfacial systems using P2(1) and pc periodic boundary conditions. Biophys. J. 82:2317-2325.

187. Steinbach PJ, Brooks BR (1994) New spherical-cutoff methods for long-range forces in macromolecular simulations. J. Comput. Chem. 15:667-683.

188. Essman U, Perera L, Berkowitz ML, Darden T, Lee H, Pedersen LG (1995) A smooth particle mesh ewald method. J. Chem. Phys. 103:8577-8593.

189. Kräutler V, van Gunsteren WF, Hünenberger PH (2001) A fast SHAKE: Algorithm to solve distance constraint equations for small molecules in molecular dynamics simulations. J. Comput. Chem. 22:501-508.

190. Shan Y, Klepeis JL, Eastwood MP, Dror RO, Shaw DE (2005) Gaussian split ewald: A fast ewald mesh method for molecular simulation. J. Chem. Phys. 122:54101.

191. Tuckerman M, Berne BJ, Martyna GJ (1992) Reversible multiple time scale molecular dynamics. J. Chem. Phys. 97:1990-2001.

192. Shen Y, Delaglio F, Cornilescu G, Bax A (2009) TALOS+: A hybrid method for predicting protein backbone torsion angles from NMR chemical shifts. J. Biomol. NMR. 44:213-223.

193. Gallop JL, McMahon HT (2005) BAR domains and membrane curvature: Bringing your curves to the BAR. Biochem. Soc. Symp. (72):223-231.

194. White SH, Wimley WC (1999) Membrane protein folding and stability: Physical principles. Annu. Rev. Biophys. Biomol. Struct. 28:319-365.

195. Bernatchez PN, Bauer PM, Yu J, Prendergast JS, He P, Sessa WC (2005) Dissecting the molecular control of endothelial NO synthase by caveolin-1 using cell-permeable peptides. Proc. Natl. Acad. Sci. U.S.A. 102:761-766.

196. Wanaski SP, Ng BK, Glaser M (2003) Caveolin scaffolding region and the membrane binding region of SRC form lateral membrane domains. Biochemistry. 42:42-56.

197. Zhu Q, Casey JR (2007) Topology of transmembrane proteins by scanning cysteine accessibility mutagenesis methodology. Methods. 41:439-450.

198. Ohnishi S, Hays A, Hagenbuch B (2014) Cysteine scanning mutagenesis of transmembrane domain 10 in organic anion transporting polypeptide 1B1. Biochemistry. 53:2261-2270.

199. Gagnon DG, Holt A, Bourgeois F, Wallendorff B, Coady MJ, Lapointe JY (2005) Membrane topology of loop 13-14 of the Na+/glucose cotransporter (SGLT1): A SCAM and fluorescent labeling study. Biochim. Biophys. Acta. 1712:173-184.

200. Pavlov PF, Glaser E (2002) Probing the membrane topology of a subunit of the mitochondrial protein translocase, Tim44, with biotin maleimide. Biochem. Biophys. Res. Commun. 293:321-326.

201. Marolda CL, Li B, Lung M, Yang M, Hanuszkiewicz A, Rosales AR, Valvano MA (2010) Membrane topology and identification of critical amino acid residues in the wzx O-antigen translocase from escherichia coli O157:H4. J. Bacteriol. 192:6160-6171.

202. Loo TW, Clarke DM (1995) Membrane topology of a cysteine-less mutant of human P-glycoprotein. J. Biol. Chem. 270:843-848.

203. Byrne DP, Dart C, Rigden DJ (2012) Evaluating caveolin interactions: Do proteins interact with the caveolin scaffolding domain through a widespread aromatic residue-rich motif? PLoS One. 7:e44879.

204. Collins BM, Davis MJ, Hancock JF, Parton RG (2012) Structure-based reassessment of the caveolin signaling model: Do caveolae regulate signaling through caveolin-protein interactions? Dev. Cell. 23:11-20.

205. Lokappa SB, Nagaraj R (2012) Interaction of peptides spanning the transmembrane domain of caveolin-1 with model membranes. J. Pept. Sci.18:696-703.

206. Sowmya BL, Jagannadham MV, Nagaraj R (2006) Interaction of synthetic peptides corresponding to the scaffolding domain of caveolin-3 with model membranes. Biopolymers. 84:615-624.

207. Nelson SC, Neeley SK, Melonakos ED, Bell JD, Busath DD (2012) Fluorescence anisotropy of diphenylhexatriene and its cationic trimethylamino derivative in liquid dipalmitoylphosphatidylcholine liposomes: Opposing responses to isoflurane. BMC Biophys. 5:5-1682-5-5.

208. Rui H, Root KT, Lee J, Glover KJ, Im W (2014) Probing the U-shaped conformation of caveolin-1 in a bilayer. Biophys. J. 106:1371-1380.

209. Pike LJ, Han X, Chung KN, Gross RW (2002) Lipid rafts are enriched in arachidonic acid and plasmenylethanolamine and their composition is independent of caveolin-1 expression: A quantitative electrospray ionization/mass spectrometric analysis. Biochemistry. 41:2075-2088.

210. Olsen BN, Bielska AA, Lee T, Daily MD, Covey DF, Schlesinger PH, Baker NA, Ory DS (2013) The structural basis of cholesterol accessibility in membranes.

Biophys. J. 105:1838-1847.

211. Zhu Q, Lee DW, Casey JR (2003) Novel topology in C-terminal region of the human plasma membrane anion exchanger, AE1. J. Biol. Chem. 278:3112-3120.

212. Daly TA, Wang M, Regen SL (2011) The origin of cholesterol's condensing effect. Langmuir. 27:2159-2161.

213. Hung WC, Lee MT, Chen FY, Huang HW (2007) The condensing effect of cholesterol in lipid bilayers. Biophys. J. 92:3960-3967.

214. Couet J, Sargiacomo M, Lisanti MP (1997) Interaction of a receptor tyrosine kinase, EGF-R, with caveolins - caveolin binding negatively regulates tyrosine and serine/threonine kinase activities. J. Biol. Chem. 272:30429-30438.

215. Bass RB, Coleman MD, Falke JJ (1999) Signaling domain of the aspartate receptor is a helical hairpin with a localized kinase docking surface: Cysteine and disulfide scanning studies. Biochemistry. 38:9317-9327.

216. Iwaki S, Tamura N, Kimura-Someya T, Nada S, Yamaguchi A (2000) Cysteine-scanning mutagenesis of transmembrane segments 4 and 5 of the Tn10-encoded metal-tetracycline/H+ antiporter reveals a permeability barrier in the middle of a transmembrane water-filled channel. J. Biol. Chem. 275:22704-22712.

217. Stratikos E, Gettins PG (1999) Formation of the covalent serpin-proteinase complex involves translocation of the proteinase by more than 70 A and full insertion of the reactive center loop into beta-sheet. Proc. Natl. Acad. Sci. U.S.A. 96:4808-4813.

218. .Borochov H, Shinitzky M (1976) Vertical displacement of membrane proteins mediated by changes in microviscosity. Proc. Natl. Acad. Sci. U.S.A. 73:4526-4530.

219. Neumoin A, Arshava B, Becker J, Zerbe O, Naider F (2007) NMR studies in dodecylphosphocholine of a fragment containing the seventh transmembrane helix of a G-protein-coupled receptor from saccharomyces cerevisiae. Biophys. J. 93:467-482.

220. Zamoon J, Mascioni A, Thomas DD, Veglia G (2003) NMR solution structure and topological orientation of monomeric phospholamban in dodecylphosphocholine micelles. Biophys. J. 85:2589-2598.

221. Hsu ST, Breukink E, Bierbaum G, Sahl HG, de Kruijff B, Kaptein R, van Nuland NA, Bonvin AM (2003) NMR study of mersacidin and lipid II interaction in dodecylphosphocholine micelles. conformational changes are a key to antimicrobial activity. J. Biol. Chem. 278:13110-13117.

222. Beswick V, Guerois R, Cordier-Ochsenbein F, Coic YM, Tam HD, Tostain J, Noel JP, Sanson A, Neumann JM (1999) Dodecylphosphocholine micelles as a membrane-like environment: New results from NMR relaxation and paramagnetic relaxation enhancement analysis. Eur. Biophys. J. 28:48-58.

223. Whitmore L, Wallace B (2004) DICHROWEB, an online server for protein secondary structure analyses from circular dichroism spectroscopic data RID C-5651-2008 RID C-3753-2008. Nucleic. Acids. Res. 32:W668-W673.

224. Nilsson I, Saaf A, Whitley P, Gafvelin G, Waller C, von Heijne G (1998) Proline-induced disruption of a transmembrane alpha-helix in its natural environment. J. Mol. Biol. 284:1165-1175.

225. von Heijne G (1991) Proline kinks in transmembrane alpha-helices. J. Mol. Biol. 218:499-503.

226. Vivian JT, Callis PR (2001) Mechanisms of tryptophan fluorescence shifts in proteins. Biophys. J. 80:2093-2109.

227. Moro F, Goni FM, Urbaneja MA (1993) Fluorescence quenching at interfaces and the permeation of acrylamide and iodide across phospholipid bilayers. FEBS. Lett. 330:129-132.

Kyle T. Root
Department of Chemistry • Lehigh University

EDUCATION

Ph.D. Chemistry 2016
Lehigh University, Bethlehem, PA
Thesis Advisor: Kerney Jebrell Glover, Ph.D.
Concentration: Biochemistry

B.S. Chemistry 2009
Mansfield University, Mansfield, PA
Advisor: Anthony Kiessling, Ph.D.

AWARDS

Mansfield University Top Senior Chemistry Student Award 2009
Lehigh University Dean's Summer Fellowship 2012
Lehigh University Department of Chemistry Fellowship 2013

RESEARCH EXPERIENCE

Graduate Research Assistant 2009-2015

Thesis Project: Topological investigation of the integral membrane protein, caveolin-1.
Brief Description: Caveolin-1 is an integral membrane protein that generates membrane invaginations in eukaryotic organisms and has a unique $N_{cyto}C_{cyto}$ topology that is postulated to be important to its function. The depth and orientation of caveolin-1 in model membranes were examined using a suite of biophysical and biochemical techniques. Various lipid or lipid-detergent aggregates were characterized for their suitability as vessels for the study of membrane proteins.

Technical Skills:

Methods

- Mixed lipid-detergent preparation/characterization using dynamic light scattering
- Chromatography: Size exclusion, affinity (Ni-NTA), preparative/analytical HPLC
- Membrane protein aggregation state analysis using analytical ultracentrifuge
- Membrane protein/soluble protein expression/purification/reconstitution
- Extensive experience working with bicellar solutions
- Nuclear magnetic resonance of ^{1}H, ^{19}F, ^{31}P nuclei
- *E. coli* shake flask culture for protein production
- Protein labeling using cysteine reactive probes
- Lipid headgroup modification chemistry
- Liposome preparation/characterization
- Gel electrophoresis/Western blotting
- Molecular cloning/PCR/Mutagenesis
- Circular dichroism spectroscopy
- Fluorescence spectroscopy
- MALDI Mass spectrometry
- UV/Vis spectroscopy

Instrumentation

- GE healthcare Akta prime plus liquid chromatography purification system
- Beckman Coulter Proteome XL-I analytical ultracentrifuge
- ALV/CGS3 goniometer Dynamic Light scattering system
- JASCO J-815 circular dichroism spectrophotometer
- Thermo Bio-mate 3 UV/Vis spectrophotometer
- Shimadzu BioSpec UV/Vis spectrophotometer
- Shimadzu UV-2101 PC spectrophotometer
- Beckman Coulter JE series centrifuges
- Beckman LS6500 scintillation counter
- BD FACSCanto II flow cytometer
- Bruker Biospin 500 MHz NMR
- Bruker microflex MALDI-MS
- Agilent Eclipse fluorometer
- BIORAD ChemiDoc XRS+

Software

- BioRad Image Lab Software
- ChemBioDraw Ultra 13.0
- KaleidaGraph
- Igor Pro

Undergraduate Research Assistant 2008-2009

Advisor: Professor Greg Carson, Ph.D.
Project: Examined the possibility of using *Klebsorbmidium*, a type of acidophilic green algae, as a bioindicator of stream health.

Technical Skills:

Methods

- Field sampling of algae
- Acid digestion techniques for plant matter
- Atomic absorption spectroscopy for analysis of heavy metals

TEACHING EXPERIENCE

Teaching Assistant, Lehigh University, Bethlehem, PA 2009-2012
Courses: General Chemistry Lab I and II
Duties: Grading, lab management, and proctoring.

PEER REVIEWED PUBLICATIONS

Kyle T. Root*, Huan Rui*, Jinwoo Lee, Kerney Jebrell Glover, Wonpil Im. "Probing the U-Shaped Conformation of Caveolin-1 in a Bilayer." *Biophys J.* **106**. 1371. (2014)

Kyle T. Root*, Sarah M. Plucinsky*, and Kerney Jebrell Glover, "Caveolin: Recent Progress in Structure, Topology, and Oligomeric Behavior" *Curr. Top. Membr.* In Press (2014)
*denotes co-first author

MANUSCRIPTS SUBMITTED/IN PREPARATION

Kyle T. Root, and Kerney Jebrell Glover. "Topological Analysis of the Caveolin-1 Scaffolding Domain Helps to Explain Its Multi-Faceted Interactome." *In preparation*. (2015)

Kyle T. Root, Monica D. Rieth, and Kerney Jebrell Glover. "Analysis of the Oligomeric Behavior of Caveolin-1 in Phospholipid Bicelles." *In preparation*. (2015)

Kyle T. Root, and Kerney Jebrell Glover. "Mutation of Proline 110 to Alanine of Caveolin-1 Results in a Modest Change in Tryptophan Accessibility." *In preparation*. (2015)

POSTER PRESENTATIONS

Biophysical Society Conference March 2011
Baltimore Convention Center, Baltimore, MD
Reconstitution and Topological Analysis of Caveolin-1 in Phospholipid Vesicles

Delaware Membrane Protein Symposium May 2011
University of Delaware, Newark, DE
Reconstitution and Topological Analysis of Caveolin-1 in Phospholipid Vesicles

Delaware Membrane Protein Symposium May 2012
University of Delaware, Newark, DE
Determining the Depth of Caveolin-1 in Bicelles

Federation of American Societies for Experimental Biology (FASEB) June 2012
The Westin Resort and Conference Center, Snowmass Village, CO
Determining the Depth of Caveolin-1 in Bicelles

Delaware Membrane Protein Symposium May 2013
University of Delaware, Newark, DE
Determining the Depth of Caveolin-1 in Bicelles

Frontiers in Membrane Protein Structural Dynamics May 2014
The Chicago Hilton**,** Chicago**,** IL
Reconstitution and Topological Analysis of Caveolin-1 in Bicelles

Federation of American Societies for Experimental Biology (FASEB) June 2014
Huntley Lodge, Big Sky, MT
Reconstitution and Topological Analysis of Caveolin-1 in Bicelles

Biophysical Society Conference February 2015
Baltimore Convention Center, Baltimore, MD
Reconstitution and Topological Analysis of Caveolin-1 in Bicelles

PROFESSIONAL SOCIETIES AND AFFILIATIONS

Biophysical Society 2011-2015

REFERENCES

Kerney Jebrell Glover, Ph.D.
Chemistry Department
Lehigh University
6 E. Packer Ave.
Bethlehem PA 18015
Email: kjg206@lehigh.edu

Robert Flowers II, Ph.D.
Chemistry Department
Lehigh University
6 E. Packer Ave.
Bethlehem, PA 18015
Email: rof2@lehigh.edu

Damien Thévenin, Ph.D.
Chemistry Department
Lehigh University
6 E. Packer Ave.
Bethlehem, PA 18015
Email: damien.thevenin@lehigh.edu

Wonpil Im, Ph.D.
Department of Molecular Biosciences
Kansas University
1200 Sunnyside Avenue
Lawrence, KS 66045
Email: wonpil@ku.edu